Cellular Dynamics and Three-Dimensional Refractive Index Distribution Studied with Quantitative Phase Imaging

THÈSE N^{O} 5100 (2011)

PRÉSENTÉE LE 29 JUILLET 2011

À LA FACULTÉ SCIENCES ET TECHNIQUES DE L'INGÉNIEUR
LABORATOIRE D'OPTIQUE APPLIQUÉE PROF. SALATHÉ
PROGRAMME DOCTORAL EN PHOTONIQUE

ÉCOLE POLYTECHNIQUE FÉDÉRALE DE LAUSANNE

POUR L'OBTENTION DU GRADE DE DOCTEUR ÈS SCIENCES

PAR

Nicolas PAVILLON

acceptée sur proposition du jury:

Prof. P. Jacquot, président du jury
Prof. C. Depeursinge, Dr P. Marquet, directeurs de thèse
Prof. P. Magistretti, rapporteur
Prof. P. Picart, rapporteur
Prof. C. Sheppard, rapporteur

ÉCOLE POLYTECHNIQUE
FÉDÉRALE DE LAUSANNE

Suisse
2011

Les sculpteurs des cathédrales gothiques mettaient, dit-on, autant de soin à bien modeler le visage de leur statues, même lorsqu'elles étaient, au sommet de l'édifice, trop éloignées des fidèles pour être visibles dans leurs lignes les plus fines. Le travail trouve sa noblesse à n'être pas toujours utile.

Maurice Pinguet, Le texte Japon, *Seuil, p. 27, 2009.*

Bref, être réaliste, c'est composer avec la nature humaine, au lieu, comme les uns, de la flétrir et de prétendre la corriger par des discours édifiants, ou, comme les autres, de la nier purement et simplement en imputant tous les vices des hommes à un mauvais fonctionnement social.

Alain Finkielkraut, La sagesse de l'amour, *Gallimard, p. 139, 1984.*

Man weiß oder ahnt: wenn das Denken nicht rein und wach und die Verehrung des Geistes nicht mehr gültig ist, dann gehen bald auch die Schiffe und Automobile nicht mehr richtig, dann wackelt für den Rechenschieber des Ingenieurs wie für die Mathematik der Bank und Börse alle Gültigkeit und Autorität, dann kommt das Chaos. Es dauerte immerhin lange genug, bis die Erkenntnis sich Bahn brach, daß auch die Außenseite der Zivilisation, auch die Technik, die Industrie, der Handel und so weiter der gemeinsamen Grundlage einer geistigen Moral und Redlichkeit bedürfen.

Hermann Hesse, Das Glasperlenspiel, *(Suhrkamp, 2002), p. 34, 1943.*

Jamais Rubens ne doutera de la totale inutilité de son travail. Au début, il en fut attristé et se reprocha son immoralisme. mais il finit par se dire : de tous les temps se trouve entièrement contenue dans le monde tel qu'il est aujourd'hui. Par conséquent : rien de plus moral que d'être inutile.

Milan Kundera, L'immortalité, *(Gallimard, trad. Eva Bloch, 1993), p. 428, 1989.*

Résumé

Nous présentons dans ce travail de thèse de doctorat différentes applications pour la microscopie holographique digitale (MHD), une technique d'imagerie basée sur une illumination cohérente qui permet la reconstruction du front d'onde complexe, i.e. l'amplitude et la phase d'un champ électro-magnétique qui a interagit avec le spécimen mesuré. La possibilité de récupérer l'information de phase avec la MHD permet de mesurer des surfaces avec une précision nanométrique, ou de l'employer comme agent de contraste endogène afin d'accéder quantitativement à la morphologie de spécimens biologiques. Cette technique a été développée durant les quinze dernière années pour atteindre actuellement un état mature, de telle manière qu'elle peut être employée pour des applications en métrologie de manière routinière. Nous étudions dans ce travail différentes applications avancées en tirant avantage du potentiel de cette technique, et en se concentrant sur une méthode de mesure par la MHD bien spécifique, qui correspond à une configuration hors-axe. Celle-ci permet de mesurer le front d'onde complexe de manière instantanée grâce à un encodage spatial de l'information, permettant ainsi une détection en temps réel.

Dans une première partie, nous développons des méthodes mathématiques basées sur les fondements de la théorie de l'enregistrement holographique, afin de supprimer l'ordre zéro, qui consiste en des termes en intensité que la détection cohérente doit supprimer pour permettre la reconstruction du front d'onde complexe. Dans le cas particulier de l'holographie hors-axe, l'ordre zéro restreint habituellement la résolution spatiale en raison de l'encodage spatial de l'information du signal cohérent. Nous avons premièrement développé une méthode itérative des relations fondamentales entre les détections cohérentes et incohérentes, afin de graduellement supprimer les termes d'ordre zéro. Dans un deuxième temps, nous avons développé une méthode non-itérative, basée sur des opérateurs non-linéaires. La technique est basée sur le transfert dans un autre espace de filtrage par l'usage du logarithme, qui permet la suppression intrinsèque des termes d'ordre zéros. Les deux méthodes présentent l'avantage de ne se baser sur aucune approximation, impliquant qu'elle peuvent être générales pour toute configuration d'holographie hors-axe. Nous présentons la possibilité de les utiliser sur différents types d'hologrammes, et démontrons que leur emploi dans le contexte

de la microscopie permet d'améliorer la résolution spatiale en holographie, de manière à obtenir des images dont la résolution n'est limitée que par la diffraction.

Dans une seconde partie, nous étudions les applications potentielles pour l'imagerie tridimensionelle grâce à des méthodes de détection cohérente par l'acquisition en série d'images avec une nouvelle méthode de balayage. La combinaison d'une reconstruction tomographique avec de l'imagerie de phase quantitative a montré un potentiel impressionnant dans plusieurs travaux publiés, menant à la mesure de la distribution 3D de l'indice de réfraction au sein de spécimens biologiques, et à de l'imagerie super-résolue en se basant sur un formalisme d'ouverture synthétique. Néanmoins, ces méthodes sont encore soumises à plusieurs limitations, tels que des problèmes pratiques comme les imprécisions mécanique dans les protocoles de mesures, ou la disponibilités d'algorithmes de reconstruction flexibles. Nous étudions ici une nouvelle approche d'acquisition de données, qui permet d'éviter tout mouvement du faisceau d'illumination ainsi que toute rotation de l'échantillon, ce qui permet potentiellement d'apporter un protocole de mesure plus stable. Nous présentons des résultats démontrant la validité de notre principe de mesure, et obtenons des distributions quantitatives d'indice de réfraction sur des grains de pollens.

Dans une troisième partie, nous appliquons la MHD à l'analyse de morphologie et de dynamique cellulaires, concentrée en particulier sur les cellules neuronales. Nous combinons la mesure par la MHD avec des méthodes caractérisées telles que l'analyse par colorant ou la fluorescence quantitative large champ, afin de dériver des indicateurs biologiques pertinents du signal de phase. En interprétant la phase comme un indicateur de régulation volumique cellulaire, nous déduisons des critères pour la détection rapide de la mort cellulaire, permettant de montrer que le suivi de cellules par la MHD mène à une détection de la mort cellulaire durant ses étapes préliminaires, grâce à la détection de mécanismes de dérégulation. En comparant notre méthode avec des contrôles de viabilité cellulaire par colorant, nous montrons que la MHD peut détecter la mort cellulaire typiquement plusieurs heures avant les procédures standard. Nous combinons aussi la MHD avec la mesure de concentrations ioniques intracellulaires par fluorescence, montrant que le signal de phase mesuré sur des cultures neuronales est intimement lié avec l'homéostasie ionique, et en particulier avec les mouvements d'eau à travers la membrane qui accompagnent les courants ioniques tels que le Ca^{2+} ou le Na^{+}. Nous obtenons des signatures en phase typiques liées au pics Ca^{2+} se produisant pendant les potentiels d'action neuronaux durant une stimulation au glutamate, un des neurotransmetteurs les plus répandus dans le système nerveux central.

Mots-clés : Holographie digitale, Microscopie quantitative de phase, holographie hors-axe, Termes d'ordre zéros, Imagerie limitée en diffraction, Imagerie tri-dimensionelle, Tomographie de phase, Biologie cellulaire, Neurosciences, Mort cellulaire, Fluorescence quantitative, Homéostasie ionique.

Abstract

We present in this PhD thesis work various applications of digital holographic microscopy (DHM), an imaging technique based on coherent illumination which enables the recovery of the full complex wavefront, i.e. the amplitude and phase of a wave field which interacted with a specimen. The possibility to retrieve the phase information with DHM allows to measure surfaces with nanometric accuracy, or to employ it as an endogenous quantitative signal to assess the morphology of biological specimens. The technique has been developed during the past fifteen years to reach nowadays a mature state, where it can be used routinely for metrology applications for example. We study in this work advanced applications by taking advantage of this technique, while focusing on a specific measurement method of DHM, namely the off-axis configuration, which makes it possible to measure the complex wave field with one-shot capability through spatial encoding, thus enabling real-time detection.

In a first part, we develop mathematical methods based on the fundamental model of holographic recording to suppress the so-called zero-order, which consists in intensity terms that coherent detection must suppress for complex wave retrieval. In the particular case of off-axis holography, the zero-order terms usually limit the spatial resolution because of the spatial encoding of the coherent signal. We first develop an iterative method which uses the fundamental relations between coherent and incoherent detection, in order to gradually suppress the zero order terms. In a second stage, we develop a non-iterative filtering method, based on nonlinear operators. The technique is based on the transfer to another filtering space through the use of the logarithm, and enables intrinsic suppression of the zero-order terms. Both methods present the advantage of not relying on any approximation, and are thus general for any off-axis holographic configuration. We show their applicability on various hologram types, and demonstrate that in the context of microscopy, their use can increase the spatial resolution of holography, in order to reach diffraction-limited imaging for any magnification.

In a second part, we study potential applications of three-dimensional imaging through coherent detection by employing multiple acquisitions with a new scanning method. The coupling of tomographic reconstruction and quantitative phase imaging showed great potential in various published works, yielding to quantitative 3D refractive index distribution measured

within biological specimens, and super-resolution imaging through synthetic aperture formalism. These methods are however still subjects to many issues, in particular due to practical limitations such as mechanical imprecision in the measurement protocols and the availability of flexible reconstruction algorithms. We study a new data acquisition method which eliminates the necessity of any scanning of the illumination pattern or object rotation during the acquisition, providing potentially a more stable acquisition protocol. We present results proving the principle of our approach by measuring the 3D refractive index distribution of pollen grain.

In a third part, we applied DHM to the analysis of cell morphology and dynamics, applied in particular to neuronal cells. We couple the phase measurement with widely assessed methods such as dye probing or quantitative wide field fluorescence, in order to derive relevant biological indicators from DHM. Through the interpretation of the phase as an indicator of cell volume regulation, we derive criteria for early label-free cell death detection, where we show that cell monitoring with DHM makes it possible to detect cell non-viability at early stage by measuring deregulation mechanisms. We compare our methods with dyes for cell viability assessment, showing that DHM can detect cell death typically hours before usual dye probing procedures. We also couple the phase signal with intracellular ionic concentration imaging through fluorescence, showing that the phase measured on neuron cultures is intimately linked with ionic homeostasis and in particular transmembrane water movements accompanying ionic currents such as Ca^{2+} or Na^{+}. We derive typical phase signatures related to the well-known Ca^{2+} bursts occurring during action potentials in neurons through stimulation with glutamate, one of the major neurotransmitters in the central nervous system.

Keywords: Digital holography, Quantitative phase microscopy, Off-axis holography, Zero-order terms, Diffraction-limited imaging, Three-dimensional imaging, Phase tomography, Cell biology, Neuroscience, Cell death, Quantitative fluorescence, Ionic homeostasis.

Acknowledgements

I would like first to thank my PhD adviser, Prof. Christian Depeursinge, for giving me the opportunity of performing my thesis in the MicroVision and MicroDiagnostics Group (MVD). His physical insight, his open-mindedness and his congenial personality provide an ideal and very pleasant work environment, in which I have been given a remarkable freedom of work. I also would like to thank my co-adviser, Dr. Pierre Marquet, for giving me the possibility of working within the Laboratory of Neuroenergetics and Cellular Dynamics (LNDC). His patience for letting me gradually learn methodologies for research in biology and his stimulating insights gave me the possibility of learning a whole new field with great pleasure.

Thanks to this stimulating environment, I had the opportunity of studying various subjects, and thus collaborating with many different people. I would to thank Prof. Michael Unser and Prof. Chandra Sekhar Seelamantula for the fruitful collaboration on the zero-order suppression through nonlinear filtering, in which the mathematical aspects could not have been solved without them. I also would like to thank the whole team of Lyncée Tec, and in particular Tristan Colomb and Frédéric Montfort for all the insightful discussions and small helping hands which have been extremely valuable to move forward. I would also like to thank specially Yves Emery, Etienne Cuche and Nicolas Aspert for their help and support in testing and improving the setup I used for biological measurements.

I would like to thank the LNDC members Pascal Jourdain and Daniel Boss, for all the insightful discussions, in particular when trying to figure out what could have happened to those poor cells we mistreated. I would also like to thank Aleksandr Benke, for all his hard work on measuring valuable cell dynamics signals, at a period when time was short for me, and thus greatly helping the project to advance. I would like finally to specially thank Corinne Moratal, for all her help and supervision, without which I would not have been able to observe one single living cell.

My thanks go also specially to the whole MVD group. In the “Real3D” team, I would like to thank Cristian Arfire for his great help in the iterative zero-order suppression project, Isabelle Bergoënd for her supervision, Shan S. Kou for all the very pleasant and instructive discussions

and specially Jérôme Parent for his mechanical design on the Zeiss microscope, that I could use during my whole PhD without daring to think about changing anything thanks to the very stable and modular design I have been granted. Even though we did not have the pleasure of working more closely, I would like to thank Olivier Seydoux, Elena Migacheva and Stéphane Chamot for their collaborations and suggestions during those four years. Within the group, my thanks also go specially to Fatih Toy and Yann Cotte, for all the discussions exploring new possibilities with our research, and the sharing of the microscope which could not have gone more smoothly, Jonas Kühn, whose invaluable experience saved me from innumerable mistakes, and Florian Charrière, whose dynamism and stimulating supervision in the past surely contributed to the work I finally performed during my PhD thesis. My final special thoughts then go to my office colleagues, Ata A. Akatay, Yves Delacrétaz and Etienne Shaffer. Many things changed during these four years (office, lab name, the type of noise nuisance due to construction…), but not our team, within which it has always been possible to share respective scientific and technical problems to advance together, while occasionally just chatting to release pressure in an impressive equilibrium. This friendly and collaborative ambiance has been invaluably precious.

Finally, I would like to deeply thank all my close people, family and friends, whose interest or patience (still working on determining which one is more accurate) made me barely feel the loneliness to which PhD studies can sometimes lead. It has always been possible for me to find refreshing ambiance and comfort within this atmosphere. Finally, I would like to thank with all my heart my wife Ruri, as her choices enabled me to pursue my professional goals, while making possible to construct our life together.

瑠利ちゃん、信じてくれたし、一緒の生活が作れたんだ。その間に、世話になって、理想的な暮らしを貰ってきた。瑠利ちゃんが居なければ、その論文ができないと思って、感謝する。 これからも、一緒に続けて貰えたら嬉しくて、愛してる。

Contents

List of Figures

List of Tables

List of Algorithms

List of Symbols

Roman Letters

A	Angular spectrum
c	Speed of light in a given medium, i.e. $c = c_0/n$
F	Fluorescence intensity signal
K_A	Amplitude ratio
$\boldsymbol{k}$	Light wave vector (k_x, k_y, k_z), $k = 2\pi/\lambda$
K_I	Intensity ratio
K_d	Dissociation constant of a chemical reaction
I	Hologram intensity
i	Imaginary number, $\mathrm{i} = \sqrt{-1}$
M	Magnification of an optical system
n	Refractive index
o	Scalar object wave
O	Object wave amplitude
Q_α	Filtered back-projection
r	Scalar reference wave
$\boldsymbol{r}$	Position vector (x, y, z)
R	Reference wave amplitude, *or* Fluorescence ratiometric measurement $R = F_{\lambda_1}/F_{\lambda_2}$
s	Variance
t	Time variable
U_α	Angular projection of a field
V	Fringe visibility
V_m	Cell membrane electric potential
$\boldsymbol{x}$	Unitary vector of the cartesian coordinate system $\boldsymbol{x} = (e_x, e_y, e_z)$
(x, y)	Spatial coordinates (in Fresnel holography, hologram plane)

Greek Letters

α	Rotation angle for tomography
Γ	Mutual coherence function
λ	Wavelength of light
λ_0	Wavelength of light in vacuum
ν	Temporal frequency
φ	Phase value
φ_o	Object wave phase
φ_r	Reference wave phase
ϕ	Azimuthal angle
θ	Off-axis angle
ρ	Radius of curvature
Ψ	Complex field
Ψ_H	Complex field in the recording (hologram) plane
Ψ_I	Complex field in the image plane
σ	Standard deviation
$\boldsymbol{\omega}$	Spatial frequency (ω_x, ω_y)
Δx	Pixel size in the image space (pixel size of detector)
Δx_o	Pixel size in the object plane
Δx_p	Scanning stage displacement
$\Delta\omega_o$	Spatial bandwidth of the object term

Operators Symbols

$[C]$	Concentration of compound C
$\langle\cdot\rangle$	Averaging function
$\bar{f}$	Averaged f
$\hat{g}$	Fourier transform of the function g
$\mathscr{F}$	Fourier transform operator
$\mathscr{C}$	Cepstrum operator
$\mathbb{C}$	Complex set
$\mathbb{N}$	Natural set
$\mathbb{R}$	Real set
$\Re$	Real part of a complex set
$\Im$	Imaginary part of a complex set
$\angle(g)$	Phase of the complex signal g (modulo 2π)
$\emptyset()$	Proportionality function
$*$	Convolution operator
$\star$	Autocorrelation operator

Acronyms

2D	Two-dimensional
3D	Three-dimensional
AM	Acetoxymethyl ester
AMPA(r)	α-amino-3-hydroxy-5-methyl-4-isoxazolepropionic acid (receptor)
ATP	Adenosine triphosphate
Ca^{2+}	Calcium
CCD	Charge-coupled device
Cl^{-}	Chloride
CMOS	Complementary metal-oxide semiconductor
CNS	Central nervous system
CTF	Coherent transfer function
CVR	Cell volume regulation
DFT	Discrete Fourier transform
DIC	Differential interference contrast
DH	Digital holography
DHM	Digital holographic microscopy
DMSO	Dimethyl sulfoxide
DNA	Deoxyribonucleic acid
DNQX	(6,7-dinitroquinoxaline-2,3-dione)
EGTA	Ethylene glycol tetraacetic acid
EPSP	Excitatory post-synaptic potential
FBP	Filtered back-projection
FDT	Fourier diffraction theorem
FFT	Fast Fourier transform
FRET	Fluorescence resonance energy transfer
FST	Fourier slice theorem
FT	Fourier transform (continuous representation)
FWHM	Full width at half-maximum
GABA	γ-aminobutyric acid
HEPES	4-(2-Hydroxyethyl)piperazine-1-ethanesulfonic
HP	High-pass filtering
IPSP	Inhibitory post-synaptic potential
IR	Infrared
K^{+}	Potassium
LED	Light-emitting diode
MK-801	Dizocilpine
MO	Microscope objective
MOPS	3-(N-morpholino)propanesulfonic acid
MP	Membrane potential
Na^{+}	Sodium
NA	Numerical aperture

NL	Nonlinear reconstruction method
NMDA(r)	N-methyl D-aspartate (receptor)
NPL	Numerical parametric lens
OPD	Optical path difference
OPL	Optical path length
PI	Propidium iodide
PMT	Photomultiplier tube
PSF	Point spread function
PZT	Piezo-electric transducer
QPM	Quantitative phase microscopy
RCH	Reference correction hologram
RI	Refractive index
ROI	Region of interest
SBFI	Benzofuran isophthalate
SF	Standard Fourier reconstruction method
SLM	Spatial light modulator
SNR	Signal-to-noise ratio
TIE	Transport intensity equation
UV	Ultraviolet
ZF	Zero-order free reconstruction method

Sources and adaptations

The work presented in chapter 3 is partly based and adapted from:

- N. Pavillon, C. S. Seelamantula, J. Kühn, M. Unser, and C. Depeursinge, "Suppression of the zero-order in off-axis digital holography through nonlinear filtering," *Appl. Opt.* **48** (34), H186–H195 (2009).
- N. Pavillon, C. Arfire, I. Bergoënd, and C. Depeursinge, "Iterative method for zero-order suppression in off-axis digital holography," *Opt. Express* **18** (15), pp. 15 318–15 331 (2010).
- N. Pavillon, C. S. Seelamantula, M. Unser, and C. Depeursinge, "Artifact-free reconstruction from off-axis digital holograms through nonlinear filtering," in *Optics, Photonics, and Digital Technologies for Multimedia Applications*, vol. 7723, 77231U–9, SPIE, Brussels, Belgium (Apr. 2010).
- C. S. Seelamantula, N. Pavillon, C. Depeursinge, and M. Unser, "Exact Complex-Wave Reconstruction in Digital Holography," *J. Opt. Soc. Am. A* **28** (6), pp. 983–992 (2011).

The work presented in chapter 5 is partly based and adapted from:

- N. Pavillon, A. Benke, D. Boss, C. Moratal, J. Kühn, P. Jourdain, C. Depeursinge, P. J. Magistretti, and P. Marquet, "Cell Morphology and Intracellular Ionic Homeostasis explored with a Multimodal Approach combining Epifluorescence and Digital Holographic Microscopy," *J. Biophotonics* **3** (7), pp. 432–436 (2010).
- N. Pavillon, J. Kühn, C. Moratal, P. Jourdain, C. Depeursinge, P. J. Magistretti, and P. Marquet, "Early Cell Death Detection with Digital Holographic Microscopy", (2011), (to be submitted).
- N. Pavillon, J. Kühn, P. Jourdain, C. Depeursinge, P. J. Magistretti, and P. Marquet, "Cell Death and Ionic Regulation Detection with Digital Holographic Microscopy," in *Digital Holography and Three-Dimensional Imaging (DH)*, OSA, DTuC25, Tokyo, Japan (May 2011).

1 Preamble

The work presented in this thesis covers various subjects, which may seem disparate at first sight, although they tend to the same purpose, which consists in employing the various unique features of quantitative phase microscopy (QPM) for cellular dynamics and morphology analysis. The diversity of subjects tackled is in our opinion the symbol of both the great potential of QPM in various fields such as cellular observation or advanced metrology, and of the great amount of work still ahead for scientists in this field, in both fundamental physics and engineering applications. We consider having had the chance of working at several levels of these developments, such as mathematical treatment to improve the reconstruction quality of holograms, advanced microscopy applications for three-dimensional imaging, or biological interpretation of the quantitative phase signal coupled with functional imaging.

The rise in QPM development which occurred in the past years denotes in our opinion the emergence of a new interest for bright field microscopy techniques. While most developments in the past decades occurred in scanned systems, such as confocal, super-resolution or near-field microscopy, often coupled with functional imaging, the ability of recovering quantitative phase information brought a new light to full-field imaging techniques, where valuable information can be retrieved with high acquisition rates through what can be considered as an intrinsic contrast agent. In this context, digital holographic microscopy (DHM) is one of the leading technologies for QPM applications, by providing a reliable way to recover the quantitative phase, while taking advantage of a widely assessed accuracy thanks to its close ties with interferometric methods employed in metrology applications.

Despite the huge efforts deployed in various research groups and its wide potential applications, QPM is still at a development stage, where large industrial and commercial applications have yet to be shown. In particular, the gap between fundamental QPM measurement demonstrated in the nineties and high quality microscopy images with accurate measurement is far from trivial, in particular when rivalling with more widespread techniques. QPM now reached for example fundamental limitations such as spatial resolution of coherent detection or hindered phase accuracy in regards to the light source bandwidth, which have to be overcome for high-end applications.

The work presented in this thesis humbly provides some contributions in this context. In this fashion, part of our work consists in employing finer methods to reduce noise on phase maps obtained through hologram reconstruction, while maintaining the full spatial resolution provided by the optical system. We also investigate a new acquisition approach to enable three-dimensional imaging through QPM, which is inherently a bright field imaging technique which does not fundamentally provide sectioning along the optical axis. Finally, we study the meaning of the phase signal in the context of neuronal dynamics, in order to derive valuable biological information.

All these subjects thus tend to bring part of answers to some of the challenges QPM must face to enlarge its application range. Typically, phase responses from biological specimens can be rather small, so that improving the phase accuracy is of tremendous importance for a better understanding and interpretation of measured signals. Furthermore, three-dimensional imaging is one possibility to solve the fundamental ambiguity of the phase signal between the physical parameters which are the refractive index distribution and the volume of the observed specimen, thus providing further insight for interpretation. The variety of subjects covered in this manuscript is thus symptomatic of the need for combined approaches taking advantage of interdisciplinary solutions to bring QPM to further applications, comprising for instance hardware development for more adapted light sources and detectors, advanced computing approaches to enhance quality of the reconstructed signal, and refined models to improve the understanding of phase measurement.

Structure of the manuscript

We first present in chapter 2 the fundamental concepts employed in our work, which consist essentially in digital holography acquisition and reconstruction methods, and quantitative fluorescence microscopy for live cell monitoring. The main work of this thesis is then presented in chapters 3–5, before providing some concluding remarks in chapter 6.

We first describe in chapter 3 the mathematical developments aiming at suppressing the zero-order in holographic detection, either through an iterative approach, or with nonlinear operators, yielding diffraction-limited imaging for DHM without noise contribution from incoherent terms recorded through interferometry. We then present in chapter 4 our work on optical tomography, where we studied a new data acquisition approach, requiring no beam scanning nor object rotation, contrarily to other methods proposed up to now. We finally present in chapter 5 results employing DHM for neuronal dynamics monitoring, where we combined the QPM measurements with functional imaging, enabling a better understanding of the biological meaning of the phase signal, yielding for example tools for early cell death detection through DHM measurements, or an interpretation of the links between the phase dynamics and ionic homeostasis.

2 Introduction

The purpose of this introductory chapter is to provide the fundamental concepts underlying the main subjects covered in this thesis. As rather various topics are explored in this manuscript, this introduction focuses mainly on the most fundamental fields such as digital holography and fluorescence imaging, while more specialised introductions are provided at the beginning of each chapter, in their respective sections. Specifically, a more detailed discussion about holographic recording conditions is provided in section 3.2 in the context of zero-order suppression, an introduction about tomographic reconstruction techniques is given in subsection 4.1, and fundamentals about neuronal dynamics is provided in subsection 5.1.

The first part of this chapter aims at providing an extensive state of the art about phase imaging and full complex wavefront retrieval techniques, and more specifically about digital holography in section 2.2. However, these research fields have been rapidly growing in the past years, so that an exhaustive literature survey is beyond the scope of this manuscript, even though it is specialised in digital holography applications. The main purpose of this introduction is therefore to provide a global context, and to summarise the main methods and applications employed for detection and reconstruction in this field. Then, a more detailed state of the art is provided for off-axis digital holography in the context of microscopy, the specific field of study of this thesis.

The second part of this introduction, given in section 2.3, is presenting some fundamental aspects about fluorescence imaging, field in which various applications were derived in the past decades, thanks to the development of many specific fluorescent probes for biological sample imaging and probing. This introduction only tends to provide the fundamentals about wide field fluorescence imaging, in order to derive the most important concepts for the specific use in the context of this thesis, which consists in quantitative fluorescence imaging, and intracellular ionic concentration probing.

Finally, in section 2.4, we take the opportunity of generality provided by this introductory chapter to present the different setups used for experiments throughout this thesis. The fact

of presenting all the setups at one place of the manuscript enables comparison between the different configurations, and avoids redundancy.

2.1 Conventions

We first provide in this section the naming conventions and definitions used through this manuscript, by emphasising the conventions used to avoid confusion during the mathematical development. For reference, most of the symbols and acronyms are also given in the list of symbols on page XXI.

Naming conventions

As most of the mathematical notations used in this thesis are representing electromagnetic fields in the context of full wavefront retrieval, it implies that a clear difference between waves and intensities must be made. For this reason, we employ small letters for complex waves, i.e. $u(x,y)$, and capital letters for intensities and real-valued amplitudes, i.e. $U(x,y)$. Furthermore, although wave fields are in general vectorial functions, the equations given in this thesis essentially represent fields in domains where the paraxial approximation holds, so that they can be mainly represented by scalar functions. When required, vectors are represented by bold letters, such as $\mathbf{k} = (k_x, k_y, k_z)$. Finally, the fields denoted in this manuscript generally represent time-averaged values, in the sense that they correspond to fields detectable by sensors, i.e. $u(\boldsymbol{r},t) \equiv \langle u(\boldsymbol{r},t)\rangle_t$, where $\langle\cdot\rangle_t$ represents the averaging on time.

As the main field of this thesis, digital holography, is typically a research topic combining continuous models through wave optics, and discrete ones through digital representation of fields for processing, a clear distinction between continuous and discrete functions is made. Continuous functions are employed with parenthesis, such as $f(x,y)$, while discrete functions use brackets, such as $g[m,n]$. The variable couple (x,y) generally denotes spatial continuous variables, while $[m,n]$ is used in the discrete spatial domain.

Spectral variables make the distinction between the temporal frequency, denoted by ν, and spatial frequencies denoted by $\boldsymbol{\omega} = (\omega_x, \omega_y)$. The distinction between continuous and discrete spatial frequencies is rather loose in the following manuscript, as whenever a Fourier space is expressed, it corresponds in practise to a discrete one, computed from discrete data. This implies that the continuous Fourier transform representation is often used for convenience and clarity of equations, but does not relate to a physical observable.

The scalar product is represented by the point multiplication $(\cdot)$, and denotes the standard Euclidean scalar product. One should note however that this symbol is also loosely used in the manuscript to improve the readability of some equations. It denotes a scalar product only when the two multiplying variables are in bold, and thus represent vectors. On the other hand, most discrete operations imply matrix multiplication, in the sense of pixel-to-pixel multiplication. In this case, this type of discrete operation is denoted by the symbol $(\times)$.

Definitions

For clarity and convenience, we provide here some fundamental definitions of commonly used mathematical operators. Those definitions do not aim at being complete in the sense of a rigorous construction of a mathematical framework, but are only given to avoid any confusion between fundamental notations.

Through this thesis, we employ the asymmetrical definition of the n-dimensional Fourier transform, written as

$$\begin{aligned}\mathscr{F}\left\{g(\boldsymbol{x})\right\}(\boldsymbol{\omega}) &= \hat{g}(\boldsymbol{\omega}) = \int_{-\infty}^{\infty} g(\boldsymbol{x}) e^{-2\pi \mathrm{i}(\boldsymbol{\omega}\cdot\boldsymbol{x})} \mathrm{d}\boldsymbol{x}, \\ \mathscr{F}^{-1}\left\{\hat{g}(\boldsymbol{\omega})\right\}(\boldsymbol{x}) &= \frac{1}{(2\pi)^n} \int_{-\infty}^{\infty} \hat{g}(\boldsymbol{\omega}) e^{2\pi \mathrm{i}(\boldsymbol{\omega}\cdot\boldsymbol{x})} \mathrm{d}\boldsymbol{\omega},\end{aligned} \tag{2.1}$$

where $\boldsymbol{x}$ and $\boldsymbol{\omega}$ are vectors such as $\boldsymbol{x}, \boldsymbol{\omega} \in \mathbb{R}^n$. Similarly, the discrete Fourier transform (DFT) is defined as

$$\begin{aligned}\mathrm{DFT}\left\{g[\boldsymbol{n}]\right\}[\boldsymbol{\omega}] &= \hat{g}[\boldsymbol{\omega}] = \sum_{\boldsymbol{n}=0}^{N-1} g[\boldsymbol{n}] e^{-\frac{2\pi \mathrm{i}}{N}\boldsymbol{\omega}\cdot\boldsymbol{n}} \\ \mathrm{DFT}^{-1}\left\{h[\boldsymbol{\omega}]\right\}[\boldsymbol{n}] &= \frac{1}{N} \sum_{\boldsymbol{\omega}=0}^{N-1} g[\boldsymbol{n}] e^{\frac{2\pi \mathrm{i}}{N}\boldsymbol{\omega}\cdot\boldsymbol{n}}\end{aligned} \tag{2.2}$$

where the vectorial notation of sums refers to multiple summations over every dimensions. One should note that we employ the hat ($\hat{}$) notation loosely to denote the transformation to the reciprocal domain for both continuous and discrete representations. We also distinguish between strict spatial frequencies denoted by $\boldsymbol{\omega}$, and defined as $\omega_x = 1/x$, and projections of k-vectors, expressed as $k_x = 2\pi/\lambda \cdot \sin\alpha$, where α is the projection angle on the considered axis.

In several places in the manuscript, the standard deviation is used as an indicator of noise contribution on the recorded data. In this context, we employ the unbiased definition of the standard deviation, which is defined as

$$s = \sqrt{\frac{1}{N-1} \sum_{n=0}^{N-1} \left(x[n] - \overline{x}\right)^2}, \quad \overline{x} = \frac{1}{N} \sum_{n=0}^{N-1} x[n]. \tag{2.3}$$

As the experimental data often consists in 2-dimensional images, the standard deviation is to be understood in this case as the one-dimensional standard deviation of the samples contained in the two-dimensional data set $M \times N$, which can be defined as

$$\begin{aligned}s &= \sqrt{\frac{1}{MN-1} \sum_{m=0}^{M-1} \left(\sum_{n=0}^{N-1} \left(x[m,n] - \overline{x}\right)^2 \right)}, \\ \overline{x} &= \frac{1}{MN} \sum_{m=0}^{M-1} \left(\sum_{n=0}^{N-1} x[m,n] \right).\end{aligned} \tag{2.4}$$

2.2 Digital holography

At the time of its discovery, holography brought new perspectives to optics, by providing the possibility of reconstructing wavefronts physically, through the recording of the interference pattern generated by the diffraction of an object on a plate, and the ability of generating of the wavefront by illuminating the plate, providing a three-dimensional image through propagation of the wave field. Various factors however made the development of the technique complicated, such as the difficulties of employing sufficiently coherent light sources, and the availability of proper photo-sensible materials with satisfying resolutions and dynamic ranges. Digital holography (DH) was then mainly developed in the nineties, renewing the wide interest for this technique by making its application far easier through the use of highly coherent sources such as lasers, developed in the meantime, and the availability of digital detectors and fast computers. The use of digital means enabled the development of wavefront processing through numerical computation of the propagation of fields. The main feature provided by DH is thus the capability to recover the quantitative phase of a recorded wave, or more generally to retrieve the full complex—amplitude and phase—information of a wavefront. This enabled the possibility of quantitative phase imaging, as employed for nearly transparent objects such as biological samples, or high-resolution topographic imaging when retrieving the wavefront of the light reflected from a sample, enabling dynamic characterisation in the tens of nanometre range, or even below.

In this section, we first discuss in subsection 2.2.1 the main methods developed in the field of microscopy for phase imaging, and situate digital holography in this context. A more detailed analysis is then made about interferometric techniques, enabling the possibility of classifying the various methods more closely related to digital holography. Then, in subsection 2.2.2, the fundamental principles of holography are presented, by taking a historical point of view. This approach makes it possible to discuss the concepts of holography in a general way, in order to provide a general framework for interferometric techniques. We then present in subsection 2.2.3 the main consequences of using a digital detector for holographic measurements, and present the main steps leading to the development of DH. We next present in details in subsection 2.2.4 the various standard experimental configurations for hologram recording and the reconstruction methods for off-axis digital holography in subsection 2.2.5. On a second stage of this introduction, we discuss in subsection 2.2.6 the application of digital holography for microscopy, where high-resolution imaging brings new challenges for this detection method. Finally, in subsection 2.2.7 we provide some examples of typical applications of DH and DHM, in the perspectives of their specific features compared to other imaging technologies.

2.2.1 Phase imaging

Digital holography is essentially a technique which enables the reconstruction of the complete information of the recorded wavefront, usually in terms of amplitude and phase. Con-

sequently, it enables the full-field recovery of quantitative information, which can be used for imaging purposes. We therefore briefly discuss here as an introduction of the state of the art the various possibilities which were developed in the past for phase-contrast imaging and phase measurement.

Developing methods to access the phase information for imaging purposes has been investigated for a long time, as biological specimens were providing only a very low contrast in standard microscopy as they possess a weak absorption. Furthermore, light detectors, would they be digital detectors, photographic films or the human eye, are sensitive only to the intensity of light, so that it is necessary to encode in a way or another the phase information into intensity.

The first method was developed by F. Zernike as phase-contrast microscopy [Zer42b; Zer42a; Zer55]. It is based on the principle of constructive and/or destructive interference between the wave diffracted by the object and the non-diffracted part, thus encoding the phase shifts into intensity contrast. The imaging system relies on a standard illumination scheme in microscopy such as Köhler illumination, with the particularity that the illumination is generated in an annular shape. It is therefore possible to separately process the non-diffracted background light (zero-order), defined as a ring of spatial frequencies in the back focal plane of the objective, from the light diffracted by the sample. Inducing a phase delay on the background light generates in the imaging plane constructive or destructive interference between the zero-order and the diffracted light, thus encoding phase shifts induced by the sample as intensity values. Zernike's phase-contrast images present a typical profile, where the intensity is proportional to the amount of refractive index (RI) variation in the specimen, providing a high-pass version of the RI distribution.

This discovery enabled the observation of cellular preparations with high contrast, and paved the way to modern cell biology. Through the years, others phase imaging methods were proposed, essentially with incoherent light at first, as lasers were still at their first steps. Moreover, the purpose was to employ available microscope systems for imaging, encouraging the addition of components in existing structures instead of developing new ones. In the fifties, a method called differential interference contrast (DIC) was proposed, which relies on polarised light (typically generated with a linear polariser). The illumination beam is separated in two components with for example a Wollatson prism, so that beams are passing at slightly different positions in the sample before recombination [All69]. As the two beams wandered through slightly different optical path lengths, the recombination (made by a linear polariser used as an analyser) generates again constructive and destructive interference, thus encoding phase in an intensity image. DIC imaging is characterised by a shear direction, thus providing a differential contrast in one direction. More recently, efforts have been made to employ DIC as a quantitative phase imaging technique [Arn04; Shr06; Fu10].

In the context of incoherent imaging, another approach consists in using of so-called transport-intensity equations (TIE), which model the propagation of light. Through the acquisi-

tion of several images taken at different depths along the optical axis and around the focus position, one can recover a quantitative phase [Bar98; Pag98; Til00]. These techniques are characterised by phase images which do not suffer from phase wrapping like interference techniques, at the cost of requiring several images with precise shifts in the object space.

Finally, methods based on wavefront characterisation, such as Shack-Hartmann detectors, were recently applied to phase imaging, thanks to the development of high resolution sensors [Bon09]. Phase recovery is based on focusing the beam into multiple focal points with a microlens array or a diffractive element, for example. The position of the focal point can be detected with a 2D sensor, and will depend on the local phase profile of the wavefront. A proper algorithm can therefore reproduce indirectly a phase map from the position information of the various focal points.

On the other hand, algorithmic methods, such as phase-retrieval, have also been developed [Ger72; Fie82]. As TIE, these approaches are also based on retrieving the phase from intensity measurements, but take a more computational approach than the use of physical propagation models as employed by TIE reconstruction. The phase retrieval is employed through constrained iterative treatment in the Fourier domain of the intensity measurement, converging to the expected phase. Compared to TIE, it is thus simpler to acquire images, as there is no requirement for precise positions of acquisition on the optical axis. However, due to the purely computational treatment of the signal, the accuracy in phase recovery is usually smaller, and difficult to employ as quantitative data.

In parallel to the methods described above, which are based essentially on incoherent light and intensity measurements, the development of coherent light sources enabled the use of interferometric methods for phase imaging, as described in details in subsections 2.2.2–2.2.5. The phase recovery is based on the interference between a so-called object wave, which interacted with the sample, and a reference wave which profile is well controlled. From this interferogram, the quantitative phase information can be extracted through spatial separation [Lei62; Cuc99b], or temporal encoding [Car66; Yam97].

One specific type of applications of holography should however be mentioned here in more details, as it is not treated in the following subsections, consisting in what could be considered as hybrid methods, where coding and decoding of the amplitude and phase information is performed through both temporal and spatial processing. A noticeable application of this approach consists in scanning holography [Ind00; Ind01], where the interference is performed in the object space instead of the image space, and can thus be considered as structured illumination holography. The method thus requires sample scanning in the fringe pattern for data acquisition, and temporal demodulation of the acquired data. One striking property of this approach is its capability of retrieving the phase information from incoherent light, such as the one emitted by fluorophores [Ind06b; Ros07; Ros08]. As the method is based on generating an interference pattern in the object space, it is also particularly suited for refined structured illumination analysis through pupil illumination design [Ind06a; Ind07]. Another

approach of hybrid method was recently proposed by Takeda *et al.* and coined as coherence holography [Tak05], where full wavefront information can be retrieved indirectly through the measurement of the mutual coherence function, instead of coherent cross-correlation terms as in standard holography.

In the paragraphs above, we presented some of the main methods employed for phase imaging in the context of microscopy. One should note however that non-imaging methods are also possible, in particular in the context of profilometry, where the phase signal corresponds to changes in height of the specimen. In this context, interferometry is widely used, also in application employing white light interferometry coupled with vertical scanning [Wya02]. One could also mention fringe projection techniques, which are not strictly spoken phase imaging techniques, but enables the retrieval of profiles under similar reconstruction processes as spatially-encoded holography [Su01; Hua03].

2.2.2 Principles of holography

Holography is a technique which concepts and first experimental demonstrations were developed by D. Gabor in 1948 [Gab48]. In this seminal work, the main purpose of employing holographic methods was to exploit its imaging capability without using any physical imaging components such as lenses, in a so-called lensless configuration. The main application at the beginning was the ability to improve spatial resolution of detection for electronic imaging, for which lenses are hardly available [Gab49].

Holography relies on an interferometric principle for detection, where two coherent waves interfere on the detection plane. The interference creates a pattern in intensity which can be recorded by a photo-sensitive material plate; one of the two waves is coming from an observed object, and corresponds to the wave diffracted by the sample under a given illumination. On the other hand, the second wave is classically taken as a reference, and thus corresponds to a well characterised wave. Typically, the interference generates on the photosensitive material a diffraction pattern which can be considered as a diffractive element. Therefore, if one illuminates the developed plate with a wave identical to the reference, the resulting diffracted wavefront will contain a replica of the object wave used to act on the plate. This exciting feature led to the first interests for this method, where a full wavefront could be recorded and regenerated.

The physical modelling of this process can be described simply by the coherent addition of the two waves, where it is considered in first approximation that they are perfectly coherent and with identical polarisation, giving

$$\begin{aligned} I(x,y,z_0) &= \left| o(x,y,z_0) + r(x,y,z_0) \right|^2, \\ &= (o+r)(o+r)^*, \\ &= |o|^2 + |r|^2 + o^* r + o r^*, \end{aligned} \tag{2.5}$$

where I is the intensity pattern acting on the plate, o is the wave diffracted by the object, and r is the reference wave. The intensity pattern is defined in (x, y) coordinates at a plane z_0, corresponding to the position of the photo-sensitive plate. In the following, as the detection is made on a given plane, this dimension will often be omitted, by considering that the detection plane is perpendicular to the optical axis z. One can identify in Eq. (2.5) four terms; the two first ones depend only on one interfering wave, and are thus considered as autocorrelation terms. They correspond to intensities as employed in incoherent imaging. The two others are cross-terms of the process of detection in intensity, and correspond mathematically to cross-correlations. They appear through the coherent detection of holography, and contain the phase information provided by holographic recording.

As the two waves have different phase advances at a given point in the (x, y) plane, the two cross-terms will generate variations in intensity leading to interference fringes, corresponding to variations between in-phase and out-of-phase positions. This can be better identified mathematically by expressing the object and reference waves in amplitude and phase, i.e. $o = Oe^{\mathrm{i}\varphi_o}$, $r = Re^{\mathrm{i}\varphi_r}$, and modifying Eq. (2.5) to

$$\begin{aligned} I &= \left|Oe^{-\mathrm{i}\varphi_o} + Re^{-\mathrm{i}\varphi_r}\right|^2, \\ &= O^2 + R^2 + ORe^{\mathrm{i}(\varphi_o-\varphi_r)} + ORe^{-\mathrm{i}(\varphi_o-\varphi_r)}, \\ &= O^2 + R^2 + 2OR\cos(\varphi_o - \varphi_r), \\ &= I_0 + I_1\cos(\Delta\varphi), \end{aligned} \tag{2.6}$$

The first term $I_0 = O^2 + R^2$ corresponds to the intensity background, $I_1 = 2OR$ is related to the fringes visibility, and $\Delta\varphi = \varphi_o - \varphi_r$ is the phase difference between the two waves at a given (x, y) position. This representation shows in a more explicit way that holographic recording possesses the ability of recording the relative phase information between the two interfering waves, along with their respective amplitudes, in an intensity pattern.

However, as it can be seen in Eq. (2.6), the various real and imaginary components of the two waves are mixed in the recording, so that recovery of a specific information is not trivial. In the case of a physical reconstruction through illumination of the plate, the process can be understood by considering the fringe pattern generated by the recorded interference as a diffraction grating, so that the illumination with a wave $u(x, y)$ will diffract in various directions. By using this model, the illumination of the hologram corresponds to a multiplication, giving

$$u \cdot I = u(|o|^2 + |r|^2) + o^* r u + o r^* u, \tag{2.7}$$

where one can identify in the last terms of the right-hand of Eq. (2.7) the original recorded wavefront multiplied by the illumination wave. This implies that the holographic process makes it possible to recover the full wavefront information of a given electromagnetic wave.

The different terms in Eq. (2.7) show the fundamental principle of reconstruction of a hologram, where the information about the wavefront used for recording will propagate again under illumination of the plate, as shown in the last term of the right hand of the equation. At the same time, a replica of the illumination wave, modified in amplitude, and the complex conjugate of the recording wave propagate along with the original wavefront. This representation also explains the nomenclature classically employed to refer to the various terms. The first term of Eq. (2.7) is often called the zero-order term, as it corresponds to the non-diffracted beam in analogy with diffraction gratings formalism. Similarly, the two last terms are usually called the first order terms (+1 and -1).

Even though Eq. (2.7) provides propagating terms corresponding to wave fields, the recovery of the object wave does not appear through this model. The imaging capabilities emerge when the illumination wavefront matches the profile of the original reference wave, namely $u = r$. In this case Eq. (2.7) simplifies to

$$\begin{aligned} r \cdot I &= r(|o|^2 + |r|^2) + o^* r r + o r^* r, \\ &= (O^2 + R^2) r + o^* r^2 + R^2 o, \end{aligned} \tag{2.8}$$

where one can identify in the last term the original object wavefront, multiplied by a real term, corresponding to the reference intensity. This possibility of recovering the original information of an unknown wavefront leads to the lensless imaging capability, as discussed in the next paragraph.

Lensless (Gabor) holography

The equations described above are very general to any holographic recording, and do not take into account any considerations about how the recording and reconstruction process is implemented. We consider here the first holographic implementation proposed by Gabor, classically called lensless or Gabor configuration [Gab49]. In this geometry, the sample is illuminated with a diverging wave, which is diffracted by the object. After the sample, two components are therefore propagating, consisting in two spherical waves with different curvature radii, defined by their distance to the detector, d_r and d_o, where the non-diffracted part acts as a reference wave through a so-called self-referenced beam. The two waves then interfere on the detection plane, thus creating an interference pattern. These recording conditions are presented in Fig. 2.1(a), where the spherical illumination wave and the diffracted object wavefront are represented. Then, as expressed in Eq. (2.8), the illumination of the plate after development with a divergent wave identical to the reference wave generates a diffraction pattern proportional to the original object wave. As the object wave is a diverging wave emanating from the sample, the forward propagating wave generated by the diffraction of the illuminating wave on the plate identically generates a diverging wave, as shown in Fig. 2.1(b), thus generating a virtual image behind the plate, at a distance $d_i = -d_o$. On the other hand, the opposite diffraction order generates a converging wave, which creates a real image at the opposite position d_i. The fact of generating both a virtual image behind the plate and a real

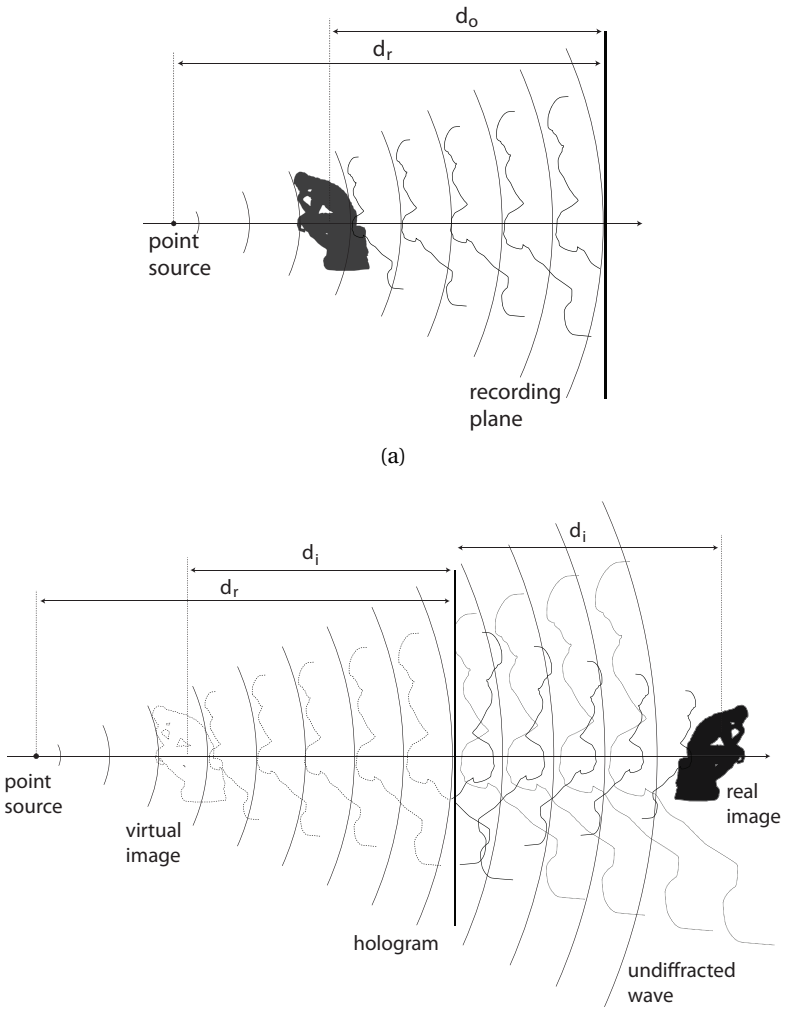

Figure 2.1: Lensless holography configuration. (a) Recording conditions, where a divergent wave illuminates the specimen. The reference point source and the diffracted wave from the specimen then interfere as two spherical waves. (b) Reconstruction, where a replica of the reference wave is employed, leading to imaging the object encoded in the hologram.

image in front of it led to the commonly used name of twin-image for the second complex term of Eq. (2.8), as already coined by Gabor.

The lensless imaging capabilities of holography go beyond the simple reproduction of the wavefront employed to record the hologram, as it is possible to magnify the original sample. This can be performed by employing illumination waves with different curvature radii between recording and reconstruction, either by changing the position of the point source, or by employing another wavelength for hologram illumination. As the illuminating wave possesses another curvature than the reference wave used for recording, the diffraction orders propagate in directions which will be determined by the difference of curvature between the

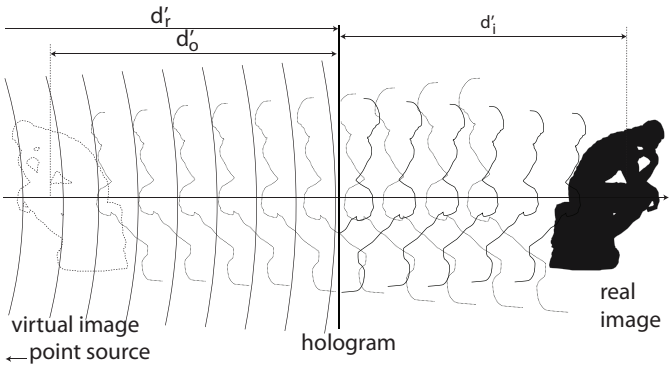

Figure 2.2: Lensless holography using magnification by employing an illumination wave with a different curvature than the one employed for recording.

recording and illuminating waves, and thus focus at a different position. One can show that the lateral magnification of the holographic imaging process can be expressed as [Goo96]

$$M_{\text{lat}} = \left| 1 + d_o \left(\frac{\lambda'}{\lambda} \frac{1}{d'_r} - \frac{1}{d_r} \right) \right|^{-1}, \tag{2.9}$$

where d_r, d'_r are respectively the positions of the recording and illuminating point sources, d_o is the distance of the object, and λ, λ' are respectively the recording and illuminating wavelength. This reconstruction process is illustrated in Fig. 2.2, where a point source with its position defined as $d'_r > d_r$ is employed, thus yielding a magnified image,

As it was already identified by Gabor in his first articles, the imaging possibilities of holography are greatly reduced in quality because of the other terms present in the propagation of the wavefront diffracted by the photo-sensitive plate, and especially because of the twin-image, which profile can be highly irregular depending on the measured object, and therefore disrupts the image. Several methods to circumvent this issue were proposed, and are discussed in the following sections. These issues, added to the fact that usually no quantitative information can be extracted from hologram recorded in this geometry, make the lensless configuration less efficient compared to other methods. Nevertheless, it is still nowadays used in various applications fields, especially in particular cases, such as harsh environments where its simplicity and robustness of implementation enables stable measurements [Xu01], or when compactness is a major design requirement [Su10].

Off-axis configuration

As mentioned above, the main problem in holography in its first developments was the disturbance caused by the twin-image. Although some methods were already proposed, such as employing a slightly defocused print of the hologram [Gab49], this issue was greatly undermining the performances of holography. The main breakthrough for solving this issue was brought by Leith and Upatniek, who proposed to use a reference wave having a slightly

different propagation direction than the object wave [Lei62], leading to the name of off-axis geometry. This idea was first proposed in the context of signal processing, where having an angle between the two waves corresponds to modulating the cross-correlation terms containing the complex wavefront information. This concept was then formalised more precisely along with examples of implementation [Lei64]. The off-axis approach has then been further analysed on a computational point of view [Wol70a] with a formalism based on diffraction, and used for the first quantitative phase measurements to our knowledge [Car70].

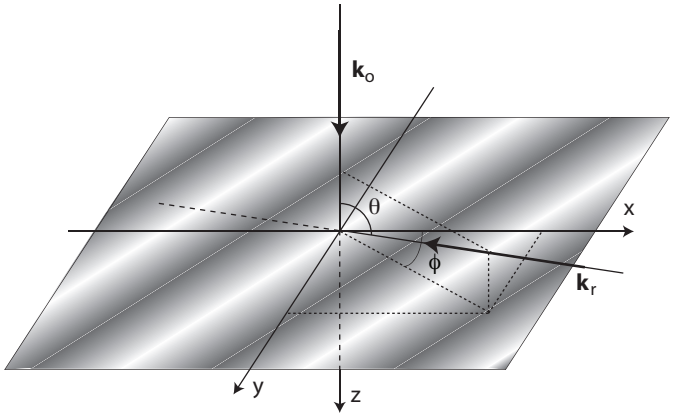

Figure 2.3: Definition of the coordinate system and angles for off-axis holography.

In order to express mathematically the introduction of an angle between the two propagation directions, we define the coordinate system employed at the detection plane. We consider, in regards to the optical axis z, an inclination angle θ and an azimuthal angle ϕ, as shown in Fig. 2.3. In order to simplify the expressions, the object wave propagation direction $\boldsymbol{k}_0$ is considered to be collinear to the optical axis. This corresponds to the ideal recording case, where the detector is parallel to the imaging plane of the object wave, thus providing optimal imaging conditions.

Introducing a tilt in the reference wave corresponds to multiplying its expression with a linear phase function, which direction is defined by the vector $\boldsymbol{k}_r$. The tilted reference wave hence becomes $r_t = re^{-\mathrm{i}(\boldsymbol{k}_r \cdot \boldsymbol{x})}$, where $\boldsymbol{x} = (e_x, e_y, e_z)$ is the unitary vector of the Cartesian coordinate system. The recording geometry is represented in Fig. 2.4(a). Inserting this expression into Eq. (2.5) leads to

$$I = |o|^2 + |r|^2 + o^* r e^{-\mathrm{i}(\boldsymbol{k}_r \cdot \boldsymbol{x})} + o r^* e^{\mathrm{i}(\boldsymbol{k}_r \cdot \boldsymbol{x})}, \tag{2.10}$$

where one can identify that the interference terms are multiplied with various phase factors, which correspond in the reciprocal domain to different modulations. The reconstruction, performed by illuminating the plate with a replica of the complex conjugate of the reference wave, yields

$$r^* I = r^* \left(O^2 + R^2\right) + R^2 o^* + o(r^*)^2 e^{2\mathrm{i}(\boldsymbol{k}_r \cdot \boldsymbol{x})}. \tag{2.11}$$

The three diffracted components emanating from the plate therefore propagate in various directions, as shown in Fig. 2.4(b). In the case the distance between the object and the recording plane d_o is sufficiently high compared to the off-axis angle θ, the imaging plane distance d_i will be far enough so that a full spatial separation will be possible between the various terms contained in Eq. (2.11), thus enabling imaging of the object wave free of any disturbance due to the twin-image or the zero-order term.

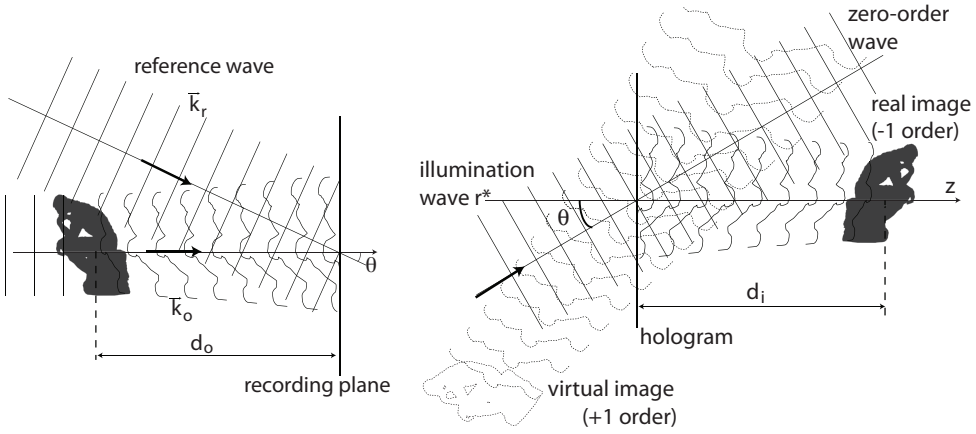

Figure 2.4: Off-axis (a) recording and (b) reconstruction.

The possibility of employing an off-axis angle is however greatly dependent on the sampling capability of the recording medium, since it corresponds to a modulation of the interference terms, as expressed in Eqs. (2.5) or (2.17). Holographic films have typical sampling capabilities in the order of thousands line pairs per millimetre (lp/mm), thus enabling off-axis angles up to tens of degrees, and ensuring easy spatial separation of terms [Wol70b]. However, as it will be described in the next subsections, the issues in sampling capabilities can become critical in the case of digital detectors.

Mutual Coherence

Up to this point in the discussion, it has been considered that the two waves interfering on the detection plane were perfectly coherent, thus greatly simplifying the equations describing the generation of the hologram. This hypothesis is in general not true, especially in the case of the early experiments of holography, where light sources such as mercury lamps were employed, before the common use of lasers. Coherence denotes the ability of two wave fields, defined temporally and spatially, to interact in a coherent way. It thus denotes the importance of the cross-correlation terms in Eq. (2.5), relatively to autocorrelation terms. The mathematical analysis of this property is commonly divided between its temporal part and spatial one.

The temporal coherence represents the capacity of two wave fields to interfere with each other when they propagated through different optical path lengths, and can thus be considered as a correlation in phase between two wavefronts. It is represented mathematically by the temporal correlation between the fields

$$\Gamma_{11}(\tau) = \left\langle u_1^*(t)\, u_1(t+\tau) \right\rangle. \tag{2.12}$$

The function $\Gamma_{11}(\tau)$ is typically maximal for a perfectly monochromatic wave, and tends to a Gaussian shape in the case of a light source possessing a certain bandwidth $\Delta\lambda$, through the Fourier relations between temporal behaviour and spectral properties. It is thus possible to define temporal coherence of a given light source by its coherence time τ_c, defined as the time shift for which the fringe contrast decreased of e^{-1}, or its coherence length L_c through the space-time duality of electromagnetic waves, i.e. $L_c = c\tau_c$. One should note that other definitions employ the full width at half maximum (FWHM), so that a scaling factor can take place depending on definitions.

On the other hand, spatial coherence represents the capacity of light emitted by two points situated at various positions on a wavefront (the condition of being on a wavefront cancels any effects defined as temporal coherence) to interfere, and can thus be represented mathematically by the spatial correlation

$$\Gamma_{12}(\boldsymbol{r}_1, \boldsymbol{r}_2) = \left\langle u(\boldsymbol{r}_1)\, u^*(\boldsymbol{r}_2) \right\rangle. \tag{2.13}$$

where $\boldsymbol{r}_1$ and $\boldsymbol{r}_2$ are the positions of the emission points. The function $\Gamma_{12}(\boldsymbol{r}_1, \boldsymbol{r}_2)$ is typically maximal for a perfect point-source and decreases for light sources of a given spatial extension.

The coherence—temporal and spatial—was one of the main issue at the development of holography, as it was rather difficult to generate light with sufficient coherence properties and powers to imprint interference fringes on plates with a satisfying contrast. This is particularly true in the case of wide field interference as performed in holography, as both temporal and spatial coherence conditions must be satisfied to ensure coherent detection. The practical effect of coherence for detection can be seen in Eq. (2.6), where the term I_1 accounts for fringe visibility. This term usually denotes for the intensity ratio between the two interfering waves, which influences the visibility, but can be changed to model also coherence effects. On the other hand, Eq. (2.5) must be rewritten to take into coherence, giving

$$I(x,y) = |o|^2 + |r|^2 + \left(o^* r + o r^*\right) G_{12}(x,y), \tag{2.14}$$

where $G_{12} \in [0,1]$ is a weighting term relatively decreasing the relative importance of cross-correlation terms, thus denoting for a partial coherence. This term denotes for a practical effect on the detection plane, and is consequently indirectly linked with the general definition of spatio-temporal coherence $\Gamma_{12}(\boldsymbol{r}_1, \boldsymbol{r}_2, t)$.

The common-path architecture of lensless implementations presents the advantages of preventing most of the problems issued by coherence limitations, as the beam is interfering with a diffracted part of itself, thus avoiding any difference in optical path length (OPL) between the interfering beams. Furthermore, it requires point-sources for generating spherical waves, which therefore imply good spatial coherence properties. The limitations in coherence thus prevented at first implementations with interferometric approaches in holographic setups. Even the first developments in off-axis configurations were performed through common-path configurations, due to the same limitations, typically with wedge prisms tilting part of the wavefront to generate the interference [Lei64]. Some attempts were however performed very rapidly to employ interferometric configurations for holography, in order to take advantage of the versatility of those implementations [Gab66], which were then commonly employed with the emergence of laser light sources, enabling very long coherence lengths allied with high powers.

One should note however that short coherence length sources have been investigated again recently in various cases [Dub06; Kem08a]. Shorter coherence lengths have great potential for use in interferometric measurements, as the phase disturbance induced by the statistical distribution in the sample can indeed be averaged out in the case of light sources having a larger spectral width. Furthermore, it can also contribute to an increase in spatial resolution, through the minimisation of coherent effects inducing ripples. These applications however require methods to enable interference on the whole field of view while employing low coherence properties. This typically requires more complicated arrangements, where the coherence zone (in both spatial and temporal domains), must be adapted to ensure optimal interference [Ans01].

2.2.3 From classical to digital holography

Classical holography brought exciting features such as lensless imaging and full wavefront recording capabilities, but was still requiring cumbersome procedures for coding and decoding the hologram. The exposure of the photo-sensible plate has to be controlled precisely, to ensure its print in the linear range of sensibility. Non-linearity in the print indeed generates higher orders of diffraction, which contribute greatly to the noise of hologram generation. Furthermore, chemical treatments to develop and fix holograms are long and critical steps, so that getting quality holograms requires great care at both detection and processing steps. On the other hand, using digital detectors enables the possibility of finely tuning the exposure time and gain of the sensor, thus easily ensuring optimal recording conditions of the hologram. Furthermore, the acquired data is directly fed to a computer, thus suppressing all the steps for developing the hologram, making possible to make rapid acquisitions for temporal analysis, at the cost however of a loss of sampling capabilities, as photo-sensible plates have typically higher resolving powers than digital detectors.

Nevertheless, classical holography still carries various applications in which promising results are to be expected. To name a few, physical generation of holograms is used nowadays in the field of cryptography [Mat09], where its most renown application is for bank notes security. Physical wavefront generation through computer-generated holograms has also been developed by using spatial light modulators (SLM) or micromirrors arrays [Hue03], enabling 3D vision applications [Yar10].

The use of digital means in holography occurred gradually from the end of the sixties, when Goodman used for the first time a vidicon detector to encode a hologram, which could then be reconstructed with a computer [Goo67]. Those results could also be reproduced also by Kronrod *et al.*, who reconstructed optically encoded holograms fed to a computer for reconstruction [Kro72]. Applications in the field of interferometry could also be considered as premises of digital holography, where measurements obtained by Twyman-Green interferometers used with diode arrays, hence corresponding also to full-field measurements comparable with holography, were reconstructed through digital means [Bru74]. Even though those preliminary results were very promising in the capability of numerically reconstructing holograms, the interest in digital holography essentially rose with the availability of cheaper digital detectors, essentially manufactured with charge-coupled device (CCD) cameras. The validation of the use of CCD cameras for holographic applications was performed in the mid-nineties, in the case of reflection macroscopic holograms [Sch94], or microscopic holograms in endoscopic applications [Coq95].

The main issue with early digital detectors lies in their sampling capabilities, which greatly limits the possibilities for using an off-axis configuration. Detectors had typical pixel sizes in the tens of microns, while photo-sensitive plates could sample up to typically 1000 lp/mm, corresponding to pixel sizes of 1 μm. This implies that the imaging resolution was greatly reduced with digital detectors employed in conjunction with an off-axis geometry which is also limiting the sampling capabilities, as this method relies on spatially modulating the signal to extract the information.

Another approach for hologram reconstruction was developed by taking advantage of the capability of digital detectors to take multiple frames rapidly, through the use of phase-shifting techniques [Yam97]. Those reconstruction methods do not rely on a spatial encoding of the information, as in off-axis geometry, but on temporal encoding, by combining several frames to recover the wavefront information as developed first for interferometry [Car66; Bru74]. This approach enables the use of the full sampling resolution of the detector, but at the cost of employing several frames.

Up to this point, holography was essentially considered as an imaging technique, enabling the possibility of lensless imaging, or the capability of focusing images recorded out-of-focus through the recovery of the full wavefront. The digital treatment, which contrarily to the classical approach, considers the wavefront as a combination of amplitude and phase, led to the development of quantitative phase imaging through holography [Cuc99b]. This approach led

to numerous applications, such as biological samples observation, or full-field topographic characterisation, as described in details in subsection 2.2.7.

The development of digital means for holography changed greatly the research field. The capability of performing holographic measurements with cheap laser light sources and digital cameras, combined with holographic reconstruction performed on computers, strongly eased the experimental process, thus leading an increasing amount of groups to this research field, as the increasing quantity of articles yearly published in the domain attests. On the other hand, it led to a specialisation of the various competences required previously for classical holography. The use of the latter for measurements and the generation of holograms can be considered at this point nearly as distinct domains. One can see various sub-domains, such as computer generation of holograms, where they are designed and then printed for instance for cryptographic applications, holographic detection, where holograms are used as an optical mean of measurement, through computation of the data sent by the detectors, or holographic generation, where the hologram is created for physical wavefront processing, such as in 3D vision systems. Those domains are of course vast by themselves, and encompass various applications. However, this distinction occurred through the emergence of digital means for recording and reconstructing holograms, so that optics and material science are not anymore both required in order to make research in holography.

The development of easily accessible detector arrays made also the distinction between holography and interferometry hard to distinguish. Holography was originally an imaging technique with striking properties, while interferometry was a metrology tool with impressive performances in resolution. With detector arrays having high dynamic ranges, the distinction between a Michelson interferometer and a Twyman-Green one is not as important as before. On the other hand, with the widespread use of laser sources having long temporal and spatial coherence properties, holography now commonly employs interferometric setups to produce holograms. The two research fields are presently widely interconnected.

2.2.4 Digital holographic recording

We describe here in more details the various methods for recording and reconstruction in the context of digital holography. Even though the detection is based on the fundamental equation of interference given in Eq. (2.5), one can identify various fundamental configurations which imply different approaches for recording and reconstruction. We start by defining those conceptual implementations.

Conceptual implementations

One can identify two main subdivisions in the implementations of an experimental setup performing holographic measurements. The first subdivision consists in the type of signal recovered, which can be either a reflection signal, in which case the diffracted wave is reflected by the sample, or a transmission signal, for which the diffracted wave travels through the

sample. Even though this distinction does not change drastically the way in which the hologram is generated and reconstructed, it modifies the interpretation of the recovered signal.

In the case of a reflection implementation (cf. Fig. 2.5(b, d)), the recovered object wave consists in a reflectivity signal in amplitude, while the phase corresponds to the topography of the sample, which is commonly a reflective surface. On the other hand, a transmission implementation (cf. Fig. 2.5(a, c)) enables the recovery of an absorption signal in amplitude, and a signal proportional to the integrated refractive index distribution along the optical axis in phase, where the sample is commonly nearly transparent, such as a biological preparation. This leads to the following interpretation for the reflected phase φ_{refl} and transmitted phase φ_{trans}

$$\varphi_{\text{refl}}(x,y) = \frac{2\pi}{\lambda_0} n_i \cdot 2h(x,y), \tag{2.15}$$

$$\varphi_{\text{trans}}(x,y) = \frac{2\pi}{\lambda_0} \int_0^{h(x,y)} n_m(x,y,z)\mathrm{d}z, \tag{2.16}$$

where n_i is the surrounding RI, n_m is the RI distribution in the specimen, and h is the height of the sample. One should note that part of the difference in the two interpretations of the phase signal given in Eqs. (2.15–2.16) are essentially sample-dependent. In this simple approach, it is considered that the sample consists either in a reflective surface with a height distribution $h(x,y)$, in a controlled environment of refractive index n_i, with the factor 2 accounting for the doubled OPL coming from the reflection, or a nearly transparent object, so that the phase is an integrated signal over the depth of the sample with a distribution of refractive index. This view is of course a greatly simplified representation of most of the cases, as non-perfectly reflecting samples are observed in reflection, such as biological preparation or multi-layered substrates, and highly absorbing samples can be observed in transmission. Nevertheless, it represents a general trend in the applications of the two configurations.

Furthermore, one should note that the signals are considered to propagate through the sample in transmission, without considering diffraction, so that the phase signal is simply an integrated signal over the depth of the sample. Even though rigorous analysis of the imaging conditions for holographic systems were derived in various works, such as in a coherent transfer function (CTF) analysis [Kou07], the usual interpretation of holographic data results in an ambiguous interpretation. On one side, imaging involves diffraction, so that the multiple interferences result in an image through the Huygens principle; on the other hand, phase is commonly considered in a geometrical model, where the it is considered in transmission to be the integrated signal along the optical axis (cf. Eq. (2.16)). The consistency of interpretation would require a model of the phase signal which would integrate diffraction, which is yet to be developed.

A second subdivision consists in the size of the observed sample, and the imaging system employed. On one side, one can consider macroscopic systems (cf. Fig. 2.5(a–b)), in which no

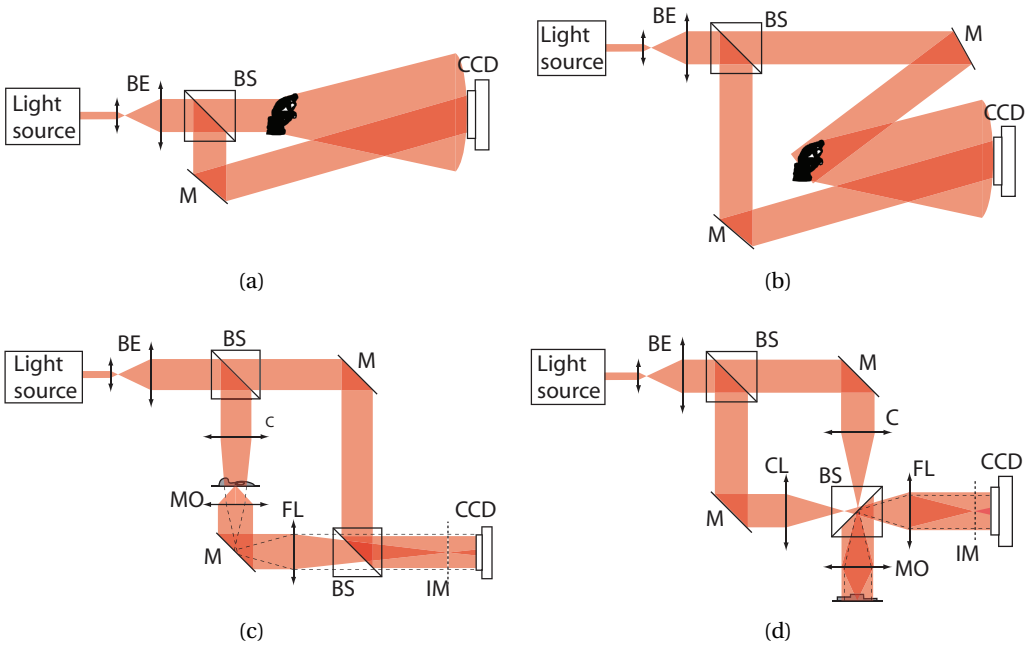

Figure 2.5: Fundamental implementations of digital holographic setups, for (a, c) transmission and (b, d) reflection, in the (a–b) macroscopic case and in the (c–d) microscopic case.

optical magnification is used. In this implementation, the field of view as well as the resolution of the imaging system will be determined respectively by the detector size and sampling capability. On the other hand, one can consider the microscopic case (cf. Fig. 2.5(c–d)), in which an optical imaging system is used, classically with magnifying optics. In this case, the field of view depends on the type of magnification used, and the resolution is determined by the numerical aperture of the optical configuration. As in the previous paragraphs, those two cases consist in extreme cases, as there are configurations in which magnification is employed and where the resolution is still determined by the pixel size of the camera. Nevertheless, this classification can be employed in a general sense for description.

The four combinations of implementations are presented in Fig. 2.5, for macroscopic and microscopic, and for transmission and reflection cases. Macroscopic setups essentially consist in a light source expanded spatially to ensure an even illumination on the sample, with a beam splitter (BS) to divide the beam into the reference and object arms. The object interacts with the specimen, and the transmitted/reflected light is collected on a camera, while the reference beam is impinging also on the detector, with a defined angle for off-axis reconstruction. For microscopic applications, a condenser lens (C) is inserted in the object arm, to ensure filling the entrance pupil of the microscope objective (MO) which collects the diffracted light emitted by the specimen. The field lens (FL), or tube lens, then forms the image at the plane IM, and the light is detected slightly out of focus by the detector (cf. Fig. 2.5(c–d)), the non-diffracted light, or zero-order, is represented by dashed lines, while the diffracted light is shown with plain beams. In the microscopic case, a BS is classically used to recombine the

two beams on the camera, thus ensuring the small angles required by the sampling capability of the digital sensor. In the case where the field lens is situated after the recombination beam splitter, as shown in the reflection configuration of Fig. 2.5(d), it is usually necessary to use a curvature lens (CL) in the reference arm, in order to match the curvature radii of the two beams on the detection plane.

Recording conditions

The fundamental recording conditions were briefly discussed in the first part of this section. We describe in this paragraph the detailed possibilities and requirements involved in the generation and detection of the hologram.

Light sources

The first key element for holographic measurement is the light source. As already mentioned, the requirement for the illumination is a certain degree of spatial and temporal coherence, in order to generate an interference at the detection plane, implying that a wide variety of sources can be employed for this purpose. While in the past, filtered mercury lamps have been used [Gab49; Lei64], laser sources are preferred nowadays for their very long coherence time properties. Gas lasers, such as He:Ne, are commonly employed thanks to their easy accessibility, as well as solid-state lasers [Kre05], or more recently laser diodes. Sources with less coherence such as light-emitting diodes (LED) were also investigated recently [Kem08a], showing promising results in terms of reduction of coherent noise. The use of particular sources for specific applications were also developed, such as the use of very short pulses light sources for time-gated measurements, or nonlinear coherent imaging for instance [Pu08; Sha10a]. The commercial availability of narrow spectral filters, which are enabling an easy selection of wavelength with sufficient temporal coherence for interferometry, and the use of spatial filters, making possible to easily generate point sources, can enable the use of virtually any light source for holography, depending on the specifications of the required application, and provided that enough intensity is available for detection after beam processing. The next requirement a light source needs to fulfil is to have a well defined polarisation state, in order to ensure a good fringe contrast at detection. Again, this can be obtained either by employing an intrinsic property of the source, such as a linearly polarised laser, or by processing the beam in the optical arrangement.

Holography has been used in a wide spectral range, going from electronic sources up to the far infrared domain, depending on the type of measurement. Through scaling laws, the basic principle of holographic measurements can be applied to any wavelength range, provided that a source with sufficient power and coherence properties is available. Outside visible range, holography has also been employed from X-ray imaging for its lensless imaging capabilities [Gab48] and for coherent detection in atomic inspection, for example [Mid01]. In the infrared range, holography has been used typically for inspection of silicon wafers and structures [All03].

Detectors

Digital holography presents the advantage of being essentially a bright field imaging technique, so that it does not require high-gain sensors. The main requirement is based essentially on the resolving power of the detector, especially in the case of off-axis holography, where one needs to sample fringes with a sufficient amount of pixels to avoid aliasing. On the other hand, holography requires classically low noise properties, as errors on pixel values can rapidly induce inaccuracy in the localisation of fringes, and thus errors in the phase recovery. For this reason in particular, CCD technology has usually been preferred to CMOS sensors, as its performance in terms of noise are generally better, although present CMOS detectors are gradually reaching noise performance of CCD cameras.

The final aspects about detectors concerns digitisation of signal through analog-to-digital conversion. Surprisingly, it was shown that holography does not require high digitisation capacities to retrieve an acceptable quality of signal. Typically, it could be shown in the context of phase-shifting holography that the difference in reconstruction quality between 6-bit and 8-bit holograms is barely distinguishable [Mil05]. More recently, it was demonstrated in the context of lensless Fourier holography that quantisation noise on phase images is inversely proportional to the digitisation level, so that noise is reduced by a factor 2 for each bit added to hologram quantisation [Pan11].

Beam arrangement

The beam arrangement consists in the geometrical configuration in which the object and reference beams are aligned at detection level. As mentioned previously, various configurations lead to different reconstruction methods. The originally developed method, consisting in a lensless arrangement (cf. Fig. 2.1(a)), makes it difficult to recover the object wavefront information free of twin-image, as only very specific configurations allow it [Mic10]. The two main arrangements implemented in interferometers are the in-line configuration, where the two beams are collinear, so that one resorts to phase-shifting methods in order to recover the wave field, or an off-axis geometry, where the two beams have a slight angle to spatially modulate the wavefront information. However, the modulation is restricted in possible spatial frequencies by the detector sampling capabilities, as one has to avoid aliasing during acquisition. Under the hypothesis that the reference wave is a plane wave, the Fourier transform of Eq. (2.5) is

$$\hat{I}(\omega_x,\omega_y) = \hat{o} * \hat{o}^*(\boldsymbol{\omega}) + R^2\delta(\boldsymbol{\omega}) + R\hat{o}(\boldsymbol{\omega}+\boldsymbol{\omega}_0) + R\hat{o}^*(\boldsymbol{\omega}-\boldsymbol{\omega}_0), \tag{2.17}$$

where $\boldsymbol{\omega}_0 = (\omega_{x,0},\omega_{y,0})$ corresponds to the frequency modulation induced by the angle between the object and reference wave. The spectral arrangement of the various terms contained in Eq. (2.17) is shown in Fig. 2.6, where one can identify the zero-order at the centre, and the two conjugated modulated terms, for the case where the spectral support is limited by a circular aperture corresponding to the numerical aperture of the imaging system, for the case of an optically-limited system.

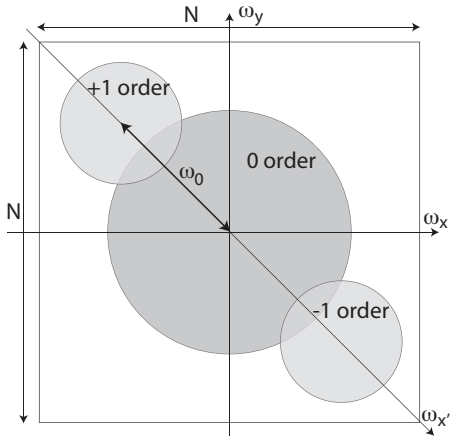

Figure 2.6: Fourier organisation of interference terms, for an optically-limited recording configuration.

If one considers the modulation frequency along an axis $\omega_{x'}$ parallel to the modulation direction, the inclination angle θ will induce a modulation frequency corresponding to

$$|\boldsymbol{\omega}_0| = \frac{\sin\theta}{\lambda}. \tag{2.18}$$

On the other hand, the detector has a sampling capacity in the x direction corresponding to a frequency of $\omega = 1/\Delta x$, where Δx is the pixel size of the camera. By considering the Nyquist theorem, and inserting a geometry similar to the one of Fig. 2.6 ($\phi = \pi/4$), the maximum angle which can be resolved by the detector is thus

$$\begin{aligned} \omega_{0,x} &= \frac{\sin\theta\cos\phi}{\lambda} \leq \frac{1}{2\Delta x}, \\ \sin\theta &\leq \frac{\lambda}{\sqrt{2}\Delta x} \end{aligned} \tag{2.19}$$

According to this equation, for the main laser line of a He:Ne laser ($\lambda = 633$ nm) and a standard pixel size of a CCD camera ($\Delta x = 6$ µm), the maximal usable angle is $\theta \leq 4.28°$. In order to enable measurement of diffracted wave vectors, one can consider in first approximation limiting the angle to one half of this value, putting the carrier frequency at the centre of the quadrant, thus yielding $\theta \leq 2.14°$.

The limitations of off-axis geometry and the reachable imaging resolution for a given imaging system are analysed in more details in section 3.2, in the context of zero-order suppression algorithms, and is thus only briefly treated here.

Another implication of the off-axis geometry is the stronger requirement on the coherence length of the light source. As shown in Fig. 2.7, the coherence zones of the two beams, defined by the coherence length L_c, are not exactly superimposed due to the inclination angle, leading to a potential loss in fringe visibility at the borders of the field of view, due to the

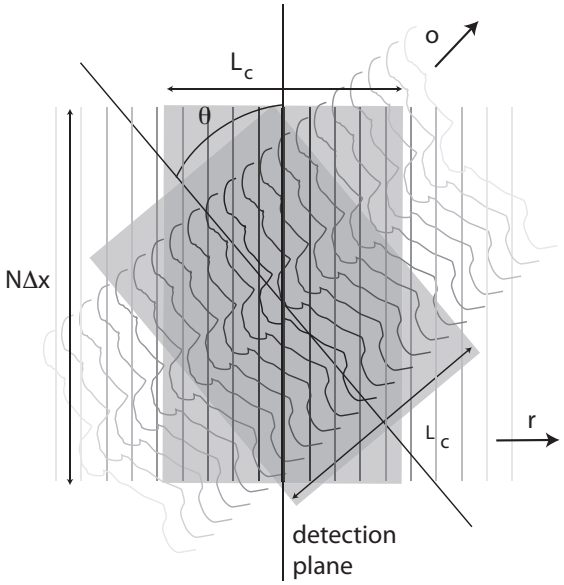

Figure 2.7: Overlap of the coherence zones of the object and reference beams in off-axis geometry.

distribution of mutual coherence function as described in subsection 2.2.2. If one defines a criterion requiring that the two coherence zones must be superimposed on the whole field of view, as shown in Fig. 2.7, it is possible to deduce from geometrical considerations a condition to ensure a sufficient fringe visibility as

$$\tan\theta \leq \frac{L_c}{N\Delta x}. \tag{2.20}$$

If one considers, for the sake of comparison, a light source with a coherence length of L_c = 100 µm (which in the typical order of magnitude of femto-second lasers), a detector having $N = 1024$ pixels and $\Delta x = 6$ µm, it requires an angle $\theta \leq 0.93°$ to ensure an overlap of coherence zones and thus a sufficient fringe contrast. By comparing the two limiting values, one can see that a light source with a coherence length of 100 µm typically becomes the limiting factors in terms of field of view with the values employed for these small calculations.

Recording domain

On an imaging point of view, digital holography differs strongly from its classical counterpart. In the case of classical holography, the interference pattern is always recorded with a defocused object wave, enabling refocusing of the object wavefront through illumination of the plate, as described in subsection 2.2.2. This configuration provides the effect of three-dimensional imaging, as the eye can focus around the focusing distance in order to identify various planes with features.

In the case of digital holography, the approach is somewhat different, as the object wavefront reconstruction is usually considered by extracting separately the amplitude and phase of the object, for analysis and measurement purposes. The fact of propagating the wavefront is therefore not necessary in order to recover this information. Furthermore, while classical holography involves physical propagation, digital propagation involves discrete finite supports, limited by the size of matrices as defined by the detector. For those reasons, digital holography usually does not involve strongly defocused waves, as this would result in a loss in field of view due to beam divergence. Similarly, due to the finite support of digital detectors, the modulation involved in the separation of the different diffraction orders in the case of off-axis holography is not considered in the spatial domain, as this would imply the use of very large sparse matrices, making the computation more complicated. A formalism based on the Fourier domain is therefore usually employed, where the reconstruction is considered in the frequency domain as shown in Fig. 2.6.

One can therefore identify three main domains in which holograms are recorded. These recording regimes are essentially defined by the imaging conditions and correspond to the classical diffraction regimes defined in optics, namely in-focus, Fresnel and Fraunhofer regimes [Bor99]. The first regime corresponds to the case where the object wave is imaged directly on the detector, as shown in Fig. 2.8(a). As it will be discussed in the next subsections, this method simplifies the reconstruction process, since the image is already formed, but at the cost of a loss of flexibility in the reconstruction possibilities.

The second regime consists in Fresnel holography, in which case the object wave is recorded defocused, as depicted in Fig. 2.8(b). This corresponds to the closest case to classical holography, as the reconstruction involves propagation in order to recover the focused image. The fact of involving propagation algorithms increases the computation complexity of the reconstruction process, but brings also several advantages in the possibilities of reconstruction.

Finally, the third regime consists in Fourier holography, where the detection plane is situated at infinity, corresponding to the Fraunhofer regime. However, in practise, placing the detector at a sufficient distance to be considered at infinity implies usually the loss of an important part of light, so that this regime is commonly generated by recording the hologram at the Fourier plane of a lens (cf. Fig. 2.8(c)). This method presents the advantage of providing directly the signal in the reciprocal domain, thus preventing the need for computation of the Fourier transform. However, this configuration classically requires high dynamic ranges for detection, in order to avoid saturation between very strong signals such as frequencies near the origin, and higher frequencies with much less intensity.

The discussion above essentially considers configurations in which an imaging system is employed, thus corresponding to configurations called as microscopic in the classification made up to now. In the case of macroscopic configurations, in which no imaging optics is employed, the regime will essentially depend on the distance between the object and the detector. In the usual case, the detector is not so far from the object, yielding the detection of a

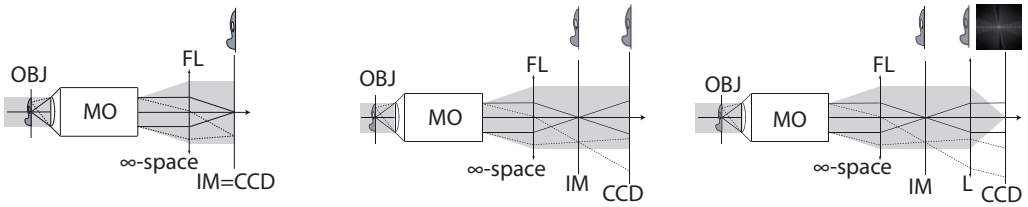

Figure 2.8: Regimes of hologram recording. (a) In-focus holography, (b) Fresnel holography, (c) Fourier holography. OBJ: object, IM: image plane, CCD: detector, MO: microscope objective, FL: field lens, L: lens.

diffraction pattern corresponding to a Fresnel regime. However, cases where the detector is rather far away from the object are also employed, leading to Fraunhofer diffraction, such as in lensless Fourier holography [Kre05].

Fringe visibility

As holography encodes the wavefront information through intensity values in the interference pattern of two waves, the fringe visibility determines ultimately the quality of the recovered wave field, would it be by the quality of extinction of fringes when combining frames in the case of phase-shifting, or in the resolving capability in the case of off-axis methods.

The fringe visibility can be defined as

$$V = \frac{I_{\max} - I_{\min}}{I_{\max} + I_{\min}}, \tag{2.21}$$

where $I_{\max}, I_{\min}$ correspond respectively to the maximum and minimum of the intensity. In the case of a standard interferometer, the visibility is typically measured by scanning a mirror to modify the relative phase advance between the two arms in a Michelson configuration. In the case of off-axis holography, the visibility can be spatially determined on the field of view of the detector, as the optical path length varies between the two arms due to the angle θ, as shown in Fig. 2.7. Various parameters can influence the fringe visibility, such as the intensity ratio between the two interfering waves, the polarisation state at the detector plane the coherence of the source, or potential vibrations of the experimental setup, occurring during the exposure time of the detector.

As it can be seen in Eq. (2.6), the modulation term I_1, which depends on the object and reference intensities, is related to the visibility of the interference pattern. The optimum in regards to fringe visibility can be obtained when the two waves have identical intensities. However, it was shown that the relation between the intensity ratio of the two waves and the reconstruction quality is more complex than being only related to fringe visibility, when taking noise into consideration [Cha06b; Cha07b].

It is classically considered that one of the main issue with interferometric measurements are the mechanical vibrations of the experimental setup. Phase-shifting methods, which employ several frames taken at different times, are particularly sensitive to this type of noise. For this reason, several works tend to minimise the amount of frames required to perform the reconstruction [Guo02; Liu09]. On the other hand, off-axis methods perform phase recovery through one measurement, so that only vibrations occurring during the exposure time of the detector influence fringe visibility. Minimising the recording time thus generally improves the quality of the measurement.

In order to circumvent problems coming from vibrations, common-path interferometers are sometimes used, where the reference follows the same path as the object wave, so that phase shifts induced by vibrations are automatically compensated at detection level [Pop04; Mic10]. However, a common-path configuration usually implies that it is impossible to induce a modulation of the fringe pattern through off-axis methods, thus again requiring several frames for reconstruction, and increasing sensitivity to vibrations. To circumvent this paradigm, one has to employ more complicated methods, such as inserting diffraction gratings to generate a reference wave from a part of the object wave, thus complicating the reconstruction process [Pop06]. Historically, vibrations were one of the main limiting factors for employing interferometric configurations as the technical means for light generation and detection were forcing long exposure times [Gab66].

Off-axis configurations, while being optimal in terms of temporal sampling for fringe visibility in regards to vibrations, possess however other limitations, due to the finite size of pixels. As a pixel delivers an average value of the light intensity over its surface, the fringe pattern is not only sampled with a finite amount of discrete points, but also averaged by regions, yielding a loss in fringe visibility, as shown in Figs. 2.9(a–b).

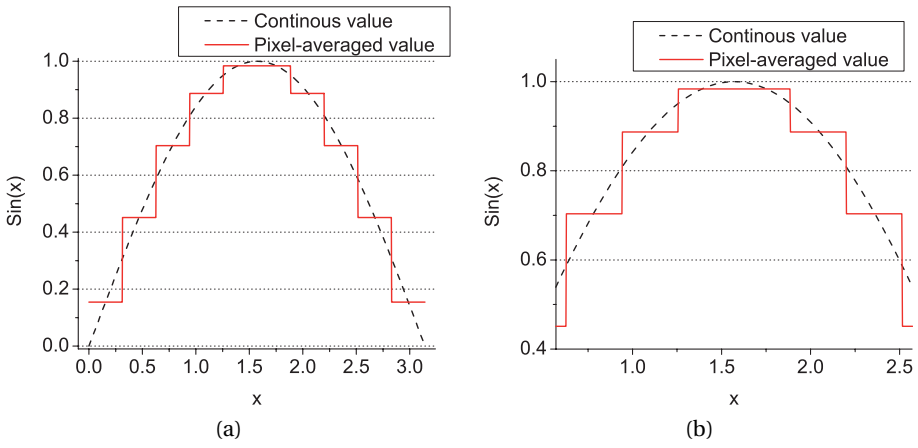

Figure 2.9: Loss of fringe visibility in high modulation case due to pixel finite size.

Sources of noise

The main sources of noise during hologram recording can be characterised by the various elements employed for measurements. We consider separately three components, which are the light source, the experimental setup itself, and the detector.

The noise generated at the light source level is mainly driven by the shot noise, as the source emits light according to the discrete nature of photons. In addition to this fundamental limit, light sources have usually fluctuations in intensity and polarisation state which will reduce fringe visibility in the interference pattern, although most commercial lasers presently available can be stabilised through feedback mechanisms. The shot noise is statistically governed by a Poisson distribution, described by

$$p(n;\mu) = \frac{\mu^n e^{-\mu}}{n!}, \tag{2.22}$$

providing the probability of having n photons impinging on the camera, when its expected number is μ. The main mathematical property of Poisson distribution is that its variance is equal to its expected value, i.e. $s = \mu$. This implies that the perturbations induced by shot noise decrease with the square root in function of the light intensity. In the case of a wide-field technique such as holography, one can consider that the amount of photons which can be detected is limited by the well depth of the camera N_e, along with the quantum efficiency Q, which determines the maximum amount of photo-electrons which can be stored in a pixel before saturation. The optical power necessary to completely fill a well depth pixel is thus given by

$$P\left[\mathrm{W/m^2}\right] = \frac{N_e hc}{\lambda Q \Delta x^2 \Delta t}, \tag{2.23}$$

where h is the Planck constant, c is the light velocity, Δx is the pixel size, and Δt is the exposure time. Typically, if one considers again a He:Ne laser and pixel sizes of $\Delta x = 6$ µm, a quantum efficiency of $Q = 0.8$, a beam power of 1 mW is plentifully sufficient to fill a well depth of $N_e = 10'000$ with an exposure time of $\Delta t = 50$ µs. Therefore, the main restrictive factor in the case of wide field holography is usually the well depth of the camera, which will limit the amount of detectable photo-electrons, as it is possible to fill pixel well depth in a time frame classically smaller than typical resonance frequencies of optical setups.

The fact that the main limiting factor consists in the well depth of the detector led to a common approach to reduce shot noise effects by recording holograms in burst with low integration times, and to average the reconstructed wavefronts to virtually increase the photon mean number. One should note however that the averaging needs to be performed on the complex values retrieved after hologram reconstruction, in order to avoid fringe blurring, as it would happen through physical averaging corresponding to an increase in shutter time.

Then, at setup level, the multiple interfaces induced essentially by the optical components employed for processing the beam and imaging the sample generate parasitic reflections,

which can potentially reach the detector. In the case of sources with long coherence lengths, those parasitic reflections will also interfere with the primary object and reference beams, thus generating a spectral pattern induced by various interferences at different modulations.

Finally, the digital detector generates electronic noise, i.e. shot noise due to the discrete nature of electrons, and thermal noise, such as dark current. The shot noise of the detector is directly linked to the shot noise related to the source, as the electron amount is directly proportional to the photons impinging on a pixel; furthermore, electrons are the measured quantity on which shot noise will manifest itself, as it corresponds to the physical observable. One should also note that the fringe pattern induced by the interference implies that while some pixel well depths are filled ($I_{\max}$), some others are empty ($I_{\min}$), so that interference measurement introduces a structured pattern in the noise, generated by the strong variations in intensity.

The behaviour of the detector in regards to noise depends strongly on the type of technology employed, such as charge-coupled devices (CCD) compared to complementary metal-oxide semiconductor (CMOS) technology. However, by considering presently available detectors, in which the electronic noise can be reduced to a few root-mean-square electrons even for ambient temperature CMOS chips, one can consider that the main source of noise for detectors employed in the context of holography, in which light intensity is rather strong compared to other new detection methods such as confocal microscopy or fluorescence, is the shot noise. Experiments showing measurements performed at low light sensitivity with DH were presented recently [Gro07], confirming the predominance of shot noise.

Effect of the sample

Up to this point, the discussion about the hologram generation considered essentially an empty interferometer, without taking into account the effects induced by the observed specimen, as its influence on the object wavefront is the signal meant to be measured. However, the sample can have multiple effects on the wavefront, with some of those which are not part of the aimed measurement, and can be considered as noise in the hologram.

In the case of a perfectly transparent specimen in transmission, or perfectly reflective in reflection, the sample does not influence directly the fringe visibility. However, in practise, the observed object alters the amplitude profile of the object wave, and thus locally modifies the fringe visibility through the intensity ratio between the two waves. This effect has usually little influence on the reconstructed wavefront, but in the case where part of the field of view has very low light intensities coming from the object, a strong intensity difference will occur between the two waves, leading to an increase in noise on the reconstructed phase. Another influence of the object can be the depolarisation of the incoming beam. If the object possesses some birefringent properties in transmission, or dielectric properties in reflection, the outgoing beam will not have the same polarisation state as the incoming one. The two interfering waves will possess different polarisation states, leading again to a loss in fringe

visibility. This effect, which makes holography dependent on the polarisation state, can be used as a mean of measurement of the birefringent properties of the sample [Col02; Col05].

Finally, the main effect the observed sample has in the case of coherent detection is the speckle, generated by a random phase pattern. Speckle occurs in the case of transmission through a medium inducing strong diffraction, or when light reflects on a rough surface. The coherent addition of multiple phasors having various propagation directions and phase advances yields a random pattern in phase, which, after propagation, generates the typical granular texture of speckle fields.

Because the phase is bounded between $[-\pi, \pi[$, one can identify two main regimes in speckle, being "partially developed" and "fully developed" speckles. In the first case, the randomness occurs essentially in a domain contained in one wavelength, thus leading to a normal distribution of phase advance in the field of view. In the second case, the randomness occurs in a domain far greater than one wavelength, implying that it is not possible anymore to distinguish between photons having one wavelength of phase advance. This results in a full randomness having a constant phase distribution of phase in the field of view. In a general point of view, the possibility of using holographic techniques will be determined by the size of speckle grains. Intuitively, in the case where it is possible to identify the fringe pattern among the speckle grains, one could consider that classical holographic techniques could be employed. The speckle grain size is determined by the so-called correlation zone, describing the length along which photons can still be considered as interfering together, and thus generating a coherent signal, as modelled by mutual coherence [Goo96].

One noticeable application in the field of speckle interferometry is subtraction holography, where a differential measurement is performed between two states of the specimen. One hologram provides only a random phase, but as the randomness is apparent in regards to the limited dynamic range of phase measurement, subtracting two holograms makes it possible to suppress this effective randomness and to retrieve the strain on mechanical parts, for example [Ost02; Dem03]. Speckle fields are also employed in the context of statistical measurements, where its random properties are employed for illumination of the sample. Several acquisitions performed with various illumination patterns, generated for instance by the rotation of a diffusing glass, were typically demonstrated to enable suppression of the incoherent terms (zero-order) [HR07] or the twin-image [Mon09].

2.2.5 Digital holographic reconstruction

After having described above the various elements influencing the recording conditions of a hologram, we discuss below the different steps required for reconstruction of the complex wave field. While the description is mainly oriented on the point of view of computation for DH, most of the reconstruction steps can be related and compared to the physical reconstruction.

Object wave recovery

The first step, denoted here as object wave recovery, consists in the main procedure involved in digital holography, and the way to perform it actually defines most of the various techniques developed in the context of DH. It consists in treating the real data acquired by the detector, in order to recover the complex information of the object wave. We divide this discussion in the two main approaches which were already distinguished above, namely temporal decoding, i.e. phase-shifting, and spatial decoding, i.e. off-axis methods.

Phase-shifting reconstruction

Phase-shifting reconstruction methods are based on the combination of several frames, enabling the suppression of the zero-order and the twin-image through temporal sampling. As the reconstruction methods employed in this manuscript are essentially based on off-axis configurations, this paragraph only aims at describing the fundamental elements of phase-shifting techniques, and is only provided for completeness. Several books provide thorough reviews in the fields, such as [Ras94] or [Kre05].

The most well-known phase-shifting algorithm, proposed by Yamaguchi [Yam97] is based on four frames separated by phase shifts of a quarter of wavelength, which can be expressed as

$$I(x,y,\delta_n),\ \delta_n = \frac{n\pi}{2},\ n \in [0,3]. \tag{2.24}$$

By combining the frames, one can retrieve the real and imaginary part of the complex wave, and by extension its amplitude and phase as

$$\begin{aligned}
\Re\left\{\Psi(x,y)\right\} &= I(x,y,\frac{3\pi}{2}) - I(x,y,\frac{\pi}{2}),\\
\Im\left\{\Psi(x,y)\right\} &= I(x,y,0) - I(x,y,\pi),\\
\left|\Psi(x,y)\right| &= \sqrt{\Re\left\{\Psi(x,y)\right\}^2 + \Im\left\{\Psi(x,y)\right\}^2},\\
\angle\left(\Psi(x,y)\right) &= \tan^{-1}\left(\frac{\Re\left\{\Psi(x,y)\right\}}{\Im\left\{\Psi(x,y)\right\}}\right),
\end{aligned} \tag{2.25}$$

where $\angle$ denotes the phase of the reconstructed wave, bounded between $[-\pi,\pi[$. Various combinations of frames, derived from interferometry, could be developed in the same manner, leading to different amounts of frames [Kre05], or generalised phase-shifts [Car66].

In the first publications employing phase-shifting in the context of holography, piezo-electric transducers were employed to move a mirror in the reference arm, providing the precise movements required to record the various phase-shifts [Yam97]. However, many different ways of producing the phase shifts were developed afterwards, such as employing acousto-optics modulators in order to use the light frequency shift in this context, or by directly using the mode changes of the laser source, for example with gas lasers or laser diodes, for example

through statistical treatment [Kre05]. Theses approaches typically modulate continuously the induced phase shift, so that the change is integrated during the exposure time of the detector, leading to the so-called n-buckets algorithms [Ras94].

The two main issues leading to reconstruction artefacts in phase-shifting methods are on one side the requirement of several frames for reconstruction in interferometric setups, which are commonly very sensitive to vibrations, so that it is usually difficult to ensure stable phase-shifts and an invariant sample state during acquisition. On the other hand, the requirements on the accuracy of the phase-shifts are rather high in regards to displacements in the order of magnitude of hundreds of nanometres, implying that high-precision transducers need to be employed. In order to solve the issue of vibrations, several attempts were made to either reduce the required amount of frames for reconstruction, leading to two-frames reconstruction [Guo04; Liu09], or to enable the recording of the various phase-shifted frames simultaneously, by employing for example multiplexing methods [Awa04].

On the other hand, more refined algorithms were developed in order to loosen the accuracy requirements of phase-shifts. Those methods rely on iterative procedures to estimate the phase shifts δ_i numerically during reconstruction, and by employing generalised phase-shits inversion methods [Guo02; Wan04; Xu08].

Finally, in the context of high-accuracy phase measurements, one has also to consider more complex issues, such as the non-linearity of induced phase shifts. The wavefront curvature of the reference reflected by the transducer mirror or passing through the acousto-optic modulator will induce inhomogeneous phase-shifts in the field of view, thus requiring more refined compensations procedures to ensure accurate phase reconstruction [Ras94].

Fourier methods

The second main approach to recover the object wave is based on off-axis configuration, so that the complex terms recorded in the hologram are propagating in different directions than the non-diffracted wave, enabling separation of the various terms for reconstruction. This configuration was the one employed for the first demonstrations of fully numerical recording and reconstruction holography [Sch94; Coq95]. However, off-axis methods in the context of digital holography are usually not based on spatial separation, contrarily to its classical counterpart. This is due to the fact that numerical methods limit the field of view to the size of the matrices employed, so that spatial separation involves very large sparse matrices in order to avoid vignetting during reconstruction.

For this reason, reconstruction methods based on off-axis configuration usually rely on spectral treatment to filter the cross-correlation terms, so that they can be considered as Fourier methods in the general sense. The recovery consists therefore essentially in filtering one of the diffraction terms, as shown in Fig. 2.6, while ensuring that the information encoded can be separated from the twin-image and the zero-order. The concept of employing modulation in the recording process and employing Fourier methods for reconstruction was first pro-

posed by Takeda *et al.* [Tak82] in the context of interferometric topography. The method was later extended for smooth topographic measurements for phase recovery [Kre86], and generalised for use in digital holographic microscopy with amplitude and phase recovery [Cuc99b].

The main characteristic of Fourier methods is their capability of recovering the complex object wave through only one acquisition, thus reducing greatly the influence of vibrations during hologram reconstruction. However, as the complex terms are spatially encoded in the hologram, this one-shot capability comes potentially at the cost of usable bandwidth, as it is necessary to ensure at the same time a modulation sufficient to guarantee the separability of the information between the various terms encoded in the hologram (cf. Fig. 2.6), and a carrier frequency induced by the modulation small enough so that all the spatial frequencies of the diffraction terms can be sampled by the detector. Through filtering, the recovered diffraction order can be expressed as

$$\begin{aligned} \Psi(x,y) = or^*(x,y) &= \mathscr{F}^{-1}\left\{\mathscr{F}\left\{I(x,y)\right\}\cdot\hat{W}(\omega_x,\omega_y)\right\}, \\ \hat{W}(\omega_x,\omega_y) &= \begin{cases} 1, & (\omega_x-\omega_{0,x})^2+(\omega_y-\omega_{0,y})^2 \leq \frac{\Delta\omega_o^2}{4} \\ 0, & (\omega_x-\omega_{0,x})^2+(\omega_y-\omega_{0,y})^2 > \frac{\Delta\omega_o^2}{4} \end{cases} \end{aligned} \tag{2.26}$$

where $\hat{W}(\omega_x,\omega_y)$ is a spectral 2D window filtering the modulated term, according to its bandwidth expressed as $\Delta\omega_o$. In the case of Eq. (2.26), the window is defined by a circle, thus corresponding to the optically-limited case. As in common Fourier filtering operations, the window borders can be smoothed to avoid ripples after Fourier inversion.

The chapter 3 of this manuscript treats in details the sampling problems occurring in off-axis digital holography, and discusses the conditions necessary to ensure the full use of spatial resolution while guaranteeing no reconstruction artefacts. For this reason, the detailed discussion will not be repeated here.

One should note however that Fourier filtering methods provide the possibility of suppressing out-of-band noise through the selection of the diffraction order. As discussed above in the recording conditions, this out-of-band noise may consists in parasitic reflections, electronic noise generated by the camera, or more generally any noise which would not be limited by the imaging system, and can thus be situated outside of the bandwidth range delimited by the object wave.

In the case of off-axis holography, a final step required to get the complex object wave consists in demodulating the filtered spectrum, in order to cancel the carrier frequency induced by the reference wave propagating with an angle in regards to the object wave. It corresponds mathematically to centring the object bandwidth in the spectrum, and can be described by

the multiplication with a phase factor, according to the Fourier shift theorem, giving

$$\begin{aligned} \Psi_H(x,y) &= \Psi(x,y)\cdot e^{\mathrm{i}(k_x x + k_y y)}, \\ k_x &= \frac{2\pi}{\lambda}\sin\theta\cos\phi, \\ k_y &= \frac{2\pi}{\lambda}\sin\theta\sin\phi, \end{aligned} \tag{2.27}$$

where angles are defined in Fig. 2.3, and $\Psi_H(x,y)$ is the demodulated field of the retrieved diffraction order. The demodulation described in Eq. (2.27) can be compared with Eq. (2.11), which corresponds to the physical reconstruction of a hologram. The phase factor in Eq. (2.27) is similar to a plane wave propagating with an angle $-\theta$, and thus is identical to the complex conjugate of the reference wave at first order. The demodulation step therefore corresponds to the physical illumination $u(x,y)$ as described in Eq. (2.7).

The so-called digital reference wave can thus be adapted numerically to fit closely the propagation direction of the physical reference wave, through the (k_x, k_y) parameter set. On a computational point of view, it corresponds to centring the imaging order in the Fourier space, or flattening the phase profile in the spatial domain. It could be demonstrated that spatial implementations of parameters adjustment were usually more accurate [Col06b], by providing spectral centring with sub-pixel accuracy.

Aberration compensation

Aberration compensation is of great importance in case of phase imaging, as the phase is classically far more sensitive to aberrations than intensity imaging. Typically, criteria to define a diffraction-limited imaging system are typically based on the intensity point-spread function (PSF), which does not take directly into account the phase information [Bor99]. Furthermore, imaging through digital holographic means implies that the sources of aberrations can be multiple. Apart from usual aberrations coming from the imaging system, apparent spherical aberrations can occur due to a curvature mismatch between the reference and the object waves. As the diffraction terms are the results of the complex multiplication between the two interfering waves (cf. Eq. (2.5)), the apparent curvature of the reference wave in regards to the object wave leads to spherical aberrations.

The principle of demodulation through phase multiplication as described in Eq. (2.27) can be extended to higher orders, thus bringing the possibility of compensating for optical aberrations. Mathematically, Eq. (2.27) can be generalised to

$$\Psi_H(x,y) = \Psi(x,y)\cdot\exp\left(\mathrm{i}k\sum_{m=1}^{M}\sum_{n=1}^{N}C_{nm}\cdot x^m y^n\right), \tag{2.28}$$

where C_{mn} represents the aberration coefficients expressed in terms of polynomials on the Cartesian space and are purely mathematical coefficients multiplying the k-vector. Eq. (2.28) consists in a generalisation of Eq. (2.27), in the sense that the tilt compensation can be ex-

pressed by the coefficients $k_x = C_{10} \cdot k$ and $k_y = C_{01} \cdot k$. This formalism enables the corrections of several aberrations, such as the spherical aberration, generated by a combination from the imaging system and the curvature mismatch between the two interfering waves, or higher orders of aberrations. The definition of the coefficients requires however a measurement in order to estimate the phase changes denoting aberrations from phase variations coming from the observed sample. This implies that a constant regions in the field of view has to be employed.

Furthermore, the formalism presented in Eq. (2.28) does not include a key element at this stage, which consists in the digital propagation, as presented in the next paragraph. In the case of Fresnel holography, it is required to numerically propagate the recovered object wave to the focusing plane, requiring the computation of a double integral, which computation cost can be high (cf. Eq. (2.31)). There are therefore two different planes where aberration compensation can be performed, namely the recording and image plane. The first methods proposed to compensate for the field curvature were proposed through estimation of the adjustment parameters in the image plane with the use of conjugation equations [Cuc99b], to be used then in the recording plane [Fer03]. The formalism of aberration compensation was then generalised by Colomb *et al.* for higher orders, where the computation method was also modified, so that the aberration compensation could be performed in the recording plane without requiring the computation of the propagation [Col06a]. This generalisation brought the concept of numerical parametric lens (NPL), where the multiplication term on the right hand of Eq. (2.28) can be considered as a phase term denoting the curvature induced by a lens, which can be parametrically designed during reconstruction to optimise the imaging quality. Another point of view is to consider this phase term as the multiplying reference wave, as expressed for the tilt compensation, where the demodulation corresponds to employing the complex conjugate of the wave used for recording. In this sense, it can be considered as the digital counterpart of the magnification capabilities of lensless holography, where employing a reconstruction wave with various curvature influences the magnification of the reconstruction.

Different variations based on the concept described in Eq. (2.28) were proposed, such as employing the derivative of the phase image for estimation of the parameters, so that the spherical aberration term could be estimated on linear slopes [Fer06]. One should also note that the concept of aberration compensation can be further extended to other representations such as Zernike polynomials [Col06b]. While the coefficients in Eq. (2.28) are given for polynomial developments, any orthonormal basis can be used to describe the aberration coefficients.

Another approach for aberrations compensation consists in acquiring a reference correction hologram (RCH) [Fer03; Col06c], which corresponds to an acquisition with an empty field of view, which can be employed for corrections. By employing the Fourier filtering described in Eq. (2.26), one can recover the complex field of the RCH, which thus accounts for the aber-

rations of the optical system. The corrected wave field can therefore be calculated through the complex division

$$\Psi_H(x,y) = \frac{\Psi(x,y)}{\Psi_{RCH}(x,y)} = \frac{\left|\Psi_H(x,y)\right|}{\left|\Psi_{RCH}(x,y)\right|} e^{\mathrm{i}[\varphi_H(x,y)-\varphi_{RCH}(x,y)]}, \tag{2.29}$$

where one can identify in Eq. (2.29) the subtraction of the phase term derived from the RCH for correction of phase aberration. Furthermore, an amplitude normalisation appears as the consequence of the complex division formalism. It was shown that this operation can further improve the aberration compensation, by accounting for the amplitude illumination pattern in the entrance pupil, before propagation to the image plane, leading to enhanced resolution in phase measurements [Küh08]. The RCH approach can again be compared with optical reconstruction, as it also consists in getting an estimate of the reference through the measurement of an empty field of view, in order to enable multiplication with the complex conjugate of the reference wave.

The compensation of aberrations in the recording plane constitutes in fact one of the main advantages of Fresnel holography, as it enables the possibility to ensure an optimised phase flatness at a defocused plane, before digital propagation. The corrected wave field can therefore be focused with a better resolution thanks to prior correction. In the context of digital implementations of optimisation procedures to compensate aberrations, this approach has some analogies with adaptive optics, where the imaging system is dynamically adapted to ensure diffraction-limited imaging conditions [Déb07].

Digital wave propagation

As already mentioned earlier, holographic measurements often rely on recording the diffracted light in a non-imaging plane, such as in lensless holography or Fresnel holography. In those cases, it is thus necessary to propagate the recovered field to retrieve a focused image, enabling NPL design for aberration compensation and optimisation of imaging capabilities in the recording plane. In the context of digital holography, this thus requires the computation of a diffraction integral in order to calculate the propagated field at a plane situated at an arbitrary distance from the recording position, corresponding to the imaging plane.

Various implementations for digital propagation were proposed. On a general point of view, one can first consider that the domain where fields are propagated correspond usually to paraxial systems, either in macroscopic measurements classically consisting in low-aperture systems, or because digital propagation is performed in the image space, where strong curvatures have been compensated by the magnifying optics. For those reasons, the Fresnel approximation is commonly employed for numerical implementations of complex field propagation. The Fresnel approximation is derived from the Fresnel-Kirchhoff diffraction integral [Bor99], where the position at which is evaluated the complex field is far enough from the aperture, and where the coordinates of the phase advance resulting from propagation are ap-

proximated at the second order of a Taylor development, leading to

$$\Psi_I(x,y,d) = \frac{\exp(\mathrm{i}kd)}{\lambda d} \iint_S \Psi_H(\xi,\eta,0) \exp\left\{\mathrm{i}\frac{\pi}{\lambda d}\left[(\xi-x)^2+(\eta-y)^2\right]\right\} \mathrm{d}\xi\mathrm{d}\eta, \tag{2.30}$$

where Ψ_I is the field in the image plane, d is the propagation distance, and S is the integration domain corresponding to the field of view. In order to enable the fast implementation of this integral, one may reorder the terms to

$$\begin{aligned}\Psi_I(x,y,d) &= \frac{\exp(\mathrm{i}kd)}{\lambda d} \exp\left\{\mathrm{i}\frac{\pi}{\lambda d}\left(x^2+y^2\right)\right\} \times \\ &\iint_S \Psi_H(\xi,\eta,0) \exp\left\{\mathrm{i}\frac{\pi}{\lambda d}\left(\xi^2+\eta^2\right)\right\} \exp\left\{-\mathrm{i}\frac{2\pi}{\lambda d}\left(\xi x+\eta y\right)\right\} \mathrm{d}\xi\mathrm{d}\eta, \\ &= \frac{\exp(\mathrm{i}kd)}{\lambda d} \exp\left\{\mathrm{i}\frac{\pi}{\lambda d}\left(x^2+y^2\right)\right\} \times \mathscr{F}\left\{\Psi_H(\xi,\eta,0) \exp\left\{\mathrm{i}\frac{\pi}{\lambda d}\left(\xi^2+\eta^2\right)\right\}\right\},\end{aligned} \tag{2.31}$$

where the Fresnel integral can be expressed as a Fourier transform, enabling fast implementations through FFT algorithms. Direct discrete implementations—detailed in the next paragraphs—of Eq. (2.31) were employed [Cuc99b], as they possess specific properties which are very close to physical propagation. Typically, the physical size of a pixel depends on the propagation distance, due to the spatial frequencies expressed in Eq. (2.31) as $\omega_x = \frac{\eta}{\lambda d}$, so that the spatial sampling is

$$\Delta\xi = \frac{\lambda d}{L_x}, \tag{2.32}$$

where L_x corresponds to the physical size of the detector; similar expressions hold for the y coordinate. These relations imply typically a dependency on the wavelength to the sampling capability, which was used for example for measurements with different wavelengths [Fer04].

However, the variation of pixel size in regards to the propagation distance is usually considered as a disadvantage, so that other implementations were proposed to circumvent this issue. By considering again Eq. (2.30), one can consider it as a convolution, given as [Dem74; Mon06]

$$\Psi_I(x,y,d) = \frac{\exp(\mathrm{i}kd)}{\mathrm{i}\lambda d}\left[\Psi^H(x,y,0)\right] * \exp\left[\mathrm{i}\frac{\pi}{\lambda d}\left(x^2+y^2\right)\right]. \tag{2.33}$$

This approach has the disadvantage to require usually two Fourier transforms in its discrete implementation, but ensures a constant pixel size through propagation.

Digital propagation based on the Fresnel approximation requires sufficiently large values of propagation distance d, corresponding to the Fresnel regime of diffraction, in order to ensure convergence of the kernel in Eq. (2.33). Another approach employed to apply a digital propagation to the recovered object wave is based on the angular spectrum, which is defined as the

Fourier transform of the field along (x, y) coordinates [Goo96]

$$A(\omega_x, \omega_y, z) = \mathscr{F}\left\{\Psi_H(x, y, z)\right\}(\omega_x, \omega_y, z), \tag{2.34}$$

which corresponds to a plane wave decomposition in the Fourier domain of the original field. In this fashion, the propagation of the wave along a distance d in the optical axis direction corresponds to a sum of phase delays depending on the angle of propagation of the given plane wave, thus corresponding to

$$A(\omega_x, \omega_y, d) = A(\omega_x, \omega_y, 0) \exp\left(\mathrm{i}kd\sqrt{1-(\lambda\omega_x)^2-(\lambda\omega_y)^2}\right), \tag{2.35}$$

which requires two Fourier transforms for computation. The implementation of numerical propagation through the angular spectrum is usually more accurate than the Fresnel approximation, as the Fresnel propagation can be retrieved from the angular spectrum representation by employing the approximation

$$\sqrt{1-(\lambda\omega_x)^2-(\lambda\omega_y)^2} \approx 1 - \frac{(\lambda\omega_x)^2}{2} - \frac{(\lambda\omega_y)^2}{2}, \tag{2.36}$$

which corresponds again to the paraxial approximation. The angular spectrum method was employed in particular to incorporate the demodulation required by off-axis geometry in the propagation algorithm, thanks to its representation of plane waves propagating at various angles [Mat03; Nic05], or to increase the propagation range to close distances [Yu05]. The angular spectrum representation corresponds fundamentally to the diffraction calculated with the Rayleigh-Sommerfeld integral at the first order [Goo96].

Other refined algorithms were also proposed in the context of hologram reconstruction and digital propagation of complex waves. Typically, wavelet-based methods were employed, by taking advantage of the local processing capabilities of this representation, where specific wavelet bases were developed for holographic signals [Lie04].

On a general point of view, one major issue in the context of algorithms for digital propagation is the validity of the physical model employed in regards to numerical artefacts which can occur when employing those methods. It was shown for example that increasing the reconstruction distance d can improve the reconstruction quality in a continuous formalism [Pic08]. However, border conditions can induce severe artefacts when propagating fields. This is due on one side to the physical models employed, which assume an infinite support for the complex wave, while discrete matrices will be limited to the detector size, and on the other side to Fourier-based implementations, which can induce aliasing. It was thus proposed to apodise the borders of holograms with smooth functions such as cubic splines in order to limit the influence of those borders effects [Cuc00], at the cost of a part of the field of view. Other methods were also proposed, such as extending the Fourier support while minimising aliasing [Dub02], although only separable one-dimensional implementations were described.

The digital propagation can be considered as one of the major advantage provided by DH, as it enables compensation for defocus during experiment, without requiring any mechanical move during the experiment. This property is particularly important in the case of high-magnification systems, which depth of focus is very narrow (typ. in the hundreds of nanometre). It was for example shown that digital propagation makes 3D tracking of particles possible in temporal data sets [Lan09], or offline autofocusing [Lan08]. The use of digital propagation was also employed to extend the depth of focus of DHM images [Col10b].

Numerical implementation of DH reconstruction

Up to this point, only continuous equations were provided for the various steps required in the context of off-axis hologram reconstruction. We briefly present in this paragraph the discrete representation of the reconstruction equations, and take this opportunity to summarise the various steps required for off-axis Fresnel hologram reconstruction, which is the main type of holograms studied in this thesis.

From the intensity pattern $I(x,y)$ generated from the optical system, the detector, characterised by pixel sizes of $\Delta x, \Delta y$, and a resolution of $M \times N$, transmits a discrete signal corresponding to

$$I[m,n] = \int_{m\Delta x}^{(m+1)\Delta x} \int_{n\Delta y}^{(n+1)\Delta y} I(\xi,\eta)\mathrm{d}\xi\mathrm{d}\eta, \quad m \in [0,M[,\ n \in [0,N[. \tag{2.37}$$

One can then retrieve the complex diffraction order through Fourier filtering as

$$\Psi[m,n] = \mathrm{FFT}^{-1}\left\{\mathrm{FFT}\left\{I[m,n]\right\} \times \hat{W}[m,n]\right\}, \tag{2.38}$$

where $\hat{W}[m,n]$ is defined to encompass the discrete bandwidth of the desired imaging term. It is then possible to demodulate the complex wave and compensate for aberrations such as spherical aberration induced by curvature mismatch as

$$\Psi_H[m,n] = \Psi[m,n] \times \exp\left[\frac{2\pi\mathrm{i}}{\lambda}\sum_{p=1}^{P}\sum_{q=1}^{Q} C_{pq}\,(m\Delta x)^p\left(n\Delta y\right)^q\right], \tag{2.39}$$

where P,Q define the order of the polynomial function used to compensate for aberrations, respectively in the x and y directions. Another approach consists in employing a RCH for demodulation, according to Eq. (2.29). The aberration-free complex field can then be focused to the image plane with a digital propagation algorithm under the Fresnel approximation either through computation of the Fresnel integral in a Fourier formalism

$$\begin{aligned}\Psi_I[m,n;d] = \frac{\exp\left[\mathrm{i}kd\right]}{\lambda d}\exp\left\{\frac{\mathrm{i}\pi}{\lambda d}\left[(m\Delta x)^2 + \left(n\Delta y\right)^2\right]\right\} \times \\ \mathrm{FFT}\left\{\Psi_H[\xi,\eta;0] \times \exp\left\{\frac{\mathrm{i}\pi}{\lambda d}\left[(\xi\Delta x)^2 + \left(\eta\Delta y\right)^2\right]\right\}\right\}[m,n],\end{aligned} \tag{2.40}$$

or through a convolution-based formalism

$$\Psi_I[m,n;d] = \frac{\exp[\mathrm{i}kd]}{\mathrm{i}\lambda d} \times \Psi_H[m,n;0] * \exp\left\{\frac{\mathrm{i}\pi}{\lambda d}\left[(m\Delta x)^2 + \left(n\Delta y\right)^2\right]\right\}. \tag{2.41}$$

Finally, the aberration compensation procedure represented in Eq. (2.39) can be employed again at focus in the image plane. One should note that while the compensation in the hologram plane is usually efficient and enables corrections before focusing the image so that it enhances image resolution, a second compensation in the image can further enhance the phase flatness, as in-focus images possess finer details.

2.2.6 Digital holography applied to microscopy

When applied to microscopy, digital holographic reconstruction requires some specific adaptation. Although the reconstruction techniques described in subsections 2.2.4–2.2.5 are valid, some particular considerations can be made due to the insertion of a microscope objective in the object arm of the holographic interferometer.

The MO will indeed induce an inherent curvature on the object, which requires a compensation for proper phase imaging, as described for example in the discussion about aberration compensation. Furthermore, the strong magnification induced by the MO implies that the resolution of the holographic detection will be essentially limited by the numerical aperture of the objective, so that it corresponds to an optically-limited system, as described previously. Typically, strong magnifications imply a small spectral sampling, through the Fourier relation $\omega_x = {}^1/_{\Delta x}$, so that it is common to have frequencies spread over a small amount of pixels in the case of DHM. As a consequence, the constraints in regards to spatial sampling in off-axis holography become less restrictive as the magnification increases.

In a general point of view, the passage from DH to DHM requires more restrictive conditions on most of the aspects discussed in subsection 2.2.4. Typically, one must satisfy at the same time off-axis conditions ensuring no aliasing, and satisfy strict imaging conditions with small depth-of-field and highly aberration-compensated MOs. In this fashion, digital focusing capabilities brought by holography loosen these limitations, and make possible to ensure in-focus images through post-processing treatment. Again, as holography can be distinguished by its capability of imaging samples without requiring recording conditions with a focused image, various configurations can be employed. Optical components such as condenser lenses and microscope objectives, which are commonly employed in microscopy can induce strong curvatures, which have to be compensated at detection level, in order to avoid fringe aliasing. Furthermore, a field lens typically focuses the diffracted light on the detector to satisfy imaging conditions, for which standard distances were defined by manufacturers, so that tube length are typically 160, 200 or 250 mm, depending on the manufacturer. These constraints added to space requirements for beam recombination in interferometers and geometrical conditions for off-axis geometry make sometimes the optical design complicated.

While the respect of strict imaging conditions is usually not mandatory for holographic imaging, as defocused recording is possible through digital focusing capabilities, other restrictions are usually in place, due to the high temporal and spatial coherence of the light employed. Typically, one has to optimise fringe visibility, in order to ensure satisfying conditions for wavefront recovery.

Furthermore, on a practical point of view, it is mandatory to avoid filling totally the field of view of the MO, due to the high spatial coherence of the light source. The beam quality is indeed extremely sensitive on interactions with apertures, so that one has to avoid any borders effects to ensure an even illumination. This limitation however does not limit the effective field of view, as a MO provides far larger images than the surface of a digital detector.

2.2.7 Applications of digital holographic microscopy

Digital holography and DHM possess various features which makes them interesting tools in fields such as metrology, microscopy, phase detection, etc. Furthermore, the fundamental principle of holographic interferometry can be employed for any coherent light, so that the means employed for generation of the interference enclose a wide range of wavelengths. Finally, the very different interpretation available between the transmitted and reflected signals also multiply the range of possible use. This subsection can therefore be considered as an insight of some high-end applications, not covered in the fundamentals presented in the rest of this chapter.

Due to its capability of accurately measuring phase on a whole field of view [Cuc99a], DH found many applications in metrology through typically reflection measurements. This encloses topographic measurements [Tak82; Nic04], which could be brought to nanometer accuracy with proper calibration [Küh08]. Phase measurements however possess some limitations, in particular with rough surfaces which generate speckle. Reliable measurement methods were also developed in this case, such as differential holography [Ped97; Yam03], comparative holography [Ost02], or multiple wavelengths measurements, where the resulting value is the relative change on the sample between two states. Depth-resolved measurements were also developed for layered structures through multiple wavelengths combination [Col10a]. Another limitation consists in phase wrapping, potentially leading to phase ambiguity in the measurement. Although phase unwrapping algorithms were developed (see [Su04] for some examples of applications), the reliability of the recovered signal is still questionable. Physical methods were thus proposed to overcome this issue, through so-called beat wavelength measurements based on the combination of two wavelengths measurements [Pol73; Par06], which can be acquired in real-time through multiplexing [Küh07]. The applications in metrology are however not limited to reflection. As DHM measures the full complex field which interacted with a surface, the transmitted wavefront can be employed for example to characterise optical components [Cha06a; Koz09]. Furthermore, other physical observables can

also be measured through coherent light, such as in the case of polarisation-resolved measurements to recover the birefringence of a specimen [Col05].

The real-time capability of DHM led to various applications in biological sample observation through phase imaging [Mar05; Kem08b; Lue07]. The quantitative nature of phase measurement has also been employed to derive morphological [Sch07; Rap09b; Par10] or biological [Rap09a] parameters. In the context of biological interpretation, several methods were developed also to decouple the volume and intracellular concentration information, which are mixed in the phase signal either through controlled change of the immersion medium [Rap05] or through multiple wavelengths measurements [Rap08].

The coherent detection scheme of DHM also brought several applications in the field of nonlinear imaging. It has been possible to detect the phase signal of second harmonic effects [Sha10a], or to employ the complex field detection for three-dimensional positioning of particles [Hsi09; Sha10b]. Other nonlinear measurements such as coherent anti-Stokes resonance were reported [Shi10]. The use of coherent detection with holography also spread to other high-end optics methods and applications, such as total internal reflection microscopy [Jia06; Ash08], or plasmonics [Lim10; Suc11].

The coherent nature of the illumination light however causes also issues in the quality of imaging, as the diffraction in the case of monochromatic light is not averaged out through large bandwidth. This issue led to several attempts to reduce the coherence of the light source in order to minimise those effect either through reducing the temporal coherence [Lan10] or the spatial coherence through speckle illumination [Dub04; Par09].

The particular imaging properties, based on the coherent monochromatic features of DHM also led to various studies of the so-called coherent transfer function (CTF)—opposed to the classical incoherent optical transfer function—either theoretical [Wol70b; Kou07] or experimental [Mar07; Cha07a]. These imaging properties also led to various methods to improve the resolution through synthetic aperture [Mic07; Pat09] More recently, it has been proposed to employ the CTF for deconvolution of complex field to improve the image resolution [Cot10]. The combination of frames based on the specific CTF of coherent imaging also leads to tomographic imaging, as detailed in section 4.1.

2.3 Fluorescence microscopy

Fluorescence microscopy is a technique providing a huge range of applications, which grew in an impressive fashion in the last decades, thanks especially to the development of a wide variety of fluorescent dyes, and of various functionalisation possibilities which enabled imaging of particular biological regions and phenomena. In this section, our aim is to present briefly the context of fluorescence imaging, and to describe the specific application employed in this thesis, which consists in the quantitative monitoring of intracellular ionic concentrations in living cells, through the use of wide field fluorescence microscopy.

2.3.1 Principle of fluorescence imaging

Unlike standard microscopy, fluorescence imaging is not based on standard linear elastic interaction between light and matter, as it relies on the absorption of light, and on its re-emission. However, most molecular structures transfer the energy acquired through absorption to vibrations, and thus dissipate it through heating, so that it requires specific molecular arrangements to ensure energy transfer to light re-emission. Fluorescence microscopy is therefore performed usually by the insertion of natural compounds or specifically designed dyes possessing the chemical properties necessary for fluorescence emission [Tsi98].

In the case of a fluorescent molecule, the energy transfer corresponds essentially to the one depicted in Fig. 2.10, where the light is absorbed, transferring the molecule from its resting ground state S_0 to an excited energy state S_1 commonly called singlet state where the energy difference corresponds to the energy carried by the exciting photon. Part of it is usually transferred to vibrational energies between close energy states in the excitation band, while most of the energy is re-emitted through light at another energy (another wavelength) in a typical time frame of nanoseconds [Pet07].

As shown in Fig. 2.10, the excited molecule can also reach a so-called "forbidden" state called triplet state T. Due to its very low probability of occurrence, this energy state is commonly preventing fast energy transfer, thus letting the molecule at high energy levels for longer times, such as microseconds or more. The re-emission from a triplet state, commonly called phosphorescence, is of a different energy, and thus emits a longer wavelength.

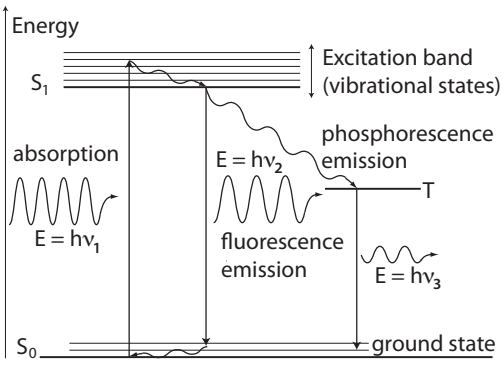

Figure 2.10: Jablonski diagram for linear fluorescence and phosphorescence.

For its applications in microscopy, this emission-detection scheme greatly modifies the imaging principle, as one needs to excite the fluorescent molecules with a specific wavelength corresponding to the absorption band of the dye. Fluorophores then act as point sources, emitting randomly in all directions, so that only a fraction of the light is collected by the microscope objective. This imaging scheme thus usually requires high intensities of exciting light focused on the sample, and high-gain sensors in order to detect the low amount of photons emitted by the fluorophores and collected by the MO.

On the other hand, the excitation-emission scheme presents very interesting capabilities for microscopy. Fluorescence images are typically background-free, as only specific regions containing the emitting dye will be imaged over a dark background. It also decouples the excitation from the detection, in opposition to standard microscopy, so that the spatial resolution is independent of the light profile employed for excitation.

Furthermore, fluorescence enables the possibility of developing functional imaging, in the sense that it is possible to chemically functionalise the fluorescent molecules to bond on specific parts of the specimen, such as DNA material [Lab80; Zam96], cytoskeleton [Tsi98], etc. The emergence of fluorescence imaging as a standard in microscopy is directly linked to the development of many of such probes, enabling the monitoring of specific biological regions and phenomena.

The measurement principle therefore usually relies on the generation of excitation light at a characterised wavelength, by employing for example spectral filters on white light, laser lines, or light processed through a monochromator. This beam is then exciting the specimen, and the fluorescence light collected through an imaging system. The collected light is then spectrally filtered in the emission range of the fluorophore, to filter out the remaining light coming from the excitation, and possible contributions from stray light. In order to minimise the effect of the excitation light, which is usually rather intense to ensure excitation of the fluorophore, a common configuration, denoted as epifluorescence, consists in exciting the sample through the microscope objective, and collect the emitted light through the same optical path, as presented for example in the optical setup of Fig. 2.17. In this case, most of the excitation light is not collected by the optical system (apart from reflections), thus greatly decreasing the requirements of emission filtering. In order to detect with a satisfying signal-to-noise ratio (SNR) the collected light, high-gain sensors are required, such as electron-multiplying CCD (EMCCD), or photomultiplier tubes (PMT) in the case of a scanning system such as in confocal fluorescence microscopy.

The fact of employing strong light intensities to maximise the emitted fluorescence can bring issues such as photo-damage, especially as excitation light is usually in high energy ranges (blue or UV light). Moreover, as fluorescence is based on an absorption principle, heat generation is enhanced by the presence of the fluorophore, which can even concentrate the heat dissipation at the observed location through functionalisation.

Fluorescence motivated various developments in high-resolution microscopy, in particular thanks to the decoupling of excitation and detection in the imaging process, as discussed above. The most important one could be considered to be the application of confocal detection schemes to fluorescence imaging [She77; Paw06]. As fluorescence is by essence emitted by point sources consisting of the fluorescent molecules, confocal imaging, by its characteristic of suppressing out-of-focus light, is particularly suited to enhance the resolution of fluorescence images, and provide depth information through sectioning. The point-source prop-

erties of fluorescence probes is also widely employed in deconvolution techniques, which enable the recovery of sharper images.

More recently, various approaches also took advantage of the excitation-detection scheme to further enhance image resolution. Structured illumination can be employed to further improve the point-spread function (PSF) of the excitation, in configurations such as the so-called 4Pi imaging scheme [Hel92; Hel97], which relies on the interference of two waves in a confocal configuration to enhance the localisation of excitation, or the I^3M, I^5M [Gus99], which is based on planar interference to enhance the localisation of the excitation. Fluorescent molecules were also employed as seeds for nonlinear imaging enhancement, such as in two-photon excited fluorescence, where infrared lasers are used to excite fluorophores which absorption band is in the visible, through nonlinear excitation [Den90; Kon00]. These nonlinear methods typically present the great advantage of enabling observation deeper in samples, as tissues have usually better transmittance properties in the infrared range.

2.3.2 Live cell imaging through fluorescence

We discuss in this section some particular aspects involved when employing fluorescence imaging for live cell observation. The fact of employing fluorescent probes in a living environment, which by definition controls its interaction with the external medium causes some specific issues that we comment here.

Loading

In the case of live cell imaging, one has first to insert the fluorescent dye inside the cellular body. The easiest method consists in fixing the cell in a permanent state with a specific solution, and permeabilising the membrane, thus enabling an easy transfer of the molecules in the intracellular environment. This technique makes possible to employ high concentrations of fluorophores, thus enhancing the detected signal, as high chemical concentrations will not damage biological structures after fixation. However, it is not suitable for dynamic measurements, which require other approaches to load the dye in the cell.

One of the most widely used methods in the context of wide field fluorescence, consists in using fluorophores that are made hydrophobic by cancelling their global net charge through the attachment of acetoxymethyl (AM) ester groups [Tsi81]. This conformation makes their transfer through the lipid membrane easier by diffusion, thus greatly enhancing the permeability of the membrane to the fluorophore. The molecule is then hydrolysed inside the cell by esterifying groups, making the molecule hydrophilic again, and thus impermeable to the cell membrane. The fluorophore is therefore stored in the cell through simple diffusion mechanisms, where the intracellular concentration of dye gradually increases in time. This method was proved however inefficient for *in vivo* measurements [Job07].

Another technique worth mentioning is the patch of cellular membranes. As various experiments require to patch cells in order for example to determine locally the type of receptors located on the membrane, or to measure membrane potential, one can employ the patch to insert fluorophores in the cell. As the patch is very localised, the influence of piercing the membrane can be neglected under some conditions, enabling live cell monitoring. This method is employed in particular with "leaking" fluorophores, that are molecules which intracellular concentration after loading typically decreases in cell bodies, to finally reach an equilibrium with the extracellular medium. In those cases, perfusion through membrane patching ensures a steady concentration of fluorophores inside the cell [Eil05]. Finally, transfection proved a very efficient method for producing cells expressing a given fluorophores [Cet05], where very high dye concentrations can be obtained. However, this technique is limited to certain types of fluorophores, as it relies on protein generation within the cell.

Functionalisation

As already stated above, one of the main advantage provided by fluorescence imaging is its capability to selectively image certain parts of a biological sample, such as its cytoskeleton [Tsi98], DNA [Lab80], or mitochondrial activity [Pen04], to name only a few of the many possibilities. Functionalisation mainly consists in chemically developing a molecule so that it will express its fluorescence properties when attached to the biologically relevant structure of observation. Therefore, in order to enable functional imaging, the fluorophore molecule must satisfy mainly two criteria: (i) the unattached fluorophore must not present any fluorescent property, in order to avoid parasitic fluorescence, and only express the required energy transitions when being chemically attached; (ii) the unattached fluorophore must have a high chemical affinity for the biological structure of interest. In classical cases, the fluorophore bonds to biological structures such as cytoskeleton or DNA material up to a saturation level corresponding to a point where the concentration of bonded fluorophores prevents other molecules to attach. In the particular case of the applications in this thesis, where fluorescent molecules are designed to fluoresce when attached to a given ion, generically denoted as C^{n+}, contained in the cytoplasm, the bond is not covalent as in the case of most fluorophores, but ionic. For this reason, the bond is reversible and the affinity expressed by fluorescence is a dynamical phenomenon which can be described by the chemical equilibrium

$$MC^{n+} \rightleftharpoons M + C^{n+}, \tag{2.42}$$

where M denotes the fluorophore molecule, in the case of a 1:1 complexation. The equilibrium concentrations, and thus the degree of affinity of the fluorophore for the probed ion, is expressed by the dissociation constant K_d, which is generally defined as

$$\begin{aligned} &A_xB_y \rightleftharpoons xA + yB, \\ &K_d = \frac{[A]^x \cdot [B]^y}{\left[A_xB_y\right]}. \end{aligned} \tag{2.43}$$

One should note that fluorophores probing for ionic concentrations are usually not absolutely specific. A non-negligible affinity for other ions typically of same valence usually occurs, so that Ca^{2+} indicators have for example a strong affinity for Mg^{2+} [Gry85], and non-negligible sensitivity for other divalent cations such as Cd^{2+}, Pb^{2+} or Mn^{2+}.

Photobleaching

Photobleaching, also often shortly named bleaching, denotes the loss of fluorescence capabilities of a molecule, due to a change in its chemical structure or conformation. The sources of bleaching can be multiple, and are not yet fully understood [Son95]. While some energetic transfers analogous to bleaching mechanisms are very well described in literature, and even used extensively in various imaging techniques such as fluorescence resonance energy transfer (FRET), other phenomena can only be explained very globally. It is commonly admitted that bleaching occurs mainly for excited molecules, when they can oxidise or form complexes with other molecules, thus changing their absorption properties [Dia06].

Most of the bleaching occurs at the triplet state T (cf. Fig. 2.10). While fluorescence mechanisms have lifetimes in the order of 1 to 10 nanoseconds, these triplet states can reach lifetimes up to milliseconds, thus letting more time for the excited molecules to chemically react with their environment. It was typically shown that the medium in which the fluorescent molecule is immersed can greatly influence the bleaching properties, demonstrating the importance of the chemical environment for complex formation. In general, it is considered that bleaching can be modelled by considering that fluorescent molecules can emit a mean maximum amount of photons, which can range from hundreds of photons to up to 10^8 photons depending on the fluorophore. However, apart from specific experiments dealing at molecular level, it is usually very difficult to know even approximately the amount of fluorescent molecules responsible for the fluorescence signal. Therefore, it is common practise to define a macroscopic model through an exponential decrease in intensity of the emitted signal to account for bleaching [Hir76]. In this fashion, the fluorescence intensity can be described as

$$I(t) = I_0 e^{-\tau t}, \tag{2.44}$$

where $I(t)$ denotes the fluorescence intensity at time t for a given exposure time of excitation light, I_0 is the original intensity at $t = 0$, and τ corresponds to an apparent lifetime of the fluorophore. It should be noted that more complicated models involving multiple exponential decays were also proposed [Son95], but it is still under debate whether the multiple decays would express physical phenomena of bleaching, or account for imperfections of the optical system [Dia06].

2.3.3 Quantitative assessment through fluorescence

The principle of quantification of intracellular ionic concentration is based on the chemical equilibrium of the fluorophore bonding with a given cation or anion, as described by

Eqs. (2.42–2.43). It implies that it is possible to image the intracellular concentration of a given ion through the fluorescence intensity of a molecule having a strong affinity for the observed ion. The retrieved signal therefore depends on the amount of fluorescent molecules bonded to ions.

In the case of quantitative imaging based on fluorescence, several parameters need to be taken into account in order to ensure relevant data extraction. As fluorescence is an intensity-based measurement method, quantitative imaging depends on the optical system, as excitation and collection patterns will influence the retrieved intensity on a given pixel. The quantification of the ionic concentration thus classically requires *in situ* calibrations in order to enable data recovery.

We detail below the principles and procedures required to perform this type of experiment. In a first part, we describe the measurement principle depending on the type of fluorophore employed, i.e. intensity-based or ratiometric. We then detail the calibration procedures necessary to recover a quantitative signal, and finally detail measurements depending on the type of fluorophore employed.

Intensity-based quantitative measurement

In the case of intensity-based fluorophores—also called single-wavelength indicators—the emission of the molecule is enhanced by its bond with the ion, as shown for the case of the calcium indicator Fluo-4 [Gee00] in Fig. 2.11(a). The global fluorescence thus increases with the calcium concentration $[Ca^{2+}]$ as more fluorescent molecules are bonded, as described by Eq. (2.42). This also implies that the fluorescence is an indicator of the free ion concentration contained in the cytoplasm, as ions bonded with organic material will not be able to react with fluorophore molecules.

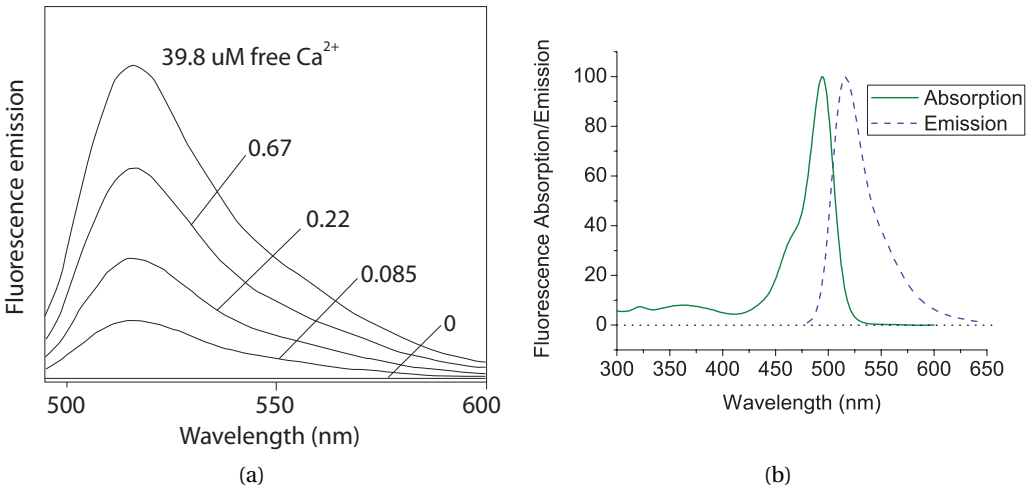

Figure 2.11: (a) $[Ca^{2+}]$-dependent emission spectrum of Fluo-4 and (b) absorption-emission spectra of Ca^{2+}-bonded Fluo-4 (extracted from [Inv]).

One major issue in the case of quantitative imaging consists in the fact that the exact concentration of fluorophores contained in the cytoplasm is not known, particularly in the case of cell loading performed with AM forms of the molecule, as only diffusion drives the final intracellular concentration. For this reason, it is necessary to calibrate the experiment *in situ* for each measured cell, by measuring the residual fluorescence when no fluorophore is attached to the ion ($F_{\min}$), and the maximum fluorescence when ionic saturation occurs, at a level depending on the dye concentration ($F_{\max}$). From those two experimental values, it is possible to determine the intracellular concentration through [Tsi89]

$$\left[C^{n+}\right]_{\text{free}} = K_d \frac{F - F_{\min}}{F_{\max} - F}. \tag{2.45}$$

where K_d is the dissociation constant of the chemical reaction between the indicator and the ion as defined in Eq. (2.43), and F is the measured fluorescence signal; the complete derivation of Eq. (2.45) is provided in appendix B. A calibration based on measuring the minimum and maximum saturation values *in situ* provides the advantage of taking into account the influence of the optical system, such as reflections detected by spectral cross-talk, stray light, collection efficiency, etc.

Single-wavelength ionic indicators present some disadvantages, particularly in regards to the accuracy of the measurements, because of their strong dependency on the illumination pattern, bleaching, etc. Various fluorophores were developed under this principle, providing monitoring with different wavelengths of excitation, and different sensitivities on the given ion. To name only a few, calcium indicators are for example Fluo-3 and its newer version Fluo-4 (490 nm/505 nm) [Gee00], higher wavelength absorption dyes like Rhod-2 (540 nm/575 nm) [Min89], or lower affinity like Fluo-5N (490 nm/516 nm, $K_d \approx 90$ µM. A general description of the many different available fluorophores is provided for example in [Par08].

Furthermore, it can be experimentally cumbersome to obtain *in situ* the values $F_{\min}$ and $F_{\max}$, so that other models were developed to minimise the amount of experimental parameters required to be measured during the experiment [Mar00]. The ionic concentration can thus also be expressed as

$$\left[\mathrm{C}^{n+}\right]_{\text{free}} = K_d \frac{\frac{F}{F_{\max}} - \frac{1}{R_f}}{1 - \frac{F}{F_{\max}}}, \tag{2.46}$$

where $R_f = {}^{F_{\max}}/_{F_{\min}}$ is the dynamic range of the fluorophore. The details of derivation are provided in appendix B. This equation is typically interesting for fluorophores with high dynamic ranges, as the term R_f^{-1} becomes negligible compared to the fluorescence signal. This parameter can be characterised *in vitro*, as it depends only on the fluorescent molecule characteristics. As an illustration, the dynamic range of Fluo-4 is typically $R_f = 85$ [Mar00]. One should note that other calibration procedures were also proposed, such as pseudo-ratio methods for intensity-based fluorophores [Che93], where the measured fluorescence signal is divided by

a control image, corresponding to the Ca^{2+} resting levels of cells, so that the presented signal becomes $F' = {}^{F}/_{F_0}$, where F_0 corresponds to the resting $[Ca^{2+}]$.

Ratiometric quantitative measurement

The drawbacks of fluorophores based on intensity measurements led to the development of other types of molecules, relying on a ratiometric principle. In this case, the bond with the ion does not enhance the fluorescence emission, but changes the absorption properties of the molecule, as shown in Fig. 2.12(a), for the case of the $[Ca^{2+}]$-dependent Fura-2 fluorophore [Gry85]. One can see that in this case, the absorption spectrum changes depending on the ion concentration, so that the maximum absorption is not situated at the same wavelength. In this fashion, the signal of interest becomes the ratio of two measurements, i.e. $R = {}^{F_{\lambda_1}}/_{F_{\lambda_2}}$. In the case of Fura-2, the wavelengths are typically taken as $\lambda_1 = 340$ nm and $\lambda_2 = 380$ nm, which are situated around the so-called isosbestic point, which corresponds to the wavelength at which absorption does not depend on the ion concentration (typ. 360 nm for Fura-2). However, as standard optical elements absorb strongly in the deep-UV, other approaches employ the isosbestic point instead of the low wavelength for ratiometric observation, thus enhancing the SNR of measurement by avoiding excitation in the far-UV.

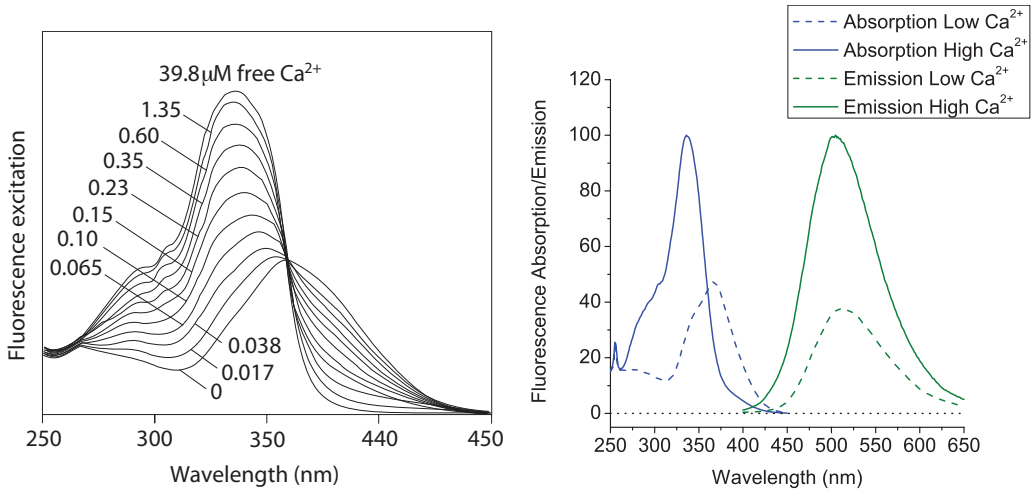

Figure 2.12: Fura-2 $[Ca^{2+}]$-dependent (a) absorption spectrum and (b) absorption-emission spectra (extracted from [Inv]).

This measurement method presents the advantage of being independent of the emission strength of the fluorophore, and is thus independent of the illumination or bleaching, as both measurements change according to those parameters. This differential approach brings more stability to the observed ionic concentration. However, one should note that this measurement principle requires two acquisitions instead of one, so that the fluorophore bleaches

twice as fast. Although the measure is independent on bleaching, the noise stability of the measurement nevertheless decreases even with this type of fluorophore.

In this case, the recovery of the ionic concentration is slightly more complex. The most common approach is based on the model proposed by Grynkiewicz *et al.* [Gry85], where the monitored ion concentration is given by

$$\left[C^{n+}\right]_{\text{free}} = K_d \frac{R - R_{\min}}{R_{\max} - R} \cdot \frac{F_{\lambda_2,\max}}{F_{\lambda_2,\min}}, \tag{2.47}$$

where $R_{\min}$ and $R_{\max}$ are the ratios with respectively no intracellular ionic concentration and ionic saturation, and F_{λ_2} is the fluorescence at the second excitation wavelength also for low and high ionic concentration. The derivation of Eq. (2.47) is provided in appendix B. One should note that the calibration method described here is valid essentially for slow changes, as the two measurements F_{λ_1} and F_{λ_2} are commonly taken at different times, so that the dynamic changes in intracellular calcium concentration must be sampled by the acquisition rate. For this reason, more refined methods were also developed to take into account the rapid changes of calcium in the calibration [Ley98].

Calibration procedure

One can see from Eqs. (2.45) and (2.47) that three parameters must be known in order to perform a quantitative measurements for both types of fluorophore, which consist in the signal with all fluorophore molecules in free form, $F_{\min}$, the signal with all fluorophore molecules bonded, $F_{\max}$ and the dissociation constant of the fluorophore K_d. In this paragraph, we denote both F and R for respectively intensity-based and ratiometric measurements by the variable F for the generality of the discussion.

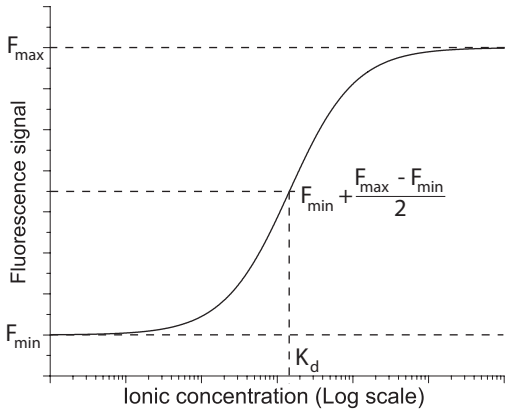

Figure 2.13: Typical response of a fluorophore depending on the intracellular ionic concentration.

Practically, the value $F_{\min}$ can be measured by decreasing the intracellular concentration of the observed ion to reach a minimal level; this can be performed by employing a chelator to

inactivate the ion, and permeabilisation of the membrane by employing a ionophore to enable fast ionic transfer. On the other hand, the value $F_{\max}$ can be obtained by saturating the intracellular concentration with to a high level; this can be achieved by increasing the extracellular concentration of the ion and permeabilising the membrane. One should note that the values $F_{\min}, F_{\max}$ must be measured *in situ*, as they strongly depend on the fluorophore intracellular concentration, which cannot be controlled, and can be different for each cell. Those values are therefore classically measured at the end of the experiment, by perfusing calibration solutions [Tak99].

The typical fluorescence response of a fluorophore in function of the ionic concentration is shown in Fig. 2.13, where the values $F_{\min}$ and $F_{\max}$ are represented, showing the linear range around K_d in which the experimental values should be situated for optimal measurement. The calibration equations given in Eqs. (2.45–2.47) typically linearise the response, implying that the raw measurement must be interpreted with care, as it does not correspond to a linear relationship with the ionic concentration.

The other required parameter is the dissociation constant K_d, which corresponds to the proportionality constant in the linear range of the fluorescence signal dynamics. This parameter can be either determined *in situ* by perfusing known ionic concentrations in the linear range while ensuring membrane permeability [Tak99], or *in vitro* by precisely determining the fluorescence intensity in media with known ionic concentrations [Gry85]. A major issue in these calibration procedures is the fact that the dissociation constant of most ionic indicators changes greatly depending on the external environment, and are thus extremely dependent on parameters such as the pH, the ionic strength, etc. The accuracy of *in vitro* calibrations is therefore extremely dependent on the type of solution employed. On the other hand, *in vivo* calibrations are usually complicated, as membrane permeabilisation induces a gradual dilution of the intracellular content, which also changes the sensitivity of the dye [Par08].

Specific ions measurement

The measurement procedures detailed above were employed in the experiments of this thesis with three different dyes, which consist in

Fura-2: a ratiometric $\left[Ca^{2+}\right]$ indicator excited in the UV range, and emitting in the green range (cf. Fig. 2.12(b)).

SBFI: a ratiometric $\left[Na^{+}\right]$ indicator excited in the UV range, and emitting in the green range (cf. Fig. 2.14(b)).

Fluo-4: an intensity-based $\left[Ca^{2+}\right]$ indicator excited in the blue range, and emitting in the green (cf. Fig. 2.11(b)).

We present in Table 2.1 the main properties of those dyes, such as their wavelengths of maximal excitation and emission, and their typical dissociation constants. The K_d values provided

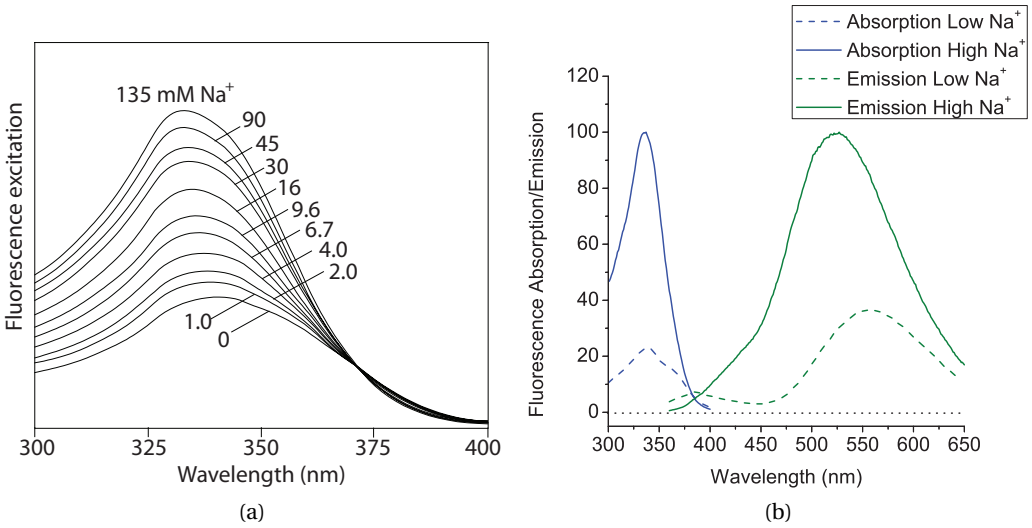

Figure 2.14: SBFI $[Na^+]$-dependent (a) absorption spectrum and (b) absorption-emission spectra (extracted from [Inv]).

Dye	Indicator for	Low ion concentration		High ion concentration		K_d *in vitro*
		λ_{exc} [nm]	λ_{em} [nm]	λ_{exc} [nm]	λ_{em} [nm]	
Fura-2	Ca^{2+}	363	512	335	505	145 nM
SBFI	Na^+	338	555	335	523	11.3 mM
Fluo-4	Ca^{2+}	–	–	494	516	345 nM

Table 2.1: Main properties of Fura-2, SBFI and Fluo-4 fluorescent dyes.

here correspond to *in vitro* calibrations, where chelators are employed to ensure that a known concentration of free ion is present in the solution. Furthermore, as SBFI as a non-negligible sensitivity to K^+, the values given here were taken with a physiological concentration of K^+, i.e. $[Na^+] + [K^+] = 135$ mM.

2.4 Experimental setups

We present in this section the various setups employed for experiments during the thesis work. The main reason for describing in details these implementations in this introduction is the fact that some setups were employed for multiple purposes along the various research topics tackled during this thesis. It thus prevents redundancy along the manuscript. Furthermore, the fact of presenting the different experimental configurations simultaneously enables the possibility of comparing them directly.

2.4.1 State of the art DHM setups

We first describe in details in this subsection standard setups for digital holographic microscopy, as some experiments were performed straightforwardly with this type of implementations. Furthermore, the more complicated setups are essentially variations on the main theme given by those generic setups. The acronyms employed in the optical schemes are listed in Table 2.2, and are employed for all the different schemes.

$\lambda/2$	Half-waveplate
BE	Beam expander
BFP	Back focal plane
BS	Beam splitter
C	Condenser lens
CCD	Charge-coupled device camera
CL	Curvature lens
CMOS	Complementary metal-oxyde semiconductor camera
DM	Dichroic mirror
EMCCD	Electron multiplying charge-coupled device camera
EXF	Excitation filter
EMF	Emission filter
FL	Field lens
FC	Fibre coupler
FM	Flip mirror
IM	Image plane
M	Mirror
MO	Microscope objective
PBS	Polarising beam splitter

Table 2.2: List of acronyms of optical schemes.

Standard DHM setups are essentially composed of a Mach-Zehnder interferometer in which a microscope objective is inserted. The light source is generally composed of a laser diode providing several milliwatts in the range of red wavelengths. This type of source is typically linearly polarised at the emission, enabling good fringe contrast. The light source is first collimated with compensation of ellipsicity, and then divided into two beams through a beam splitter (BS). Classically, a polarising beam splitter (PBS) is employed with half-wave plates, in order to ensure a stable linear polarisation state, and to enable the adjustment of the intensity ratio between the two arms by rotating the half-wave plate before the BS. A second half-wave plate is then used in one of the two arms to orient the two polarisation states in the same way to optimise the fringe visibility at detection.

In each of the two arms, a beam expander (BE) distributes the light intensity on a spatial region sufficient to fill the entrance pupil of the imaging system in the object arm, and to

ensure full coverage of the detector surface in the reference arm. The beam expanders are classically used as spatial filters by inserting a pinhole at the focal point, in order to ensure an optimal beam quality by using a point-source for illumination. The fact of performing this operation on the two arms separately makes it possible to filter out eventual imperfections of the wavefront induced by optical elements situated before the BE, and thus ensures an optimal beam quality.

After interaction with the sample, which is described in details for both configurations below, the two beams are recombined through a non-polarising BS. The field lens (FL), imaging the sample on the image plane IM, is classically placed after the recombining BS, implying that a curvature lens (CL) must be employed in the reference arm, to match the curvature of the non-diffracted wave passing in the MO, in order to ensure straight interference fringes. Guaranteeing straight fringes is not required for recording the hologram, but makes it easier to avoid aliasing, and suppresses physically part of the spherical aberration which should be otherwise numerically compensated. The interference pattern is then recorded typically with a CCD camera in the off-axis configuration, where the inclination angle determining the modulation of the imaging orders can be adjusted by rotating the recombination beam splitter. The detection plane is classically several centimetres before or after the actual imaging plane, to ensure recording in the Fresnel regime in regards to apertures of the optical system.

This configuration thus corresponds to wide field imaging conditions, although some specific aspects must be taken into account. Due to the high spatial coherence of the employed light, one needs to avoid any contact with apertures in the MO, implying that it is usually better to avoid filling the whole entrance pupil. This method is also better in terms of light efficiency, as detectors have an available surface which is far smaller than the field of view provided by standard MOs, so that avoiding full illumination of the entrance pupil does not reduce the observed field of view in practise.

Transmission DHM

A typical transmission DHM setup is presented in Fig. 2.15(a), according to the description above. In case of transmission, the object beam converges into the entrance pupil of the microscope objective by using a condenser lens (C), and interacts with the sample, where the diffracted light is collected by the MO. In Fig. 2.15(a), the beam shown after the exit pupil of the MO consists in the non-diffracted beam, in order to show the curvature matching with the reference wave at the detector level, while the imaging beam is represented in dashed lines, showing the recording in the Fresnel regime.

Reflection DHM

A typical reflection setup is presented in Fig. 2.15(b). In this fashion, the object beam is focused with the condenser lens (C) in the back focal plane (BFP) of the microscope objective, generating a plane wave at the entrance pupil, which impinges on the sample. The reflected

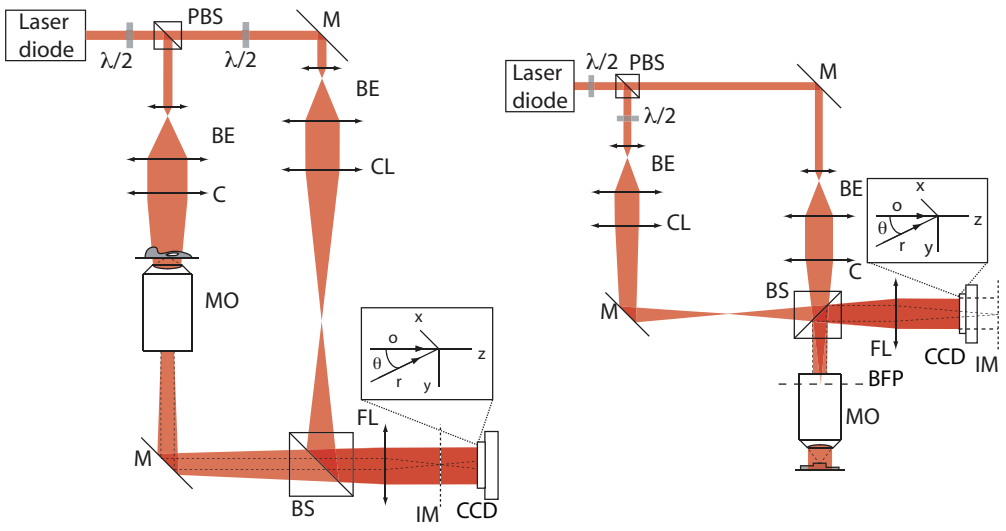

Figure 2.15: Standard digital holographic microscopy setups in (a) transmission and (b) in reflection. The beam outgoing the microscope objective (MO) represents the non-diffracted part of the wave, with the imaging diffracted light represented in dashed lines.

wave is collected back by the MO, and imaged by the field lens (FL). The interfering scheme is similar to the transmission setup, where the reference wave curvature is matched with the one of the zero-order of the object wave. As in the transmission configuration, the interaction with apertures in the MO should be avoided, by choosing carefully the focusing power of the condenser lens, in order to fill only partly the entrance pupil.

This setup configuration was typically employed for the reflection measurements of chapter 3.

2.4.2 Multimodal DHM setup

We present in this subsection an experimental setup which was designed with the purpose of providing multimodal imaging capabilities. DHM was adapted on a commercial microscope system (Zeiss AxioObserver Z1), which provides a generic imaging platform with bright field incoherent imaging, and epifluorescence capabilities (cf. Fig. 2.16). Functionalities such as bright field, Zernike phase-contrast and differential interference contrast (DIC) are typically available. The purposes of the development of this setup were first to test the possibility of adding the DHM capability on a commercial microscope, primarily developed for incoherent imaging applications. It was also making possible to characterise the phase quality retrieved from an optical system specifically optimised for microscopic imaging, to be compared with designs specifically developed for DHM applications. The approach taken in this case was to employ free-space optics, as it had been shown that employing fibre optics was perturbing

the polarisation state of light, thus greatly decreasing the fringe contrast at recording. Preliminary tests assessing the possibility of measuring both fluorescence emission and holograms of the same specimen were also performed on this setup, leading then to the development of a dedicated setup, as described in subsection 2.4.3.

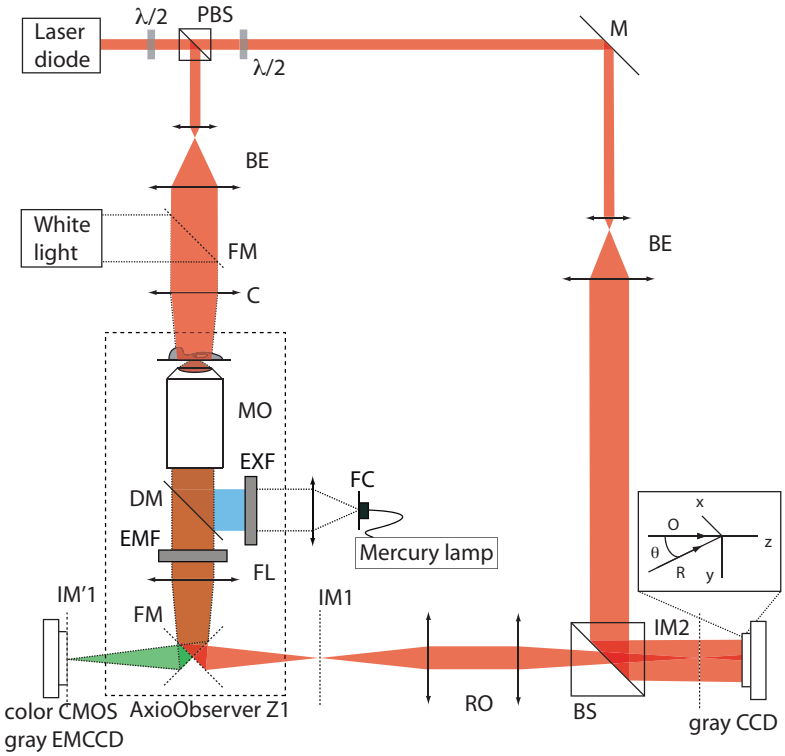

Figure 2.16: Multimodal implementation of DHM, enabling combined measurements with DHM, epifluorescence and incoherent wide field imaging.

The wide field system consists in a standard inverted microscope system with infinity-corrected objectives, with a halogen lamp as the incoherent light source. The epifluorescent system employs a Mercury lamp brought to the system through a fibre coupler (FC). The excitation light is selected through an excitation filter (EXF) and sent into the MO with a dichroic mirror (DM). The fluorescence light emitted from the sample is collected back by the MO, passes through the dichroic mirror, and is filtered from any remaining excitation light with an emission filter (EMF). The fluorescent image is then focused at plane IM'1 where a high-gain camera records it.

The DHM functionality was added to this commercial system by implementing a standard transmission setup around it. The coherent light is sent on the sample by mechanically changing the illumination path, so that coherent light is sent on the condenser lens for transmission imaging. Flipping mirrors (FM) are then employed to send the collected light to another port of the microscope system, where the image is formed at plane IM1. As the image plane is commonly close to the camera port, a relay optics (RO) is used to image back the sig-

nal further away from the microscope at image plane IM2, in order to create the space necessary for recombining the object wave with the reference beam, and detect the interference pattern on a separate CCD camera. The beams represented in Fig. 2.16 in the image space represent the imaging beams.

The implementation of the DHM capability is rather similar from the standard setup presented in Fig. 2.15(a), apart from the position of the field lens. As the whole imaging system is enclosed in the microscope, it implies that the reference wave does not pass through the field lens. The curvature matching can therefore be performed by the RO directly, so that the non-diffracted part of the object wave is a plane wave, or by using a CL in the reference arm. Furthermore, the RO enables the possibility of adjusting finely the effective imaging conditions of the whole system, in which a microscope turret is available, enabling magnifications ranging from 4× to 100× on a single system.

The multiple imaging possibilities provided by this setup imply that it is necessary to employ calibration for image comparison, in order to compensate for the magnification difference induced by the RO and by the different pixel sizes of the cameras. Typically, a scaling and a translation has to be performed in order to obtain proper merged images, which can be characterised by measuring a well-known object.

This setup was typically employed in the transmission measurements of chapter 3, for the tomographic measurements of chapter 4, and for the measurements involving colour images in chapter 5.

2.4.3 Combined fluorescence-DHM setup

The experimental setup described in subsection 2.4.2 enables imaging of fluorescence and DHM signals on the same sample, but does not provide simultaneous imaging, as flip mirrors are still necessary to switch between the two imaging systems. Another setup was thus designed, with the purpose of providing simultaneously the two type of signals without involving any mechanical movement.

The system consists in a standard transmission DHM setup, taken in this case as the DHM T1000 designed by Lyncée Tec SA, which was specially modified to incorporate fluorescence imaging (cf. Fig. 2.17). This is performed by employing two different dichroic mirrors in the infinity space behind the microscope objective, enabling first the separation of the wavelength employed for holography, which can be easily selected in the red range. A second dichroic mirror is then used to enable the epifluorescence excitation. Employing a specific spectral mirror to reflect the laser line makes possible to avoid that the fluorescence signal is perturbed by the light used for interference. Furthermore, the epifluorescence configuration does not require any light excitation from the condenser side, so that holographic imaging can be performed easily in transmission without having to incorporate specific optics to combine incoherent and coherent optics at the excitation level.

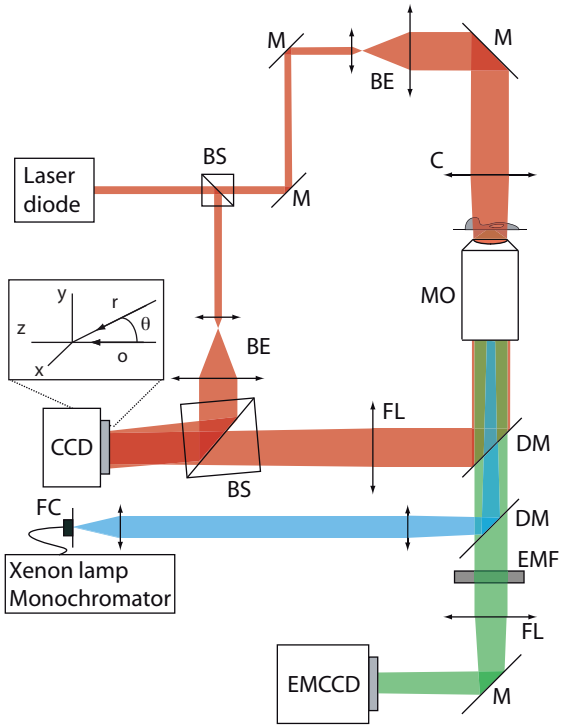

Figure 2.17: Dual DHM transmission setup and epifluorescence system, based on a DHM microscope developed by Lyncée Tec SA.

The fluorescence excitation light is provided by a monochromator (Polychrome V, Till Photonics), delivering light ranging from 320 nm to 680 nm, with a power of typically 10 mW at 470 nm and a bandwidth of $\Delta\lambda = 15$ nm. The excitation is brought to the system with a liquid light guide, where an optical system specifically designed to ensure sufficient transmittance in the spectral range provided by the monochromator fills the exit pupil of the microscope objective. Employing a monochromator enables the possibility of switching rapidly the excitation wavelength without using any emission filter, thus avoiding any mechanical movement, but at the cost of available optical power. The excitation optical system after the FC was specifically designed to optimise the available optical power, and to enable sufficient illumination in the UV range, in order to ensure the possibility of measuring specimen dyed with fluorophores absorbing typically in the $320-340$ nm range. The fluorescence light is detected by an electron-multiplying camera (EMCCD) (iXon 887, Andor Technology), cooled at $-45\,^{\circ}$C and recording 16-bit images.

This setup was employed for the measurements performed in chapter 5, where combined fluorescence and quantitative phase signals are involved.

References

[All03] E. Allaria, S. Brugioni, S. De Nicola, P. Ferraro, S. Grilli, and R. Meucci, "Digital holography at 10.6 mm," *Opt. Commun.* **215** (4–6), pp. 257–262 (2003).

[All69] R. Allen, G. David, and G. Nomarski, "The Zeiss-Nomarski differential interference equipment for transmitted-light microscopy," *Z. Wiss. Mikrosk.* **69** (4), pp. 193–221 (1969).

[Ans01] Z. Ansari, Y. Gu, M. Tziraki, R. Jones, P. French, D. Nolte, and M. Melloch, "Elimination of beam walk-off in low-coherence off-axis photorefractive holography," *Opt. Lett.* **26** (6), pp. 334–336 (2001).

[Arn04] M. Arnison, K. Larkin, C. Sheppard, N. Smith, and C. Cogswell, "Linear phase imaging using differential interference contrast microscopy," *J. Microsc.* **214** (1), pp. 7–12 (2004).

[Ash08] W. Ash and M. Kim, "Digital holography of total internal reflection," *Opt. Express* **16** (13), pp. 9811–9820 (2008).

[Awa04] Y. Awatsuji, M. Sasada, and T. Kubota, "Parallel quasi-phase-shifting digital holography," *Appl. Phys. Lett.* **85** (6), pp. 1069–1071 (2004).

[Bar98] A. Barty, K. Nugent, D. Paganin, and A. Roberts, "Quantitative optical phase microscopy," *Opt. Lett.* **23** (11), pp. 817–819 (1998).

[Bon09] P. Bon, G. Maucort, B. Wattellier, and S. Monneret, "Quadriwave lateral shearing interferometry for quantitative phase microscopy of living cells," *Opt. Express* **17** (15), pp. 13 080–13 094 (2009).

[Bor99] M. Born and E. Wolf, *Principles of Optics*, 7th ed. Cambridge University Press (1999).

[Bru74] J. H. Bruning, D. R. Herriott, J. E. Gallagher, D. P. Rosenfeld, A. D. White, and D. J. Brangaccio, "Digital Wavefront Measuring Interferometer for Testing Optical Surfaces and Lenses," *Appl. Opt.* **13** (11), pp. 2693–2703 (1974).

[Car66] P. Carré, "Installation et utilisation du comparateur photoélectrique et interférentiel du Bureau International des Poids et Mesures," *Metrologia* **2** (1), pp. 13–23 (1966).

[Car70] W. p. Carter, "Computational Reconstruction of Scattering Objects from Holograms," *J. Opt. Soc. Am.* **60** (3), pp. 306–314 (1970).

[Cet05] M. Cetinkaya, A. Zeytun, J. Sofo, and M. C. Demirel, "How do insertions affect green fluorescent protein ?," *Chem. Phys. Lett.* **419** (1), pp. 48–54 (2005).

[Cha06a] F. Charrière, J. Kühn, T. Colomb, F. Montfort, E. Cuche, Y. Emery, K. Weible, P. Marquet, and C. Depeursinge, "Characterization of microlenses by digital holographic microscopy," *Appl. Opt.* **45** (5), pp. 829–835 (2006).

[Cha06b] F. Charrière, T. Colomb, F. Montfort, E. Cuche, P. Marquet, and C. Depeursinge, "Shot-noise influence on the reconstructed phase image signal-to-noise ratio in digital holographic microscopy," *Appl. Opt.* **45** (29), pp. 7667–7673 (2006).

[Cha07a] F. Charrière, A. Marian, T. Colomb, P. Marquet, and C. Depeursinge, "Amplitude point spread function measurement of high NA microscope objectives by digital holographic microscopy," *Opt. Lett.* **32** (16), pp. 2456–2458 (2007).

[Cha07b] F. Charrière, B. Rappaz, J. Kühn, T. Colomb, P. Marquet, and C. Depeursinge, "Influence of shot noise on phase measurement accuracy in digital holographic microscopy," *Opt. Express* **15** (14), pp. 8818–8831 (2007).

[Che93] H. Cheng, W. Lederer, and M. Cannell, "Calcium sparks: Elementary events underlying excitation-contraction coupling in heart muscle," *Science* **262** (5134), pp. 740–744 (1993).

[Col02] T. Colomb, P. Dahlgren, D. Beghuin, E. Cuche, P. Marquet, and C. Depeursinge, "Polarization imaging by use of digital holography," *Appl. Opt.* **41** (1), pp. 27–37 (2002).

[Col05] T. Colomb, F. Dürr, E. Cuche, P. Marquet, H. Limberger, R.-P. Salathé, and C. Depeursinge, "Polarization microscopy by use of digital holography: Application to optical-fiber birefringence measurements," *Appl. Opt.* **44** (21), pp. 4461–4469 (2005).

[Col06a] T. Colomb, E. Cuche, F. Charrière, J. Kühn, N. Aspert, F. Montfort, P. Marquet, and C. Depeursinge, "Automatic procedure for aberration compensation in digital holographic microscopy and applications to specimen shape compensation," *Appl. Opt.* **45** (5), pp. 851–863 (2006).

[Col06b] T. Colomb, F. Montfort, J. Kühn, N. Aspert, E. Cuche, A. Marian, F. Charrière, S. Bourquin, P. Marquet, and C. Depeursinge, "Numerical parametric lens for shifting, magnification, and complete aberration compensation in digital holographic microscopy," *J. Opt. Soc. Am. A* **23** (12), pp. 3177–3190 (2006).

[Col06c] T. Colomb, J. Kühn, F. Charrière, C. Depeursinge, P. Marquet, and N. Aspert, "Total aberrations compensation in digital holographic microscopy with a reference conjugated hologram," *Opt. Express* **14** (10), pp. 4300–4306 (2006).

[Col10a] T. Colomb, S. Krivec, H. Hutter, A. A. Akatay, N. Pavillon, F. Montfort, E. Cuche, J. Kühn, C. Depeursinge, and Y. Emery, "Digital holographic reflectometry," *Opt. Express* **18** (4), pp. 3719–3731 (2010).

[Col10b] T. Colomb, N. Pavillon, J. Kühn, E. Cuche, C. Depeursinge, and Y. Emery, "Extended depth-of-focus by digital holographic microscopy," *Opt. Lett.* **35** (11), pp. 1840–1842 (2010).

[Coq95] O. Coquoz, R. Conde, F. Taleblou, and C. Depeursinge, "Performances of endoscopic holography with a multicore optical fiber," *Appl. Opt.* **34** (31), pp. 7186–7193 (1995).

[Cot10] Y. Cotte, M. F. Toy, N. Pavillon, and C. Depeursinge, "Microscopy image resolution improvement by deconvolution of complex fields," *Opt. Express* **19** (19), pp. 19 462–19 478 (2010).

[Cuc00] E. Cuche, P. Marquet, and C. Depeursinge, "Aperture apodization using cubic spline interpolation: Application in digital holographic microscopy," *Opt. Commun.* **182** (1–3), pp. 59–69 (2000).

[Cuc99a] E. Cuche, F. Bevilacqua, and C. Depeursinge, "Digital holography for quantitative phase-contrast imaging," *Opt. Lett.* **24** (5), pp. 291–293 (1999).

[Cuc99b] E. Cuche, P. Marquet, and C. Depeursinge, "Simultaneous amplitude-contrast and quantitative phase-contrast microscopy by numerical reconstruction of Fresnel off-axis holograms," *Appl. Opt.* **38** (34), pp. 6994–7001 (1999).

[Déb07] D. Débarre, M. Booth, and T. Wilson, "Image based adaptive optics through optimisation of low spatial frequencies," *Opt. Express* **15** (13), pp. 8176–8190 (2007).

[Dem03] N. Demoli, J. Meštrovic, and I. Sovic, "Subtraction digital holography," *Appl. Opt.* **42** (5), pp. 798–804 (2003).

[Dem74] T. H. Demetrakopoulos and R. Mittra, "Digital and Optical Reconstruction of Images from Suboptical Diffraction Patterns," *Appl. Opt.* **13** (3), pp. 665–670 (1974).

[Den90] W. Denk, J. Strickler, and W. Webb, "Two-photon laser scanning fluorescence microscopy," *Science* **248** (4951), pp. 73–76 (1990).

[Dia06] A. Diaspro, G. Chirico, C. Usai, P. Ramoino, and J. Dobrucki, "Photobleaching," in *Handbook of Biological Confocal Microscopy*, J. B. Pawley, Ed., Springer (2006), pp. 690–702.

[Dub02] F. Dubois, O. Monnom, C. Yourassowsky, and J.-C. Legros, "Border processing in digital holography by extension of the digital hologram and reduction of the higher spatial frequencies," *Appl. Opt.* **41** (14), pp. 2621–2626 (2002).

[Dub04] F. Dubois, M. Requena, C. Minetti, O. Monnom, and E. Istasse, "Partial spatial coherence effects in digital holographic microscopy with a laser source," *Appl. Opt.* **43** (5), pp. 1131–1139 (2004).

[Dub06] F. Dubois, N. Callens, C. Yourassowsky, M. Hoyos, P. Kurowski, and O. Monnom, "Digital holographic microscopy with reduced spatial coherence for three-dimensional particle flow analysis," *Appl. Opt.* **45** (5), pp. 864–871 (2006).

[Eil05] J. Eilers and A. Konnerth, "A Practical Guide: Dye Loading with Patch Pipettes," in *Imaging in Neuroscience and Development: A Laboratory Manual*, R. Yuste, Ed., Cold Spring Harbor Laboratory Press (2005), pp. 277–282.

[Fer03] P. Ferraro, S. De Nicola, A. Finizio, G. Coppola, S. Grilli, C. Magro, and G. Pierattini, "Compensation of the inherent wave front curvature in digital holographic coherent microscopy for quantitative phase-contrast imaging," *Appl. Opt.* **42** (11), pp. 1938–1946 (2003).

[Fer04] P. Ferraro, S. De Nicola, G. Coppola, A. Finizio, D. Alfieri, and G. Pierattini, "Controlling image size as a function of distance and wavelength in Fresnel–transform reconstruction of digital holograms," *Opt. Lett.* **29** (8), pp. 854–856 (2004).

[Fer06] P. Ferraro, D. Alferi, S. De Nicola, L. De Petrocellis, A. Finizio, and G. Pierattini, "Quantitative phase-contrast microscopy by a lateral shear approach to digital holographic image reconstruction," *Opt. Lett.* **31** (10), pp. 1405–1407 (2006).

[Fie82] J. R. Fienup, "Phase retrieval algorithms: a comparison," *Appl. Opt.* **21** (15), pp. 2758–2769 (1982).

[Fu10] D. Fu, S. Oh, W. Choi, T. Yamauchi, A. Dorn, Z. Yaqoob, R. R. Dasari, and M. S. Feld, "Quantitative DIC microscopy using an off-axis self-interference approach," *Opt. Lett.* **35** (14), pp. 2370–2372 (2010).

[Gab48] D. Gabor, "A new microscopic principle," *Nature* **161** (4098), pp. 777–778 (1948).

[Gab49] D. Gabor, "Microscopy by Reconstructed Wave-Fronts," *P. Roy. Soc. Lond. A Mat.* **197** (1051), pp. 454–487 (1949).

[Gab66] D. Gabor and W. P. Goss, "Interference Microscope with Total Wavefront Reconstruction," *J. Opt. Soc. Am.* **56** (7), pp. 849–856 (1966).

[Gee00] K. Gee, K. Brown, W.-N. Chen, J. Bishop-Stewart, D. Gray, and I. Johnson, "Chemical and physiological characterization of fluo-4 Ca^{2+}-indicator dyes," *Cell Calcium* **27** (2), pp. 97–106 (2000).

[Ger72] R. Gerchberg and W. Saxton, "Practical algorithm for the determination of phase from image and diffraction plane pictures," *Optik* **35** (2), pp. 237–250 (1972).

[Goo67] J. Goodman and R. Lawrence, "Digital image formation from electronically detected holograms," *Appl. Phys. Lett.* **11** (3), pp. 77–79 (1967).

[Goo96] J. W. Goodman, *Introduction to Fourier Optics*, 2nd ed. Mc Graw Hills Companies, Inc., New York (1996).

[Gro07] M. Gross and M. Atlan, "Digital holography with ultimate sensitivity," *Opt. Lett.* **32** (8), pp. 909–911 (2007).

[Gry85] G. Grynkiewicz, M. Poenie, and R. Tsien, "A new generation of Ca^{2+} indicators with greatly improved fluorescence properties," *J. Biol. Chem.* **260** (6), pp. 3440–3450 (1985).

[Guo02] C.-S. Guo, L. Zhang, H.-T. Wang, J. Liao, and Y. Zhu, "Phase-shifting error and its elimination in phase-shifting digital holography," *Opt. Lett.* **27** (19), pp. 1687–1689 (2002).

[Guo04] P. Guo and A. Devaney, "Digital microscopy using phase-shifting digital holography with two reference waves," *Opt. Lett.* **29** (8), pp. 857–859 (2004).

[Gus99] M. Gustafsson, D. Agard, and J. Sedat, "I^5M: 3D widefield light microscopy with better than 100 nm axial resolution," *J. Microsc.* **195** (1), pp. 10–16 (1999).

[Hel92] S. Hell and E. H. Stelzer, "Properties of a 4Pi confocal fluorescence microscope," *J. Opt. Soc. Am. A* **9** (12), pp. 2159–2166 (1992).

[Hel97] S. Hell, M. Schrader, and H. Van Der Voort, "Far–field fluorescence microscopy with three–dimensional resolution in the 100–nm range," *J. Microsc.* **187** (1), pp. 1–7 (1997).

[Hir76] T. Hirschfeld, "Quantum efficiency independence of the time integrated emission from a fluorescent molecule," *Appl. Opt.* **15** (12), pp. 3135–3139 (1976).

[HR07] J. Herrera Ramírez and J. Garcia-Sucerquia, "Digital off-axis holography without zero-order diffraction via phase manipulation," *Opt. Commun.* **277** (2), pp. 259–263 (2007).

[Hsi09] C.-L. Hsieh, R. Grange, Y. Pu, and D. Psaltis, "Three-dimensional harmonic holographic microscopy using nanoparticles as probes for cell imaging," *Opt. Express* **17** (4), pp. 2880–2891 (2009).

[Hua03] P. Huang, C. Zhang, and F.-P. Chiang, "High-speed 3-D shape measurement based on digital fringe projection," *Opt. Eng.* **42** (1), pp. 163–168 (2003).

[Hue03] M. Huebschman, B. Munjuluri, and H. Garner, "Dynamic holographic 3-D image projection," *Opt. Express* **11** (5), pp. 437–445 (2003).

[Ind00] G. Indebetouw, P. Klysubun, T. Kim, and T.-C. Poon, "Imaging properties of scanning holographic microscopy," *J. Opt. Soc. Am. A* **17** (3), pp. 380–390 (2000).

[Ind01] G. Indebetouw and P. Klysubun, "Spatiotemporal digital microholography," *J. Opt. Soc. Am. A* **18** (2), pp. 319–325 (2001).

[Ind06a] G. Indebetouw, W. Zhong, and D. Chamberlin-Long, "Point-spread function synthesis in scanning holographic microscopy," *J. Opt. Soc. Am. A* **23** (7), pp. 1708–1717 (2006).

[Ind06b] G. Indebetouw and W. Zhong, "Scanning holographic microscopy of three-dimensional fluorescent specimens," *J. Opt. Soc. Am. A* **23** (7), pp. 1699–1707 (2006).

[Ind07] G. Indebetouw, Y. Tada, J. Rosen, and G. Brooker, "Scanning holographic microscopy with resolution exceeding the Rayleigh limit of the objective by superposition of off-axis holograms," *Appl. Opt.* **46** (6), pp. 993–1000 (2007).

[Inv] (Feb. 2011). Invitrogen by Life Technologies, [Online]. Available: http://www.invitrogen.com/site/us/en/home.html.

[Jia06] Z.-C. Jian, P.-J. Hsieh, H.-C. Hsieh, H.-W. Chen, and D.-C. Su, "A method for measuring two-dimensional refractive index distribution with the total internal reflection of p-polarized light and the phase-shifting interferometry," *Opt. Commun.* **268** (1), pp. 23–26 (2006).

[Job07] P. D. Jobsis, C. Rothstein Emily, and R. S. Balaban, "Limited utility of acetoxymethyl (AM)-based intracellular delivery systems, in vivo: interference by extracellular esterases," *J. Microsc.* **226** (1), pp. 74–81 (2007).

[Kem08a] B Kemper, S. Stürwald, C. Remmersmann, P. Langehanenberg, and G. von Bally, "Characterisation of light emitting diodes (LEDs) for application in digital holographic microscopy for inspection of micro and nanostructured surfaces," *Opt. Laser Eng.* **46** (7), pp. 499–507 (2008).

[Kem08b] B. Kemper and G. Von Bally, "Digital holographic microscopy for live cell applications and technical inspection," *Appl. Opt.* **47** (4), A52–A61 (2008).

[Kon00] K. Konig, "Multiphoton microscopy in life sciences," *J. Microsc.* **200** (2), pp. 83–104 (2000).

[Kou07] S. Kou and C. Sheppard, "Imaging in digital holographic microscopy," *Opt. Express* **15** (21), pp. 13 640–13 648 (2007).

[Koz09] T. Kozacki, M. Józwik, and R. Jó wicki, "Determination of optical field generated by a microlens using digital holographic method," *Opto-electron. Rev.* **17** (3), pp. 211–216 (2009).

[Kre05] T. Kreis, *Handbook of Holographic Interferometry*. Wiley-VCH, Weinheim (2005).

[Kre86] T. Kreis, "Digital holographic interference-phase measurement using the Fourier-transform method," *J. Opt. Soc. Am. A* **3** (6), pp. 847–855 (1986).

[Kro72] M. A. Kronrod, N. S. Merzlyakov, and L. P. Yaroslavsky, "Reconstruction of holograms with a computer," *Sov. Phys. Tech. Phys.* **17**, pp. 333–334 (1972).

[Küh07] J. Kühn, T. Colomb, F. Montfort, F. Charrière, Y. Emery, E. Cuche, P. Marquet, and C. Depeursinge, "Real-time dual-wavelength with digital holographic microscopy with a single hologram acquisition," *Opt. Express* **15** (12), pp. 7231–7242 (2007).

[Küh08] J. Kühn, F. Charrière, T. Colomb, E. Cuche, F. Montfort, Y. Emery, P. Marquet, and C. Depeursinge, "Axial sub–nanometer accuracy in digital holographic microscopy," *Meas. Sci. Technol.* **19** (7), p. 074 007 (2008).

[Lab80] C. Labarca and K. Paigen, "A simple, rapid, and sensitive DNA assay procedure," *Anal. Biochem.* **102** (2), pp. 344–352 (1980).

[Lan08] P. Langehanenberg, B. Kemper, D. Dirksen, and G. Von Bally, "Autofocusing in digital holographic phase contrast microscopy on pure phase objects for live cell imaging," *Appl. Opt.* **47** (19), pp. D176–D182 (2008).

[Lan09] P. Langehanenberg, L. Ivanova, I. Bernhardt, S. Ketelhut, A. Vollmer, D. Dirksen, G. Georgiev, G. von Bally, and B. Kemper, "Automated three-dimensional tracking of living cells by digital holographic microscopy.," *J. Biomed. Opt.* **14** (1), p. 014 018 (2009).

[Lan10] P. Langehanenberg, G. v. Bally, and B. Kemper, "Application of partially coherent light in live cell imaging with digital holographic microscopy," *J. Mod. Optic.* **57** (9), pp. 709–717 (2010).

[Lei62] E. N. Leith and J. Upatnieks, "Reconstructed wavefronts and communication theory," *J. Opt. Soc. Am.* **52** (10), pp. 1123–1130 (1962).

[Lei64] E. N. Leith and J. Upatnieks, "Wavefront Reconstruction with Diffused Illumination and Three–Dimensional Objects," *J. Opt. Soc. Am.* **54** (11), pp. 1295–1301 (1964).

[Ley98] L. Leybaert, J. Sneyd, and M. J. Sanderson, "A Simple Method for High Temporal Resolution Calcium Imaging with Dual Excitation Dyes," *Biophys. J.* **75** (4), pp. 2025–2029 (1998).

[Lie04] M. Liebling, T. Blu, and M. Unser, "Complex-wave retrieval from a single off-axis hologram," *J. Opt. Soc. Am. A* **21** (3), pp. 367–377 (2004).

[Lim10] Y. Lim, J. Hahn, S. Kim, J. Park, H. Kim, and B. Lee, "Plasmonic light beaming manipulation and its detection using holographic microscopy," *IEEE J. Quantum Elect.* **46** (3), pp. 300–305 (2010).

[Liu09] J.-P. Liu and T.-C. Poon, "Two-step-only quadrature phase-shifting digital holography," *Opt. Lett.* **34** (3), pp. 250–252 (2009).

[Lue07] N. Lue, W. Choi, G. Popescu, T. Ikeda, R. Dasari, K. Badizadegan, and M. Feld, "Quantitative phase imaging of live cells using fast Fourier phase microscopy," *Appl. Opt.* **46** (10), pp. 1836–1842 (2007).

[Mar00] M. Maravall, Z. Mainen, B. Sabatini, and K. Svoboda, "Estimating intracellular calcium concentrations and buffering without wavelength ratioing," *Biophys. J.* **78** (5), pp. 2655–2667 (2000).

[Mar05] P. Marquet, B. Rappaz, P. Magistretti, E. Cuche, Y. Emery, T. Colomb, and C. Depeursinge, "Digital holographic microscopy: A noninvasive contrast imaging technique allowing quantitative visualization of living cells with subwavelength axial accuracy," *Opt. Lett.* **30** (5), pp. 468–470 (2005).

[Mar07] A. Marian, F. Charrière, T. Colomb, F. Montfort, J. Kühn, P. Marquet, and C. Depeursinge, "On the complex three-dimensional amplitude point spread function of lenses and microscope objectives: Theoretical aspects, simulations and measurements by digital holography," *J. Microsc.* **225** (2), pp. 156–169 (2007).

[Mat03] K. Matsushima, H. Schimmel, and F. Wyrowski, "Fast calculation method for optical diffraction on tilted planes by use of the angular spectrum of plane waves," *J. Opt. Soc. Am. A* **20** (9), pp. 1755–1762 (2003).

[Mat09] O. Matoba, T. Nomura, E. Pérez-Cabré, M. Millán, and B. Javidi, "Optical techniques for information security," *Proc. IEEE* **97** (6), pp. 1128–1148 (2009).

[Mic07] V. Micó, Z. Zalevsky, and J. García, "Synthetic aperture microscopy using off-axis illumination and polarization coding," *Opt. Commun.* **276** (2), pp. 209–217 (2007).

[Mic10] V. Micó and J. García, "Common-path phase-shifting lensless holographic microscopy," *Opt. Lett.* **35** (23), pp. 3919–3921 (2010).

[Mid01] P. Midgley, "An introduction to off-axis electron holography," *Micron* **32** (2), pp. 167–184 (2001).

[Mil05] G. Mills and I. Yamaguchi, "Effects of quantization in phase-shifting digital holography," *Appl. Opt.* **44** (7), pp. 1216–1225 (2005).

[Min89] A. Minta and R. Tsien, "Fluorescent indicators for cytosolic sodium," *J. Biol. Chem.* **264** (32), pp. 19 449–19 457 (1989).

[Mon06] F. Montfort, F. Charrière, T. Colomb, E. Cuche, P. Marquet, and C. Depeursinge, "Purely numerical compensation for microscope objective phase curvature in digital holographic microscopy: Influence of digital phase mask position," *J. Opt. Soc. Am. A* **23** (11), pp. 2944–2953 (2006).

[Mon09] D. Monaghan, D. Kelly, N. Pandey, and B. Hennelly, "Twin removal in digital holography using diffuse illumination," *Opt. Lett.* **34** (23), pp. 3610–3612 (2009).

[Nic04] S. de Nicola, P. Ferraro, A. Finizio, S. Grilli, G. Coppola, M. Iodice, P. de Natale, and M. Chiarini, "Surface topography of microstructures in lithium niobate by digital holographic microscopy," *Meas. Sci. Technol.* **15** (5), pp. 961–968 (2004).

[Nic05] S. de Nicola, A. Finizio, G. Pierattini, P. Ferraro, and D. Alfieri, "Angular spectrum method with correction of anamorphism for numerical reconstruction of digital holograms on tilted planes," *Opt. Express* **13** (24), pp. 9935–9940 (2005).

[Ost02] W. Osten, T. Baumbach, and W. Jüptner, "Comparative digital holography," *Opt. Lett.* **27** (20), pp. 1764–1766 (2002).

[Pag98] D. Paganin and K. Nugent, "Noninterferometric phase imaging with partially coherent light," *Phys. Rev. Lett.* **80** (12), pp. 2586–2589 (1998).

[Pan11] N. Pandey and B. Hennelly, "Quantization noise and its reduction in lensless Fourier digital holography.," *Appl. Opt.* **50** (7), B58–B70 (2011).

[Par06] D. Parshall and M. Kim, "Digital holographic microscopy with dual wavelength phase unwrapping," *Appl. Opt.* **45** (3), pp. 451–459 (2006).

[Par08] R. Paredes, J. Etzler, L. Watts, W. Zheng, and J. Lechleiter, "Chemical calcium indicators," *Methods* **46** (3), pp. 143–151 (2008).

[Par09] Y. Park, W. Choi, Z. Yaqoob, R. Dasari, K. Badizadegan, and M. S. Feld, "Speckle-field digital holographic microscopy," *Opt. Express* **17** (15), pp. 12 285–12 292 (2009).

[Par10] J. Park, C. A. Best, T. Auth, N. S. Gov, S. A. Safran, G. Popescu, S. Suresh, and M. S. Feld, "Metabolic remodeling of the human red blood cell membrane," *P. Natl. Acad. Sci. U* **107**, pp. 1289–1294 (2010).

[Pat09] M. Paturzo and P. Ferraro, "Correct self-assembling of spatial frequencies in super-resolution synthetic aperture digital holography," *Opt. Lett.* **34** (23), pp. 3650–3652 (2009).

[Paw06] J. Pawley, Ed., *Handbook of Biological Confocal Microscopy*, 3rd ed. Springer (2006).

[Ped97] G. Pedrini and H. Tiziani, "Quantitative evaluation of two-dimensional dynamic deformations using digital holography," *Opt. Laser Technol.* **29** (5), pp. 249–256 (1997).

[Pen04] W. Pendergrass, N. Wolf, and M. Pool, "Efficacy of MitoTracker Green^{TM} and CMXrosamine to measure changes in mitochondrial membrane potentials in living cells and tissues," *Cytom. Part A* **61** (2), pp. 162–169 (2004).

[Pet07] H. Petty, "Fluorescence microscopy: Established and emerging methods, experimental strategies, and applications in immunology," *Microsc. Res. Techniq.* **70** (8), pp. 687–709 (2007).

[Pic08] P. Picart and J. Leval, "General theoretical formulation of image formation in digital Fresnel holography," *J. Opt. Soc. Am. A* **25** (7), pp. 1744–1761 (2008).

[Pol73] C. Polhemus, "Two-Wavelength Interferometry," *Appl. Opt.* **12** (9), pp. 2071–2074 (1973).

[Pop04] G. Popescu, L. Deflores, J. Vaughan, K. Badizadegan, H. Iwai, R. Dasari, and M. Feld, "Fourier phase microscopy for investigation of biological structures and dynamics," *Opt. Lett.* **29** (21), pp. 2503–2505 (2004).

[Pop06] G. Popescu, T. Ikeda, R. Dasari, and M. Feld, "Diffraction phase microscopy for quantifying cell structure and dynamics," *Opt. Lett.* **31** (6), pp. 775–777 (2006).

[Pu08] Y. Pu, M. Centurion, and D. Psaltis, "Harmonic holography: a new holographic principle," *Appl. Opt.* **47** (4), A103–A110 (2008).

[Rap05] B. Rappaz, P. Marquet, E. Cuche, Y. Emery, C. Depeursinge, and P. Magistretti, "Measurement of the integral refractive index and dynamic cell morphometry of living cells with digital holographic microscopy," *Opt. Express* **13** (23), pp. 9361–9373 (2005).

[Rap08] B. Rappaz, F. Charrière, C. Depeursinge, P. J. Magistretti, and P. Marquet, "Simultaneous cell morphometry and refractive index measurement with dual-wavelength digital holographic microscopy and dye-enhanced dispersion of perfusion medium," *Opt. Lett.* **33** (7), pp. 744–746 (2008).

[Rap09a] B. Rappaz, E. Cano, T. Colomb, J. Kühn, C. Depeursinge, V. Simanis, P. Magistretti, and P. Marquet, "Noninvasive characterization of the fission yeast cell cycle by monitoring dry mass with digital holographic microscopy," *J. Biomed. Opt.* **14** (3), 034049 (5 pages) (2009).

[Rap09b] B. Rappaz, A. Barbul, A. Hoffmann, D. Boss, R. Korenstein, C. Depeursinge, P. J. Magistretti, and P. Marquet, "Spatial analysis of erythrocyte membrane fluctuations by digital holographic microscopy," *Blood Cell Mol. Dis.* **42** (3), pp. 228–232 (2009).

[Ras94] P. K. Rastogi, Ed., *Holographic Interferometry: Principles and Methods*, ser. Springer Series in Optical sciences. Springer-Verlag, New York (1994), vol. 68, ch. 5.

[Ros07] J. Rosen and G. Brooker, "Fluorescence incoherent color holography," *Opt. Express* **15** (5), pp. 2244–2250 (2007).

[Ros08] J. Rosen and G. Brooker, "Non-scanning motionless fluorescence three-dimensional holographic microscopy," *Nat. Photon.* **2** (3), pp. 190–195 (2008).

[Sch07] J. Schnekenburger, I. Bredebusch, W. Domschke, B. Kemper, P. Langehanenberg, and G. von Bally, "Digital holographic imaging of dynamic cytoskeleton changes," *Medical Laser Application* **22** (3), pp. 165–172 (2007).

[Sch94] U. Schnars and W. P. O. Jüptner, "Direct recording of holograms by a CCD target and numerical reconstruction," *Appl. Opt.* **33** (2), pp. 179–181 (1994).

[Sha10a] E. Shaffer, C. Moratal, P. Magistretti, P. Marquet, and C. Depeursinge, "Label-free second harmonic phase imaging of biological specimen by digital holographic microscopy," *Opt. Lett.* **35** (24), pp. 4102–4104 (2010).

[Sha10b] E. Shaffer, P. Marquet, and C. Depeursinge, "Real time, nanometric 3D-tracking of nanoparticles made possible by second harmonic generation digital holographic microscopy," *Opt. Express* **18** (16), pp. 17 392–17 403 (2010).

[She77] C. Sheppard and A. Choudhury, "Image formation in the scanning microscopy," *Opt. Acta* **24** (10), pp. 1051–1073 (1977).

[Shi10] K. Shi, H. Li, Q. Xu, D. Psaltis, and Z. Liu, "Coherent Anti-Stokes Raman Holography for Chemically Selective Single-Shot Nonscanning 3D Imaging," *Phys. Rev. Lett.* **104** (9), p. 093 902 (2010).

[Shr06] M. Shribak and S. Inoué, "Orientation-independent differential interference contrast microscopy," *Appl. Opt.* **45** (3), pp. 460–469 (2006).

[Son95] L. Song, E. Hennink, I. Young, and H. Tanke, "Photobleaching kinetics of fluorescein in quantitative fluorescence microscopy," *Biophys. J.* **68** (6), pp. 2588–2600 (1995).

[Su01] X. Y. Su and W. J. Chen, "Fourier transform profilometry: a review," *Opt. Laser Eng.* **35** (5), pp. 263–284 (2001).

[Su04] X. Su and W. Chen, "Reliability-guided phase unwrapping algorithm: A review," *Opt. Laser Eng.* **42** (3), pp. 245–261 (2004).

[Su10] T.-W. Su, S. O. Isikman, W. Bishara, D. Tseng, A. Erlinger, and A. Ozcan, "Multi-angle lensless digital holography for depth resolved imaging on a chip," *Opt. Express* **18** (9), pp. 9690–9711 (2010).

[Suc11] S. Suck, S. Collin, N. Bardou, Y. Wilde, and G. Tessier, "Imaging the three-dimensional scattering pattern of plasmonic nanodisk chains by digital heterodyne holography," *Opt. Lett.* **36** (6), pp. 849–851 (2011).

[Tak05] M. Takeda, W. Wang, Z. Duan, and Y. Miyamoto, "Coherence holography," *Opt. Express* **13** (23), pp. 9629–9635 (2005).

[Tak82] M. Takeda, H. Ina, and S. Kobayashi, "Fourier-transform method of fringe-pattern analysis for computer-based topography and interferometry," *J. Opt. Soc. Am.* **72** (1), pp. 156–160 (1982).

[Tak99] A. Takahashi, P. Camacho, J. Lechleiter, and B. Herman, "Measurement of intracellular calcium," *Physiol. Rev.* **79** (4), pp. 1089–1125 (1999).

[Til00] J. Tiller, A. Barty, D. Paganin, and K. Nugent, "The holographic twin image problem: A deterministic phase solution," *Opt. Commun.* **183** (1–4), pp. 7–14 (2000).

[Tsi81] R. Y. Tsien, "A non-disruptive technique for loading calcium buffers and indicators into cells," *Nature* **290** (5806), pp. 527–528 (1981).

[Tsi89] R. Y. Tsien, "Fluorescent Probes of Cell Signaling," *Annu. Rev. Neurosci.* **12** (1), pp. 227–253 (1989).

[Tsi98] R. Tsien, "The green fluorescent protein," *Annu. Rev. Biochem.* **67**, pp. 509–544 (1998).

[Wan04] Z. Wang and B. Han, "Advanced iterative algorithm for phase extraction of randomly phase-shifted interferograms," *Opt. Lett.* **29** (14), pp. 1671–1673 (2004).

[Wol70a] E. Wolf, "Determination of the Amplitude and the Phase of Scattered Fields by Holography," *J. Opt. Soc. Am.* **60** (1), pp. 18–20 (1970).

[Wol70b] E. Wolf and J. Shewell, "Diffraction theory of holography," *J. Math. Phys.* **11** (8), pp. 2254–2267 (1970).

[Wya02] J. Wyant, "White light interferometry," in *Holography: A Tribute to Yuri Denisyuk and Emmet Leith*, vol. 4737, pp. 98–107, Orlando, FL (2002).

[Xu01] W. Xu, M. Jericho, I. Meinertzhagen, and H. Kreuzer, "Digital in-line holography for biological applications," *P. Natl. Acad. Sci.* **98** (20), pp. 11 301–11 305 (2001).

[Xu08] X. F. Xu, L. Z. Cai, Y. R. Wang, X. F. Meng, W. J. Sun, H. Zhang, X. C. Cheng, G. Y. Dong, and X. X. Shen, "Simple direct extraction of unknown phase shift and wavefront reconstruction in generalized phase-shifting interferometry: algorithm and experiments," *Opt. Lett.* **33** (8), pp. 776–778 (2008).

[Yam03] I. Yamaguchi, J. Kato, and H. Matsuzaki, "Measurement of surface shape and deformation by phase-shifting image digital holography," *Opt. Eng.* **42** (5), pp. 1267–1271 (2003).

[Yam97] I. Yamaguchi and T. Zhang, "Phase-shifting digital holography," *Opt. Lett.* **22** (16), pp. 1268–1270 (1997).

[Yar10] F. Yara , H. Kang, and L. Onural, "State of the art in holographic displays: A survey," *J. Disp. Technol.* **6** (10), pp. 443–454 (2010).

[Yu05] L. Yu and M. K. Kim, "Wavelength scanning digital interference holography for tomographic three-dimensional imaging by use of the angular spectrum method," *Opt. Lett.* **30** (16), pp. 2092–2094 (2005).

[Zam96] L. Zamai, E. Falcieri, G. Marhefka, and M. Vitale, "Supravital exposure to propidium iodide identifies apoptotic cells in the absence of nucleosomal DNA fragmentation," *Cytometry* **23** (4), pp. 303–311 (1996).

[Zer42a] F. Zernike, "Phase contrast, a new method for the microscopic observation of transparent objects part II," *Physica* **9** (10), pp. 974–986 (1942).

[Zer42b] F. Zernike, "Phase contrast, a new method for the microsopic observation of transparent objects," *Physica* **9**, pp. 686–698 (1942).

[Zer55] F. Zernike, "How I discovered phase contrast," *Science* **121** (3141), pp. 345–349 (1955).

3 Zero-order suppression in off-axis digital holography

The occurrence of the so-called zero-order term in interferometry is a fundamental consequence of the recording process, for which the measurement consists in recording the interference between two beams, where one is classically taken as a reference. The measurement principle relies on extracting the mutual coherence between the two beams, from which the complex wavefront of the object can be retrieved. However, as the mutual coherence corresponds to cross-correlation terms in the interference equation, it is inevitable to record also at the same time the autocorrelation terms, which are a direct physical consequence of recording electromagnetic waves in intensity, as it is the case for all means of detection in optics. This issue brings back fundamentally to the interaction of light with matter, where—in the case of digital detection devices—photo-electrons are generated from the occurrence probability of photons, thus intrinsically interacting with light intensity.

This issue appeared from the very beginning of research in holography, when Gabor developed the first holographic measurement principle for X-rays (although validation of the principle was performed with wavelengths in the visible range), and is a field that has been investigated up to now in the digital era. However, most of the early research in this field focused on the so-called twin-image, which is the second consequence of the recording process of holography. As autocorrelation terms are recorded due to the measurement in intensity, the complex conjugate of the measured cross-correlation is also present, as a direct consequence of the real nature of the measured signal.

The methods to extract one of the mutual coherence term can be mainly divided in two main categories in regards to the developments made during the last decades, which correspond to spatial and temporal methods, as described in details in subsection 2.2.5. Both methods rely on the modulation induced on cross-correlation terms by the interference process in order to separate the information. In both cases, the occurrence of the zero-order implies a reduction of the bandwidth, either in the spatial or in the temporal domain, making thus reconstruction techniques requiring a reduction of spatial bandwidth to ensure sampling, or the acquisition of more images to guarantee proper extraction of the cross-correlation terms.

In this chapter, we first review the state of the art of reconstruction methods specifically aimed to account for zero-order suppression in section 3.1. One should note that as this field closely relates to fundamental reconstruction methods of digital holography, some redundancy may occur with the introduction of section 2.2. Then, in section 3.2, the implications of the presence of the autocorrelation terms on the extraction of the complex data is discussed in more details and in a rigorous way. We then describe the methods developed during our work for suppressing the zero-order: we first present an iterative method based on the interference equation in section 3.3, and secondly a method relying on a nonlinear operator, which provides intrinsic zero-order suppression in section 3.4. We then discuss the obtained results and potential improvements in section 3.5.

The material presented in this chapter was partly adapted from various publications. The section 3.3 was adapted from [Pav10b], and section 3.4 was adapted mainly from [See09; See11; Pav09; Pav10a].

3.1 State of the art

The occurrence of the autocorrelation parasitic terms in holographic detection has been identified from the very beginning of the invention of holography by Gabor [Gab48; Gab49], and affects all methods based on coherent detection through interferometry. Already in his seminal works, Gabor discussed the presence of those terms and proposed ways to attenuate their effects, such as using a strong reference wave to minimise the relative intensity of the object autocorrelation, or by using a slightly defocused print of the hologram during illumination [Gab49]. Those methods are however essentially suitable for detection performed with photographic plates, which have a large dynamic range, but are generally not applicable for digital detectors.

Historically, the first methods developed were meant to suppress the twin-image in particular, which provides the strongest artefact in in-line reconstructed holograms; it was proposed by Leith and Upatnieks through the use of a spatial modulation of the object wavefront during recording, in the configuration commonly referred to as off-axis. The method was presented first on a communication theory point of view [Lei62], before describing the potential optical implementations [Lei64]. This configuration was employed simultaneously by Goodman *et al.* for the first digital hologram, where the interference pattern was generated by a computer, and imaged optically [Goo67]. Those results were reproduced some years later by Kronrod *et al.* [Kro72b], who also performed the counterpart, where an optically recorded hologram was fed to a computer for numerical reconstruction [Kro72a]. Those first developments did not lead to noticeable applications, as the process was still involving optical and numerical processing, thus making the acquisition and reconstruction rather difficult. The appearance of digital detectors, such as charge-coupled devices (CCD) or complementary metal-oxide semiconductor (CMOS) detectors, yielded the emergence of fully digital applications [Coq93; Sch94], leading to digital off-axis holography, as discussed in more details in subsection 2.2.

On the other hand, the development of electronic detectors opened the path for sequential acquisition, and thus made possible the developments of the so-called phase-shifting techniques [Yam97]. Those methods enable the suppression of the twin-image and zero-order through the combination of several frames, as described in subsection 2.2. One should note also that phase-shifting is also commonly used with two frames to specifically suppress the zero-order, by taking two out-of-phase interferograms.

The other coherent methods which were developed for complex wavefront detection, denoted in subsection 2.2.1 as hybrid techniques, such as scanning holography, are not subject to these issues. This is due to the fact that the scanning employed in those methods implies a modulation/demodulation reconstruction technique, which suppresses directly the zero-order generated at the interference in the object plane. One should also note that the occurrence of these terms is specific to coherent detection, so that incoherent phase recovery techniques such as phase retrieval algorithm [Fie82] or TIE [Bar98] do not need to resort on such suppression methods. This is due to the fact that these methods are strictly spoken phase recovery techniques and not complex wavefront detection methods, so that the phase is directly recovered from the reconstruction process.

With the emergence of digital recording, many different methods were proposed in order to suppress the zero-order. First, the spatial resolution of digital detectors being smaller than holographic plates, inducing more overlap between the interference terms, the problems induced by the zero-order terms became more important. Secondly, many people tried to take advantage of the acquisition rate provided by digital detectors and increased computation capabilities coming from computers to numerically suppress it. The first methods employing digital detectors used filtering in the Fourier domain to separate the various orders contained in the interferogram. This is a key difference between physical methods which rely on spatial separation through propagation; in this case, the signal is Fourier transformed, making thus possible to recover the required term. This method was first validated by Takeda *et al.* on interferometric differential measurements [Tak82], and has been later validated for holography [Cuc00b]. As the zero-order is essentially a low frequency term, it has also been proposed to suppress the average value on the hologram to suppress the DC value [Kre97]. More refined filtering methods, such as employing the Laplacian, were also proposed to selectively suppress the low frequencies, where the zero-order is mainly contained [Liu02], or designing complex filters with linear phase response [Ma09].

These methods are essentially based on using window filters in the Fourier domain in order to recover the required term for reconstruction, and thus assume that the various terms are well separated for windowing. Most of the approaches described below then proposed methods in order to enable suppression of the unwanted terms in a more general way, i.e. also when overlap occurs. They can essentially be divided in two main categories, based on the type signal they provide.

On one side, several techniques rely on the statistical properties of speckle formation. Demoli *et al.* proposed a method for zero-order suppression on rough sample, by subtracting two measurements, where the zero-order is constant through measurement and thus suppressed [Dem03]. A similar approach was employed by Herrera *et al.* through the use of diffuse illumination created with a ground glass in the object beam [HR07]; rotating the glass then provides various measurements for subtraction with different speckle realisations. This type of methods require at least two measurements in order to suppress the zero-order through combination of the temporally changing speckle pattern. Their main limitation is that they can only provide amplitude signals, as they rely often on diffuse illumination, so that the phase signal induced by the sample cannot be retrieved. Similar methods were also developed to selectively suppress the twin image [Mon09].

On the other hand, several methods are based on numerical computation for zero-order suppression from the hologram. Those methods often rely on approximations of the hologram generation equations, in order to enable numerical treatment. The type of signals recovered from those algorithms is highly dependent on the type of processing.

A first method which was proposed to suppress the zero-order numerically was to minimise the influence of the object wave by performing measurements with a strong reference. The contribution from the object would be then neglected by reconstructing the hologram through its logarithm. This method was employed with simulations in the context of phase-shifting, in order to minimise the amount of frames required for reconstruction [Zha04b]. Various approximations applied to the interference equation (cf. Eq. (3.1)) were also proposed, such as employing the square of the interference pattern in order to neglect zero-order terms [Che07a]; this method however employs strong hypothesis, such as amplitude-only object, and precisely controlled phase of the reference wave. Another approach has been to use a Taylor series development at first order for the phase part of the interference equation in a wavelet-based reconstruction [Wen08]. Such numerical methods were often employed in phase-shifting holography, where the zero-order suppression enables the acquisition of less frames for reconstruction. This approach was used for example in conjunction with the square approximation mentioned above [Che07b], or by employing independent measurements of the interfering beams [Guo04], or reducing to two holograms through approximations [Liu09]. Phase-shifting methods performed in off-axis configuration through angular changes were also employed for zero-order suppression, also combined with independent measurements of the intensities [Tak99; Zha04a].

Another approach which was employed for hologram reconstruction and more specifically zero-order suppression consists in using phase-shifting method in the spatial domain, where phase-shifted values for each position can be retrieved in off-axis holograms from adjacent pixels [Lie04; Gar08]. Those methods however require slow variations of the phase signal regards to the spatial resolution in order to retrieve reliable values.

We propose essentially two new methods to suppress the zero-order in the context of off-axis holography. Both aim at improving the complex wavefront reconstruction through this process, implying that the phase signal must be preserved. Furthermore, the main advantage of off-axis holography, namely its one-shot reconstruction capability, is to be preserved. The first method relies on an iterative procedure, and on the hypothesis of a weak spectral overlap between the various orders recorded in the holographic process. The second method relies on nonlinear operators, and provides exact reconstruction in the absence of noise, at it interestingly does not rely on any approximation.

3.2 Statement of the problem

As described already in chapter 2, the interference between two waves can be described as the coherent addition of two complex waves, usually represented in holography as o and r respectively for the object and reference wave. Then, the detection in intensity generates the following interference pattern

$$\begin{aligned} I(x,y) &= \big(o(x,y)+r(x,y)\big)\big(o(x,y)+r(x,y)\big)^* \\ &= |o(x,y)|^2 + |r(x,y)|^2 + o(x,y)^* r(x,y) + o(x,y) r(x,y)^*, \end{aligned} \tag{3.1}$$

where one can identify four terms. The first two terms of the right hand of Eq. (3.1) are the intensities of respectively the object and reference waves. Those two terms are commonly called the zero-order, in analogy with diffraction on gratings where the measured wave passed through an object contains the diffracted imaging information and the non-diffracted wave (zero-order of diffraction), consisting in a constant background. The two following terms are called the imaging terms, as they enable the recovery of the complex field of the object wave with with an image can be formed, also called +1 and -1 diffraction terms.

In this chapter, we focus our attention on the consequences of the occurrence of the zero-order, and its consequences on the complex field reconstruction. Mainly, the presence of the zero-order during reconstruction can lead to two different consequences, which are often partly combined when employing standard reconstructions. First, off-axis reconstruction relies on spectral separation in order to make possible to recover the object wave, implying that the spatial modulation produced by the angle of the propagation direction of the reference wave has to be sufficient enough to ensure full separation between the terms contained in Eq. (3.1). However, the resolution of the recording device is usually limited, especially in the case of electronic detectors, so that ensuring a full spectral separation often leads to a loss of resolution in the reconstruction of the object wave, which bandwidth cannot be fully recovered between those two constraints.

Consequently, in many off-axis holographic setups, the separation between the different terms is not completely fulfilled, granting some gain on the potential resolution of images. However, this can lead to noise in the reconstruction, due to zero-order components that

are present in the reconstruction. The zero-order problem is thus composed of two different aspects; it can either be considered as noise suppression in case there is some overlap between interference terms, or a resolution improvement method in case the filtering ensured no overlap, potentially at the cost of spatial bandwidth.

As the two interfering waves have very different purposes, the information contained in the hologram terms can be treated fairly differently. Specifically, the reference wave has usually a well-controlled profile, commonly considered as a plane wave. This implies that its intensity is a constant value which can be easily subtracted from the hologram, as some publications suggested [Kre97]. However, this assumption is strongly restrictive for the type of reference wave which can be employed, and does not apply to various types of interferometers, such as Mirau or Linnik interferometer types [Wya92], where some curvature is induced in the reference arm, in order to compensate for aberrations during holographic reconstruction. Furthermore, in practise, some noise will be present, such as aberrations of the wavefront due to spatial coherence, misalignment of the setup, etc., which implies that more refined methods should be found to suppress this term. On the other hand, the object wave has generally an unknown profile, as it interacted with the studied sample.

The goal of the work presented in this chapter is to address the suppression of the object zero-order, in order to increase the potential spatial resolution of the reconstructed object wave field, without inducing additional noise. It thus focuses on the suppression of the object zero-order, without requiring any *a priori* knowledge about the specimen observed. In this context, the reference is thus considered to be well-controlled, so that it is possible to suppress it through a calibration step. Generally, the subtraction of a constant to account for the reference term is rather restrictive and can lead to residual noise, as described above. Therefore, the general procedure for reference wave zero-order is to record the intensity pattern of this wave alone during a calibration step, for further subtraction during post-processing. This method presents the advantage of not jeopardising the one-shot capability of off-axis holography, while accounting for the real reference wave profile.

3.2.1 Spatial frequency coverage and consequent artefacts

The problem of separation of the different terms of Eq. (3.1) can be better analysed in the frequency domain, so that taking the two-dimensional Fourier transform of Eq. (3.1) corresponds to

$$\hat{I}(\omega_x,\omega_y) = \hat{o} * \hat{o}^* + \hat{r} * \hat{r}^* + \hat{o}^* * \hat{r} + \hat{o} * \hat{r}^*. \tag{3.2}$$

To simplify the analysis of Eq. (3.2), we make the assumption that the reference is a plane wave with a constant amplitude R, and which propagation vector makes an angle with the propagation direction of the object. In this fashion, the spectrum of the reference wave becomes a Dirac function. The relation between the reference wave, its phase function and the angles θ

and ϕ, defined in Fig. 2.3, can be expressed as

$$\begin{aligned} r(x,y) &= R\exp\left[-\mathrm{i}\varphi_r(x,y)\right], \\ \varphi_r(x,y) &= \frac{2\pi}{\lambda}\sin\theta\cdot\left(x\cos\phi + y\sin\phi\right), \end{aligned} \tag{3.3}$$

where $\varphi_r(x,y)$ is the linear phase function defining the tilt. In this case, the different terms of Eq. (3.2) will be modulated in the spectral domain as

$$\begin{aligned} \hat{I}(\omega_x,\omega_y) = &\hat{o} * \hat{o}^*(\omega_x,\omega_y) + R^2\delta(\omega_x,\omega_y) + \\ &R\hat{o}(\omega_x+\omega_{0,x},\omega_y+\omega_{0,y}) + R\hat{o}^*(\omega_x-\omega_{0,x},\omega_y-\omega_{0,y}), \end{aligned} \tag{3.4}$$

where $(\omega_{0,x},\omega_{0,y})$ corresponds to the frequency shift induced by the tilt function $\varphi_r(x,y)$. The reference having a constant intensity, its spectrum results in a Dirac function δ. In the spectral domain, one can clearly identify the zero-order terms, situated at the origin, and the modulated terms providing the information about the measured complex field.

The relation between the angle variables (θ,ϕ) defining the relative propagation directions of the object and reference waves and the modulation frequency $(\omega_{0,x},\omega_{0,y})$ can be related through the projections of the reference wave vector $\boldsymbol{k}_r$ (we assume $\boldsymbol{k}_o$ to be perpendicular with the detection plane)

$$\begin{aligned} \omega_{0,x} &= \frac{k_x}{2\pi} = \frac{k}{2\pi}\sin\theta\cos\phi, \\ \omega_{0,y} &= \frac{k_y}{2\pi} = \frac{k}{2\pi}\sin\theta\sin\phi. \end{aligned} \tag{3.5}$$

The reference wave being a Dirac function in the Fourier space, its intensity has a punctual support. This also implies that the imaging terms support is not modified by the convolution with the Dirac, so that their bandwidth is the one of the object term, denoted as $\Delta\omega_o$. On the other hand, the object intensity is the convolution of the object wave by its complex conjugate, which corresponds to its autocorrelation, defined as

$$(f\star f)(x,y) = \iint_{-\infty}^{\infty} f^*(x,y)f(x-x',y-y')\mathrm{d}x'\mathrm{d}y', \tag{3.6}$$

which implies that its bandwidth is twice the one of the object wave.

In the case of off-axis holography, the primary need is to separate the different terms contained in Eq. (3.2), which leads to an optimal spectral configuration as shown in Fig. 3.1. We assume along this chapter a detector which sampling is identical along the two directions, i.e. $\Delta x = \Delta y$, as it is the case for most detectors in the market. Furthermore, we limit our discussion to a square detector of resolution $N\times N$. Most of the detectors do not have a square resolution (a ratio of 4/3 is typically employed), but as most of the numerical treatment in DHM is done in the Fourier domain, and thus computed with FFTs, square matrices are commonly used. This is performed either by limiting the field of view provided by the detector, or

by padding the acquired hologram to a square matrix. One should note however that those hypotheses do not limit the discussion while keeping equations simpler, as a generalisation is straightforward.

We present in Fig. 3.1 the two main possibilities of spectral coverage, corresponding respectively to a square bandwidth (cf. Fig. 3.1(a)) or a circular bandwidth (cf. Fig. 3.1(b)). The square shape corresponds to a configuration where the bandwidth is limited by the resolution of the camera, i.e. the pixel size. This happens when the spectral information of the object is not resolved by the sampling power of the camera, so that a zone corresponding to the chip limitation is visible in the Fourier domain, corresponding to macroscopic setups as shown in Fig. 2.5(a–b). On the other side, a circular shape corresponds to a limitation in resolution by the optical system, commonly cylindrically symmetrical regards to the optical axis. The latter case is the common one in DHM, as the magnification provided by the microscope objective (MO) typically ensures that the resolution will not be limited by the detector, as shown in Fig. 2.5(c–d). The terms in Fig. 3.1 are positioned on a diagonal, which is the

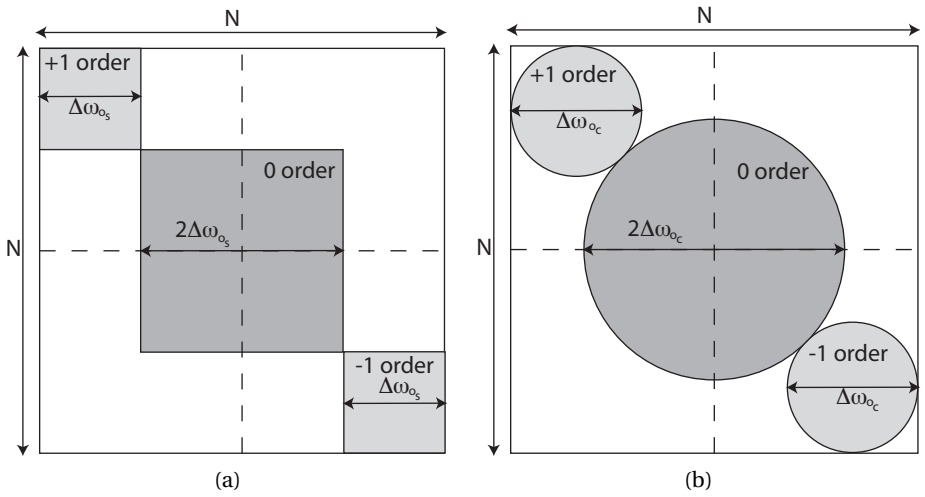

Figure 3.1: Optimal spectral configuration for off-axis holography, ensuring that no spectral overlap occurs between the different recorded terms, for (a) a camera-limited system, and (b) an optically-limited system.

optimal configuration to ensure full spectral separation. In the spatial counterpart, it corresponds to sampling the interference fringes at an angle of 45° in regards to the referential of the detector, where artefacts of discretisation due to the finite size of pixels are minimised.

From geometrical considerations, it is possible to calculate the possible optimal bandwidth — expressed here in pixel units — of the object wave to prevent overlap for respectively the square ($\Delta\omega_{o_s}$) and the circular ($\Delta\omega_{o_c}$) shape in the case of standard filtering (SF)

$$\Delta\omega^{SF}_{o_{s,\max}} = \frac{N}{4}, \qquad \Delta\omega^{SF}_{o_{c,\max}} = \frac{\sqrt{2}}{3+\sqrt{2}}N, \tag{3.7}$$

as the vertical filling can be expressed by $N = \frac{\Delta\omega_{o_c}}{2} + \frac{3\Delta\omega_{o_c}}{\sqrt{2}} + \frac{\Delta\omega_{o_c}}{2}$. This implies that under those conditions, the measurement of the object wave in off-axis holography is restricted to respectively 25% and 32% of the detector resolution. This limitation is one of the main drawback of off-axis holography, and is the cost of employing a spatial method to encode the measured complex wave field.

In the case the zero-order terms are suppressed, a large part of the sampling power of the detector can be employed to increase the available bandwidth of the imaging orders, as shown in Fig. 3.2, respectively for the camera-limited (cf. Fig. 3.2(a)) and optically-limited (cf. Fig. 3.2(b)) cases. In this configuration, as the only remaining condition for the reconstruction is the absence of spectral overlap between the two imaging orders, at least one full quadrant is available for sampling the object wave, thus giving the optimal bandwidth for the zero-order free filtering (ZF), where we employ that $N = \frac{\Delta\omega_{o_c}}{2} + \frac{\Delta\omega_{o_c}}{\sqrt{2}} + \frac{\Delta\omega_{o_c}}{2}$

$$\Delta\omega^{ZF}_{o_{s,\max}} = \frac{N}{2}, \qquad \Delta\omega^{ZF}_{o_{c,\max}} = \frac{\sqrt{2}}{1+\sqrt{2}}N. \tag{3.8}$$

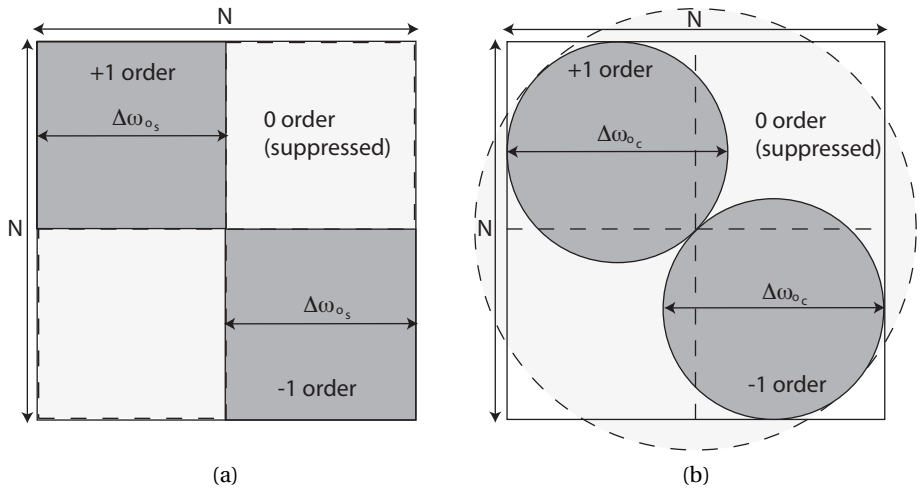

Figure 3.2: Optimal spectral configuration when the zero-order terms are suppressed, providing at least a full quadrant for the imaging orders bandwidth, for (a) a camera-limited system, and (b) an optically-limited system.

On the other hand, methods employing phase-shifting do not suffer from this resolution limitation, but are limited in their time bandwidth, as several frames are required to recover the object wave free of artefacts generated by the other terms of Eq. (3.2). The respective advantages of the two methods—spatial versus temporal encoding—is still source of debate in the community, without reaching a consensus up to now. One could note that both methods are based on rather different reconstruction techniques, making very difficult to compare them in a unified framework.

The conditions expressed in Eq. (3.7) give the optimal bandwidth preventing any spectral overlap between the different terms recorded in the interference pattern. This condition is usually strictly observed for periodic samples, such as in X-ray holography [Fai99], or highly diffusive objects, which generate uniformly distributed spectra in the object wave bandwidth, such as in speckle holography. However, this condition is commonly loosened for smooth objects, as the spectral contributions of the object term are less important, making it possible to neglect them. This can be justified by the fact that typical spectra of smooth objects are composed of weaker high frequencies, as shown in Fig. 3.3(a). This implies that its autocorrelation is strong in a region contained in the bandwidth of the object wave, and much smaller outside of it, as shown in Fig. 3.3(c). On the contrary, rough objects have a constant spectral energy in the bandwidth (cf. Fig.3.3(b)), leading to an autocorrelation resembling the standard OTF of an incoherent imaging system (cf. Fig.3.3(d)).

The fact of loosening the condition makes it therefore possible to extend the spatial resolution of the object wave, but implies that the spectral separation condition between the imaging terms and the autocorrelation will not be fully fulfilled, so that some artefacts will be present in the reconstruction. In off-axis holography, a step of demodulation of the imaging term is necessary to reconstruct the phase of the wavefront, as discussed in subsection 2.2.5. Consequently, as the artefacts generated by the autocorrelation are situated at the centre of the spectrum, they will be modulated after reconstruction. This yields artefacts composed mainly of phase terms, and consequently generating a modulation in the amplitude.

One should also note that the discussion above considers that the bandwidth of the object wave can be controlled before interfering with the reference wave. On the implementation side, this corresponds essentially to limit the aperture of the system, leading to optically-limited recording, schematically represented in Fig. 3.1(b). In the case of macroscopic measurements which usually lead to recording with camera-limited resolution, this limitation is usually not possible, so that the condition will not be satisfied.

Finally, the frequency profiles and limitations derived above are considering a plane wave as reference, implying that the object is not distorted by the multiplication with the reference. This can be identified in Eq. (3.4), where the reference wave corresponds in the reciprocal space to a Dirac function. This approximation is valid when both the object and reference are plane waves, or when both waves have the same curvature, i.e. no relative difference of curvature is present. On the contrary, when the reference possess a residual curvature compared

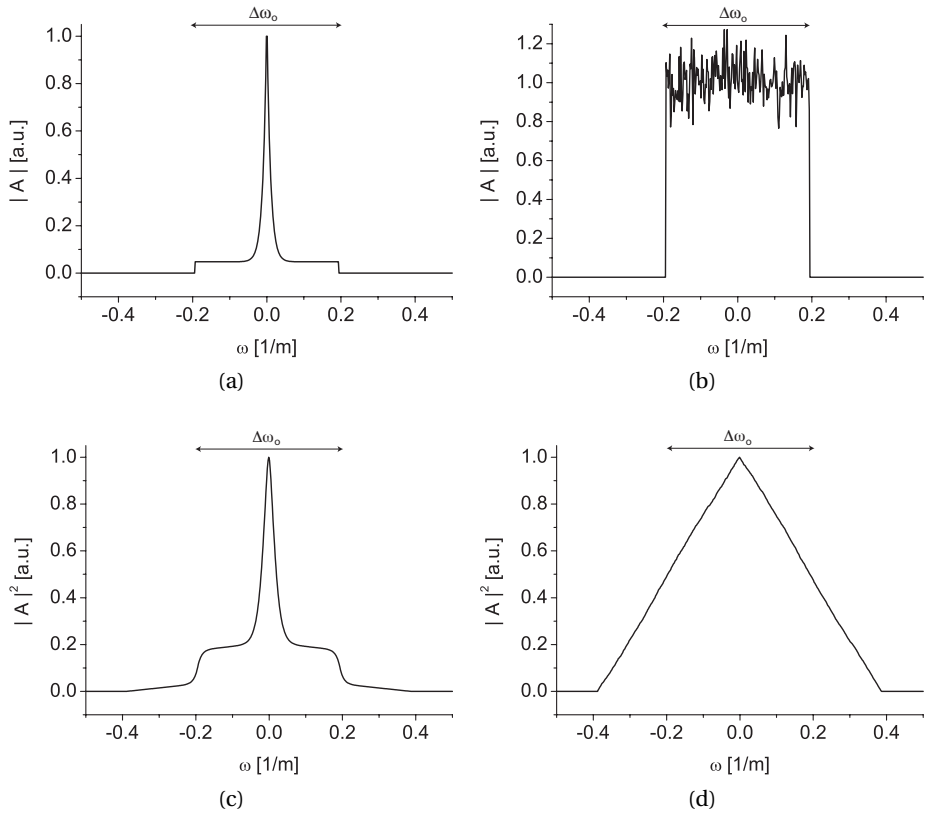

Figure 3.3: Typical amplitude spectrum profile of (a) a smooth object and (b) a rough one, and (c–d) their respective autocorrelation.

to the object wave, Eq. (3.3) does not hold anymore, as a quadratic term needs to be added to the phase function

$$\begin{aligned} r(x,y) &= R \cdot e^{-\mathrm{i}\varphi_r(x,y)} \cdot e^{-\mathrm{i}\varphi_{r,2}(x,y)}, \\ \varphi_{r,2}(x,y) &= \frac{2\pi}{\lambda}\frac{1}{2\rho}\left(x^2+y^2\right), \end{aligned} \tag{3.9}$$

where ρ is the radius of curvature of the wavefront. This equation can be derived in the same manner as the standard thin lens equation for a plano-convex shape [Sal91]. The main consequence of curvature is to modify the spectral profile of the hologram, by spreading the frequencies through the convolution with a function which is not anymore a Dirac. This implies that the spectral support of the imaging order increases due to curvature causing in some cases problems in spectral separation and aliasing.

3.2.2 Off-axis separation and Fresnel digital holography

In subsection 3.2.1, we discussed the resolution limitations implied by the occurrence of the different terms of the interference equation. Up to now, we did not consider the propagation

distance in the discussion, so that the case discussed above corresponds to recording cases such as in-focus holography (cf. subsection 2.2.1). Historically, the off-axis configuration was introduced to separate the recorded terms through physical propagation [Lei64]; one can indeed always fully separate the terms by employing a sufficiently large propagation distance, as the waves propagate along different directions. This approach is however not fully satisfying in the case of digitally recorded holograms.

The waves are indeed gradually separated by the propagation as the field of view increases. In the case of digital propagation, as the field of view—the size of the matrix—does not change during propagation, this separation can be identified mathematically through the change in pixel size of the Fresnel integral (cf. Eq. (2.32)), for digital propagation performed according to Eq. (2.31). One can see that the pixel size $\Delta\xi$ increases linearly with the propagation distance, which corresponds to the enlargement of the field of view with a matrix of constant size. In the case of convolution formalism, as both the matrix size and the pixel sampling are constant, the reconstruction corresponds to a limited field of view, implying that the various terms go gradually out of the field of view.

Typically, an off-axis hologram containing a carrier frequency at the quarter of its spectrum —corresponding to the centre of the usable spectral zone—requires a propagation distance of several tens of centimetres to ensure full separation between the orders. This rough estimation is independent of physical parameters, as having the carrier at a given position corresponds to a given set of variables (λ, Δx, θ), leading to identical propagation distances. The calculation for full separation is made difficult by the diffraction in the Fresnel zone, in which an analytical derivation of the spatial support of a given function cannot be performed.

In this context, the need for refined algorithms ensuring the suppression of the zero-order could seem as unimportant, as one could always rely on a long distance of propagation to ensure full spatial separation of the different terms. However, this solution is usually not satisfying for the recent developments in DH. One of the main difference between physical separation and off-axis digital holography is the fact that DHM commonly employs the spectral approach to reconstruct the complex signal, i.e. Fourier filtering at the hologram plane, leading even in some cases to Fourier or in-focus holography, in which no propagation is applied.

It could be shown through mathematical analysis that the reconstruction quality increases with longer propagation distances [Pic08], when considering a continuous model of computation. However, the main limiting factor for propagation distance in digital holography are the numerical artefacts induced by the discrete nature of the recorded hologram. Most of the propagation algorithms are assuming infinite support for the recorded waves, so that border effects generate strong artefacts along propagation. On a physical point of view, the field of view represented by the matrix of the complex field corresponds to an aperture, which generates diffraction at its borders. Although different attempts were made to circumvent this drawback, such as apodisation of the complex field [Cuc00a], or border processing satisfying certain continuity relations [Dub02], those artefacts are still present to a certain extent. Be-

cause those effects are increasing with longer propagation distances, most implementations of DHM setups favour small reconstruction distances, making it necessary to develop specific solutions to suppress the zero-order, which contribution is not negligible in those configurations.

3.2.3 Diffraction-limited imaging in off-axis digital holography

We described in the previous subsections the limitations of spatial resolution which are a consequence of the presence of the zero-order terms, and the potential improvement in resolution that can provide their suppression, through the enlargement of the available bandwidth. However, at this stage, the discussion was limited to numerical aspects, represented by the resolution of the detector. We extend here the analysis to enable a comparison with the physical parameters representing the measurement system. As we are interested essentially in optical parameters for physical comparison, we limit our discussion to optically-limited resolution, as shown in Fig. 3.1(b).

It is well know that the resolution of an optical system is related to the acceptance angle of the imaging system and the wavelength of the light source, giving

$$\omega_{x,\max} = \frac{\sin\alpha}{\lambda} = \frac{\mathrm{NA}}{n_i\lambda}, \tag{3.10}$$

where NA is the numerical aperture of the MO, and n_i is the immersion medium in the object space. To relate this spatial frequency with the discrete bandwidth of the measured wavefront as defined in Eq. (3.7), one needs to multiply by the pixel size in the image space (Δx), and by the detector resolution (N), because of factors in the definition of the DFT (cf. Eq. (2.2)). Finally, it is necessary to divide by the magnification of the imaging system (M), to account for the change in sampling capability. This gives finally for the discrete bandwidth of the measured object

$$\Delta\omega_o = 2\frac{N\Delta x}{M}\omega_{x,\max} = 2\frac{\mathrm{NA}}{Mn_i}\cdot\frac{1}{\lambda}\cdot N\Delta x \tag{3.11}$$

where the factor 2 accounts for the bandwidth instead of the spatial frequency (cf. Fig. 3.1). The terms have been separated between the different elements determining the resolution in an experimental setup, respectively the imaging system (represented by the MO), the light source, and the detector. We present in Fig. 3.4 the behaviour of the function described by Eq. (3.11) in function of the wavelength λ and the pixel size of the detector Δx for an imaging system composed of a MO having a magnification 10×, NA = 0.25, in air. One can clearly identify the expected increase in numerical bandwidth with the reduction of wavelength or the increase of pixel size, shown here for a value normalised in respect to the detector resolution N.

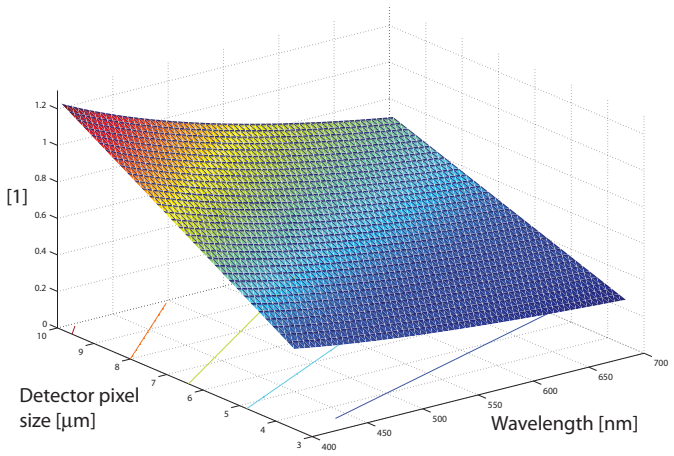

Figure 3.4: Three-dimensional representation of Eq. (3.11), in function of the wavelength and the detector pixel size, normalised in respect to the detector resolution N.

It is then possible to relate Eq. (3.11), representing the physical resolution of the system, and Eq. (3.7), which gives the boundary at which physical resolution is limited by the recording conditions of holography

$$2\frac{\mathrm{NA}}{Mn_i}\cdot\frac{1}{\lambda}\cdot\Delta x \leq C_{SF,ZF}, \quad C_{SF}=\frac{\sqrt{2}}{3+\sqrt{2}}, \quad C_{ZF}=\frac{\sqrt{2}}{1+\sqrt{2}}, \tag{3.12}$$

where C_i is a constant dependent on the reconstruction method, being either the standard filtering C_{SF} or the zero-order free C_{ZF}. The condition expressed in Eq. (3.12) provides a limit that the imaging system, the light source and the detector must satisfy in order to ensure a measurement that is not limited by holography recording conditions, but diffraction-limited. One can note that as it can be intuitively understood, this limitation is not dependent on the resolution of the detector N. As the surface shown in Fig. 3.4 is monotonously decreasing/increasing in function of the parameters, one can see that the inequality in Eq. (3.12) will be satisfied for a half-space defined by the variables $(\lambda, \Delta x)$ for a given imaging system, corresponding to variable couples where the pixel size of the detector is sufficient to sample the given wavelength.

We present in Fig. 3.5 the half-spaces satisfying Eq. (3.12) for various microscope objectives having standard specifications. The regions are represented each time in grey and dashed for two MOs, with respectively the SF and ZF methods. The wavelength range is shown in the visible region ($400-700$ nm), while the pixel size ranges from the smallest pixel sizes available on the market presently (approximately 3 µm) to typical pixel size of high-quality CCD cameras, such as high-gain detectors employed for low-light application (in the order of 10 µm). One can see that in every case, the suppression of the zero-order increases greatly the available range where diffraction-limited imaging can be performed with off-axis digital holography. Furthermore, it enables employing the full resolution of the optical system in the whole visible range, provided that one uses small pixel size detectors. Typically, standard CCD de-

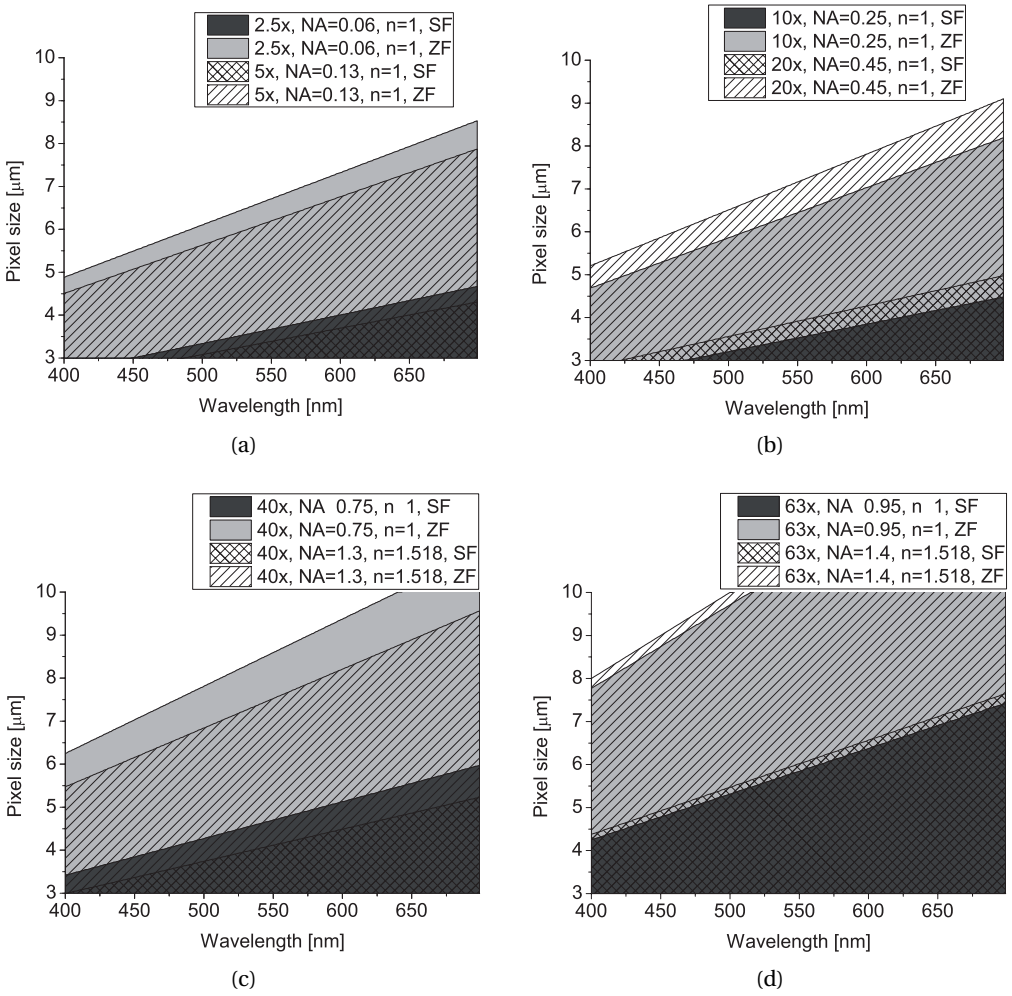

Figure 3.5: Graphical representation of Eq. (3.12) for the possible combinations providing diffraction-limited imaging for different microscope objectives (MO). Greyed or dashed regions show the $\lambda - \Delta x$ couples enabling diffraction-limited systems for standard filtering (SF) and zero-order free (ZF) reconstructions in the case of (a) low magnification objectives (2.5× and 5×), (b) middle range magnifications (10× and 20×), (c) 40× objectives both in air and oil immersion, (d) 63× objectives both in air and oil immersion. The tables are valid for the case of curvature matched between the object and reference waves.

tectors, having pixel sizes of $4-6$ μm can provide diffraction-limited recording on the whole visible range with every type of magnification, provided that ZF methods are employed. Another advantage of enabling the use of larger pixels without limiting resolution is that larger pixel sizes typically reduce noise by keeping electronic noise (e.g. dark current) lower, and reduce the effect of shot noise thanks to their larger well depth.

One can identify that low magnification system are more restrictive than high ones. This is due to the fact that the NA of objectives does not increases at the same pace as the magnifi-

cation with standard MOs, so that the magnification makes it easier for sampling the spatial frequencies of the object, thus compressing the frequencies in the reciprocal domain, and loosening the constraints for no overlapping between the interference terms. However, as it is shown in Fig. 3.5(c), the fact of using larger numerical apertures such as in immersion objectives can weaken this consideration, as it is limiting the diffraction-limited range through an improvement in NA.

One should remember that we considered here only the systems which were described previously as optically-limited. In the case where the object wave spatial frequencies are not limited by an optical element, the spectral configuration becomes the ones represented in Fig. 3.1(a), where the pixel size of the detector is the limiting parameters for the resolution.

3.3 Iterative zero-order suppression

We present in this subsection the first method developed in our work in order to suppress the zero-order. It relies on employing an estimator of the object wave, in order to subtract the object zero-order by having computed the autocorrelation of the estimated object wave. One way of estimating the imaging term is to use the result of a standard filtering reconstruction, as described in section 2.2. However, as one can intuitively understand from the discussion of previous sections, some spectral overlap between the object wave and the zero-order is usually occurring in this configuration, making thus necessary to improve the zero-order suppression through an iterative procedure, which will be described in details in the following subsections.

The main features of the iterative method is that it is based only on post-processing operations based on fundamental equations modelling the physical hologram generation. It thus keeps the one-shot capability of off-axis holography during acquisition, although it is not suitable for live reconstruction.

3.3.1 Functioning principle

The principle of the iterative method is to subtract the zero-order from the computation of the autocorrelation of the imaging order. This operation suppresses the object intensity, while the reference intensity is suppressed by employing a measurement of the reference only, as explained in section 3.2. In this fashion, the result of this computation will become

$$I'(x,y) = I(x,y) - |r_{\text{exp}}|^2 - |o_{\text{est}}|^2 \approx or^* + o^* r, \tag{3.13}$$

where $|r_{\text{exp}}|^2$ is the measurement of the reference wave intensity, and $|o_{\text{est}}|^2$ is the estimation of the object zero-order, computed from the hologram. One can see that it reduces to the two imaging orders, if the conditions $|r_{\text{exp}}|^2 \approx |r|^2$ and $|o_{\text{est}}|^2 \approx |o|^2$ are fulfilled. The fact of employing an estimation of the imaging order to compute the autocorrelation makes it possible

to be independent of the type of specimen during measurement, as the object is estimated during post-processing.

In order to get an estimator of the object wave intensity, one can use the reconstructed signal described in chapter 2, corresponding to Eq. (2.26) which is recalled here for convenience

$$\Psi(x,y) = or^*(x,y) = \mathscr{F}^{-1}\left\{\mathscr{F}\left\{I(x,y)\right\} \times \hat{W}(\omega_x,\omega_y)\right\}\right\}, \tag{3.14}$$

where $\hat{W}(\omega_x,\omega_y)$ is the Fourier transform of the window function employed to filter the imaging order from the hologram. As this subtraction is done in the hologram plane, no propagation is needed during zero-order suppression steps, as the subtraction occurs in the hologram plane. The computation of the autocorrelation can then be performed, in order to get the estimation of the object zero-order, where the signal is normalised by the reference intensity to account for the change in amplitude generated by the multiplication by the reference wave, giving

$$|o_{\text{est}}|^2(x,y) = \frac{\left|\Psi(x,y)\right|^2}{\left|r_{\text{exp}}\right|^2} = \frac{1}{|r_{\text{exp}}|^2}\left(oRe^{\mathrm{i}\varphi_r}\right)\left(oRe^{\mathrm{i}\varphi_r}\right)^* \approx |o|^2, \tag{3.15}$$

where it is considered in first approximation that $|r_{\text{exp}}|^2 \approx R^2$, and where the reference wave is again considered as a plane wave, given by $r(x,y) = R\exp\left[-\mathrm{i}\varphi_r(x,y)\right]$. Through this computation, it is therefore possible to get an estimation of the object zero-order, which can be then subtracted from the hologram for further processing.

In this very simple consideration, it is considered in Eq. (3.14) that the filtering operation recovers the imaging order perfectly. It implies that there is no spectral overlap with the zero-order, thus providing perfect reconstruction regards to zero-order suppression. However, as described in subsection 3.2.1, the different terms of the hologram are often overlapping in the spectral domain; this configuration is even necessary in most cases in order to improve the spatial resolution of the object wave reconstruction, as described in subsection 3.2.3. This implies that Eq. (3.15) will be disturbed by some parts of the zero-order, which must be taken into account in the object estimation. The object wave estimation becomes in this case

$$\begin{aligned} o_{\text{est}}(x,y) &= \frac{1}{|r_{\text{exp}}|^2}\mathscr{F}^{-1}\left\{\hat{I}(\omega_x,\omega_y) \times \hat{W}(\omega_x,\omega_y)\right\} \\ &= \frac{1}{|r_{\text{exp}}|^2}\left(oRe^{\mathrm{i}\varphi_r} + |o|^2 * W(x,y)\right). \end{aligned} \tag{3.16}$$

This equation is already more complex than Eq. (3.14), and does not provide directly a proper estimation of the object wave, due to the artefacts generated by the zero-order. The principle of the proposed method is therefore to use an iterative approach by employing I' of Eq. (3.13) at step k in order to get a more accurate estimator $|o_{\text{est},k+1}|^2$ for further suppression. In order to work, this method requires that the second term on the right hand of Eq. (3.16) tends to zero when increasing the amount of iterations.

The discussion about the correctness of those assumptions is done in subsection 3.3.2. Under the hypothesis that the method indeed converges, we can state the different steps involved in the proposed iterative method, which are be summarised in the Algorithm 1.

Algorithm 1 Iterative zero-order suppression

1: Compensate for the reference intensity by subtracting the term $|r_{\text{exp}}|^2$.
2: Extract the imaging term $(or^*)_0(x,y)$ from the hologram $I(x,y) - |r_{\text{exp}}|^2$ according to Eq. (3.14), where $(or^*)_0(x,y) = \Psi(x,y)$.
3: **while** zero-order is not fully suppressed **do**
4: Compute the estimator $|o_{\text{est},k}|^2$ according to Eq. (3.15).
5: Compute the hologram with attenuated zero-order $I'_k(x,y)$ according to Eq. (3.13).
6: Extract the new imaging term $(or^*)_{k+1}(x,y)$ from $I'_k(x,y)$.
7: **end while**
8: Further processing on the object wave, such as demodulation and digital propagation.

One can already understand that the performance of the algorithm will mainly depend on how strong the spectral overlap between the terms is, and the proposed method has clearly a usability range. In the case no spectral overlap occurs, the reconstruction will be exact without using zero-order suppression methods. On the other hand, if the spectral overlap is too important, and/or if the zero-order intensity is too strong, i.e. the spectral energy of the second term on the right hand of Eq. (3.16) is too important, the algorithm will not provide an exact reconstruction, as convergence will not occur.

3.3.2 Convergence of the algorithm

This subsection cannot be considered as a rigorous proof of convergence of the algorithm, as various approximations are employed during the derivation. Nevertheless, it makes possible to derive the main conditions for convergence, and provides an estimation of the error generated with this iterative approach, through a recurrent demonstration. We first analyse the influence of the different terms involved in Eq. (3.16), and their respective influence on the efficiency of the algorithm. Then, we show a development providing an intuitive understanding of the conditions required for the algorithm to converge, and emphasising the main causes of errors which can be identified when employing this method for zero-order suppression.

As stated before, the part of zero-order contained in the second term of the right-hand of Eq. (3.16) will be reflected in the calculation of the estimator, giving rise to several terms. If we express the filtered object intensity as $O_W(x,y) = |o|^2 * W(x,y)$, the zero-order estimator at the first iteration, i.e. when recovering the object wave from the original hologram I, becomes

$$
\begin{aligned}
|o_{\text{est},1}|^2 &= \frac{1}{|r_{\text{exp}}|^2}\left(oRe^{\mathrm{i}\varphi_r} + O_W(x,y)\right)\left(oRe^{\mathrm{i}\varphi_r} + O_W(x,y)\right)^* \\
&= \frac{R^2}{|r_{\text{exp}}|^2}\left(|o|^2 + \frac{|O_W|^2}{R^2} + \frac{o}{R}O_W^* e^{\mathrm{i}\varphi_r} + \frac{o^*}{R}O_W e^{-\mathrm{i}\varphi_r}\right).
\end{aligned}
\tag{3.17}
$$

One can see four terms in Eq. (3.17), resulting from the autocorrelation operation. The first is the estimator employed for suppressing the object zero-order as in Eq. (3.6), while the three others are error terms induced by the presence of some object intensity in the filtering window, as shown by the presence of O_W in several terms. The second term corresponds to the square of the object intensity, while the two last ones are modulated cross-terms.

The estimator calculated with Eq. (3.17) can be inserted in Eq. (3.13), giving a more detailed expression of the processed hologram at first iteration, in which the zero-order is attenuated

$$
\begin{aligned}
I_1' = {} & oRe^{\mathrm{i}\varphi_r} + o^* Re^{-\mathrm{i}\varphi_r} + R^2 - |r_{\text{exp}}|^2 + \left(1 - \frac{R^2}{|r_{\text{exp}}|^2}\right)|o|^2 \\
& - \frac{|O_W|^2}{|r_{\text{exp}}|^2} - \frac{oR}{|r_{\text{exp}}|^2}O_W^* e^{\mathrm{i}\varphi_r} - \frac{o^* R}{|r_{\text{exp}}|^2}O_W e^{-\mathrm{i}\varphi_r}.
\end{aligned}
\tag{3.18}
$$

This equation can be simplified by considering that $R^2 - |r_{\text{exp}}|^2 \approx 0$, thus neglecting the potential discrepancies between the calibration reference intensity and the one recorded in the hologram. The processed hologram becomes in this case

$$
I_1' = oRe^{\mathrm{i}\varphi_r} + o^* Re^{-\mathrm{i}\varphi_r} - \frac{|O_W|^2}{|r_{\text{exp}}|^2} - \frac{oR}{|r_{\text{exp}}|^2}O_W^* e^{\mathrm{i}\varphi_r} - \frac{o^* R}{|r_{\text{exp}}|^2}O_W e^{-\mathrm{i}\varphi_r}. \tag{3.19}
$$

The new signal I_1' corresponds to the processed hologram in which the zero-order has been subtracted at the first iteration. In order to get the object wave estimator at second iteration, the processed hologram is then again filtered in the Fourier domain with the window function. This filtering operation suppresses some terms of Eq. (3.19), namely the ones modulated by the expression $e^{-\mathrm{i}\varphi_r}$, as those terms have a different spectral support than the one of the window. Finally, the modulus is calculated, in order to calculate once again the autocorrelation. Those operations give the expression

$$
\begin{aligned}
|o_{\text{est},2}|^2 &= \left|I_1' * W\right|^2 \\
&= \left|oRe^{\mathrm{i}\varphi_r} * W + \left(1 - \frac{R^2}{|r_{\text{exp}}|^2}\right)|o|^2 * W - \frac{|O_W|^2}{|r_{\text{exp}}|^2} * W - \frac{oR}{|r_{\text{exp}}|^2}O_W^* e^{\mathrm{i}\varphi_r} * W\right|^2 \\
&= \left|oRe^{\mathrm{i}\varphi_r} + \left(1 - \frac{R^2}{|r_{\text{exp}}|^2}\right)O_W - \frac{|O_W|^2}{|r_{\text{exp}}|^2} * W - \frac{oR}{|r_{\text{exp}}|^2}O_W^* e^{\mathrm{i}\varphi_r} * W\right|^2,
\end{aligned}
\tag{3.20}
$$

where the fact that $oRe^{\mathrm{i}\varphi_r} * W = oRe^{\mathrm{i}\varphi_r}$ has been used, thanks to their identical support. In Eq. (3.20), several terms rise because of the modulus calculation. Among them, the term $R^2|o|^2$ can be identified, which is the wanted expression for zero-order estimation, while all

the others are parasitic terms. Due to the calculation complexity and the multiplicity of terms, we limit our calculation to the proportionality relation between the second iteration of the estimator and the composing terms. To accomplish this, we consider from this point the various terms as contributions in amplitude, in terms of proportionality functions Ø(). This implies that we consider, for example, the following approximation $O_W \propto \text{Ø}(o^2)$. One should note that those approximations overestimate the real error, as the multiplication with the window function in the Fourier domain will suppress some of the contributions. Moreover, as the final value is an intensity value, we neglect the phase terms, so that modulus operations can be neglected. The zero-order estimator at the second iteration becomes in this case

$$\begin{aligned}
\frac{|o_{\text{est},2}|^2}{|r_{\text{exp}}|^2} &\propto \frac{1}{R^2}\left|oRe^{\mathrm{i}\varphi_r} + \text{Ø}\left(o^2\right) + \text{Ø}\left(\frac{o^4}{R^2}\right) + \text{Ø}\left(\frac{o\cdot o^2}{R}\right)\right|^2 \\
&= R^2\left|\frac{oe^{\mathrm{i}\varphi_r}}{R} + \text{Ø}\left(\frac{o^2}{R^2}\right) + \text{Ø}\left(\frac{o^3}{R^3}\right) + \text{Ø}\left(\frac{o^4}{R^4}\right)\right|^2 \\
&\propto R^2\left(\frac{|o|^2}{R^2} + \text{Ø}\left(\frac{o^3}{R^3}\right) + \text{Ø}\left(\frac{o^4}{R^4}\right) + \ldots\right) \\
&= |o|^2 + R^2\sum_{j=3}^{8}\text{Ø}\left(\frac{o^j}{R^j}\right),
\end{aligned} \tag{3.21}$$

In the development above, the first term of the right hand of Eq. (3.21) was kept out of summation, as it enables to express the object zero-order for suppression. This expression can then be used again to get the new processed hologram, at the second iteration

$$\begin{aligned}
I_2' &= oRe^{\mathrm{i}\varphi_r} + o^*Re^{-\mathrm{i}\varphi_r} - \frac{|o_{\text{est},2}|^2}{|r_{\text{exp}}|^2} \\
&\propto oRe^{\mathrm{i}\varphi_r} + o^*Re^{-\mathrm{i}\varphi_r} - R^2\sum_{j=3}^{8}\text{Ø}\left(\frac{o^j}{R^j}\right).
\end{aligned} \tag{3.22}$$

By employing once again the operations used to get Eqs. (3.20) and (3.21), the estimator at the third iteration becomes

$$\begin{aligned}
\frac{|o_{\text{est},3}|^2}{|r_{\text{exp}}|^2} = \frac{\left|I_2' * W\right|^2}{|r_{\text{exp}}|^2} &\propto \frac{1}{R^2}\left|oR - R^2\sum_{j=3}^{8}\text{Ø}\left(\frac{o^j}{R^j}\right)\right|^2 \\
&\propto |o|^2 + R^2\sum_{j=3}^{16}\text{Ø}\left(\frac{o^j}{R^j}\right).
\end{aligned} \tag{3.23}$$

By looking at the sums in Eqs. (3.21) and (3.23), one can see a progression coming from the multiple cross terms of the autocorrelation operations. Under those approximations, we can therefore deduce by recurrence that the error at step k coming from the successive subtractions is

$$\epsilon_{\mathrm{th},k} = |o|^2 - \frac{|o_{\mathrm{est},k}|^2}{|r_{\mathrm{exp}}|^2} \propto R^2 \sum_{j=3}^{2^{k+1}} \emptyset\left(\frac{o^j}{R^j}\right). \tag{3.24}$$

One can see an analogy between the summation of Eq. (3.24) and a geometric series, which converges to

$$\begin{aligned} \sum_{j=0}^{k-1} ar^j &= a\frac{1-r^k}{1-r}, \quad r \neq 1 \\ \lim_{k\to\infty} \sum_{j=0}^{k-1} ar^j &= \frac{1}{1-r}, \quad r < 1. \end{aligned} \tag{3.25}$$

However, $\emptyset(\frac{o^j}{R^j})$ being a more complex function, the expression cannot be considered as a simple geometric series, and getting the real convergence value is rather difficult. Moreover, strong approximations were employed to get this expression, so that it should be used only as a rough indicator.

Nevertheless, the analogy enables to understand some elements about the convergence of the proposed method. First, one can see that, the sum expressed in Eq. (3.24) is a function of the amplitude ratio, which can be defined as

$$K_A(x,y) = \frac{\Re\big(o(x,y)\big)}{\Re\big(r(x,y)\big)} = \frac{O(x,y)}{R(x,y)}. \tag{3.26}$$

In analogy with the geometric series, one can see that it should be required that K_A should be below one, i.e. $R(x,y) > O(x,y)$. This can be intuitively understood as the fact that, if the object wave is relatively too strong compared to the reference wave, the spectral power of the object zero-order $|o|^2$ will be strong compared to the one of the imaging orders $oRe^{\pm \mathrm{i}\varphi_r}$, so that the error coming from the spectral overlap will induce errors in the suppression process. This shows that a first condition for the algorithm to converge is that the reference amplitude has to be stronger than that of the object, so that the summation in Eq. (3.24) does not diverge. Indeed, the error in the estimation at first iteration will be once again multiplied by the factor K_A at the next iteration, making them thus decrease.

For practical reasons, the criterion defined in Eq. (3.26) is difficult to use, as measured signals are expressed in intensity. Furthermore, one issue of the definition is that it is defined for each pixel, with values which can change tremendously because of variations in amplitude of the two signals. Specifically, the object wave is modulated by its interaction with the sample, implying that its values are strongly object-dependent. Furthermore, the criterion defined here in the spatial domain for the iterative method should be considered only in the global

sense, as it is an indirect indicator, though convenient, of the respective spectral energy of the various terms of the interference equation. For this reason, we employ through this chapter a criterion based on the mean intensity ratio, which can be defined as

$$\overline{K_I} = \frac{\sum_{m,n=0}^{m,n<N} |o[m,n]|^2}{\sum_{m,n=0}^{m,n<N} |r[m,n]|^2} = \frac{\overline{O^2}}{\overline{R^2}}. \tag{3.27}$$

The fact of taking separately the mean value of the two beams ensures a better robustness of the computation of the ratio in practical cases, where some "dead" pixels could be present on the detector, thus inducing aberrant values of zero for pixels. It also suppresses the problems occurring at low intensity with quantisation, where low values of pixels could be translated in null values.

One can also note that the efficiency of the object zero-order suppression will strongly depend on the accuracy of the estimation of the reference intensity $|r_{\text{exp}}|^2$, in order to minimise the error induced by the first term on the right hand of Eq. (3.18).

Finally, the error estimation shows that the iterative technique enables efficient zero-order suppression, although it will not fully suppress it. The summation in the error expression will not converge to zero, implying that some artefacts will remain even at convergence. However, as it will be shown in the following sections, those artefacts can fairly be neglected in practical cases.

One should note also that the reconstruction quality will also depend on the shape of the reference wave. In our model, we have considered a plane wave, which leads to the results presented in section 3.2.3. However, a reference wave having a strongly irregular phase profile will induce errors in the reconstruction, since the estimator of the object autocorrelation is based on the imaging order, which is multiplied by the reference wave. The procedure proposed in this article prevents some errors to propagate by normalising with an experimental reference, but this does not compensate for reference waves with strong aberrations.

3.3.3 Simulation analysis

We present here the applicability of the proposed method on simulated holograms, which enables analysing the accuracy and the speed with which the algorithm converges to the solution. The simulations make also possible to confirm the deductions obtained from the approximated convergence of the method presented in subsection 3.3.2.

In regards to zero-order suppression, the type of holograms can be divided mainly in two categories, which are the ones generated by smooth and rough samples. This classification can be justified first by the fact that these two categories of holograms provide different types of signal, as shown in Fig. 3.3. On the point of view of signal processing, those holograms therefore generate rather different types of spectra, where one can intuitively understand that

rough holograms possess a strong zero-order, due to the wide distribution of spatial frequencies, which will be more difficult to suppress, because of the stronger spectral overlap between the zero-order and the imaging orders.

Another reason for this classification is the usual interpretation of those signals. The phase of smooth holograms can be easily retrieved through holographic reconstruction, and can be used for precise topographic imaging in reflection, or OPL measurement in transmission. On the other hand, in the case of rough samples, the roughness generates speckle, which disrupts the phase in a random pattern, so that measurements are essentially considered in amplitude. Therefore, due to the different interpretation of the signal, the artefacts generated by the zero-order order have different consequences. For smooth holograms, the main importance will be the accuracy of the phase measurement. On the other hand, the main artefacts influencing the reconstruction of rough samples is in amplitude.

Topographic holography

We consider first the case of topographic measurement. The hologram employed for this type of measurement is a representation similar to an image of a USAF 1951 test target (cf. Fig. 3.6.(a)), which contains specific spatial frequencies. To simulate the hologram recording process, we consider the synthetic image as being the field on the image plane in the case of a perfect imaging system. Then, to account for the optical resolution, we apply a low-pass filter which bandwidth can be calculated according to Eq. (3.10). In this particular case we consider a wavelength of $\lambda = 661$ nm, a pixel size of $\Delta x = 6.45$ µm, and a 20× MO (NA = 0.4) in air. Those parameters correspond to the ones employed during experimental validation in subsection 3.3.4. The filtered image is then propagated from the image plane to the recording plane with the Fresnel approximation ($d = 4.9$ cm), according to Eq. (2.33), where the coherent addition with a plane wave acting as reference is computed. The angle between the propagation vectors of the two waves is chosen as $\theta = 2°$, ensuring that the imaging order and the twin image are separated, but that some overlap with the zero-order is occurring. As discussed in subsection 3.3.2, the intensity ratio between the two waves determines the efficiency of the method, and has been taken as $\overline{K_I} = 1/5$ in this case. The simulated hologram is finally obtained by computing the intensity of the wave field, as shown in Fig. 3.6(b). The steps described above are summarised in Algorithm 2.

Algorithm 2 Computer generation of a smooth hologram

1: Apply a low-pass filter to the input complex field $o(x, y)$, where the filter is taken as a $circ$ function, with a diameter calculated according to Eq. (3.10).
2: Propagate the low-pass filtered version of the complex field from the image plane to the recording plane, separated by a distance d, according to Eq. (2.33).
3: Generate the reference wave in function of the angles (θ, ϕ), according to Eq. (3.3)
4: Calculate the modulus of the coherent addition between the object field and the reference wave, according to Eq. (3.1)
5: Save the hologram in an 8-bit image to account for quantisation of the camera.

The spectrum of the hologram is presented in Fig. 3.6(c), where one can see lines in the spectrum, representing the directional spatial frequencies of the pattern in the image. Those lines overlap between the zero-order and the imaging term, thus generating potential artefacts during reconstruction. However, since the object is rather smooth in this case, most of the spectral information is given by frequencies close to the origin, implying that the spectral bandwidth of the object autocorrelation is mostly contained in the $[-\omega_c, \omega_c]$ range.

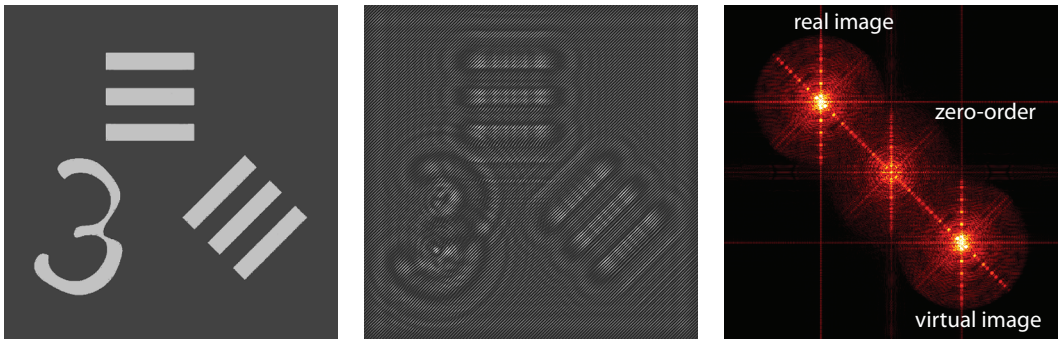

(a) (b) (c)

Figure 3.6: Synthetic image similar to a USAF 1951 target, with (a) its topography represented by the phase map generated by the reflection of light, (b) the hologram simulated for a 20× (NA = 0.4) imaging system, and (c) the spectrum of the hologram.

In these simulations, we mainly compare the standard reconstruction (SF) as described in section 2.2 with the proposed zero-order free (ZF) method. The iterative method consists mainly in changing the filtering part of the reconstruction method, while the other steps of the retrieval algorithm are identical (demodulation, propagation, etc.). By employing a synthetic image, we can first show the different terms expressed in Eq. (3.17), in order to estimate their relative strength, presented in Fig. 3.7. The estimated object autocorrelation is shown in Fig. 3.7(a), corresponding to the required term for object zero-order suppression. Then, in Fig. 3.7(b) the term of power 4, situated at the centre, is shown with an amplification of a factor 100 to make it visible in the figure. Then, in Fig. 3.7(c–d), the two modulated terms are shown with an amplification of 10. As all images are normalised in the same way, and since the maximal amplitude is mainly identical in all the figures, those factors show approximately the respective spectral strength of the various terms, in the case of an intensity ratio of $\overline{K_I} = 1/5$.

In order to compare the SF technique and the ZF iterative one, we reconstructed the hologram of Fig. 3.6(b) by employing a square filter on a quadrant of the spectrum, as shown by the dashed square in Fig. 3.8(c). The fact of employing a square filter enables making the zero-order visible in the spatial reconstruction. Recovered fields are then back-propagated with the Fresnel integral (cf. Eq. (2.31)), enabling an easier identification of the respective contribution of the interference terms through spatial separation.

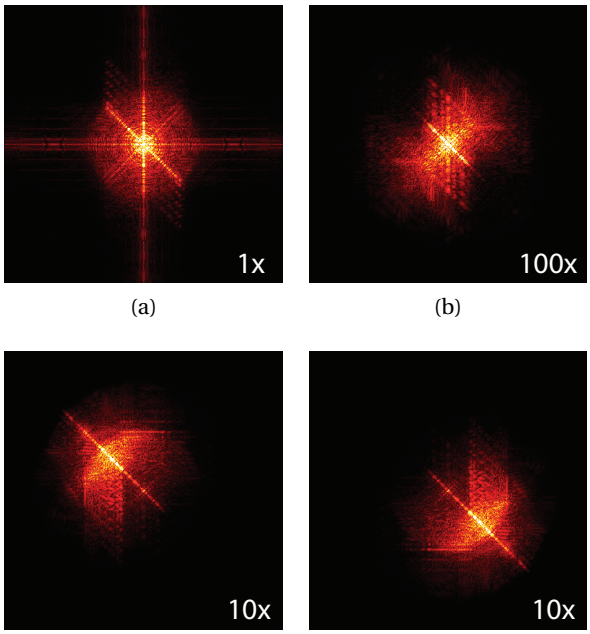

(a) (b)

(c) (d)

Figure 3.7: Representation of the terms of Eq. (3.17) at the first iteration for the hologram of Fig. 3.6(b), showing (a) the object autocorrelation estimator, $|o|^2$, (b) the $\frac{|O_W|^2}{R^2}$ error term and (c–d) the modulated error terms $\frac{o}{R} O_W^* e^{i\varphi}$. On each figure, the multiplicative factor to make the term visible is given.

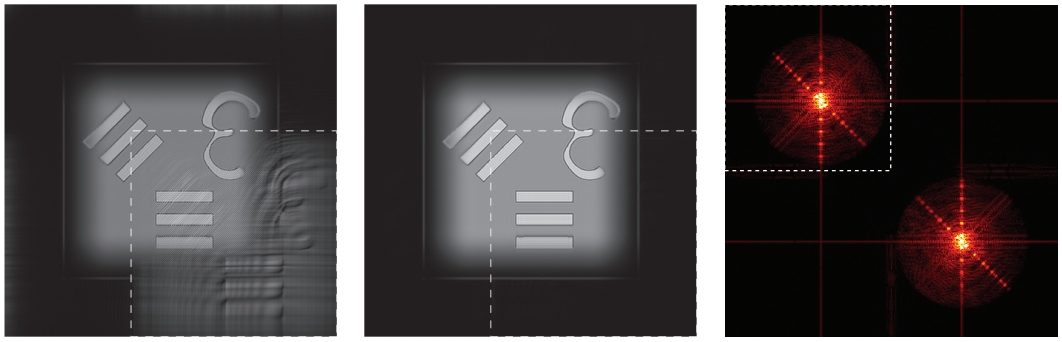

(a) (b) (c)

Figure 3.8: Reconstruction of the hologram of Fig. 3.6(b) with (a) standard reconstruction and (b) the iterative method. (c) The spectrum of the iterative reconstruction shows no zero-order contribution in the wave field.

The reconstruction for the SF method is shown in amplitude on Fig. 3.8(a). The zero-order can be identified as a ghost in the bottom-right corner of the figure, highlighted by a dashed square in Fig. 3.8(a–b). The iterative ZF reconstruction was applied to this hologram, so that the object zero-order is suppressed, as it can be seen from the spectrum of the wave field in the hologram plane shown in Fig. 3.8(c). Accordingly, the reconstruction of the hologram shows

an imaging order free of ghost in amplitude (cf. Fig. 3.8(b)). The results were obtained with 10 iterations, which is plentifully sufficient in those conditions to suppress the zero-order. However, depending on the recording conditions, such as the value of $\overline{K_I}$ or the spectral overlap between terms, more iterations could possibly be needed in order to get sufficient extinction.

As the results are here obtained through simulations, it is possible to compute exactly the discrepancy function which was derived in Eq. (3.24), as the object zero-order is known. The error is thus defined by the difference between the object zero-order and the estimator computed through the reconstruction, summed for each pixels. It is further normalised by the overall intensity of the zero-order, as the normalisation performed through the division by the reference wave can introduce a bias. The error is therefore computed as

$$\epsilon_{\text{sim},k} = \frac{\sum_{m=0}^{M}\sum_{n=0}^{N}\left||o[m,n]|^2 - \frac{|o_{\text{est},k}|^2}{|r_{\text{exp}}|^2}[m,n]\right|}{\sum_{m=0}^{M}\sum_{n=0}^{N}\left(|o[m,n]|^2\right)}. \tag{3.28}$$

One can see in Fig. 3.9 that the error converges to a value of 3%, which corresponds to the theoretical residue of the algorithm ϵ_{th}, as described in section 3.3.2. One should note that the first value presented is $\epsilon_{\text{sim},1}$, implying that it corresponds to the first attempt of suppressing the object zero-order with o_{est}. This explains why the error starts with a rather low value, as the criterion defined in Eq. (3.28) cannot be computed for $\epsilon_{\text{sim},0}$.

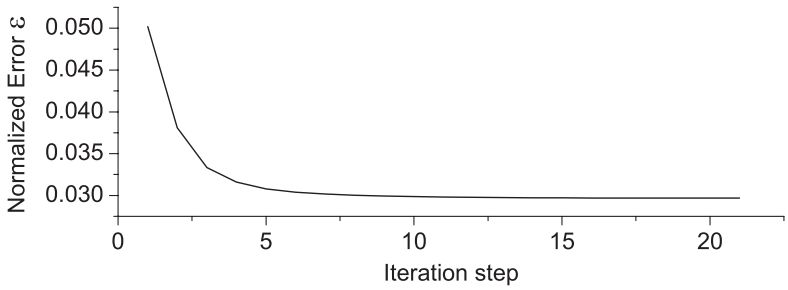

Figure 3.9: Convergence of the sum of the error estimator for the object intensity as defined in Eq. (3.28).

Speckle hologram simulations

We present in a second stage simulation results based on the reconstruction of speckle holograms, generated by rough surfaces. The synthetic hologram is based on the same object shown in Fig. 3.6(a), where the phase is set in this case to a random value uniformly distributed between $[-\pi,\pi]$, according to the "fully developed" speckle discussed in subsection 2.2.4. The generation of the hologram is however somewhat different from the one of the smooth hologram, as the image and the speckle are not formed in the same plane. This simulation considers a low aperture optical system, composed of a $2f$ lens system, as shown in Fig. 3.10.

The field diffracted by the specimen and containing the random phase is propagated to the first lens of the optical system, where a low-pass filter is applied to account for the optical component aperture. Applying the low-pass filter at the aperture of the first lens of the imaging enables the speckle to develop through propagation. Therefore, contrarily to the case of the smooth hologram, the low-pass filter is not applied on an image plane, enabling the formation of the speckle pattern. The field is next propagated to the second lens where its curvature is compensated. Then, it is propagated to the hologram plane where the interference with a tilted reference wave is computed. This procedure, enabling a more realistic model for speckle hologram is summarised in Algorithm 3.

Algorithm 3 Computer generation of a rough speckle hologram

1: Compute a random phase $[-\pi,\pi]$ and generate the complex field with input amplitude and random phase.
2: Propagate the complex field to a distance f_1, corresponding to the focal distance of the first lens, according to Eq. (2.33).
3: Apply a low-pass filter to the propagated complex field, where the filter is taken as a $circ$ function, with a diameter calculated according to Eq. (3.10).
4: Add a quadratic term to the phase to account for the curvature of the field induced by lens L_1, according to Eq. (3.9), where the radius of curvature is $\rho_1 = f_1$.
5: Propagate the low-pass filtered version of the complex field to a distance $f_1 + f_2$, to the second lens of the modelled telescope, according to Eq. (2.33).
6: Add a quadratic term to the phase to account for the curvature of the field induced by lens L_2, according to Eq. (3.9), where the radius of curvature is $\rho_2 = f_2$.
7: Propagate the field to the recording plane, at a distance $f_2 + d$, according to Eq. (2.33).
8: Generate the reference wave in function of the angles (θ,ϕ), according to Eq. (3.3).
9: Calculate the modulus of the coherent addition between the object field and the reference wave, according to Eq. (3.1)
10: Save the hologram in an 8-bit image to account for quantisation of the camera.

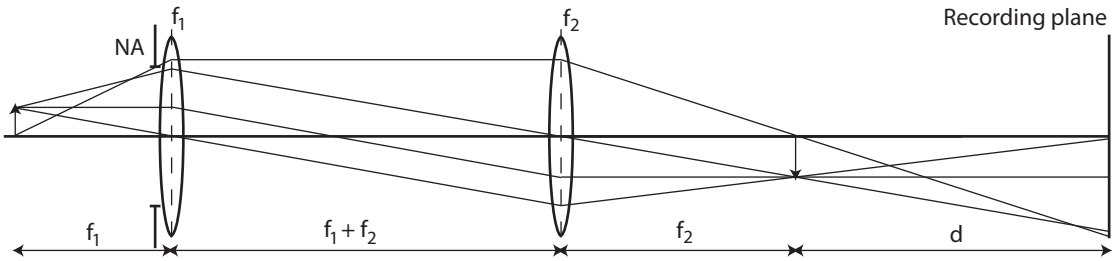

Figure 3.10: Optical system model used for the generation of the speckle hologram.

The optical system was made in this case with a numerical aperture of NA = 0.05, a magnification of $M = 1.5$, a wavelength of $\lambda = 760$ nm and $\Delta x = 6.45$ µm. The two lenses of the telescope were chosen as $f_1 = 3$ cm and $f_2 = 4.5$ cm, and the image distance was taken as $d =$ 6 cm. The intensity ration is again taken as $\overline{K_I} = 1/7$.

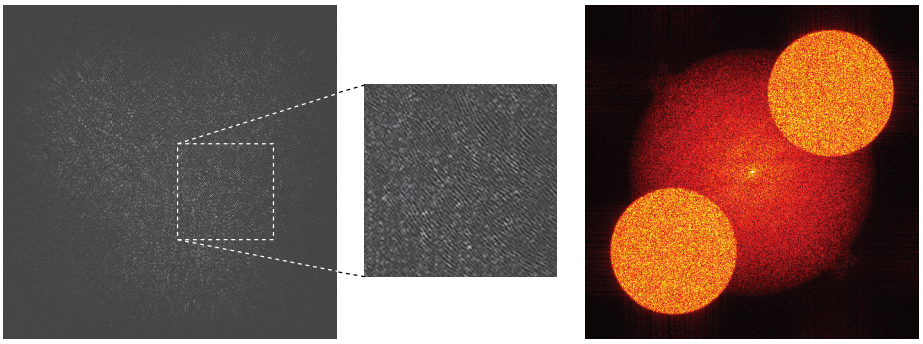

(a) (b)

Figure 3.11: Speckle hologram generated from the image shown in Fig. 3.6(a) with a random phase comprised between $[-\pi,\pi]$, shown (a) in the spatial domain, with a zoom a part of the field of view to emphasise the fringes, and (b) in the spectral domain, where the zero-order with twice the size compared to the imaging orders can be clearly identified.

The hologram created with this method is shown in Fig. 3.11(a). One can identify the speckle pattern generated from the random phase, where the size of the speckle grain depends on the aperture of the optical system, chosen here so that fringes can still be resolved, enabling reconstruction with standard DH approach. High spatial frequencies can be identified in the spectrum of the generated hologram as an approximately constant spectral energy in the aperture of the MO, as presented in Fig. 3.11(b).

The results of the reconstruction are shown in Fig. 3.12. One first can identify the artefacts in amplitude generated by the zero-order in the wavefront reconstructed with the SF method (cf. Fig. 3.12(a)), to be compared with the reconstruction through ZF iterative filtering (cf. Fig. 3.12(b)), for 10 steps of iteration. As it can be seen in the spectrum of the image shown in Fig. 3.12(b), the iterative reconstruction efficiently suppresses the zero-order. However, some spectral energy can still be identified at the centre of the spectrum, although not seen in Fig. 3.12(b). This is due to the residues after convergence, which are larger in this case compared to the smooth hologram of the previous paragraph, since the spectral overlap is more important in this case. Nevertheless, one can see from the amplitude reconstruction that the residues are still negligible, giving an imaging order free of artefacts.

Divergent reconstruction

We present then a case where the intensity ratio $\overline{K_I}$ is not fulfilling the condition $R > |o|$, in order to show the consequences of wrong starting conditions on the iterative procedure. For this purpose, we consider again the speckle hologram generated in the last paragraph (cf. Fig. 3.11(a)), but with $K_I = 2$.

As it can be seen both in the amplitude reconstruction (cf. Fig. 3.13(a)) and in the spectrum (cf. Fig. 3.13(b)), the reconstruction diverges rapidly after only 3 iterations. This fast diver-

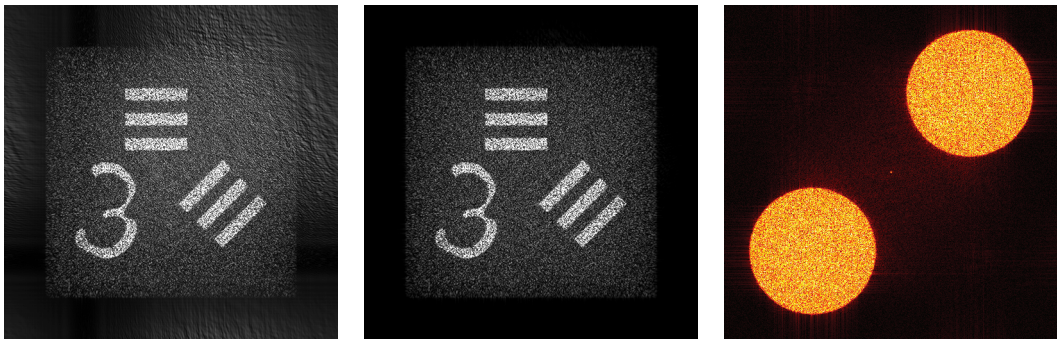

(a) (b) (c)

Figure 3.12: Reconstruction of the speckle hologram of Fig. 3.11(a) with (a) the standard filtering method and (b) the iterative method. The zero-order suppression can also be seen in (c) the spectrum of the wavefront reconstructed with the iterative method.

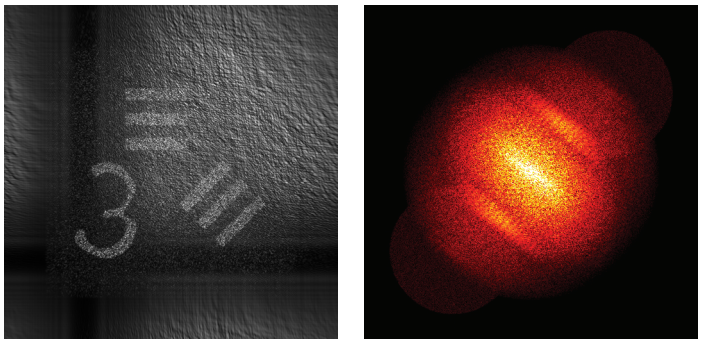

(a) (b)

Figure 3.13: Iterative reconstruction in the case of an inadequate intensity ratio $\overline{K_I}$, yielding a diverging reconstruction, as it can be seen (a) from the strong artefact in amplitude, and (b) from the distorted spectrum of the processed hologram I'_k.

gence is due to a conjugation of factors, as the intensity ratio $\overline{K_I}$ is strongly out of validity range, and as the spectral overlap is large. Those elements add to make the term O_W far from negligible in Eq. (3.18), without attenuation through iterations as $\overline{K_I} > 1$.

3.3.4 Experiments

We present in this subsection experimental results showing the performances of the iterative method. As in subsection 3.3.3, we divide the results for smooth and rough holograms, in order to analyse the efficiency for those two types of signals. The simulations were performed in a way to facilitate the comparison with experiments, as the smooth sample is a USAF 1951 target, and speckle holograms were generated with the reflection on a Swiss coin.

Topographic measurements

A USAF 1951 test target has been measured with a standard reflection DHM setup, as described in subsection 2.4.1 and shown in Fig. 2.15(b), providing topographic measurement of its surface. Parameters are similar to the simulation of subsection 3.3.3, so that the specimen is illuminated with a plane wave of wavelength $\lambda = 661$ nm, through a 20× MO (NA = 0.4). The reflected light then interferes with a reference wave, which profile is well controlled and matched in curvature with the object wave. The interference pattern is recorded by a CCD camera, with a pixel size of $\Delta x = 6.45$ µm, for a field of view of 512×512.

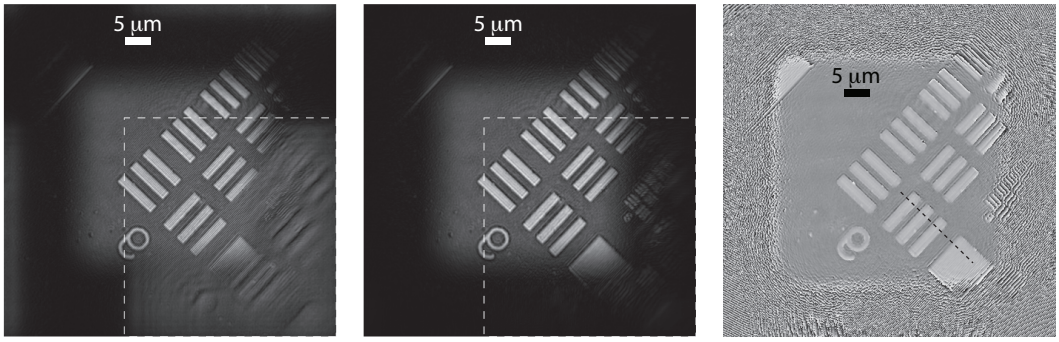

(a) (b) (c)

Figure 3.14: Reconstruction of the hologram of a USAF test target. Amplitude reconstructed with (a) the standard method and (b) the iterative method. (c) Phase image reconstructed with the iterative procedure.

The target was placed in a configuration where the elements generate strong spatial frequencies in the direction of the interference fringes, giving rise to a spectrum similar to the one used in section 3.3.3. The results of the reconstruction are shown in Fig. 3.14, with a similar filtering window consisting of a quadrant as shown in Fig. 3.8(c), and a propagation distance of $d = 4.8$ cm. The amplitude of the reconstruction for the SF method (cf. Fig. 3.14(a)) contains a strong part of zero-order, which is suppressed with the ZF iterative technique as shown in Fig. 3.14(b).

The corresponding phase image is presented in Fig. 3.14(c) for the ZF iterative case, where it can be identified that the noise on the signal is approximately constant, which is an indicator that the zero-order has been suppressed, so that the phase signal is not disrupted by the phase artefacts of the zero-order. We show in Fig. 3.15 a phase profile of the steps generated by the chromium layer (cf. dashed line in Fig. 3.14(c)) for both SF and ZF reconstructions. One can see that the iterative technique keeps the quantitative information of the phase, by providing the same mean phase change on steps. However, the iterative technique is free from a strong phase noise which can be identified on the phase profile of the standard method, due to artefacts generated by the zero-order term.

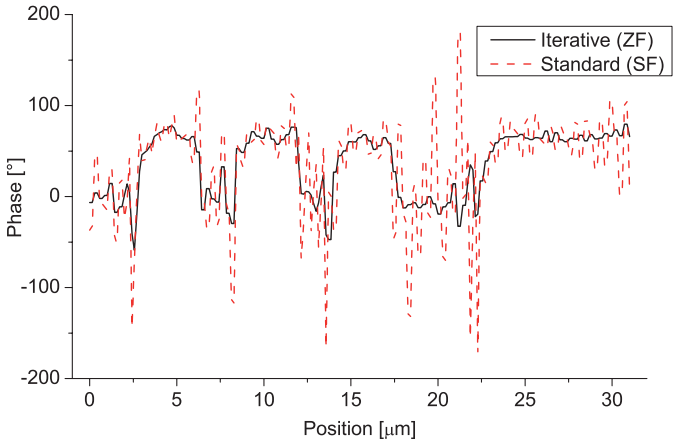

Figure 3.15: Topographic phase profile along the dashed line of Fig. 3.14(c) for the standard (SF) and iterative (ZF) techniques, where a strong artefacts can be identified in the case of the standard technique, due to the zero-order term.

Speckle hologram

We present then experimental results based on the iterative method for speckle holograms. We measured a part of coin surface on a reflection setup similar to the one employed in the last paragraph, but with low aperture. In this case, a magnification of 3× is employed, provided by an achromatic lens, with a source wavelength of $\lambda = 760$ nm. Apart from those elements, all other experimental parameters are identical.

The results of the reconstruction are shown in Fig. 3.16, with the hologram spectrum (cf. Fig. 3.16(a)), in which the uniform spectral energy E generated in the bandwidth of the aperture can be clearly identified, giving a similar signal as in the simulations of subsection 3.3.3. This behaviour is due to the roughness of the coin, which generates approximately random phasors in some parts of the field of view.

The reconstructed amplitude of the letter "A" engraved on a Swiss coin for the SF and ZF iterative reconstructions are shown respectively in Figs. 3.16(b) and 3.16(d), demonstrating also in this case the suppression of the zero-order. The spectrum of the signal after using the iterative procedure is shown in Fig. 3.16(c), where the zero-order is very strongly attenuated.

In order to quantify the efficiency of the method, we measured the mean spectral energy in parts of the spectrum for respectively the standard (std) and iterative (iter) techniques, on regions of the zero-order (zero), and in parts containing measurement noise outside the imaging orders (noise). Those regions are identified in Fig. 3.16(c).

One can estimate the efficiency of the zero-order suppression by calculating

$$S = \frac{E_{\text{iter,zero}} - E_{\text{iter,noise}}}{E_{\text{std,zero}} - E_{\text{std,noise}}}. \tag{3.29}$$

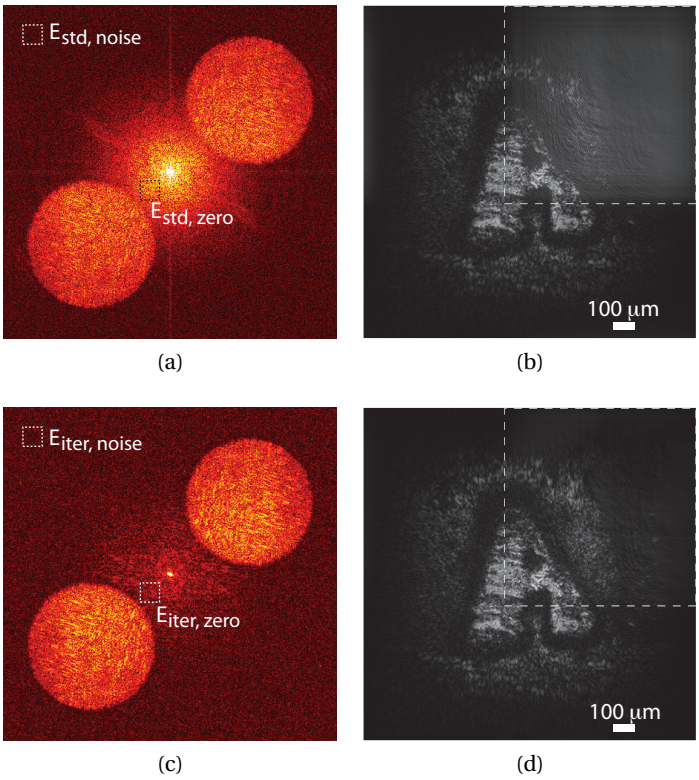

Figure 3.16: Spectrum (a) of a reflection hologram on a Swiss coin containing the letter "A", along with (b) its reconstruction performed with standard method. Spectrum (c) and amplitude (d) after employing the iterative method.

The meaning of Eq. (3.29) is the calculation of the ratio of the spectral energy of the zero-order before and after employing the iterative method, giving an indicator of the relative attenuation of the zero-order. The subtraction of the spectral energy of a zone outside of the interference terms (where no information is contained) accounts for the electronic noise generated by the camera. This computation gives an efficiency of $S = 97.8\%$ for the measurements shown in Fig. 3.16, indicating that most of the spectral energy carried by the zero-order has been suppressed.

3.3.5 Discussion

As it was shown in the previous subsections, the iterative method can suppress the object zero-order term on various types of holograms, such as smooth holograms recorded in DHM, or speckle holograms at low magnification. The two main requirements in order to employ this method is first an accurate estimation of the reference wave intensity, and an intensity ratio between the two interfering beams globally below one, i.e. the reference wave should be globally stronger than the object one.

The reference intensity can be recorded during a calibration step before experiment. An advantage of this calibration is that it makes possible to compensate for experimental instabilities, and takes into account the inevitable spatial variations of the reference intensity. Furthermore, this estimation can be considered as rather accurate through time, as vibrations of the experimental setup should not influence greatly the intensity of the beam. However, some problems could occur with unstable light sources, with which strong intensity changes can occur, thus disrupting this calibration.

One the other side, the fact of having a reference intensity stronger than that of the object wave could be considered as being the best measurement scenario. First, it is quite common that the reflection on some surfaces, or the transmittance of certain samples is not high, implying that the intensity of the object wave can be limited by the nature of the sample, thus imposing a fundamental limitations leading to a stronger reference wave. Furthermore, it was shown that having a stronger reference wave intensity yields better results regards to shot noise [Cha06].

The condition on intensity ratio is also rather loose in the case of the iterative method, as it should only be satisfied in a global sense. This implies that the intensity ratio does not need to be extremely high, so that the fringe visibility does not need to be greatly reduced, thus ensuring a good SNR of measurement and providing some versatility in the applicability of the proposed method. One should also note that the convergence is not exclusively ensured by the intensity ratio, but also by the amount of spectral overlap induced by the experimental conditions. The intensity ratio could thus be considered as a tuneable parameter enabling convergence regards to various experimental conditions. It could be shown that in standard conditions, convergence occurs typically in less than 10 iterations.

3.4 Zero-order suppression through nonlinear filtering

We present in this section another approach employed to suppress the zero-order term in digital holography. Its aims at solving the main drawback of the iterative method presented in previous section, namely the fact that the reconstruction algorithm cannot provide real-time imaging. While the iterative method does not limit the acquisition rate, it limits the reconstruction speed, making it impossible to reach a live feed because of the multiple steps of the iterative procedure.

The method described in this section is non-iterative and can thus provide a high reconstruction rate, and is based on a nonlinear filtering method. It consists in employing the logarithm of the spatial spectrum as a filtering space, enabling intrinsic zero-order suppression through the additive property of this operator. We first provide some definitions about the mathematical tools employed, enabling more understanding about the underlying concepts in the use of nonlinear operators in the context of homomorphic filtering.

3.4.1 Definitions

The nonlinear filtering method described in this section can be considered as a particular case of homomorphic filtering, as defined by Oppenheim *et al.* [Opp68; Opp04]. This framework tends to extend the possibilities of standard filtering operations to more complex systems, by generalising the concept of superposition for additive systems. We still first define the concept of homomorphic filtering in a general sense, before showing the links with our proposed reconstruction method. If we consider an additive system, its basic properties can be summarised as

$$f(t) = f_1(t) + f_2(t), \tag{3.30}$$

where we restrict our discussion to the one-dimensional case for simplicity, as generalisation for higher dimensions is straightforward. This fundamental property enables for example the use of filtering in the Fourier domain in order to separate the two signals f_1 and f_2, leading to the following properties for an additive system with the Fourier transform

$$\begin{aligned} \mathscr{F}\left\{f(t)\right\} &= \mathscr{F}\left\{f_1(t)\right\} + \mathscr{F}\left\{f_2(t)\right\}, \\ \mathscr{F}\left\{c \cdot f(t)\right\} &= c \cdot \mathscr{F}\left\{f(t)\right\}, \end{aligned} \tag{3.31}$$

provided that the spectral supports of the two signals are disjoint. These properties have been typically used for spatial filtering in subsection 2.2.5 and in section 3.3 in order to recover the object wavefront.

Generalised filtering

In the concept of homomorphic filtering, it is proposed to extend the superposition principle to other systems, such as for instance multiplicative or convolutive systems. If we consider a general operator $\circ$ of addition in the same way as Eq. (3.30), defined as

$$f(t) = f_1(t) \circ f_2(t), \tag{3.32}$$

a general filter H must satisfy the following properties for general superposition

$$\begin{aligned} H\left\{f(t)\right\} &= H\left\{f_1(t)\right\} \circ H\left\{f_2(t)\right\} \\ H\left\{c : f(t)\right\} &= c : H\left\{f(t)\right\}, \end{aligned} \tag{3.33}$$

where : is the general scalar multiplication. One can thus define a general transformation $\mathscr{G}$ for filtering which must satisfy the following properties

$$\begin{aligned} \mathscr{G}\left\{f_1(t) \circ f_2(t)\right\} &= \mathscr{G}\left\{f_1(t)\right\} + \mathscr{G}\left\{f_2(t)\right\}, \\ \mathscr{G}\left\{c : f_1(t) \circ f_2(t)\right\} &= c \cdot \mathscr{G}\left\{f_1(t) \circ f_2(t)\right\}, \\ \mathscr{G}^{-1}\left\{\mathscr{G}\left\{f_1(t) \circ f_2(t)\right\}\right\} &= f_1(t) \circ f_2(t). \end{aligned} \tag{3.34}$$

The concepts as defined in Eq. (3.34) make possible to consider a general system for standard filtering method, as shown graphically in Fig. 3.17. The use of the transformation $\mathscr{G}$ enables the conversion from a complex system to a standard linear additive system, making possible to use a linear filter defined as L, which has the same effect in the linear domain as the general filter H. Thanks to the transformation of the general operator to an addition in the reciprocal domain, all principles of superposition can be applied straightforwardly during filtering.

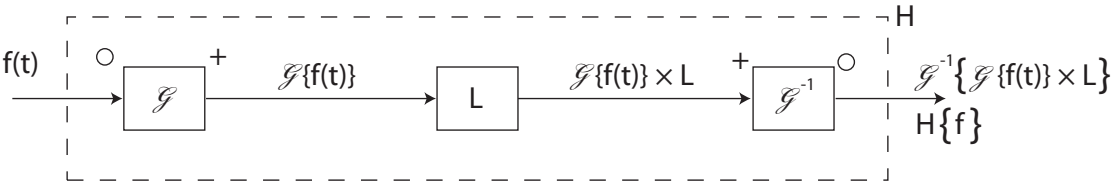

Figure 3.17: Scheme of the filtering steps when employing the general superposition principle.

Application to interferometry

As it will be shown in subsection 3.4.2, the interference process as defined by Eq. (3.1) can be considered as a multiplicative system, so that in this particular case, the general operator $\circ$ of Eq. (3.32) is the multiplication, for which the general transformation must satisfy the properties given in Eq. (3.33). For this purpose, one can use the logarithm operator, which possesses the fundamental property

$$\ln\left[f_1(t)\cdot f_2(t)\right] = \ln\left[f_1(t)\right] + \ln\left[f_2(t)\right]. \tag{3.35}$$

This general concept and its application for multiplicative systems have been used for example for echo removal or for deconvolution in image processing, where several phenomena are of multiplicative nature [Opp68]. Finally, the logarithm itself is not sufficient for the application in off-axis DH, as the filtering is based on spectral separation, so that the needed operator is the Fourier transform of the logarithm of the hologram, thus providing for general filtering

$$\begin{aligned} \mathscr{G}\{f\} &= \mathscr{F}\{\ln(f)\}, \\ \mathscr{G}^{-1}\{f\} &= \exp\left[\mathscr{F}\{f\}\right], \end{aligned} \tag{3.36}$$

with which standard Fourier filtering can then be employed for object wave recovery.

Analogy with cepstrum filtering

The operation defined in Eq. (3.36) is somewhat similar to a transformation used often in homomorphic filtering, which was proposed by Bogert *et al.*. This particular transform has been labelled as "cepstrum" when defining this operation [Bog63], in order to describe this pseudo-frequency space without bringing ambiguity with the standard spectrum. By extending the approach of employing anagrams, a whole vocabulary has been created, ranging from *que-*

frency, or *rahmonics* to the operation of *liftering*, for instance. In this thesis, we only employ the word cepstrum, which is nowadays commonly employed in the literature.

In the first publication defining the cepstrum, it was used to suppress echoes in the measurement of seismologic data, and was thus defined for real numbers. This operation was later referred to as the *amplitude cepstrum*, in order to emphasise its use for real numbers, and is defined as

$$\mathscr{C}\left\{f(t)\right\} = \mathscr{F}^{-1}\left\{\ln\left|\mathscr{F}\left\{f\right\}\right|\right\}, \quad f \in \mathbb{R}. \tag{3.37}$$

One can note that this definition differs from the one given in Eq. (3.36), as two Fourier transforms are employed, and as the order of the operators are different. It is possible to emphasise the difference by noting that the unit of the cepstrum in the case of temporal signals is seconds [Bog63].

Various definitions, leading for example to the *power cepstrum*, were also developed instead of employing the absolute value [Chi77]. Of particular interest for the application described in this chapter is the *complex cepstrum*, defined for complex numbers and which has the advantage of being fully invertible for square-integrable functions. However, the use of complex numbers rises the problem of convergence of the logarithm operator, which does not possess a unique solution in phase. The complex cepstrum is thus usually defined as

$$\mathscr{C}\left\{f(t)\right\} = \frac{1}{2\pi}\int_{-\infty}^{\infty}\left[\ln\left|\hat{f}(\omega)\right| + \mathrm{i}\cdot\arg\left(\hat{f}(\omega)\right)\right]e^{\mathrm{i}\omega t}\mathrm{d}\omega, \quad f \in \mathbb{C}, \tag{3.38}$$

where $\arg\left(\hat{f}(\omega)\right)$ is the unwrapped phase of the spectrum of the function f, ensuring the uniqueness of the logarithm operator. While those considerations in convergence are of great importance, one should note that the case of holography is simpler, and can be treated sufficiently by Eq. (3.36), as the signal recovered by a detector in intensity is by definition defined real positive. The logarithm operator is thus uniquely defined in this case, ensuring the convergence of the transformation. Furthermore, the complex cepstrum is indeed required, as the data is then complex in the frequency domain, but the inversion through the exponential operator is unambiguous in regards to complex numbers, so that the uniqueness is also guaranteed during inversion.

One can note that the main difference between Eq. (3.36) and Eqs. (3.37–3.38) is the use of only one Fourier transform, and the use of either a modulus operation, or of a definition of the logarithm operation ensuring the uniqueness of the operator. The fact of using only one Fourier transform is due to the fact that in-focus or Fresnel holography, which is the case considered here, provide readily a signal in the spatial domain, so that the first Fourier transform is not required. Interestingly, it implies that applications of homomorphic filtering to Fourier holography would lead to definitions closer to the commonly used ones, as a first Fourier transform would be required to enable the logarithm operation in the spatial domain, and would also require care in the definition of the operators, due to convergence problems

with complex signals. Finally, for our particular application, one can consider the definition of Eq. (3.36) as a *complex cepstrum*, where the *a priori* knowledge that the hologram, or signal f, is real-defined due to recording conditions, is employed to simplify Eq. (3.38).

Use of cepstrum in holography

The concepts of homomorphic filtering and in particular logarithm operators and cepstrum have been used in various contexts for holographic acquisition. Homomorphic filtering has been proposed for adapting digital propagation algorithms, which are conventionally based on the convolution with a propagation kernel (cf. section 2.2.5), in order to apply a superposition principle [Aok82]. A treatment based on cepstrum filtering has also been proposed to model the logarithmic response of retina, for applications in polarisation detection in holography [Tit03]. More recently, homomorphic filtering has been proposed for speckle reduction, by considering it as a multiplicative system [Cai10; Sri10]. Finally, the logarithm was also employed for zero-order suppression by making it possible to neglect its contribution under given conditions [Zha04b]. The method described in this section has also been proposed for use in optical coherence tomography (OCT), based on a similar principle, as the acquisition process is also based on an interferometric principle [See08], but in the temporal domain.

3.4.2 Functioning principle and demonstrations

After having defined the general concepts in the previous subsection, we derive here the reconstruction formulae for the particular case of holography filtering, and provide the demonstrations of convergence. We provide on a first stage the derivation for continuous equations, and discuss the consequences for discrete signals only in a second stage.

In order to derive the reconstruction equation, we consider again the interference equation given in Eq. (3.1), that we recall here for convenience.

$$I = (o+r)(o+r)^* . \tag{3.39}$$

One can clearly identify in Eq. (3.39) the multiplicative property of the recording process, on which the principles of general superposition described in subsection 3.4.1 can be applied. As it will be seen later, it is necessary to rearrange slightly the terms of Eq. (3.39) to make the demonstration possible, in order to get

$$\frac{I}{|r|^2} = \left(1+\left(\frac{o}{r}\right)\right)\left(1+\left(\frac{o}{r}\right)^*\right), \tag{3.40}$$

on which it is possible to apply the logarithm operator

$$\begin{aligned} \ln\left(\frac{I}{|r|^2}\right) &= \ln\left[\left(1+\left(\frac{o}{r}\right)\right)\left(1+\left(\frac{o}{r}\right)^*\right)\right] \\ &= \ln\left(1+\left(\frac{o}{r}\right)\right) + \ln\left(1+\left(\frac{o}{r}\right)^*\right), \end{aligned} \tag{3.41}$$

where superposition can indeed be applied for filtering thanks to the conversion into an addition between the two terms. One can thus identify only two components which can be related to the two imaging terms of Eq. (3.1), without zero-order term contributions, as the terms were not distributed in Eq. (3.39).

Applying the Fourier transform on Eq. (3.41) enables filtering in a frequency space, where one can use the spectral separation of the various terms as in off-axis holography, giving

$$\mathscr{F}\left\{\ln\left(\frac{I}{|r|^2}\right)\right\} = \mathscr{F}\left\{\ln\left(1+\left(\frac{o}{r}\right)\right)+\ln\left(1+\left(\frac{o}{r}\right)^*\right)\right\}. \tag{3.42}$$

At this stage, we need to demonstrate that the two terms on the right hand of Eq. (3.42) have a disjoint spectral support, to enable recovery of one term representing the wavefront through linear filtering. For this purpose, we employ the Taylor series of the logarithm, given as

$$\ln\left(1+f(x)\right) = \sum_{n=1}^{\infty} \frac{(-1)^{n-1}}{n} f^n(x), \quad |f(x)|<1, \quad \forall x. \tag{3.43}$$

By applying the Fourier transform and using linearity on Eq. (3.43), we obtain

$$\mathscr{F}\left\{\ln\left(1+f\right)\right\}(\omega) = \sum_{n=1}^{\infty} \frac{(-1)^{n-1}}{n} \mathscr{F}\left\{f^n\right\}(\omega), \tag{3.44}$$

where one can identify that the right hand of Eq. (3.44) is a sum of Fourier transforms of powers of the function f. By recalling the convolution theorem, one can see that each term of the sum corresponds to

$$\mathscr{F}\left\{f^n\right\}(\omega) = \left(\mathscr{F}\left\{f\right\} * \mathscr{F}\left\{f\right\} * \mathscr{F}\left\{f\right\} * \cdots * \mathscr{F}\left\{f\right\}\right)(\omega), \tag{3.45}$$

where the convolution is applied n times. Therefore, if the function $\mathscr{F}\{f\}$ has a support contained in a half-plane of the Fourier space, so will a convolution with itself, as further modulation from convolution compensates for the spectral support extension. As the two terms in Eq. (3.42) are complex conjugates, if the function o/r has its support in a half-plane, so will the function $(o/r)^*$. Therefore, they can be separated through Fourier filtering as no overlapping is occurring under these conditions. Moreover, one can see that a condition for this demonstration to hold is that $|o/r|<1$, for the Taylor development to converge. This condition is rather similar to the condition on the intensity ratio which was defined for the iterative technique as described in subsection 3.3.

Therefore, if those conditions are fulfilled, it is possible to separate the two terms on the right hand of Eq. (3.42), making it possible to select one of them by spatial filtering. The filtered diffraction order in the spatial domain is given by

$$I_F(x,y) = \ln\left(1+\frac{o}{r}\right) = \mathscr{F}^{-1}\left\{\mathscr{F}\left\{\ln\left(\frac{I}{|r|^2}\right)\right\} \times \hat{W}(\omega_x,\omega_y)\right\}, \tag{3.46}$$

where $\hat{W}(\omega_x, \omega_y)$ is a window function selecting the required term in the Fourier domain. Ultimately, the object wavefront is retrieved by applying the inverse operations to recover the original space of analysis, giving

$$\frac{o}{r} = \exp\big(I_F(x,y)\big) - 1 = \exp\left(\mathscr{F}^{-1}\left\{\mathscr{F}\left\{\ln\left(\frac{I}{|r|^2}\right)\right\}\hat{W}(\omega_x,\omega_y)\right\}\right) - 1, \tag{3.47}$$

which specifies the reconstruction through nonlinear filtering. By using homomorphic filtering as defined in subsection 3.4.1, one can also express the nonlinear reconstruction as

$$\frac{o}{r} = \mathscr{G}^{-1}\left\{\mathscr{G}\left\{\frac{I}{|r|^2}\right\}\hat{W}(\omega_x,\omega_y)\right\} - 1, \tag{3.48}$$

where the definition of the general filtering operator of Eq. (3.36) is employed.

By comparing Eq. (3.14), which describes the standard Fourier filtering applied in a linear way, and Eq. (3.47), we find that the proposed algorithm is similar to the standard Fourier filtering method, except for the logarithm and exponential operations. Those differences are consistent with the definitions of homomorphic filtering, where one can see that the reconstruction defined through the general filtering operator is similar to Eq. (3.14). The object complex wavefront can be reconstructed by multiplying the filtered signal with a digital reference wave, as in standard off-axis DHM, and by digitally propagating to obtain the in-focus image, as described in subsection 2.2.5.

One should note however that in the case of the standard reconstruction, the multiplication by r as a digital version of the reference wave generates a constant real term corresponding to the reference wave intensity, as shown in Eq. (2.8). In the case of Eq. (3.48), this term is not directly implied, as it is cancelled by the division by r on the left hand of the equation.

Moreover, as it can be seen from Eq. (3.47), prior knowledge of the reference intensity is required, since this algorithm suppresses the object zero-order, i.e. $|o|^2$, but not $|r|^2$. It corresponds in fact to a subtraction of $|r|^2$ before processing, as

$$\ln\left(\frac{I}{|r|^2}\right) = \ln(I) - \ln\big(|r|^2\big). \tag{3.49}$$

As in subsection 3.3.1, the reference can thus be acquired during a calibration step before experiment, by acquiring the intensity of the reference wave while blocking the object beam.

The new technique just presented requires some specific conditions to be satisfied during hologram recording. The first condition, namely $|r| \gg |o|$, is usually readily fulfilled in a global sense, since it was shown that higher intensity in the reference wave yields a better signal-to-noise ratio (SNR) of the phase signal [Cha06]. However, this condition may not be fulfilled for every pixel in the hologram plane, particularly in the case of out-of-focus images, which can contain strong intensity regions, mainly induced by the highly diffracting parts of the sample.

It is also required that the spectra of the +1 and -1 diffraction orders do not overlap. This condition is however naturally fulfilled in the case of off-axis DHM, which requires disjoint support for the two imaging terms in order to enable spatial filtering.

Discrete implementation and harmonics

In the demonstration above, we derived the nonlinear reconstruction method in the continuous domain for convenience. However, the implementation of this technique will be done on discrete matrices, as recorded by digital detectors. The transfer to a discrete representation of Eq. (3.47) is straightforward, as the mathematical operations such as divisions, logarithm, and exponential are performed locally, and can thus be applied pixel by pixel. As an illustration, the logarithm in the discrete representation would be

$$\ln\left(\frac{I}{|r|^2}\right) = \ln\left(\frac{I[m,n]}{|r[m,n]|^2}\right), \quad 0 < \forall\ m,n < N. \tag{3.50}$$

With analogical treatment for the other operations, it implies that Eq. (3.47) can represent continuous as well as discrete implementation.

The main differences in the case of a discrete representation lies in the use of FFT algorithms to compute the Fourier transform, and the consequent periodisation of the signal and the influence of discretisation on nonlinear operators which can lead to the generation of harmonics. These harmonics are represented by powers of the original function, so that the error between the ideal function and the computed one can be expressed as

$$\epsilon[m,n] = \sum_{k=2}^{\infty} \alpha_k (f[m,n])^k, \tag{3.51}$$

where α_k is a real factor related to the intensity of each harmonics in accordance with Eq. (3.44). As the demonstration above is performed in the spectral domain, the function f is modulated by the reference wave as expressed in Eq. (3.3), thus giving shifted terms in the Fourier domain (cf. Eq. (3.4)).

This implies that the error in Eq. (3.51) can be expressed in as

$$\hat{\epsilon}[m,n] = \sum_{k=2}^{\infty} \alpha_k \hat{f}\left[\omega_m - k\cdot\omega_{0,m}, \omega_n - k\cdot\omega_{0,n}\right], \tag{3.52}$$

thus giving terms modulated at multiples of the modulation frequency $\boldsymbol{\omega}_0$ induced by the reference wave. If discrete Fourier transforms are employed, some harmonics overlap with the reconstructed signal through periodisation. As the harmonics respective intensities decrease with higher orders, it is possible to circumvent this problem through an extension of the domain on which the Fourier transform is performed in order to avoid spectral overlap. This can be done by interpolating the signal in the spatial domain, extending the size of the matrix by a factor of interpolation p, and therefore increasing the reachable frequencies of the FFT

by the same factor. This interpolation at order p can be expressed mathematically as

$$I^{(p)}[m,n] = I\left[\frac{m}{p}, \frac{n}{p}\right], \quad 0 < \forall\ m,n < pN. \tag{3.53}$$

This method makes it possible to avoid the periodisation on the lower orders of harmonics. As the energy carried by the error orders decreases rapidly, we could identify that frequency extension through standard spline interpolation with a factor $p = 2$ was plentifully sufficient to avoid problems due to the harmonics in standard conditions.

3.4.3 Simulations

As in section 3.3.3, we first perform simulations in order to assess the validity of the technique under controlled conditions for various types of signals. However, some differences are to be noted compared to previous simulations. In the case of the iterative technique, the main purpose of the simulations was to assess the validity of the technique, as it does not theoretically fully suppress the zero-order, and to quantify the residue after filtering. In the case of homomorphic filtering, the method is supposed to perfectly suppress the zero-order in the absence of noise. The main purpose of the simulations is therefore to assess the efficiency of the method when noise is present, and in particular its capability to recover a quantitative phase in those conditions, and its validity on various types of signal.

Another main difference between the signals reconstructed with the nonlinear method and the iterative method described in subsection 3.3 is the exclusivity of the condition on amplitude ratios of the two interfering waves. While with the iterative method, this criterion had to be considered in a global sense, it has to be true for each pixel in the field of view in the case of the nonlinear method. This implies that the criterion defined in Eq. (3.27) is a necessary but not sufficient condition for the method to converge. For this reason, we define here a second criterion, the maximum intensity ratio $\max(K_I)$, which enables to define a sufficient condition for the nonlinear method based on the intensity ratio as $\max(K_I) < 1$. This criterion can be defined as

$$\max(K_I) = \max\left(\frac{\left|o(x,y)\right|^2}{\left|r(x,y)\right|^2}\right). \tag{3.54}$$

Control on accuracy of phase reconstruction

The purpose of these simulations is to ensure that the implementation of the reconstruction as described by Eq. (3.47) provides quantitative phase even when some noise occurs in the recording process. As described in subsection 3.4.1, the problem in this case does not suffer from the potential instabilities coming from the computation of a complex logarithm.

For this purpose, we created a phantom representing a cell culture in amplitude and phase (cf. Fig. 3.18(a)), where a strong amplitude profile was generated, in order to create large

spatial frequencies. Furthermore, some noise was added on the phase of the phantom to represent roughly measurement conditions, by adding a uniformly distributed random value comprised between $\left[-\frac{\pi}{25}, \frac{\pi}{25}\right]$ radians. This value still corresponds to a smooth object, but can be considered as a fairly strong noise under normal recording conditions. The simulations parameters are chosen so that the two conditions required by our proposed algorithm are satisfied, i.e. separation of imaging orders and $\max(K_I) < 1$. The reference intensity is made 3 times stronger than the constant background of the object, so that the mean intensity ratio in the image is $\overline{K_I} = 0.233$, and the maximum ratio is $\max(K_I) = 0.69$. The range between the maximal and minimal ratio can be explained by the strong amplitude of the considered object, which therefore induces strong variations of the ratio K_I. The parameters of the simulation are taken as $\lambda = 680$ nm, and $\Delta x = \Delta y = 6.45$ µm. The hologram is generated with the method given in Algorithm 2.

We concentrate our attention to the reconstruction of the phase part of the field, since keeping a quantitative signal is of great importance. The results are shown in Fig. 3.18, where the phase of the original object used for generating the hologram (cf. Fig. 3.18(a)) is compared with the reconstruction made with the SF method (cf. Fig. 3.18(b)) and the ZF nonlinear technique (cf. Fig. 3.18(c)), where a square filtering similar to the one employed in subsection 3.3.3 has been employed. One can see that strong artefacts are present in the standard reconstruction, which are parts of zero-order disrupting the signal; those components are fully suppressed by employing the nonlinear method, which retrieves the quantitative information without artefacts.

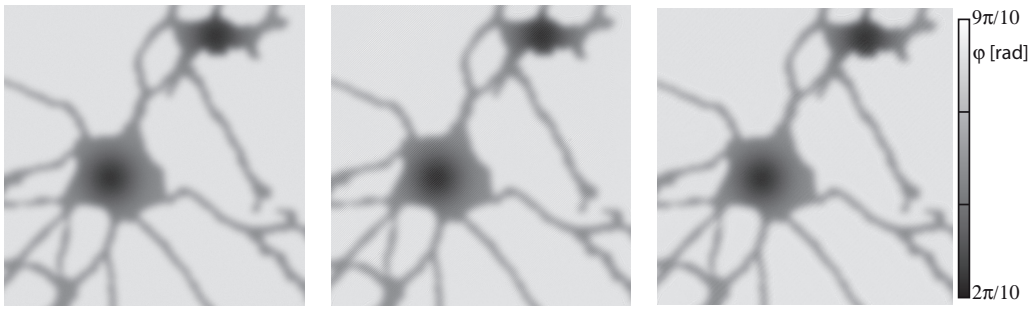

(a) (b) (c)

Figure 3.18: Phase part of the phantom image used during simulations. (a) Original object used to generate the simulated hologram, which is compared with the phase retrieved by (b) the standard Fourier method and (c) the nonlinear technique, where the zero-order artefact is suppressed.

In order to get more insight on the efficiency of the process, differences were calculated between the ideal reconstructed signal and the studied methods. Since some parts of the differences could be due to numerical errors induced by other steps of the reconstruction process, such as digital propagation, an ideally reconstructed signal was generated by using a zero-order-free hologram computed as: $I_{\text{ideal}} = I - |r|^2 - |o|^2$, where all information is known

in the case of numerical simulations. The phase differences between the reconstruction of this ideal signal and the phase images of Fig. 3.18(a) are presented in Fig. 3.19. In the case of the SF reconstruction (cf. Fig. 3.19(a)), very strong phase variations in the order of $\pi/4$ are occurring. These variations are suppressed with the ZF nonlinear method (cf. Fig. 3.19(b)), where no strong artefacts can be identified although the signal dynamic is 5 times smaller. One can identify a small pattern in the reconstruction of Fig. 3.19(b), which is due to frequency harmonics generated by the nonlinear process. These harmonics could be further minimised by for example increasing the intensity ratio between the reference and object waves, which in this case just satisfies the requirements of the method, since the maximum ratio is only slightly below 1 (0.69).

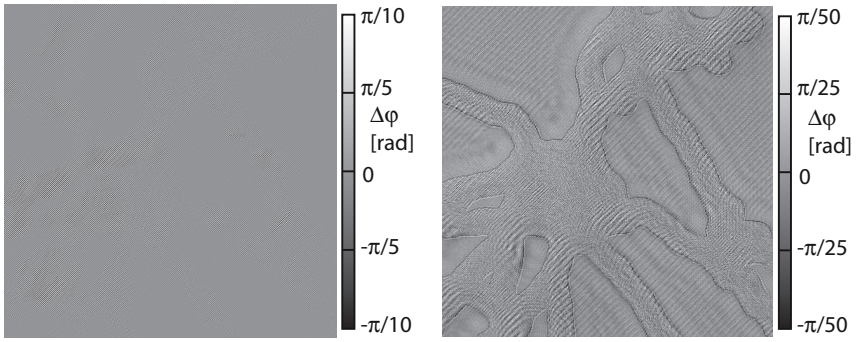

Figure 3.19: Phase difference between an ideal wavefront of the phantom and (a) the standard Fourier reconstruction and (b) the nonlinear one.

Results on speckle holograms

We then perform simulations for speckle hologram, in the same way as in subsection 3.3.3, to validate the reconstruction procedure on objects generating strong spatial frequencies. The object used for simulation is a USAF 1951 target phantom (cf. Fig. 3.6(a)), to generate a rough hologram according to Algorithm 3, providing a hologram as shown in Fig. 3.11(a).

One main difference compared to the results of subsection 3.3.3 is that generated data were saved in 16-bit images instead of 8-bit, to avoid pixels becoming zero because of quantisation. The nonlinear filtering technique indeed requires data with an intensity ratio K_I strictly below 1 for each pixel, in order to ensure convergence for the logarithm operation. This issue did not occur with the iterative technique, as it requires a ratio above 1 in a global sense only.

The amplitude of the object reconstructed through nonlinear filtering is presented in Fig. 3.20(a), where the typical granular texture of speckle images can be readily identified. The spectrum of the object field after nonlinear reconstruction is shown in Fig. 3.20(b), where zero-order has been suppressed. This can be readily seen by identifying the constant background around the imaging term, showing no zero-order left in the centre of the spectrum.

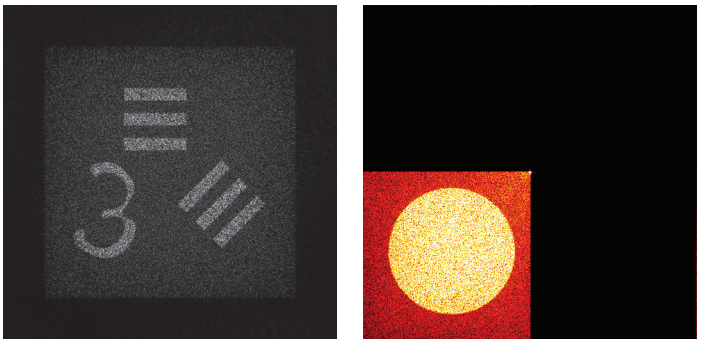

(a) (b)

Figure 3.20: (a) Amplitude of the wavefront reconstructed with the nonlinear method, after generation of the speckle hologram, corresponding to (b) a zero-order-free spectrum after reconstruction.

The three other quadrants were filtered out during the reconstruction process, according to the reconstruction method described in subsection 3.4.2.

The simulation presented in this section shows that nonlinear reconstruction can be applied to rough samples measurement, giving rise to speckle holograms. However, one should note that this type of signal can lead to several issues if not handled properly. The nonlinear reconstruction method requires that the amplitude of the reference wave has to be strictly stronger than that of the object, which can be difficult to satisfy in a case where random constructive interferences can lead to strong intensities in the object wave.

3.4.4 Experiments

In this section, we demonstrate the capability of the proposed method through different experiments. First, we present results obtained through the use of the nonlinear reconstruction without filtering, providing an insight about the respective contributions of the various terms of the interference equation. Then, we show the improvements on details of the reconstructed image, when employing optimal reconstruction parameters. In this subsection, we apply the proposed method on experimental data, in order to assess the capabilities in practical conditions. As in subsection 3.3.4, the simulations were performed with rather similar conditions as the experiments, enabling easy comparison.

Results with a phase object

We imaged a solution of yew pollen cells immersed in water with a transmission DHM, as shown in Fig. 2.15(a). The sample is illuminated with a laser diode (λ = 680 nm), and the diffracted field is collected with a 10× MO (NA = 0.25). We chose a low magnification to ensure that some spectral overlap occurs between the imaging order and the zero-order. The signal is recorded in the Fresnel domain with an 8-bit monochrome CCD camera (Basler A102f, pixel

size: $\Delta x = 6.45\,\mu m$) an employed field of view of 512×512 pixels, and an exposure time of approximately 1 ms, leading to a reconstruction distance of $d = 4.85\,cm$. The intensity ratio between reference and object waves can be controlled through polarisation optics, and was systematically checked before measurements by comparing an image of the object beam with that of the reference beam alone.

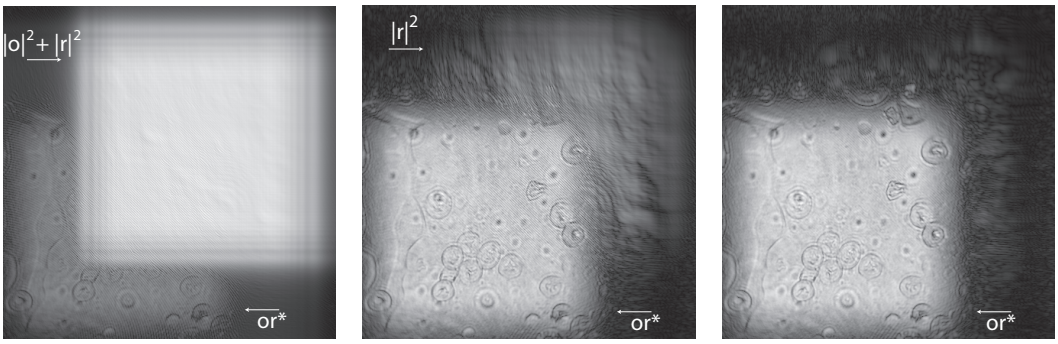

(a) (b) (c)

Figure 3.21: Solution of yew pollens reconstructed with (a) the linear Fourier technique, with the full zero-order term, (b) the nonlinear technique, with the reference intensity term, and (c) the nonlinear technique, with subtraction of the experimental reference and mean suppressed, where the zero-order is suppressed (each image is scaled independently on full dynamic).

The mean and maximum intensity ratios between the object and reference waves, as defined in Eqs. (3.27) and (3.54) were computed as respectively $\overline{K_I} = 4.5 \cdot 10^{-2}$ and $\max(K_I) = 0.45$. This big difference is due to strongly diffracting points, so that the reference intensity has to be high enough to ensure that the intensity condition is fulfilled at each pixel.

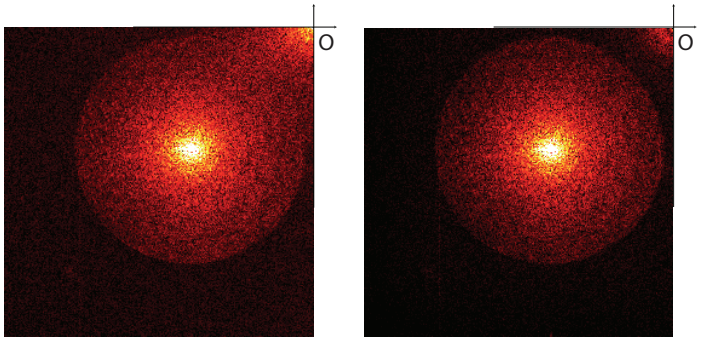

(a) (b)

Figure 3.22: Relevant quadrant of the yew pollen cells hologram spectrum after (a) linear Fourier filtering and (b) nonlinear method.

The hologram was reconstructed by filtering one quadrant of the Fourier plane with the standard Fourier (SF) method and the proposed nonlinear (NL) method. The results are presented in Fig. 3.21, where one can see the very strong influence of the zero-order term in the case of the linear method (cf. Fig. 3.21(a)), while a strong part of this parasitic term has been suppressed by using the nonlinear method (cf. Fig. 3.21(b)). Although a great amount of the DC term has been suppressed, an important part is still present, which corresponds to the reference intensity term $|r^2|$. As it can be seen in Fig. 3.21(b), this term is not constant, which shows that the approximation made by considering it as a plane wave is not appropriate for proper suppression of the reference intensity term. The reconstruction with nonlinear filtering and reference subtraction is shown in Fig. 3.21(c), where the DC component of the hologram is also suppressed, i.e. the spectral component at the origin. Suppressing the frequency at the origin corresponds to subtracting the mean value of the hologram. This mean value can still be present after reference intensity suppression, because for example of stray light contributing as an incoherent addition on the camera, for example.

The selected quadrant of the hologram spectrum is shown in Fig. 3.22 for the two methods, where it is possible to identify the overlap of frequencies between the zero-order and the imaging order for linear filtering (cf. Fig. 3.22(a)). On the other hand, the nonlinear method suppresses the zero-order term (cf. Fig. 3.22(b)), so that spectral energy near the origin reaches back the noise level, so that is is possible to identify the spatial cut-off frequency of the MO around the whole circumference.

One must observe that, despite the subtraction of the residual $|r|^2$ term, some spectral components are still present in the vicinity of the origin even for the nonlinear case. These components are due to some differences between the reference intensity recorded for subtraction and the one used during the hologram generation, due to experimental noise, such as vibrations of the experimental setup, or shot noise. As mentioned earlier, the power stability of the laser can also be a parameter inducing some discrepancies between calibration and effective measurement. Typically, temporal averaging could be used during the calibration step, by acquiring several images of the reference intensity in order to circumvent those issues. Then, another effect causing part of the residual components is the discretisation of the hologram, which leads to harmonics and to some errors in the computation when performing the logarithm operation.

The same hologram was reconstructed by using the method employed for Fig. 3.21(c), and by only keeping the spatial region containing the imaging order, making it possible to estimate the improvement provided by the proposed method in finer details, as shown in Fig. 3.23. In order to increase the visibility of the various terms in the image plane, the Fresnel propagation is employed (cf. Eq. (2.31)).

The SF method (cf. Figs. 3.23(a–b)) and the nonlinear technique (cf. Figs. 3.23(c–d)), are shown in amplitude and phase, respectively. The zero-order effect can be identified as a parasitic high-frequency term in some part of the images; this is due to the fact that after de-

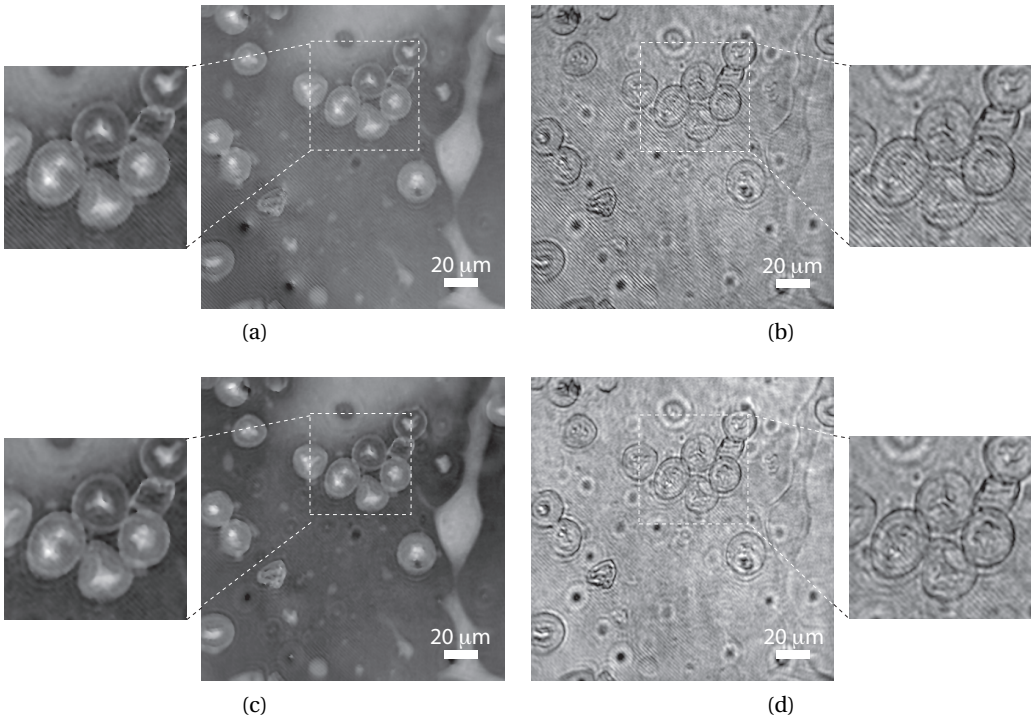

(a) (b)

(c) (d)

Figure 3.23: Specimen: solution of yew pollen cells. Reconstruction with (a, b) the linear Fourier technique and (c, d) the nonlinear method, with comparison in phase (a, c) and amplitude (b, d). Insights (scaled independently) in a part of the field of view are shown.

modulation of the off-axis hologram, the DC component becomes an AC term, i.e. gets modulated. These high frequencies are efficiently suppressed in the case of the nonlinear filtering method, as shown in the insights of Fig. 3.23.

Although the zero-order is efficiently suppressed through the proposed nonlinear filtering approach, some small remnants of high frequencies can be identified in the reconstruction shown in Fig. 3.23(d). These components are indeed not fully suppressed, because the approximations made in the theoretical analysis are not exactly satisfied. However, as it will be shown in the subsequent section, those strong frequencies are situated at the origin, where no overlap is occurring between the zero-order and the imaging term, so that they can be filtered out by using for example a Fourier mask computed with Eq. (3.11). This filtering was not done in the results shown in Fig. 3.23, to demonstrate the intrinsic performance of the proposed method by using square filtering.

Results on speckle holograms

The measurements presented here were performed on a reflection DHM (cf. Fig. 2.15(b)) on a coin, in an identical way as in subsection 3.3.4.

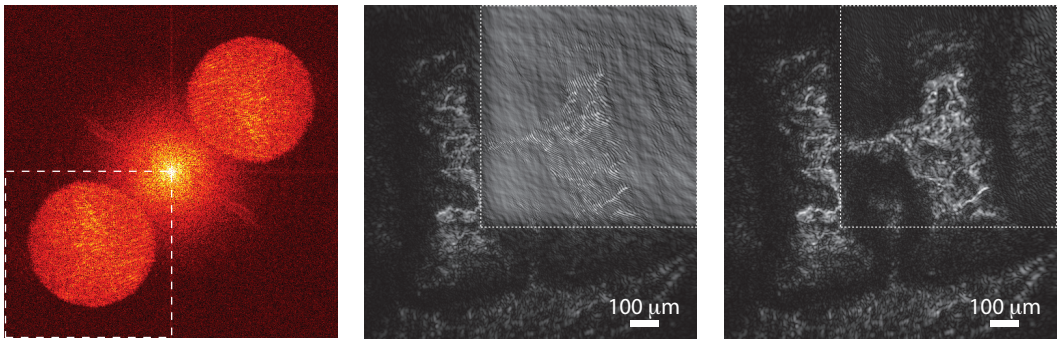

(a) (b) (c)

Figure 3.24: (a) Fourier transform of the hologram made from the reflection on a coin. Amplitude of the reconstructed object field with (b) standard linear Fourier filtering and (c) the nonlinear method, where the zero-order, identified by the dotted square is suppressed.

We reconstructed the hologram by filtering a quadrant of the Fourier plane (cf. dashed line in Fig. 3.24(a)), and employed both SF and ZF nonlinear method. The object is the letter "H" of the word "Helvetia" engraved on a Swiss coin. The zero-order can be readily identified in the amplitude reconstructed with linear filtering, as presented in Fig. 3.24(b), where the object autocorrelation position is emphasised with a dotted square. On the other hand, the nonlinear method provides a zero-order-free amplitude, as shown in Fig. 3.24(c), where the autocorrelation in the top-right of the image have been suppressed, and no ghost in the reconstruction can be identified.

3.4.5 Discussion

The results shown above show that the nonlinear reconstruction method can be used for zero-order suppression with experimental data, and presents a satisfactory behaviour in regards to robustness towards noise. However, some discrepancies in the efficacy of the method between simulations and experiments could be identified during various experiments. This is visible for example when comparing the spectrum of the reconstructed simulation in Fig. 3.20(b), where a fully constant background is clearly visible, showing that no spectral energy from the zero-order is left, while in Fig. 3.22(b), some small remnants of zero-order can be seen in the top-right corner, near the origin of the hologram.

Those discrepancies were studied in more details, although they are of very small intensities, thus usually not inducing noticeable errors on the reconstruction. By employing various experimental conditions it was identified that those errors are strongly dependent on the fringe visibility on the hologram. This could be explained by the fact that a loss in fringe visibility corresponds to a change of respective spectral power ratio between autocorrelation terms and the modulated terms, as expressed for the mutual coherence in Eq.(2.14). The fact

that the mutual coherence term was not taken into account could lead to some errors in the zero-order suppression.

However, one should note that this dependence on fringe visibility is also linked to problems related to the spatially discrete recording of the hologram. Some fringe visibility is lost due to the averaging of the sinus pattern over the pixel surface as discussed in subsection 2.2.4, so that a fundamental limitation on the algorithm performance appears because of the discrete nature of the signal. The visibility is then further limited because of remaining elliptical polarisation of the light source, for example. Incorporation of the mutual coherence in the model of nonlinear reconstruction was not investigated in the framework of this thesis, but could potentially further improve the performances of the method.

Comparison with linear zero-order suppression methods

We compare here the nonlinear method described above with other well-established methods for suppressing the zero-order term. We employ here for comparison an approach consisting in using high-pass filtering (HP) before processing the hologram to attenuate the zero-order, seen as a low frequency term, while keeping the spatially modulated components, namely the imaging terms [Liu02].

A high-pass filtered version of the hologram can be obtained by subtracting a low-pass filtered component from the original signal

$$I^{\mathrm{HP}} = I - I * h_k, \quad h_k[m,n] = \frac{1}{k^2},\ \forall\, |m,n| \leq \left\lfloor \frac{k}{2} \right\rfloor, \tag{3.55}$$

where $h_k[m,n]$ is a low-pass filter consisting in a normalised matrix of size $k \times k$.

To demonstrate the effect of this type of filters, we selected two high-pass kernels, with respectively $k = 3$ and $k = 7$. The frequency response of those filters are given in Fig. 3.25, where the positions of the interference terms are shown for the measurements of Fig. 3.26.

As it is shown in Fig. 3.25, the high-pass filters have a strong attenuation in the low frequency region, and ripples at higher frequencies. Consequently, the zero-order term is strongly attenuated, but phase artefacts arise in the imaging terms since the response is not necessarily symmetric around the modulation frequency.

To enable quantitative comparison between the various methods, we measured in reflection a mirror with a scratch with a 20× MO (NA = 0.4) and a wavelength of $\lambda = 661$ nm. The scratch induces strong directional frequencies, as shown in Fig. 3.26. Those components create artefacts in the amplitude, which can be seen at the bottom right of the image (cf. dashed region in Fig. 3.27(a)). Although they cannot readily be identified in the phase image (cf. Fig. 3.27(b)), those artefacts are also present. The mean intensity ratio of the presented hologram is $\overline{K_I} = 0.59$, and the images were obtained with a propagation distance of $d = 4.3$ cm. The reconstruction made with the SF method highlights these artefacts.

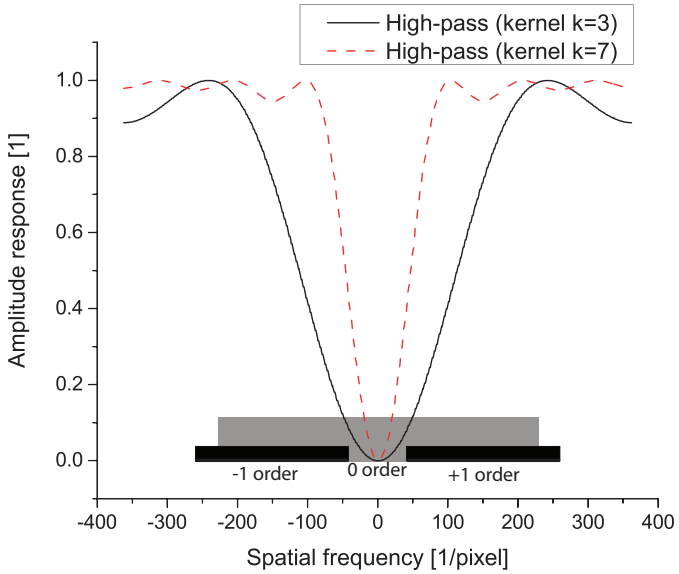

Figure 3.25: Frequency response of the high-pass filters corresponding to different kernel sizes, as defined in Eq. (3.55). The position of the interference terms is shown, corresponding to the spectrum presented in Fig. 3.26.

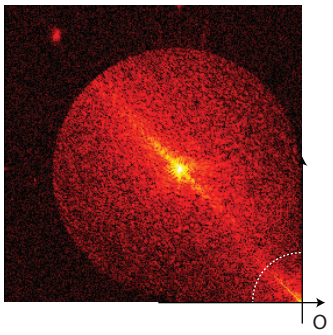

Figure 3.26: Magnitude of a quadrant of the Fourier transform of the hologram of the mirror scratch. The dashed circle shows the region of the spectrum which is spatially filtered, to account only for overlapping frequencies.

In order to make a fair comparison between the two techniques, the measured reference intensity was subtracted in all cases, to account for the $|r|^2$ term. All the holograms were spatially filtered before propagation with the same circular mask at the origin, so that only overlapping zero-order is considered (see dashed circle in Fig. 3.26). The radius of the circle was computed in order to stay outside of the bandwidth of the imaging order, according to Eq. (3.11), where the numerical bandwidth is measured as $\Delta\omega_o = 210$ pixels.

The phase standard deviation is computed in a 200 pixel square zone shown in Fig. 3.27(b), for different intensity ratios, as defined by Eq. (3.27), between the reference and object waves. The results are shown in Fig. 3.28(a), where the standard deviation values were fitted with a fourth-order polynomial, in order to show the main trend of the curve.

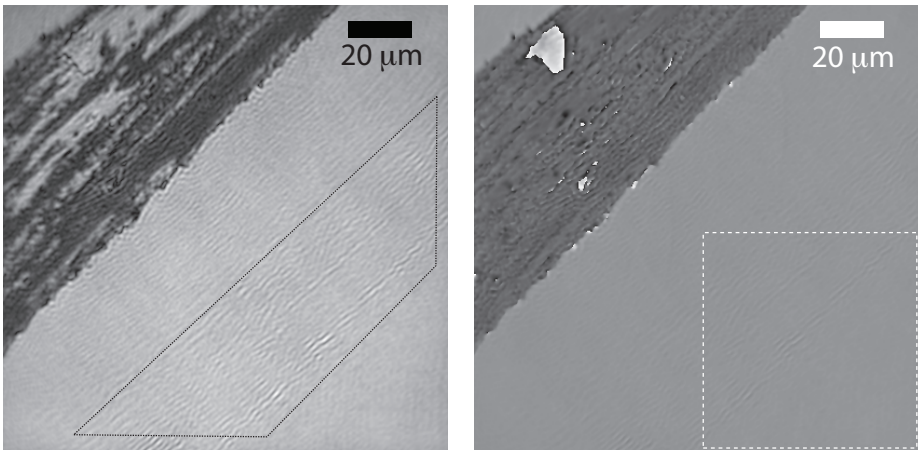

(a) (b)

Figure 3.27: Specimen: mirror with a scratch; (a) amplitude and (b) phase reconstructed with the standard linear technique. The black dashed square in (a) shows the artefacts induced by the zero-order in amplitude. The white dashed square in (b) shows the region in the phase image where the standard deviation is computed.

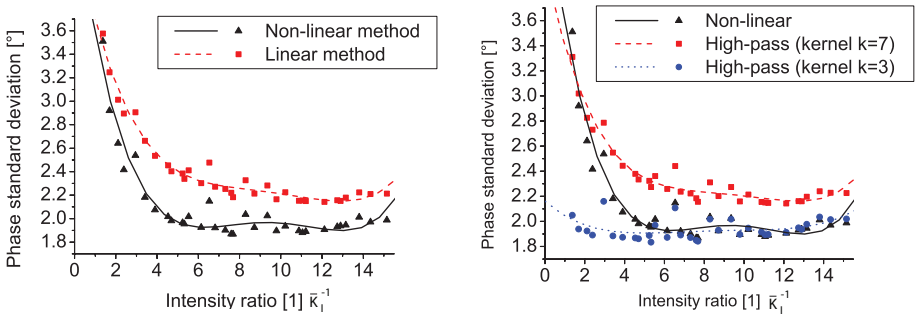

(a) (b)

Figure 3.28: Phase standard deviation on the measured zone of Fig. 3.27(b) as a function of the mean intensity ratio between the reference and object waves, comparing the nonlinear technique (a) with the linear reconstruction and (b) with high-pass filters of different kernels as defined in Eq. (3.55).

One can identify that, for the two reconstruction techniques, the standard deviation seems to have a minimum in the middle of the intensity ratio values. The higher standard deviations at low ratios are due to the fact that the phase is distorted by the spectral power of the zero-order, which depends directly on the power of the object wave. On the other hand, one can assume that for high intensity ratios, the amount of available photons in the object wave is decreasing, leading to higher standard deviations due to the increase of the influence of shot noise. This implies that there is an optimum for the phase SNR, which corresponds to a reference wave intensity comprised approximately between 75% and 90% of the total power. This

result showing an improvement in signal quality for a reference wave stronger than the object one is in agreement with previously published studies on SNR of phase signals [Cha06].

In the case of the ZF technique, the standard deviation is rather high for low intensities, since the assumption of the reference wave being stronger than the object is not fulfilled. Then, it rapidly reaches a minimum at a mean intensity ratio of $\overline{K_I} = 1/5$, and stays at a standard deviation of approximately 2°. One should note that this value is obtained for one-shot measurements, taken in conditions which were optimised to show the influence of the zero-order on noise, and not to minimise noise values. The quantitative analysis makes also possible to compare the proposed nonlinear technique with the high-pass filters. The same procedure as described above was applied for reconstructions where the hologram was previously filtered with high-pass filters of kernels $k = 3$ and $k = 7$, as defined in Eq. (3.55), and shown in Fig. 3.25.

As it can be seen in Fig. 3.28(b), the high-pass filtering method can get similar results as nonlinear filtering in the case of a kernel $k = 3$, which corresponds to a very strong filtering, showing that this phase standard deviation is obtained at the cost of a strong loss of spatial resolution (cf. Fig. 3.25). On the other hand, a weaker filtering ($k = 7$) does not improve significantly the standard deviation of the signal compared to linear filtering without any HP filter.

This result shows that the nonlinear filtering efficiently suppresses the zero-order. It can indeed be assumed that the very strong high-pass filtering ($k = 3$) suppresses the contributions of the DC term (cf. Fig. 3.25), so that only the intrinsic standard deviation coming from the light source and the sample remains. It can be seen that the nonlinear method can reach back the minimum noise for this measurement, by fully suppressing the zero-order term.

These results also show that since the intensity ratio is sufficient to fulfil the assumptions required by the algorithm, the optimum of reconstruction quality is reached, without any need to finely tune this key parameter, making the technique rather flexible.

Resolution improvement

As discussed in subsection 3.2.3, suppressing the zero-order makes it possible to extend the usable bandwidth for the imaging order. We showed that in the context of off-axis DHM, enabling the use of a full quadrant of the Fourier plane leads to diffraction-limited imaging. In order to demonstrate the advantage in resolution provided by ZF methods, we processed the experimental data shown in Fig. 3.27 with a circular filter.

Employing a circular filter enables controlling the effective NA of the imaging order numerically, and suppresses the non-overlapping part of the zero-order, which cannot be suppressed through high-pass filtering without altering the original wavefront. According to Eq. (3.11), it is possible to calculate the effective NA of the numerical reconstruction from the bandwidth in pixels. We measured the effective magnification of the system by employing a USAF target

(cf. appendix A, leading to a value of $M = 18.98\times$, and employed a diameter of circular filter of 209 px, corresponding to visible bandwidth in the spectrum, which leads to an effective $NA_{eff} = 0.395$ for the full bandwidth measured by the system, which is in good agreement with the nominal value of NA = 0.4 (cf. Fig. 3.29(a)).

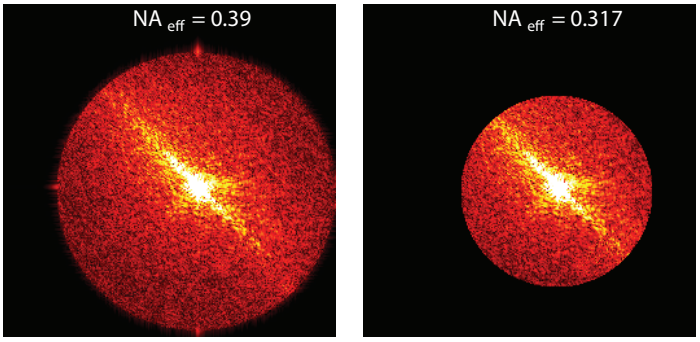

(a) (b)

Figure 3.29: (a) Quadrant of the Fourier plane containing the imaging order for the nonlinear reconstruction. (b) Quadrant of the Fourier plane corresponding to the linear reconstruction, where the imaging order was filtered with a smaller bandwidth to reach the same phase standard deviation as for the nonlinear method on the measured on the line shown in Fig. 3.27(b). Effective numerical apertures (NA_{eff}) corresponding to each reconstruction are shown in the spectra.

We then consider the same area in the phase image of the scratched mirror, which standard deviation on a flat part of the mirror is taken as an indicator of the artefacts induced by the overlapping zero-order (cf dashed square in Fig. 3.27(b)), giving a standard deviation for the nonlinear reconstruction method of $\sigma_{ZF} = 1.939°$. Measuring the standard deviation at the same location on the phase map reconstructed with the standard linear method yields $\sigma_{SF} = 2.227°$, because of the modulated zero-order term.

We then varied the diameter of the circular filter for the standard reconstruction in order to reach back the phase standard deviation provided by the nonlinear filtering, by suppressing the zero-order through standard spatial filtering. The resulting phase standard deviation in function of the filter diameter is presented in Fig. 3.30, where one can see that the same value of phase standard deviation is reached for a diameter of 168 pixels, giving $\sigma_{SF} = 1.94°$ which corresponds to an effective $NA_{eff,SF} = 0.317$, as shown in Fig. 3.29(b). This shows the ability of nonlinear filtering to extend the spatial resolution of images obtained through DHM, without the cost of disrupting the phase signal with artefacts.

One should note however that the treatment presented above is an illustration of the capability of increasing the spatial resolution through intrinsic zero-order suppression, but the derived values should be handled with care. Indeed, changing the size of the numerical filter is by itself inducing variations in the standard deviation through numerical effects. This

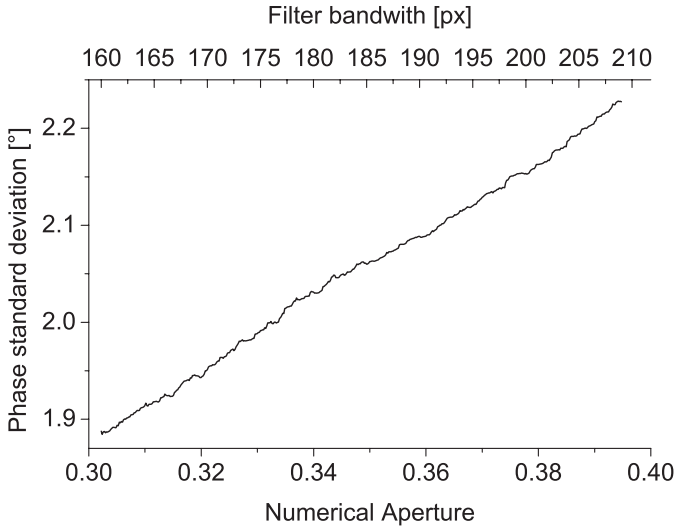

Figure 3.30: Phase standard deviation on the dashed square of Fig. 3.27(b) with standard linear reconstruction, in function of the diameter of the circular filter, corresponding to a given effective NA.

can be identified in the variations of the curve of Fig. 3.30, where the standard deviation does not change exactly in a proportional way with the diameter. Moreover, this filtering process makes the standard deviation measurement object-dependent, so that cutting some spatial frequencies could induce stronger standard deviation through blurring. However, those effects should be rather small in the case of the considered object, and a fairly linear tendency can be seen in the curve, so that those effects do not heavily disrupt the results above, but surely induce uncertainties.

3.5 Discussion and perspectives

We demonstrated in the sections above the applicability of the proposed algorithms for zero-order suppression. One characteristics of most of the experimental examples that were presented is that they were performed in the reflection case, as this configuration enables measurements with usually less noise than in transmission. This is due for example to the fact that in transmission, the beam passes usually through various interfaces in the sample, such as several glass layers in which the specimen is sandwiched. Those different interfaces add noise, compared to the reflection on one interface. Furthermore, well characterised samples are available for reflection, while specimens with well known transmission characteristics are classically hard to find. These reasons justify for example the fact that no transmission demonstration was made in the speckle case, as those samples are usually difficult to characterise, due to their complexity and large thickness.

In the same point of view, experimental demonstrations were essentially presented in what was defined in section 2.2.4 as the optically-limited case. Part of this limitation is due to the

practical availability of experimental setups, essentially meant for microscopy applications. One should also note that, although the theoretical principle are identical, the limitations in bandwidth are usually more complicated to control in a detector-limited setup, as its macroscopic configuration does not let many freedom parameters for changing the bandpass characteristics, apart from changing hardware, which is experimentally more complicated for proofs of concepts than adapting optics components. Furthermore, it must be admitted that it is more difficult in a detector-limited system to fulfil some conditions required by the proposed methods, such as the full spectral separation of the imaging order and its twin-image. One could therefore consider that the methods may be more limited in their use in the case of macroscopic systems, as the fundamental conditions are more complicated to comply to.

The two methods presented above are rather different in their approach, performance and application range. One one side, the iterative technique is less demanding in terms of the required conditions on the measurements. Typically, it requires globally a reference wave which is stronger in intensity than the object wave, but can cope with local regions where it would be the opposite. This looseness on requirements also implies that the method could provide unexpected results in some cases, as the limits at which the algorithm will diverge are more complicated to derive. Typically, as the main limitation of the method resides in the quantity of spectral overlap between the various terms, the method could be considered as specimen-dependent, since objects with larger spectral information will increase the spectral overlap.

On the other hand, the nonlinear approach is fully independent of the type of object measured, as it typically does not depend on the amount of spectral overlap. Its main limitation consists in the requirement that the reference wave has to be stronger than the object one, in a local sense. This limitation can be difficult to fulfil in some cases where the specimen generates a large distribution of intensity, such as in speckle holography. Practically, the nonlinear method diverges in cases for which the intensity of a pixel on the hologram is zero. Therefore, employing detectors with finer digitisation capabilities, such as 12-bit or 16-bit cameras, can circumvent this issue by making it easier to ensure that a non-zero value is recorded on each pixel, even with low photon rates. Furthermore, although this possibility was not employed in the proof of concept demonstrated in this thesis, one may develop cleverer treatment of the hologram data, in order to selectively treat the diverging pixels, in analogy with desaturation methods, for example. These development could enable a wider use of the nonlinear method by circumventing its restrictions.

As two different methods were developed in this chapter, a natural question that can arise is the possibility to combine both techniques to improve the global performance of zero-order suppression algorithms. As the first computation step—the so-called "seed"—is commonly critical for iterative algorithms, one may want for example to employ the nonlinear method to generate a first reconstruction, which could be employed as a starting condition for the iterative method. This approach does in fact usually not bring any advantage, as tests performed on simulations similar to the ones in subsections 3.3.3 and 3.4.3 showed. This is due

to the large difference in requirements and approach of the two methods. Critical cases, such as ones yielding a divergence of the iterative method, commonly do not fulfil the more restrictive requirements of the nonlinear approach. Similarly, cases fulfilling the conditions for the nonlinear method provide already good results, as its solution is not approximated by the reconstruction model, and usually converge with the iterative method thanks to its looser conditions. Again, the development of methods to treat separately pixels not fulfilling the intensity condition of the nonlinear method could bring other perspectives to these combined approaches.

In conclusion, we would like to remind that the zero-order suppression problem in holography covers two main aspects, depending on the original approach for reconstruction, that we tried to clearly distinguish in the introductory part in section 3.2. In the case where spectral overlap is tolerated in the reconstruction, it implies that the reconstruction already provides the full resolution of the system. The zero-order suppression can be considered in this context as an artefact suppression method, as noise generated by the presence of spectral information from the zero-order will be suppressed. Contrarily, if the reconstruction is based on avoiding any artefact even at the cost of resolution, such as in X-ray holography, where periodic structures forbid the inclusion of any zero-order portion, suppression methods can be considered as a resolution improvement method, by providing again the full resolution (diffraction-limited) of the detection system in the reconstruction.

Finally, the two methods proposed in this chapter are both based on the fundamental interference equation, and do not require any approximation for their derivation. This implies that they can be used in all generality for any type of specimen, under the conditions which define their application range, would it be in phase and/or amplitude, as the reconstructions are globally independent from the specimen nature. Furthermore, the nonlinear zero-order suppression method provides in theory exact reconstruction, free from any artefact that could occur due to the reconstruction approach, as the derivation does not require any approximation, and that no residue of reconstruction is present in the derivation. However, it could be shown that the discrete nature of data implies a fundamental limitation.

References

[Aok82] Y. Aoki, T. Kuniyoshi, H. Amber, and Y. Takahashi, “Method of automatic image reconstruction from holograms by a homomorphic system of logarithmic tranform type,” *Electron. Commun. Jpn.* **65** (1), pp. 109–116 (1982).

[Bar98] A. Barty, K. A. Nugent, D. Paganin, and A. Roberts, “Quantitative optical phase microscopy,” *Opt. Lett.* **23** (11), pp. 817–819 (1998).

[Bog63] B. P. Bogert, M. J. R. Healy, and J. W. Tukey, “The quefrency analysis of time series for echoes: Cepstrum, pseudo-autocovariance, cross-cepstrum, and saphe cracking,” in *Proc. Symp. on Time Series Analysis*, Wiley, New York (1963).

[Cai10] X.-O. Cai, "Reduction of speckle noise in the reconstructed image of digital holography," *Optik* **121** (4), pp. 394–399 (2010).

[Cha06] F. Charrière, T. Colomb, F. Montfort, E. Cuche, P. Marquet, and C. Depeursinge, "Shot-noise influence on the reconstructed phase image signal-to-noise ratio in digital holographic microscopy," *Appl. Opt.* **45** (29), pp. 7667–7673 (2006).

[Che07a] G.-L. Chen, C.-Y. Lin, M.-K. Kuo, and C.-C. Chang, "Numerical suppression of zero-order image in digital holography," *Opt. Express* **15** (14), pp. 8851–8856 (2007).

[Che07b] G. Chen, C. Lin, H. Yau, M. Kuo, and C. Chang, "Wavefront reconstruction without twin-image blurring by two arbitrary step digital holograms," *Opt. Express* **15** (18), pp. 11 601–11 607 (2007).

[Chi77] D. Childers, D. Skinner, and R. Kemerait, "The cepstrum: A guide to processing," *P. IEEE* **65** (10), pp. 1428–1443 (1977).

[Coq93] O. Coquoz, C. Depeursinge, R. Conde, and E. d. Haller, "Performance of on-axis holography with a flexible endoscope," in *Holography, Interferometry, and Optical Pattern Recognition in Biomedicine III*, vol. 1889, pp. 216–223, SPIE, Los Angeles, CA (1993).

[Cuc00a] E. Cuche, P. Marquet, and C. Depeursinge, "Aperture apodization using cubic spline interpolation: Application in digital holographic microscopy," *Opt. Commun.* **182** (1–3), pp. 59–69 (2000).

[Cuc00b] E. Cuche, P. Marquet, and C. Depeursinge, "Spatial filtering for zero-order and twin-image elimination in digital off-axis holography," *Appl. Opt.* **39** (23), pp. 4070–4075 (2000).

[Dem03] N. Demoli, J. Mestrovi , and I. Sovi , "Subtraction digital holography," *Appl. Opt.* **42** (5), pp. 798–804 (2003).

[Dub02] F. Dubois, O. Monnom, C. Yourassowsky, and J.-C. Legros, "Border processing in digital holography by extension of the digital hologram and reduction of the higher spatial frequencies," *Appl. Opt.* **41** (14), pp. 2621–2626 (2002).

[Fai99] G. Faigel and M. Tegze, "X-ray holography," *Rep. Prog. Phys.* **62** (3), pp. 355–393 (1999).

[Fie82] J. Fienup, "Phase retrieval algorithms: a comparison," *Appl. Opt.* **21** (15), pp. 2758–2769 (1982).

[Gab48] D. Gabor, "A new microscopic principle," *Nature* **161** (4098), pp. 777–778 (1948).

[Gab49] D. Gabor, "Microscopy by Reconstructed Wave-Fronts," *P. Roy. Soc. Lond. A Mat.* **197** (1051), pp. 454–487 (1949).

[Gar08] E. Garbusi, C. Pruss, and W. Osten, "Single frame interferogram evaluation," *Appl. Opt.* **47** (12), pp. 2046–2052 (2008).

[Goo67] J. Goodman and R. Lawrence, "Digital image formation from electronically detected holograms," *Appl. Phys. Lett.* **11** (3), pp. 77–79 (1967).

[Guo04] P. Guo and A. Devaney, "Digital microscopy using phase-shifting digital holography with two reference waves," *Opt. Lett.* **29** (8), pp. 857–859 (2004).

[HR07] J. Herrera Ramírez and J. Garcia-Sucerquia, "Digital off-axis holography without zero-order diffraction via phase manipulation," *Opt. Commun.* **277** (2), pp. 259–263 (2007).

[Kre97] T. M. Kreis and W. P. O. Jüptner, "Suppression of the dc term in digital holography," *Opt. Eng.* **36** (8), pp. 2357–2360 (1997).

[Kro72a] M. A. Kronrod, N. S. Merzlyakov, and L. P. Yaroslavsky, "Reconstruction of holograms with a computer," *Sov. Phys. Tech. Phys.* **17**, pp. 333–334 (1972).

[Kro72b] M. Kronrod, L. Yaroslavsky, and N. Merzlyakov, "Computer synthesis of transparency holograms," *Sov. Phys. Tech. Phys.* **17**, pp. 329–332 (1972).

[Lei62] E. N. Leith and J. Upatnieks, "Reconstructed wavefronts and communication theory," *J. Opt. Soc. Am.* **52** (10), pp. 1123–1130 (1962).

[Lei64] E. N. Leith and J. Upatnieks, "Wavefront Reconstruction with Diffused Illumination and Three–Dimensional Objects," *J. Opt. Soc. Am.* **54** (11), pp. 1295–1301 (1964).

[Lie04] M. Liebling, T. Blu, and M. Unser, "Complex-wave retrieval from a single off-axis hologram," *J. Opt. Soc. Am. A* **21** (3), pp. 367–377 (2004).

[Liu02] C. Liu, Y. Li, X. Cheng, Z. Liu, F. Bo, and J. Zhu, "Elimination of zero-order diffraction in digital holography," *Opt. Eng.* **41** (10), pp. 2434–2437 (2002).

[Liu09] J.-P. Liu and T.-C. Poon, "Two-step-only quadrature phase-shifting digital holography," *Opt. Lett.* **34** (3), pp. 250–252 (2009).

[Ma09] L. Ma, H. Wang, Y. Li, and H. Zhang, "Elimination of zero-order diffraction and conjugate image in off-axis digital holography," *J. Mod. Optic* **56** (21), pp. 2377–2383 (2009).

[Mon09] D. S. Monaghan, D. P. Kelly, N. Pandey, and B. M. Hennelly, "Twin removal in digital holography using diffuse illumination," *Opt. Lett.* **34** (23), pp. 3610–3612 (2009).

[Opp04] A. Oppenheim and R. Schafer, "From frequency to quefrency: a history of the cepstrum," *IEEE Signal Proc. Mag.* **21** (5), pp. 95–106 (2004).

[Opp68] A. Oppenheim, R. Schafer, and J. Stockham T.G., "Nonlinear filtering of multiplied and convolved signals," *P. IEEE* **56** (8), pp. 1264–1291 (1968).

[Pav09] N. Pavillon, C. S. Seelamantula, J. Kühn, M. Unser, and C. Depeursinge, "Suppression of the zero-order term in off-axis digital holography through nonlinear filtering," *Appl. Opt.* **48** (34), H186–H195 (2009).

[Pav10a] N. Pavillon, C. S. Seelamantula, M. Unser, and C. Depeursinge, "Artifact-free reconstruction from off-axis digital holograms through nonlinear filtering," in *Optics, Photonics, and Digital Technologies for Multimedia Applications*, vol. 7723, 77231U, Brussels, Belgium (2010).

[Pav10b] N. Pavillon, C. Arfire, I. Bergoënd, and C. Depeursinge, "Iterative method for zero-order suppression in off-axis digital holography," *Opt. Express* **18** (15), pp. 15 318–15 331 (2010).

[Pic08] P. Picart and J. Leval, "General theoretical formulation of image formation in digital Fresnel holography," *J. Opt. Soc. Am. A* **25** (7), pp. 1744–1761 (2008).

[Sal91] B. E. A. Saleh and M. C. Teich, "Wave Optics," in *Fundamentals of Photonics*, 1st ed., John Wiley & Sons, Inc. (1991), pp. 41–79.

[Sch94] U. Schnars and W. P. O. Jüptner, "Direct recording of holograms by a CCD target and numerical reconstruction," *Appl. Opt.* **33** (2), pp. 179–181 (1994).

[See08] C. S. Seelamantula, M. Villiger, R. Leitgeb, and M. Unser, "Exact and efficient signal reconstruction in frequency-domain optical-coherence tomography," *J. Opt. Soc. Am. A* **25** (7), pp. 1762–1771 (2008).

[See09] C. S. Seelamantula, N. Pavillon, C. Depeursinge, and M. Unser, "Zero-order-free image reconstruction in digital holographic microscopy," in *IEEE International Symposium on Biomedical Imaging: From Nano to Macro (ISBI '09)*, pp. 201–204, Boston, MA (2009).

[See11] C. S. Seelamantula, N. Pavillon, C. Depeursinge, and M. Unser, "Exact Complex-Wave Reconstruction in Digital Holography," *J. Opt. Soc. Am. A* **28** (6), pp. 983–992 (2011).

[Sri10] R. Srivastava, J. Gupta, and H. Parthasarthy, "Comparison of PDE based and other techniques for speckle reduction from digitally reconstructed holographic images," *Opt. Laser Eng.* **48** (5), pp. 626–635 (2010).

[Tak82] M. Takeda, H. Ina, and S. Kobayashi, "Fourier-transform method of fringe-pattern analysis for computer-based topography and interferometry," *J. Opt. Soc. Am.* **72** (1), pp. 156–160 (1982).

[Tak99] Y. Takaki, H. Kawai, and H. Ohzu, "Hybrid holographic microscopy free of conjugate and zero–order images," *Appl. Opt.* **38** (23), pp. 4990–4996 (1999).

[Tit03] V. Titar and O. Shpachenko, "Cepstrum analysis in holographic information systems," in *Proceedings of Laser and Fiber-Optical Networks Modeling (LFNM)*, pp. 137–139 (2003).

[Wen08] J. Weng, J. Zhong, and C. Hu, "Digital reconstruction based on angular spectrum diffraction with the ridge of wavelet transform in holographic phase-contrast microscopy," *Opt. Express* **16** (26), pp. 21 971–21 981 (2008).

[Wya92] J. C. Wyant and K. Creath, "Advances in interferometric optical profiling," *Int. J. Mach. Tool. D. R.* **32** (1-2), pp. 5–10 (1992).

[Yam97] I. Yamaguchi and T. Zhang, "Phase-shifting digital holography," *Opt. Lett.* **22** (16), pp. 1268–1270 (1997).

[Zha04a] Y. Zhang, Q. Lü, and B. Ge, "Elimination of zero-order diffraction in digital off-axis holography," *Opt. Commun.* **240** (4-6), pp. 261–267 (2004).

[Zha04b] Y. Zhang, G. Pedrini, W. Osten, and H. Tiziani, "Reconstruction of in-line digital holograms from two intensity measurements," *Opt. Lett.* **29** (15), pp. 1787–1789 (2004).

4 Quantitative phase tomography

Three-dimensional imaging based on coherent imaging has been studied during the last decades, and has recently been demonstrated as a new way of recovering depth-resolved images in the context of microscopy. This approach for recovering tomographic images is rather different from most methods developed in microscopy to recover three-dimensional information. While most techniques are based on sectioning, i.e. resolving the optical axis dimension through point-like detection combined with scanning procedures, coherent tomography relies on full-field acquisition, where the measurements are then recombined through computation in order to retrieve the 3D image, or tomogram. This acquisition approach presents the interesting feature of requiring scanning in less dimensions than the retrieved information, so that a three-dimensional reconstructions typically requires a two-dimensional scan, or even a one-dimensional scan in a 2D space.

Furthermore, the fact of employing tomographic reconstruction with coherent imaging brings the advantage of combining quantitative phase measurement and three-dimensional imaging. This approach is able to solve one of the main drawbacks of phase measurement in transmission, where an ambiguity between the refractive index distribution and the object height is present, as discussed in more details in section 5.1.5. Furthermore, it enables the recovery of quantitative three-dimensional information, where the phase measurement resolved along the optical axis makes it possible to reconstruct a 3D map of the refractive index of the measured sample.

While the ground principles for coherent tomography were proposed in the seventies, their use for experimental configurations enabling reliable measurements and high quality images within microscopy applications have been hindered by several issues involving for example practical problems in the precision of scanning procedures or the development of accurate inversion algorithms. While most approaches are based on a scanning using a rotation, in accordance with the fundamental principles relying on angular views, we investigate in this chapter another data acquisition procedure, based on a linear scanning of the object.

In this chapter, we first review the state of the art about coherent tomography in section 4.1, focused specially on the different experimental approaches. We then briefly present the main motivation for this work in section 4.2, before presenting the fundamentals of coherent tomography principle in section 4.3. We then describe the approach of linear scanning investigated in our work in section 4.4, and highlight the main difference with usual methods, before presenting in section 4.5 preliminary experimental results obtained with this approach. Finally, we discuss some perspectives brought by this method and present the various potential improvements which could be performed following our preliminary results in section 4.6.

4.1 State of the art

Three-dimensional imaging is a very general problem which has been addressed in many various fields and applications. We present here a brief state of the art for tomographic microscopy based on coherent imaging. We also shortly mention other widely known techniques, essentially in order to situate our main application field in the context of the more general developments for microscopy.

The theoretical foundations for tomography based on coherent imaging were proposed at the end of the sixties by Wolf and then Dändliker *et al.* [Wol69; Dän70]. These seminal publications stated the relations between multiple frames acquired in various conditions—such as different illumination angles or different monochromatic wavelengths—and the information they provide on the three-dimensional volume, based on a diffraction formalism. In order to enable an analytical representation of the problem, one has to resort to an approximation of diffraction at first order, chosen either as the Born or as the Rytov approximations, as described for example in [Bor99]. The general concepts defined in these articles already laid the foundations of most of the methods employed in more recent works, such as the Fourier approach for frame combination, tightly linked with 3D coherent transfer function (CTF) formalism.

The problem of resolving the integrated information along the optical axis in microscopy has been addressed in many various ways in the last decades, both through a deeper understanding of the theoretical models governing the imaging conditions in microscopy, and through different implementations enabling sectioning along the optical axis. One of the most widely known method enabling sectioning is confocal microscopy, where the out-of-focus information is discarded before acquisition [Paw06]. This method has been widely described theoretically, pushing towards a generalised theory about three-dimensional optical transfer functions (OTF) in microscopy [Gu92], and extensively employed experimentally, yielding a mature technology presently sold as “turn-the-key” products. Optical sectioning could also be performed through structured illumination, where two interfering beams in the object or image plane discard the out-of-focus information through constructive/destructive interference, which has been applied to both confocal (4Pi [Hel92; Bah01]) and full-field (I^3M [Gus99]) configurations. While these methods enable 3D imaging in microscopy, they rely on

principles of optical sectioning which are not directly related to the approach described in this thesis. The sectioning typically requires the detection of a small 3D volume coupled with scanning procedures to recover the 3D information, with typically intensity-based detection.

Another widely known approach is the optical coherence tomography (OCT). As its name indicates, it is based on coherence properties of the light source with an interferometric detection scheme, and is thus close in its principle to the methods developed in this chapter. OCT methods are based typically on reflection measurements, and rely on the spectral bandwidth of coherent light to generate an optical sectioning effect [Sch99]. The method is however usually employed with rather small numerical apertures, as increasing the NA reduces greatly the depth of focus and thus the z detection range. This imaging method found numerous applications, such as in dermatology or ophthalmology [Fuj03], and can typically be described with a formalism similar to the one proposed for coherent three-dimensional imaging: the fact of employing a broadband source corresponds indeed to changing the wavelength—or k-vector norm—as proposed initially by Dändliker [Dän70]. A more straightforward link between this formalism and the detection method can be found with measurements based on full-field coherent imaging through DHM, where frames recorded at different wavelengths are combined to recover a sectioning effect based on computation [Kim00; Mon06; Küh09]. These two methods are however equivalent in terms of sectioning principle, in the sense that the latter discretely scans different wavelengths and recombines them numerically, while Fourier OCT is based on a physical spread of frequencies, then analysed with a spectrometer.

Even in the small field of coherent tomography, a multitude of methods and approaches have been developed. The first reconstruction methods proposed for practical applications were based on computer tomography (CT)—commonly called straight ray tomography—thus neglecting diffraction [Kak79]. The use of this type of algorithm was justified by their extensive use for CT applications, and reduced computational requirements, thanks to spatial algorithms such as the inverse Radon transform. A spatial approach for diffraction tomography has also been proposed rapidly [Dev82], although only 2D implementations for diffraction were proposed. However, these implementations are rather demanding in computational power, so that reconstructions taking into account diffraction are mainly based on Fourier mapping techniques. The development of fast and reliable algorithm for tomographic inversion taking into account tomography has been the subject of numerous publications since then, such as to estimate the validity of first order diffraction approximations [Che98; Gbu01], defining general resolution limitations in diffraction tomography [Sla84; Wed95b], or estimating the effect of a partial angular coverage [Tam81]. The experimental configuration for microscopy can also take several forms, in particular in regards to the scanning strategy. The two main approaches consist in either rotating the object, or to scan the beam around the object. These two methods were explored in various studies, and lead to different reconstruction approach and resolution, as discussed in subsection 4.3.3.

A first attempt to relate 3D coherent imaging with microscopy imaging models can be attributed to Streibl [Str85], where partially coherent light is considered. The first experimental

realisation of tomographic imaging in the context of microscopy with angular views can then be attributed to our knowledge to Kawata *et al.*, based on intensity measurements from an incoherent source [Kaw87] or a laser [Kaw90], where a treatment of the OTF is employed to retrieve the desired information, similar to [Str85]. Various implementations of this approach were then proposed with annular illumination [Nod90] and beam scanning [Nod92]. These results were followed by the first 3D refractive index distribution obtained with angular view methods, where the refractive index of a fibre could be measured with diffraction inversion algorithms [Wed96]. These results were based on intensity measurements combined with phase retrieval methods. Lauer then employed a beam scanning approach in the first tomographic reconstruction with full complex field reconstruction, by employing a Fourier holography detection scheme [Lau02], where a full description of the imaging properties of the tilted illumination in a diffraction formalism is provided.

These works were then followed by various applications, where the applicability of the tomographic approach could be validated with various phase recovery methods. Barty *et al.* applied TIE equations to non-diffractive tomographic measurements with object rotation to measure the refractive index (RI) distribution of an optical fibre [Bar00; Dra08]. Similar results were obtained with phase measured by digital holography [Gor06; Gor07]. A similar approach of object rotation also enabled the reconstruction of the 3D RI of non-cylindrically symmetrical object such as pollen grain [Cha06a] and amoebas [Cha06b]. The results could also be reproduced with a common-path interferometer with phase-shifting holography [MF06], although the reconstruction was however done in amplitude, as no phase could be recovered with this setup. All these experiments demonstrated the capability of recovering quantitative data through tomographic measurements in various configurations. However, they were globally performed with low NA, and were limited in resolution by the use of non-diffractive inversion algorithms. An interesting application, performed with intensity images, was shown at the same time by Fauver *et al.*, where the projections were averaged by moving rapidly the object along the optical axis, apparently improving the 3D resolution with projection-based inversion [Fau05].

Measurements with high NA and quantitative phase recovered by phase-shifting were then demonstrated by Choi *et al.* with a beam-scanning approach, also with non-diffractive inversion [Cho07]. The use of diffraction tomography was then shown with a similar setup [Deb08; Sun09]. Most of the recent work then published with this approach relate to improving the acquisition speed by employing faster detectors and off-axis holography [FY11], or analysing the resolution of the tomogram, in regards to synthetic aperture methods [Deb09]. An approach of beam-scanning, based on averaging the data in a single frame, was proposed by Fiolka *et al.* with annular illumination [Fio09].

In parallel to the various experimental results presented above, tomographic reconstruction based on coherent imaging has been studied in more details on a theoretical point of view. The CTF obtained respectively for object rotation method—denoted as an “apple core” [Ver09]—and for the beam scanning approach—denoted as a “peanut” [Kou08]—have been

analysed in details numerically. Furthermore, it could be demonstrated that the three-dimensional CTF obtained in the case of high NA measurements presents a spectral extension in the direction of the optical axis at the origin of the spectrum, demonstrating the sectioning capability of this approach [Kou09]. One should note that several articles are recently proposing methods to refine the reconstruction quality, such as describing inversion methods for spherical illumination waves in the paraxial case [Ana05], or to employ iterative algorithms to account for higher orders of diffraction during inversion [Mai10].

Acquisition type	Incoherent		Coherent	
	Z-stacks	Phase retrieval	Interferometry	
Scanning method	Object rotation		Beam scanning	
Typical range	$0-180°$		NA of the excitation MO	
Scanning type	Perpendicular to optical axis		Linear	Annular
Inversion domain	Spatial		Fourier	
Main limitation	Computation time		Accuracy of mapping	
Inversion method	Projections		Diffraction	
Typical limitation	Diffraction		Approximation used	
in resolution	of light		Born	Rytov

Table 4.1: Review of the various approaches for tomographic measurement with coherent imaging.

As it can been seen from the state of the art presented above, a large variety of approaches can be chosen for performing tomographic measurements based on coherent imaging or phase detection, that we summarise very briefly in Table 4.1. The first distinctive element is the signal measured and the detection method, which can be either coherent in order to detect the complex field, or based on other methods such as phase-retrieval from intensity signals when only phase is employed as in back-projection algorithms. In particular, methods based on pure intensity measurements were also developed for diffraction tomographic inversion [Gbu02]. The main approaches then consist in either object rotation or beam scanning for acquisition, and projection-based or diffraction-based model for tomographic inversion, which can be indiscriminately combined. Then, the computation can be performed either in the spatial domain, such as inverse Radon transform, or direct Fourier inversion. While most of recent developments presented in this section can be classified within these characteristics, the various combination presented in Table 4.1 demonstrate the vast diversity of possibilities and explain the difficulty of providing of global picture of this specialised field.

In this context, the work presented in this chapter consists in proposing another approach for scanning, based on a linear scanning instead of rotations, where the various angular illuminations are provided by a convergent beam. Then, in order to provide a proof of principle of the reconstruction capability with this approach, we employ a Fourier implementation for inversion, based on a non-diffractive model.

4.2 Motivation

The work presented in this chapter has been motivated by previous works on quantitative tomography, where promising results have been obtained through an approach based on object rotation. These measurements enabled the reconstruction of the three-dimensional RI distribution of pollens [Cha06a] and of amoebas [Cha06b]. Typical results obtained in this fashion are shown in Fig. 4.1, where RI intervals were colour-coded in a transparency view, showing various features, such as the amoeba itself (yellow) contained with its shell (blue), with vacuoles within the dense part (green). These measurements were mainly performed with low numerical apertures, as the rotation of the object requires rather long working distances for the collection system. Furthermore, it could be identified that the main limitation in resolution was induced by positioning errors during rotation, which generate artefacts during reconstruction.

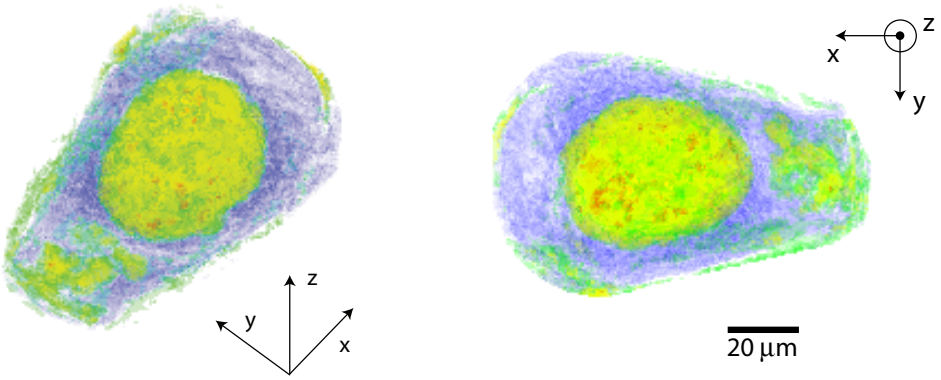

(a) (b)

Figure 4.1: Transparency view of a tomographic measurement of a tek amoeba, in (a) angular view and (b) x-y projection. Colours correspond to refractive index value range: Blue: 1.448-1.467, Green: 1.474-1.478, Yellow: 1.478-1.493, Red: 1.493-1.513. The gap non represented corresponds to the refractive index of the immersion medium.

On the other hand, various results were reported in the last years by employing beam scanning approaches, where a plane wave scanned through various angles of incidence is used to illuminate the specimen. This approach led coherent tomography to higher NA for microscopy, by suppressing the need for object rotation, and thus enabling the use of far shorter working distances. While this method is similar to object rotation —varying the angle of light excitation during measurement— in the concept of data acquisition, it could be shown that these different scanning methods lead to different 3D resolutions (cf. subsection 4.3.3). The beam scanning approach however requires long and precise calibration procedures which can lead to reconstruction artefacts when not handled properly. As it is based on changing the illumination pattern during the acquisition, it indeed varies the imaging conditions between the

different frames, so that it is necessary to compensate for these changes at post-processing level in order to enable the coherent addition of the retrieved information.

The fundamental idea underlying the work presented in this chapter was thus to propose a new data acquisition method, which avoids object rotation in order to enable measurement with high-NA objectives, while ensuring a fixed illumination pattern, in order to ease the calibration procedures. We employ thus in this context convergent beams, which provide a distribution of propagation vectors within the field of view, to enable recovering the information from various angular views, by then performing the acquisition while moving the specimen in the illumination pattern.

4.3 Optical tomography

We present in this section the fundamental principles and theoretical concepts required for tomographic imaging under coherent illumination. As already stated before, this measurement approach is rather different from usual methods for three-dimensional recovery of information, as it relies on full-field acquisition, without any sectioning along the optical axis during acquisition. This capability is made possible through the coherent detection, which possesses imaging properties which are different from standard intensity measurements, thus making possible to retrieve the volume information at computation stage.

4.3.1 Tomography principle

The principle of tomographic imaging through coherent detection is attributed originally to Wolf [Wol69], who proposed a theoretical framework for coherent detection from holography in order to retrieve the 3D information, and to Dändliker *et al.* [Dän70], who expressed the problem with an approach based on frequency by detailing the experimental possibilities offered by the theorem.

As shown schematically in Fig. 4.2(a), the measurement principle simply consists in a plane wave propagating through the specimen, with the scattered wave measured in the far-field on an infinite plane. The measurement process is then repeated for different directions of $\boldsymbol{k}_0$, in order to retrieve various angular views of the specimen. The main interest of this method lies in the fact that the measurement is made for coherent fields, so that the relation between the scattered field and the complex RI distribution of the specimen is linear. In the case the complex wave field is measured, the Fourier transform of the measured signal corresponds to the coherent transfer function (CTF) of the field, which can be coherently added with different CTFs, as shown in Fig. 4.2(b), where the addition of different angular distributions generates a distribution of spatial frequencies also in the direction of the optical axis, thus synthetically providing an optical sectioning effect.

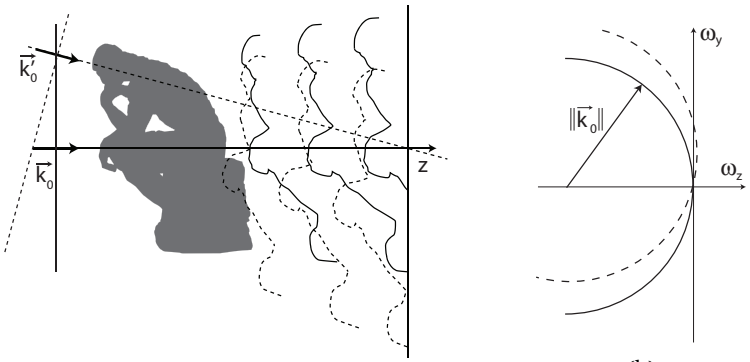

(a) (b)

Figure 4.2: Fundamental measurement scheme of coherence tomography, shown here in 2D. (a) Illumination at various angles with measurement of the scattered wave. (b) Corresponding spatial frequencies for an angular view, situated on half a circle.

4.3.2 Fourier slice theorem

The capability of retrieving the 3D information of a specimen through the measurement of a transmitted wave can be demonstrated through mathematical theorems which relate the measurement in 2D to the 3D distribution within the specimen. We present here the case of the Fourier slice theorem (FST), which neglects diffraction. It can be expressed as:

The one-dimensional Fourier transform of a parallel projection $U_\alpha(t)$ of an object $O(x,y)$ taken at an angle α corresponds to a slice of the two-dimensional Fourier transform of the object, subtending an angle α with the ω_x axis.

$$\mathscr{F}\{U_\alpha(t)\}(\omega_t) = \mathscr{F}\left\{O(x,y)\right\}(\omega_x \cos\alpha, \omega_y \sin\alpha) \tag{4.1}$$

where the theorem is here considered for the 2D case, as the generalisation can be straightforwardly done by separability. The FST is graphically represented in Fig. 4.3(a), where the projection of straight rays is measured for various angles, which correspond to a line in the Fourier domain, as shown in Fig. 4.3(b). The FST can be demonstrated by first considering the definition of the Fourier transform of the object function

$$\hat{O}(\omega_x,\omega_y) = \iint_{-\infty}^{\infty} O(x,y) e^{-\mathrm{i}2\pi(\omega_x x+\omega_y y)} \mathrm{d}x\mathrm{d}y. \tag{4.2}$$

Identically, the Fourier transform of the measured projection can be defined as

$$\hat{U}_\alpha(\omega_t) = \int_{-\infty}^{\infty} U_\alpha(t) e^{-\mathrm{i}2\pi\omega_t t} \mathrm{d}t, \tag{4.3}$$

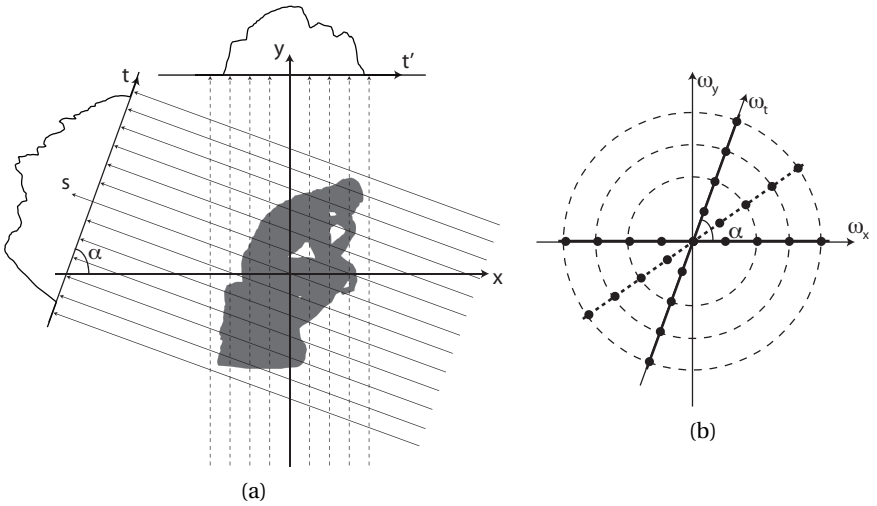

Figure 4.3: Graphical representation of the Fourier slice theorem. (a) Projections at various angular illuminations are measured, corresponding to (b) lines in the Fourier domain. Black dots represent the sampling of a discrete detector.

where variables are chosen accordingly to the definition given in Fig. 4.3, which can be expressed as

$$\begin{pmatrix} t \\ s \end{pmatrix} = \begin{pmatrix} \cos\alpha & \sin\alpha \\ -\sin\alpha & \cos\alpha \end{pmatrix} \begin{pmatrix} x \\ y \end{pmatrix}. \tag{4.4}$$

In this referential, the projection along the object can be defined as

$$U_\alpha(t) = \int_{-\infty}^{\infty} O(t,s)\mathrm{d}s. \tag{4.5}$$

Then, by substituting Eq. (4.5) into Eq. (4.3), and employing the variable change of Eq. (4.4), the Fourier transform of the projection becomes

$$\begin{aligned} \hat{U}_\alpha(t)(\omega_t) &= \int_{-\infty}^{\infty} \left[\int_{\infty}^{\infty} O(t,s)\mathrm{d}s \right] e^{-\mathrm{i}2\pi\omega_t t}\mathrm{d}t, \\ &= \iint_{-\infty}^{\infty} O(x,y) e^{-\mathrm{i}2\pi\omega_t(x\cos\alpha + y\sin\alpha)}\mathrm{d}x\mathrm{d}y, \end{aligned} \tag{4.6}$$

where one can identify the Fourier transform expressed in Eq. (4.2), so that Eq. (4.6) becomes

$$\hat{U}_\alpha(\omega_t) = \hat{O}(\omega_t\cos\alpha, \omega_t\sin\alpha), \tag{4.7}$$

which demonstrates that the Fourier transform of a projection corresponds to a line of the 2D Fourier transform of the original object. The spectral correspondence of the FST is shown in Fig. 4.3, where one can see the line of spatial frequencies corresponding to the measurement of the projection of Fig. 4.3(b). The measurement performed under the FST thus corresponds

to multiple acquisitions of projections under various angles, which can be typically taken over the domain $[0,\pi]$ for a complete data set. The stack at this stage is commonly called a sinogram, due to the typical sinusoidal trace of a single point [Kak87].

One can see that the FST is usually expressed for real numbers, as expressed by the variables in capitals. It indeed corresponds only to a mathematical theorem, which does not take into account a physical model. It is thus valid for pure projections without considering diffraction, and is used typically with X-rays such as in CT scanners [Kak87]. Although the theorem can be identically demonstrated for complex numbers such as fields, it only provides approximate solutions for optical wavelengths. A more complete theorem, commonly denoted as the Fourier diffraction theorem (FDT), is required in order to take into account diffraction of light. A complete derivation of the FDT is provided in appendix C, showing that the spatial frequencies measured in the same fashion as in the FST lie in a circle instead of a line when taking diffraction into account, as shown in Fig. 4.2(b). The FDT however provides also only an approximate solution, as only diffraction at first order is considered, so that the validity of this model for accurate tomographic inversion of fields having interacted with biological specimens is still under debate. One can finally note that the FST can be considered as a particular case of the FDT, as the radius of the circle on which spatial frequencies are situated for one measurement has a radius $k = 2\pi/\lambda$ (cf. Fig. 4.2(b)), so that the FST corresponds to a case where $\lambda \to 0$, for which no diffraction occurs.

In this chapter, although we employed mainly the FST during computation for reasons detailed in section 4.4, we will in the rest of this section employ the results of the FDT when describing the various steps required for tomographic measurements and inversion, due to its better adequacy with physical models.

Fan beam excitation

As stated before, the theorems employed for tomographic inversion are based on plane wave excitation beams, thus imposing restrictive conditions for the potential applications. Various works were thus developed in order to enable the use of for example point-sources. In the context of the FST, this leads to the so-called fan beam algorithms, based on projections measured with diverging rays [Kak87], as shown in Fig. 4.7(a). One should note that these algorithms however do not generalise the FST for use with more complicated profiles than plane waves, but instead propose methods to rearrange the measured data, in order to retrieve from a fan beam excitation the projections which would have been measured with parallel rays. These algorithms thus require a larger angular range in order to enable this preliminary step of arranging data to parallel rays before employing standard inversion algorithms such as the inverse Radon transform. As these methods are based on an arrangement of the measured data, they can only be applied to methods based on the FST, for which the value on one pixel is independent from adjacent values.

4.3.3 Data acquisition strategies

As already discussed briefly previously, various scanning approaches can be employed in order to acquire the different angular views required to fill the 3D spatial frequency space in the context of microscopy, and can mainly be divided in two scanning procedures, as shown in Table 4.1. The two methods however are based on common principles, consisting in illuminating the specimen with plane waves having different directions of propagation vectors.

The first method is based on rotating the object such as performed in various experiments described in section 4.1, or identically rotating the illumination source around the object, as typically performed in CT scanners. This configuration is shown schematically in Fig. 4.4(a), with its corresponding spatial frequency filling presented in 4.4(b), for a rotation along the y axis, and under the FDT formalism. This scanning scheme is characterised by a rather isotropic synthesised 3D CTF thanks to the possibility of rotating the object along the whole 2π angular range, with typically a missing cone along the direction of rotation, which was coined as a "missing apple core" [Ver09] in literature, as shown in Fig. 4.4(c). Although the retrieved spatial frequencies are well distributed within the 3D frequency space, this approach suffers from different technical issues. As stated before, the rotation of the object is rather difficult to accomplish precisely, so that the mechanical imprecision during scanning yields a degraded reconstruction. Furthermore, the requirements in space are rather high, so that this approach can only be performed with long working distance MO, thus implying low NA and consequently lower resolution.

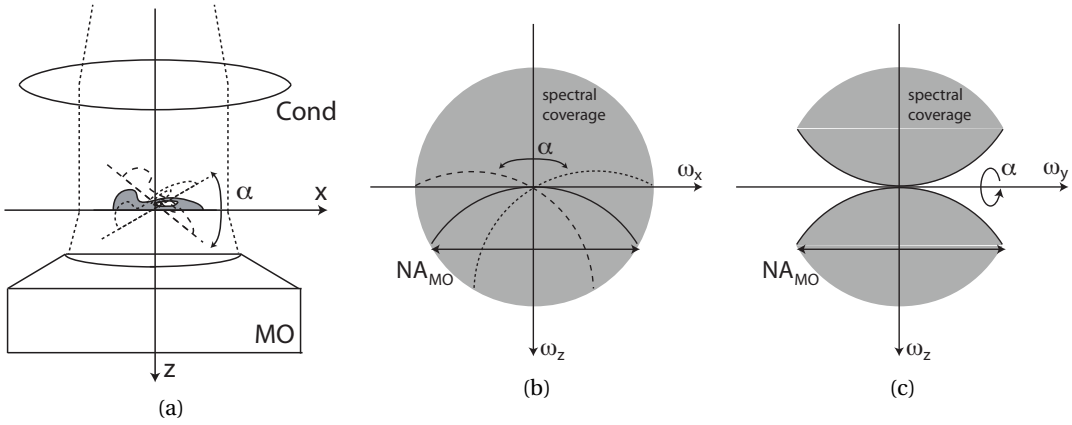

Figure 4.4: (a) Tomographic acquisition through object rotation, with (b–c) the corresponding frequency space filling shown by 2D projections perpendicular to (b) the ω_y axis and (c) the ω_x axis.

On the other hand, the second common scanning strategy consists in scanning the beam through optical means. This is typically performed by scanning the back focal plane of a lens, as depicted in Fig. 4.5(a). In this fashion, the accessible angular views are limited by the NA of the condenser lens, thus yielding a less efficient filling of the frequency space. Furthermore, this scanning scheme implies that the detection optics, classically taken as a microscope ob-

jective, is static while the excitation beam is changing. This implies that the CTF is not rotated, so that the frequencies of each angular view are shifted, as shown in Fig. 4.5(b), leading to a 3D synthesised CTF in the shape of a "peanut", as denoted in the literature [Kou08]. Although being less efficient in the recovery of spatial frequencies in an isotropic way, the beam scanning approach generally leads to better results than object rotation in terms of resolution, due to its better stability during scanning thanks to a static object.

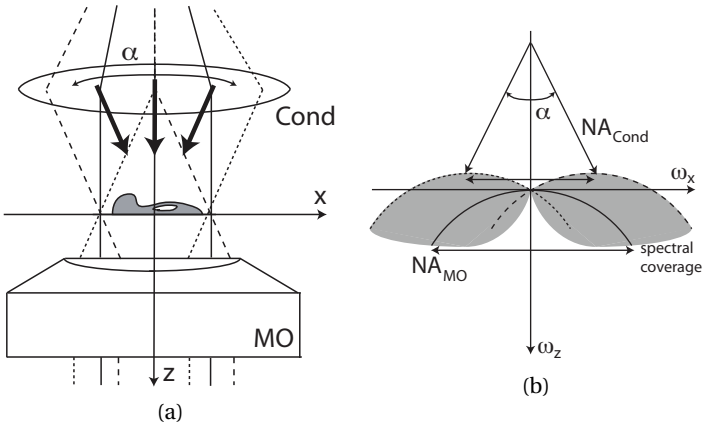

Figure 4.5: (a) Tomographic acquisition through beam scanning, with (b) the corresponding frequency space filling shown in 2D projection, where the CTF is cylindrically symmetric around ω_z.

4.3.4 Reconstruction methods

The FST and FDT theorems provide an equivalence between the spatial frequencies of respectively the measured projection or field outside the object and spatial frequencies of the object itself, thus enabling to fill the Fourier space with multiple angular views, before recovering the spatial information of the object through inverse Fourier transform. One can intuitively understand that the resolution and accuracy of the reconstruction thus depends essentially of the sampling capabilities of the measurement system, and on the amount of angular views. In particular, the data set becomes sparser for higher spatial frequencies, so that the angular sampling capability becomes a key factor in order to retrieve sufficient information to correctly recover fine details of the object. Indeed, by considering Eq. (4.1), one can see that the problem of tomographic inversion mainly lies in a mapping of spatial frequencies equally distributed in a cylindrical space $(\omega_r, \omega_\alpha)$ to a Cartesian reciprocal space (ω_x, ω_y). This implies that the sampling of discrete measurements is highly non-evenly distributed, with an overrepresentation of low frequencies, and potentially sparse information at high frequencies, as shown schematically in Fig. 4.2(b), where numerous lines are represented.

While the FST and FDT theorems provide a relation in the Fourier domain, implementations in the spatial domain proved to be very efficient to reconstruct data. In the case of the FST,

the so-called inverse Radon transform enables direct inversion through the formula [Kak87]

$$\begin{aligned} O(x,y) &= \int_0^{\pi} Q_\alpha(x\cos\alpha, y\sin\alpha)\mathrm{d}\alpha, \\ Q_\alpha(t) &= \int_{-\infty}^{\infty} \hat{U}_\alpha(\omega_t)|\omega_t| e^{\mathrm{i}2\pi\omega_t t}\mathrm{d}\omega_t, \end{aligned} \tag{4.8}$$

where Q_α is called a filtered projection, due to the term $|\omega_t|$ resulting from the cylindrical variable change employed during derivation. This inversion method is commonly denoted as filtered back-projection (FBP) because of this term, which corresponds to a high-pass filter. This can be interpreted as a compensation for the over-representation of low frequencies in the data set because of the cylindrical to Cartesian mapping implied by the FST. Similarly, spatial implementations of the tomographic inversion for the FDT has also been proposed [Dev82], also based on a filtering function of the measured data before transferring it on the Cartesian space, which have been called by analogy filtered back-propagation algorithms. These algorithms are however modelling diffraction only in 2D, so that alternate solutions have to be employed to extend this inversion approach to 3D, such as slice by slice combination. Furthermore, their computation time is rather high, limiting their advantage when compared to the inverse Radon transform.

Generally, spatial methods have been preferred, especially in cases where diffraction is not taken into account. This is due to the easy discretisation and implementation of Eq. (4.8), which provides a direct inversion of the data set. On the other hand, Fourier methods require specific care in their implementation, in order to avoid numerical artefacts which can occur due to discretisation errors during mapping of frequencies measured in a cylindrical basis to the Cartesian basis used for inversion. It could nevertheless be demonstrated that Fourier approaches can lead to similar reconstruction qualities as spatial methods when interpolation is employed, through for example the padding of data before Fourier transforms [Pan83].

More recently, Fourier methods have been essentially employed for results recovered in the context of microscopy. This is due essentially to the long computation time of spatial implementations including diffraction, and to their lack of flexibility. Spatial derivations require indeed the incorporation of the acquisition model within the derivation of analytical formulas, which typically do not cover the case of beam scanning, where a frequency shift of the measured scattered fields is induced. Furthermore, spatial inversions such as the inverse Radon transform require constant angular sampling in the data set, which is not always the case with acquisitions performed in microscopy applications. The Fourier methods enable in this context the possibility of incorporating directly the specific imaging conditions during mapping, and make possible to employ straightforwardly data sets with non-equally sampled measurements.

4.3.5 Application of tomographic inversion on microscopy

When applied to microscopy, theorems such as the FST and the FDT suffer from a very simplistic model, as the imaging system is not taken into account. In the case of the FST, this can be clearly seen from the fact that the theorem simply states a geometrical equivalence, where no physical model is taken into consideration. On the other hand, the FDT considers the field scattered from an object, measured on an infinite plane situated at a fixed distance, thus corresponding to a measurement in the far-field, without any imaging system. This model is in contradiction with the measurement approach employed when applying this tomographic reconstruction to microscopy, where microscope objectives typically limit the accessible spatial frequencies by their numerical aperture, and induce strong changes of the field curvature, which is not considered in the fundamentals of the FDT. The fact of measuring an object in focus thanks to an imaging system can thus be considered as making the reconstruction of the image of the object, and not of the object as described in the FDT, implying that the magnification and the NA of the MO must be taken into account during reconstruction.

In this context, the fact of employing an imaging system to measure the transmitted field is of particular importance when considering a model based on the FST which neglects diffraction that is partly compensated by the imaging system which ensures in-focus measurement, so that back-propagation is performed physically. The concept of "hybrid" filtered back-projection was thus proposed, where inverse diffraction is employed before tomographic inversion, showing that results with FBP and filtered back-propagation are similar in this case, as the inverse diffraction accounts for most of the effects of diffraction [Wed95a]. The case of high NA imaging systems was not analysed in literature, but one can hypothesise that the performance of the hybrid FBP method is comparable to the propagation case within the depth of focus of the imaging system, where sharp details can be recovered thanks to the in-focus measurement.

4.4 Linear scanning tomography

We present in this section the acquisition principle and consequent reconstruction developed in our work, which aims at avoiding any movement of the illuminating beam and any rotation of the object, in order to try to improve mechanical stability during scanning. The data acquisition approach is thus based on a spherical convergent beam spread in the field of view, thus providing the propagating vectors at different angles, while scanning is performed by moving the object in the $x-y$ plane. As it will be shown in the following sections, these slight differences compared to usual methods imply a rather different treatment for reconstruction.

4.4.1 Data acquisition approach

The data acquisition is based on a convergent wave in the field of view, typically generated by employing a high NA condenser lens. The object is then scanned in the field of view through a

translation in the $x-y$ plane, enabling measurement with the object in various positions, corresponding to different propagation directions of the incoming beam, as shown in Fig. 4.6. As this approach is based on generating an angular distribution through the use of a condenser lens, on can readily see that the 3D CTF is similar to the beam scanning case (cf. Fig 4.5(b), as the resolution along the optical axis is essentially limited by the NA of the illumination.

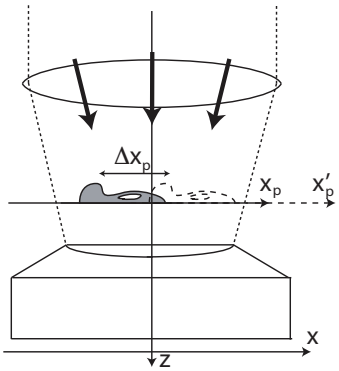

Figure 4.6: Tomographic acquisition under a convergent beam, where the object is linearly scanned in the $x-y$ plane in the x_p, y_p referential.

Furthermore, the proposed approach may be seen as being slightly similar to the fan beam configuration. However, in the case of the linear scanning, the distance between the point source and the object changes depending on the angle, which implies some discrepancy in the data acquired between the two configurations, especially at large angles of incidence. This difference is illustrated in Fig. 4.7, where the acquisition under fan beam is shown in Fig. 4.7(a), under the perspective of a fixed source, where the object moves on a circle, while the linear scanning principle is shown in Fig. 4.7(b), where the object is displaced on a line, thus breaking the cylindrical symmetry. For this reason, the two acquisition methods provide different data sets, so that the reconstruction are not identical. Furthermore, as discussed in subsection 4.3.2, the reconstruction based on a fan beam excitation relies on reordering the data in order to retrieve a sinogram as if it had been acquired with parallel rays. This typically requires a scanning range over a domain larger than π [Kak87], so that it is not directly suitable for an acquisition performed in microscopy, where the angular range is limited by the NA of the condenser lens.

4.4.2 Tomographic inversion method

In order to invert the data measured with this method, we employ an approach similar to the one used for fan beam inversion, where we first arrange the data to enable the use of reconstruction algorithms based on the FST through Fourier mapping methods, but without requiring a full angular coverage. In the proof of principle presented in this chapter, the reconstruction does thus not take into account diffraction, as arrangement methods require independent value on pixels. We present below the various steps employed for reconstruct-

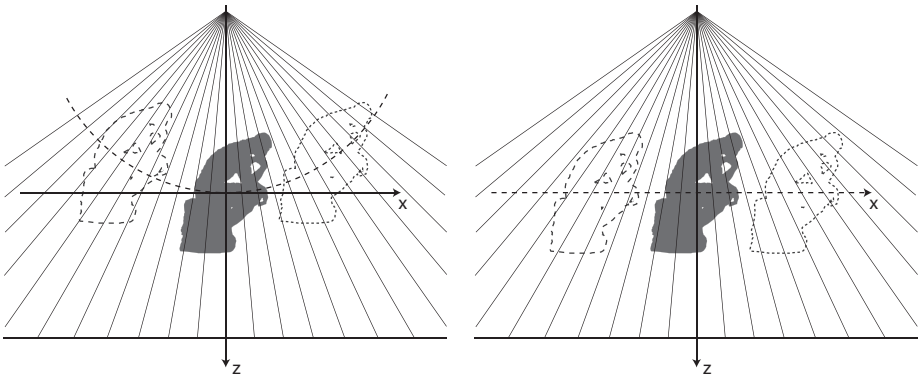

(a) (b)

Figure 4.7: (a) Fan beam configuration in the referential of the source, where the object moves on a circle. (b) Linear scanning, where the object moves on a line.

ing the tomogram, which are illustrated by simulated signals shown for the different stages, while the whole procedure is summarised in the algorithm 4.

The fact of employing DHM for acquisition implies that the hologram must first be reconstructed to retrieve the quantitative phase image transmitted through the specimen. The phase of the recovered raw wavefront is represented in Fig. 4.8(a), where a strong curvature can be identified due to the excitation profile. This reconstruction step enables to compensate for the wavefront curvature induced during acquisition, and thus to suppress aberrations before tomographic inversion, as shown in Fig. 4.8(b). As the curvature can be rather important depending on the NA of the condenser, the compensation is better performed through RCH methods (cf. subsection 2.2.5), as polynomial-based compensation would require high-orders to reach phase flatness. The object can then be brought in focus through digital propagation procedure. One of the main advantage of compensating for aberrations is that the convergent wave can be considered as a spherical aberration, which thus implies that the in-focus distance is not identical for each positions in the field of view. Ensuring a flat phase profile before digital propagation thus makes it possible to get fully in-focus images, as shown in Fig. 4.8(c). One should note however that this method implies that the reconstruction is performed with a digital reference wave having a different curvature than the one employed for acquisition, so that the magnification of the system can be slightly changed due to this procedure, as expressed in Eq. (2.9).

This acquisition scheme is then employed to acquire frames for different object positions to retrieve the angular information. We consider here for the sake of simplicity an object smaller than the field of view. Furthermore, we limit our discussion to a linear scan in the x direction, as performed later in the experiments. The size of the stack is $N_x \times N_y \times P$, where N_x, N_y is the resolution of the detector, and P is the amount of frames acquired during scanning. In this fashion, the raw 3D stack of data is measured in a $(x, y, \Delta x_p)$ space as represented in Fig. 4.9(a), where (x, y) corresponds to the fixed referential of the detector, and (x_p, y_p) is the referential

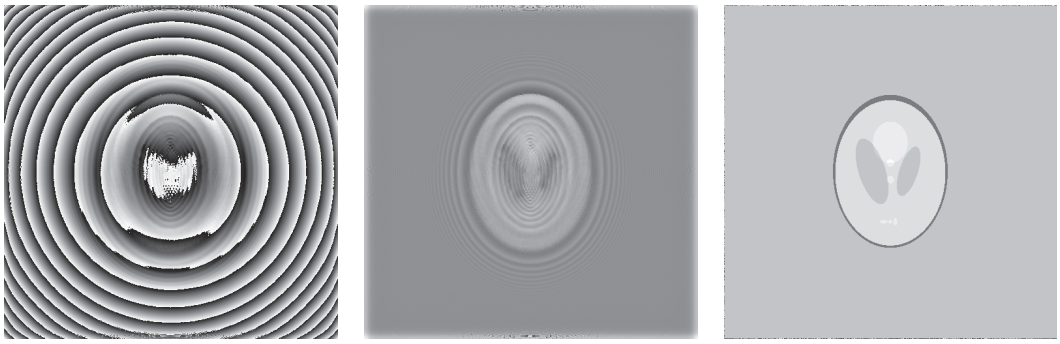

(a) (b) (c)

Figure 4.8: Stages of the reconstruction for tomographic reconstruction, with (a) raw reconstructed phase with the strong curvature induced by the spherical excitation wave, (b) flattened phase, through RCH calibration, (c) phase of the digitally propagated wave, brought in focus.

of the moving stage (cf. Fig. 4.6). The two referential are assumed to be collinear, and related only by a translation, so that $x = x_p - \Delta x_p$. The frames are linked to a fixed angular distribution (α_x, α_y) corresponding to the spherical wave employed for excitation.

In the case of an object smaller than the field of view, each frame can be cropped to a region of interest (ROI) $M_x \times M_y$, as shown in Fig. 4.9(b). The principle of linear scanning induces a coupling between the position (x, y) and the illumination angles (α_x, α_y) which must be suppressed in order to enable the use of standard reconstruction algorithms based on angular views with their rotation axis centred in the field of view.

Each ROI can thus be translated in the (x_p, y_p) referential, in which the object is static, as shown in Fig. 4.10(a), thus providing a specific angular distribution for each frame, depending on the position Δx_p. Thanks to the bijective relation between the position Δx_p and the angle α_x, this data set can be represented in a space (x_p, y_p, α_x), as shown in Fig. 4.10(b). The fact that frames are shown on diagonal lines here results from the assumption of an equi-angular sampling, i.e. $\Delta\alpha_x = cte$, which corresponds to a parabolic profile of the illumination wave.

One can identify in the representation of Fig. 4.10(b) that triangular regions of unmeasured data are present. They correspond to the extremities of the measurement stack, where the object is only partly present in the field of view. It is indeed necessary to ensure that the specimen is illuminated by all the angles available in the illumination pattern, so that the scanning range must be larger than the field of view. Typically, the scanning must encompass a discrete range of $N_x + 2M_x$. The data set can thus be arranged to suppress these unmeasured portions by translating each (y_p, α_x) frame to the same origin for each x_p value, finally providing a data stack which corresponds to a sinogram by suppressing the triangular unwanted portions.

In summary, the data arrangement proposed above corresponds to two translations in the data set, in order to cancel the specimen movement induced by the linear scanning, and to

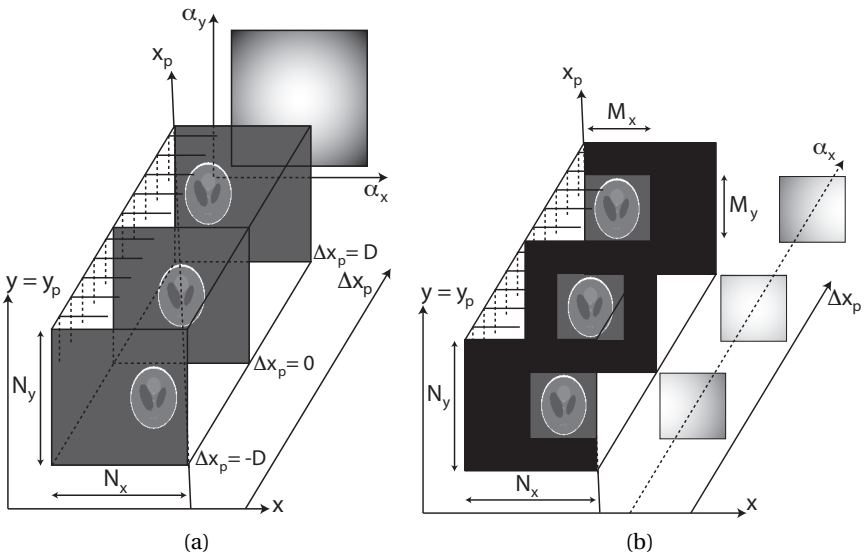

Figure 4.9: Data organisation of (a) the raw measurements in a $(x, y, \Delta x)$ domain, where the object is scanned in the field of view, (b) after data cropping, where each ROI corresponds to a different angular profile for excitation.

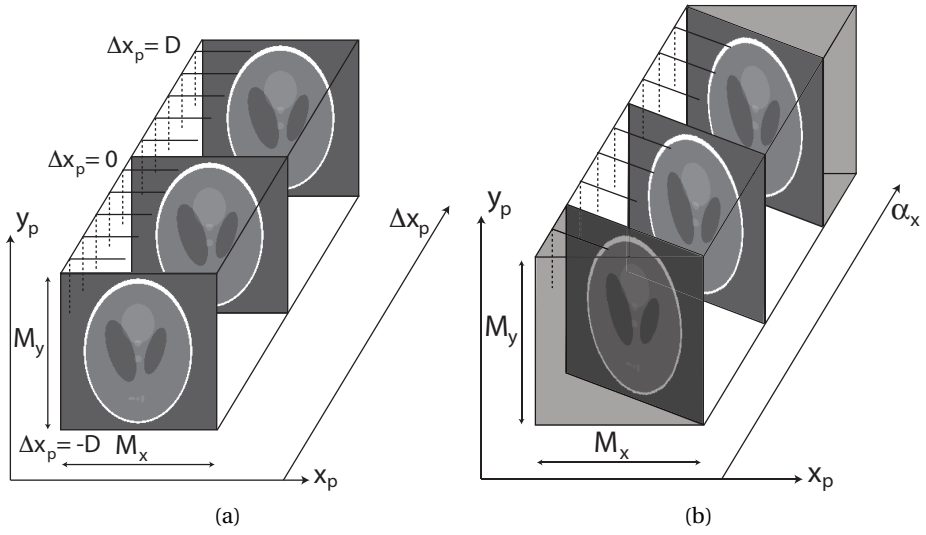

Figure 4.10: (a) Data organisation after translation to the $(x_p, y_p, \Delta x_p)$ domain of the cropped data and (b) representation of the same data set in the (x_p, y_p, α_x) domain corresponding to the sinogram space, where triangular regions must be suppressed.

ensure the similarity with a sinogram, where each slice corresponds to an angular view. It can be seen as a change of basis, passing from the raw data referential $(x, y, \Delta x_p)$ to the sinogram basis (x_p, y_p, α_x), in order to enable tomographic inversion through standard procedures.

In the context of discrete data, this change of basis is however not always trivial, and can involve several interpolation stages. The referential of the detector and the one of the moving stage are related by the displacement Δx_p, while data is discretised by the detector sampling Δx. In the case the two values are not matched, it is necessary to interpolate the measured data to ensure a proper sorting of the sinogram. Similarly, we assumed in the discussion above a constant angular sampling $\Delta\alpha_x$ for the sake of simplicity, but other sampling could require further interpolations to generate the sinogram, as the data set must be represented in an orthonormal direction to the α_x axis.

4.4.3 Validation of inversion procedure

We present in this subsection simulations in order to validate the inversion algorithm based on a Fourier mapping. As discussed in subsection 4.3.4, spatial algorithms such as the inverse Radon transform are commonly preferred for inversions based on the FST, thanks to their easy implementation. However, their use is limited to very defined cases, as only an equidistant sampling $\Delta\alpha$ can be employed. We thus developed inversions based on a Fourier implementation in order to enable more flexibility for our analysis of the linear scanning method. Throughout this subsection, we consider 2D data sets, since a generalisation to 3D can straightforwardly be performed through separability.

Fourier inversion methods are relying on a direct interpretation of the FST described in Eq. (4.1), where the Fourier transforms of the projections are transferred in a 2D Fourier space before performing an inverse Fourier transform to recover the object. It thus corresponds to map a (ω_t, α) space having a cylindrical symmetry into a (ω_x, ω_z) Cartesian space. In the case of discrete data, the main issue in this operation is related to the over-representation of low spatial frequencies because of the rotation symmetry, as shown in Fig. 4.3(b).

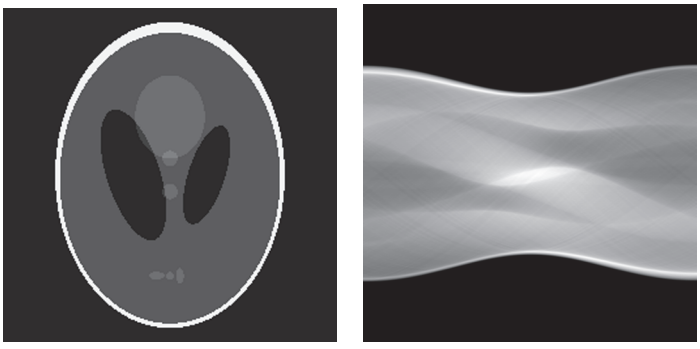

(a) (b)

Figure 4.11: (a) Shepp-Logan phantom employed for simulations, and (b) its sinogram generated with the `radon` function with the projections shown vertically.

For our validations, we employ the Shepp-Logan phantom (cf. Fig. 4.11(a)) sampled on a 256×256 grid. We then generate the angular views by employing the `radon` function of MATLAB®, with an angular sampling of $\Delta\alpha = 1°$. During these computational validations, we assume a full angular coverage of $\alpha \in [-\pi/2, \pi/2[$. This transformation leads to a sinogram as shown in Fig. 4.11(b), where the various features of the phantom can be identified in the different projections. The implementation of `radon` generates a matrix of odd size, which can generate artefacts in the reconstruction when employing Fourier transforms. For this reason, we compute the Fourier transform of the projections by extending the size to the next power of 2 to avoid these issues, so that the Fourier transform of the projections employed for the analyses below is of size 512×180.

In many aspects, the validations presented here can be partly considered as a reproduction of the results published by Pan *et al.*, where they demonstrated that the direct Fourier inversion methods can lead to results similar in quality to the inverse Radon transform, when handled properly [Pan83].

Fourier mapping strategy

We first analyse different Fourier mapping methods, in order to transfer the measured data from the cylindrical space to the 2D Cartesian reciprocal space. A straightforward way is to transfer the measured values measured in the (ω_t, α) domain through the polar representation given as

$$\tan(\alpha) = \frac{\omega_z}{\omega_x}, \qquad \omega_t = \pm\sqrt{\omega_x^2 + \omega_z^2}. \tag{4.9}$$

By inverting these relations and selecting the closest discrete coordinates (ω_x, ω_z), one can straightforwardly transfer each measured pixel to the Cartesian Fourier space. In the case of a polar sampling as measured with angular views which generates an over-representation of low spatial frequencies, several (ω_t, α) values are however transferred to the same frequency values, so that a selection is necessary to fill the 2D Fourier space.

We present in Fig. 4.12(a) the result of an inversion where the Fourier mapping has been performed by selecting the Fourier value with the highest value when more than one was available for a given (ω_x, ω_z) position, under the hypothesis that the maximum values are the most representative. One can see however that this method generates a strong artefact at the centre, which can be interpreted as an over-estimation of the value of spatial frequencies in the high frequency range. On the other hand, we show in Fig. 4.12(b) the case where the frequencies were averaged when more than one is available at a (ω_x, ω_z) position. In this case, the strong artefact at the centre is suppressed, and the main structures are correctly reconstructed. However, various circular artefacts as well as a background noise can be readily seen in the reconstruction.

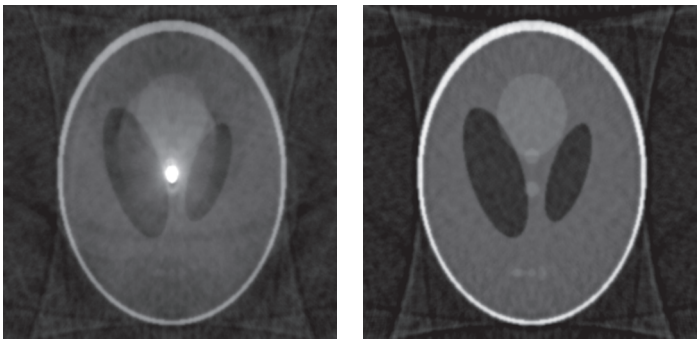

(a) (b)

Figure 4.12: Illustration of the tomographic inversion performed through direct mapping with selection of over-sampled frequencies through (a) maximum value method and (b) averaging of all present frequencies.

These artefacts are mainly due to the data sparsity for high frequencies in the 2D Fourier plane, where many pixels are not filled due to the absence of corresponding frequencies in the measured data. In order to avoid these artefacts, one would have to reduce greatly the angular sampling, thus increasing greatly the amount of frames, and rendering the method quite inefficient, as this would imply to repeat many times measurements of low frequencies. In order to circumvent this issue, another approach consists in filling all (ω_x, ω_z) spatial frequencies values, by interpolating them through available data in the (ω_t, α) space. We present in Fig. 4.13(a) an inversion performed in this fashion, where for each (ω_x, ω_z) the closest available value is determined through the relations of Eq. (4.9), thus corresponding to a nearest-value interpolation. As expected, the high-frequency noise is suppressed compared to the straightforward transfer of Fig. 4.12 thanks to the non-sparsity in the 2D Fourier plane, but circular artefacts are still present, with lines appearing in the reconstruction, probably due to the selection of inadequate frequencies in the nearest-neighbour procedure. Finally, we present in Fig. 4.13(b) a reconstruction performed through bilinear interpolation. In this case, most artefacts are suppressed, and the value distribution is rather constant without artefacts in the defined zones of the phantom, although circular artefacts are still present.

These examples show the importance of the mapping strategy during inversion, where the sparsity of data when performing direct mapping such as shown in Fig. 4.12 can lead to the generation of several artefacts, so that interpolation methods ensuring a complete filling of frequencies in the (ω_x, ω_z) space is necessary to ensure correct reconstruction.

Comparison with the inverse Radon transform

In the last paragraph, the bilinear inversion method was shown to provide the best results, although some artefacts were still present. We compare here this method with the inverse Radon transform implemented spatially through the `iradon` method from MATLAB®, shown in Fig. 4.14(a), corresponding to a discrete implementation of Eq. (4.8). The images in Fig. 4.14

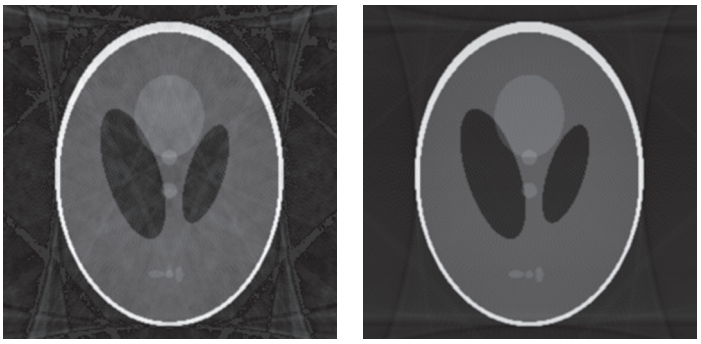

(a) (b)

Figure 4.13: Illustration of the tomographic inversion performed through data interpolation in the Cartesian space with (a) nearest-neighbour and (b) bilinear interpolation.

are all shown in log-scale, in order to enhance the visibility of the potential artefacts. The inverse Radon transform is compared with the bilinear inversion as performed in the last paragraph in Fig. 4.14(b), where the circular artefacts can be readily observed. In order to improve the reconstruction quality, we increased the frequency sampling in the (ω_t, α) domain by padding data in the t direction to twice the size of the matrix before performing the Fourier transform, leading to the inversion presented in Fig. 4.14(c). One can see that in this case, all artefacts are suppressed, with a reconstruction quality being at least comparable with the inverse Radon transform. By looking at the background noise in constant zones, one can see that the Fourier mapping method with bilinear interpolation yields even better results than the FBP, by minimising the noise.

(a) (b) (c)

Figure 4.14: Comparison of inversions performed (a) with the inverse Radon transform, (b) Fourier inversion through bilinear interpolation and (c) bilinear interpolation with interpolation in cylindrical frequencies by a factor of 2. All images are shown in log-scale.

In summary, we present in the algorithm 4 the steps required for reconstructing the tomogram from measured data acquired through the linear scanning procedure, based on the arrangement of data presented in subsection 4.4.1, and on the Fourier inversion based on

the interpolated bilinear mapping presented above. The algorithm is presented under the assumption of a scan in the x direction, according to the description of subsection 4.4.1.

Algorithm 4 Tomographic inversion algorithm for linear scanning approach

for all measured hologram **do**
  Reconstruction of the complex wavefront through off-axis holography methods.
  Compensation of the wavefront curvature with RCH methods.
  Adjustment of the focus position with digital propagation.
  Subtraction of the phase offset of the background, to account for experimental vibrations.
  Selection of the ROI containing the measured object, where the position of the ROI is determined by the movement of the moving stage (transformation from $(x, y, \Delta x_p)$ domain to $(x_p, y_p, \Delta x_p)$ domain).
  Unwrapping of the phase signal.
  Insertion of the ROI in the 3D data set.
end for
Alignment of equi-angular lines (cf. Fig. 4.10(b)) to obtain data similar to a sinogram (transformation from $(x_p, y_p, \Delta x_p)$ domain to (x_p, y_p, α) domain).
for all $x_p \in [0, M_x]$ **do**
  Padding of the data set $(y_p, \alpha) \in [(0,0), (M_x, P)]$ into a $[(0,0), (2M_x, P)]$ domain.
  Fourier transform in the y_p direction to get the spatial frequencies of the projections in (ω_{y_p}, α).
  for all $(\omega_x, \omega_z) \mid |\tan(\omega_z/\omega_x)| \leq \sin^{-1}(\text{NA})$ **do**
    Determining the (ω_x, ω_z) value with bilinear interpolation from the (ω_{y_p}, α) data set through the relations of Eq. (4.9).
  end for
end for
2D Fourier inversion of the (ω_x, ω_z) data set to retrieve the spatial information in the (x, z) domain.
Data cropping to account for the interpolation in the spectral domain.

Expected resolution

Finally, we assess the expected resolution through our reconstruction method based on data limited by the NA of the condenser, similarly to our experimental configuration presented in subsection 4.5.1. The projections were generated with the same phantom as previously, and an angular sampling of $\Delta\alpha = 0.5°$ within the angular range delimited by NA = 0.4. The available frequencies in the (ω_t, α) data set are shown in the Cartesian reciprocal space in Fig. 4.15(a), where the limitation in frequencies can be readily identified. The inset in the figure shows the data sparsity at high spatial frequencies. The reconstruction through Fourier inversion is then shown in Fig. 4.15(b), where a dramatic loss in spatial resolution can be identified. While most of the main structures are resolved, the smaller ones such as the dots at the centre and bottom of the phantom (cf. Fig. 4.11(a)) are not visible in the reconstruction, and large ones are distorted by triangular shapes. A sectioning effect can still be identified in

the reconstruction, but it is limited by lines in triangular shapes, generated by the absence of spectral information in the z direction.

These triangular artefacts are due to the shape of the synthesised Fourier mapping shown in Fig. 4.15(a), where the so-called missing cone reduces the resolution, because of the angular views limited by the NA. Typically, the theoretical spatial resolution of an imaging system with $\lambda = 668$ nm and NA = 0.95 is 351.5 nm. Due to the excitation NA limitation, the smallest resolution resulting from the projection of the spatial frequency with an angle α on the z axis results in a resolution of 878.9 nm, which is furthermore situated at extremities of the mapping, so that it does not correspond to the sectioning resolution.

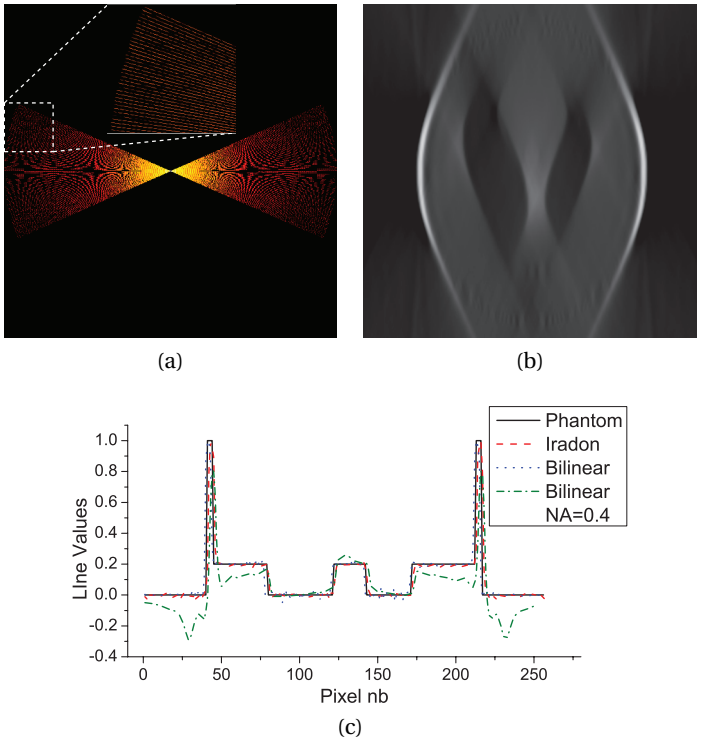

Figure 4.15: Tomographic reconstruction based on data limited in the angular range by NA = 0.4. (a) Available spatial frequencies shown in the (ω_x, ω_z) domain, resulting in (b) a reconstruction where smaller structures are not resolved anymore.

While the resolution is largely hindered by the limitation in NA, one should note that the retrieved values are still rather accurate in terms of amplitude, particularly at the centre of the reconstruction. This can be seen by comparing the original phantom in Fig. 4.11(a) and the reconstruction in Fig. 4.15(b), which were scaled in the same manner. We present in Fig. 4.15(c) several horizontal lines extracted from the centre of the phantom, for the original signal, the inverse Radon transform, and the Fourier mapping bilinear inversion (with full and limited (NA = 0.4) angular coverage). One can see that most techniques provide rather accurate values and are in agreement. In the case of NA-limited reconstruction, the lines present a

degradation in resolution, consistent with the 2D reconstruction of Fig. 4.15(b), in particular near regions with high gradients. Nevertheless, the values remain rather accurate in smooth regions, as seen at the centre of the phantom.

4.5 Experimental results

We present in this section preliminary results obtained according to the method presented above, where we thus move the specimen with a standard $x-y$ moving stage in a microscope setup, with a convergent wave as an illumination pattern.

4.5.1 Experimental setup

The setup employed for these measurements consists in the optical arrangement shown in Fig. 2.16, which was slightly modified to accommodate the measurement protocol of linear scanning. The illumination is provided in this case by a laser diode having a wavelength of $\lambda =$ 668 nm, shaped as a spherical wave in the object plane. The light is then collected by a 63× MO (NA = 0.95) in air, and imaged near the detector by a relay optics, so that the hologram is recorded in the Fresnel regime by a CCD camera ($\Delta x = 6.45$ µm) with a resolution of 1024 × 1024.

The illumination pattern is generated by employing a 20× MO (NA = 0.4) as a condenser, which provides a high quality convergent beam with minimal aberrations. As depicted in Fig. 4.16, the beam size is adapted by a couple of lenses mounted in a $2f$ configuration to fill the exit pupil of the excitation optics with a collimated beam, in order to use the infinity-corrected MO in its design conditions. A diaphragm is placed at the conjugated plane of the object position, enabling fine adjustment of the beam diameter to the size of the exit pupil, while avoiding rings artefacts generated by the spatial coherence of the source.

The converging beam then illuminates the specimen, where it fills the field of view in the object space. For this purpose, the excitation MO is placed on a moving stage, enabling also fine adjustments on the z axis in order to ensure full illumination of the measured region. The MO was chosen as a 20× for these preliminary measurements, since the typical working distances of this type of objectives in the millimetre range makes it possible to use standard microscopic preparation on glass slides, which thickness is generally in this range. On the detection side, a cover slip (0.17 mm) is used for standard imaging conditions.

To enable linear scanning with high precision, the specimen is mounted on a closed-loop 3D piezo-electric stages (PI, P-517) having a positioning positioning precision in the nanometre range, and a moving range of 100 × 100 × 10 µm. As the sample must be moved along the whole field of view, the relay optics has been adapted to adjust the magnification to ensure that measurement zone is smaller than the moving range of the piezo-electric stage.

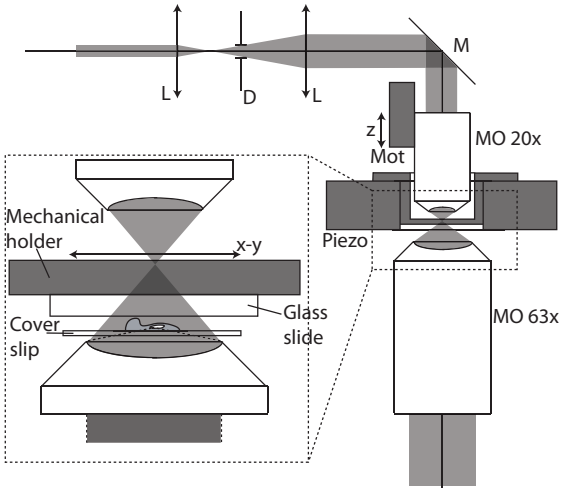

Figure 4.16: Optical scheme for tomographic acquisition. D: Diaphragm, L: Lens, M: Mirror, Mot: Linear Motor, Piezo: 3D closed-loop piezo-electric stage.

4.5.2 Experimental protocol

The measurement are performed on paper mulberry pollen grains having a typical size of $10-15\,\mu$m, immersed in glycerol. Typical pollens are shown in Fig. 4.17, in bright field and phase-contrast imaging, where the cell wall and internal structures, such as the nucleus, can be identified. These pollens were chosen for their ease of manipulation, while having sizes comparable to most animal cells which can be observed *in vitro*. We present in the next paragraphs the measurements performed, along with the various calibration steps required to ensure proper reconstruction.

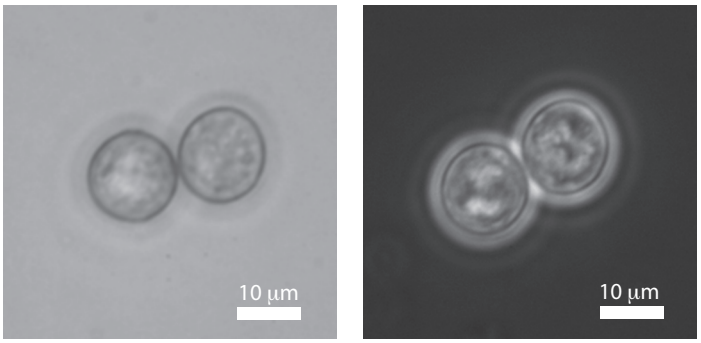

(a) (b)

Figure 4.17: Images of paper mulberry pollens in (a) bright field and (b) phase-contrast imaging, similar to the ones used for tomographic measurements.

As the complex wavefront is measured with DHM, it implies that it relies on the interference between the object and reference waves for coherent detection, so that the recovered wavefront is a relative measurement of the phase shifts on both arms of the interferometer.

In usual cases, the aberrations coming from the optical system as well as the wavefront mismatch between the two waves can be compensated with various procedures, as described in subsection 2.2.5. However, in our particular case, it is mandatory to know accurately the wavefront shape of the object wave, in order to be able to determine the excitation profile in the object plane. It is thus necessary to calibrate the system in order to minimise the wavefront mismatch between the two interfering beams.

For this purpose, calibration measurements are first performed with the setup in its standard implementation, where the illumination in the object space is performed with a low NA condenser lens (NA $\approx$ 0.033), which can be approximated to a flat illumination, and the reference wave is chosen to be collimated, so that the beams at camera level also mimic plane waves. The relay optics is then adjusted in the object arm in order to minimise curvature. This procedure makes it possible during measurement with convergent beams to then rely on the phase profile acquired on the camera for estimation of the illumination pattern, and thus for determination of the angles of excitation on different parts of the field of view.

After this calibration, the setup is changed to the configuration presented in Fig. 4.16 in order to enable measurement with converging waves. The excitation profile is then adjusted by changing the height of the excitation MO, with the specimen already placed in the field of view. As strongly convergent waves are employed for illumination, it is indeed mandatory to adjust the excitation with the specimen mounted, as the glass slide changes the curvature of the beam. It is thus possible to adjust the excitation beam to the size of the field of view and measure a reference hologram for further compensation at reconstruction stage by moving the specimen to a region with no specimen. We present in Fig. 4.18(a) a typical hologram measured at this stage, where one can identify the round shape of the diaphragm situated in the conjugated plane of the excitation MO, which is encompassed in the detector field of view. The corresponding phase pattern is shown in Fig. 4.18(b), where the different angles of excitation can be seen in the phase profile.

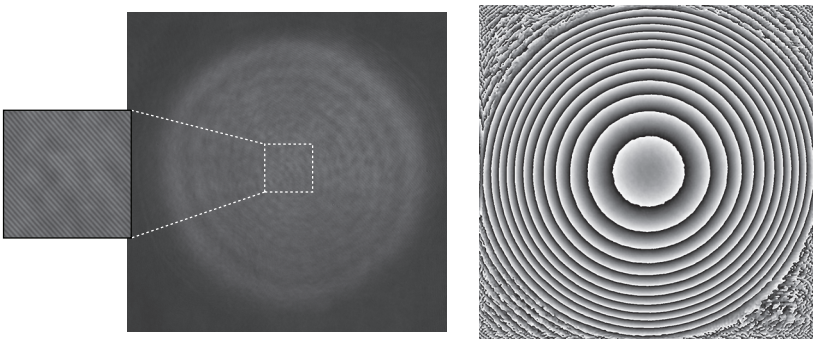

(a) (b)

Figure 4.18: (a) Empty curved hologram employed as a RCH during reconstruction, with (b) its phase map, where the curved profile can be identified, and used for calibration of illumination angles.

Finally, the object pixel size is determined by moving the specimen in the field of view with the piezo-electric actuator, where the precision of the PZT enables a precise determination of the dimensions in the object space. Typical measurements with our configuration provide a pixel size of $\Delta x_o \approx 75\,\text{nm/px}$, thus corresponding to an effective magnification of $M = 86$, and a field of view of 76.8 µm. These values are the consequence of the adjustment of the magnification through the relay optics, which ensures that the field of view is smaller than the range of the moving stage (100 µm).

For the measurement itself, we perform the scan in a one-dimensional way, as discussed in subsection 4.4.1, where we ensure that the camera orientation is aligned with the one of the moving stage, so that the scanning direction is perpendicular to one of the axis of measurement. The fact of performing a one-dimensional scan parallel to an axis of the detector makes it possible to easily use separability in the FST formalism, in order to reconstruct the object slice by slice to recover the 3D volume. We chose for these preliminary measurements to match the scanning step and the object pixel size, i.e. $\Delta x_p = \Delta x_o$. As expressed in subsection 4.4.2, this minimises the amount of necessary interpolation necessary. The measurements are then performed by sequentially scanning the moving stage to the different positions.

We present in Fig. 4.19 phase images for different positions of a pollen grain, which were reconstructed by employing the reference hologram shown in Fig. 4.18(a), and digitally propagated in focus, thus corresponding to the step 5 of algorithm 4. It is possible to identify in these images that the pollen is in focus without the spherical aberrations present in the raw holograms, thanks to the RCH compensation during reconstruction. The scan is performed on the full range provided by the PZT, thus leading to a stack of $P = 1332$ images. In the present implementation of the sequential acquisition, each frame acquisition takes approximately 0.5 seconds, leading to an acquisition time of approximately 11 min, where most of the time for acquisition is due to the stabilisation of the PZT to each position.

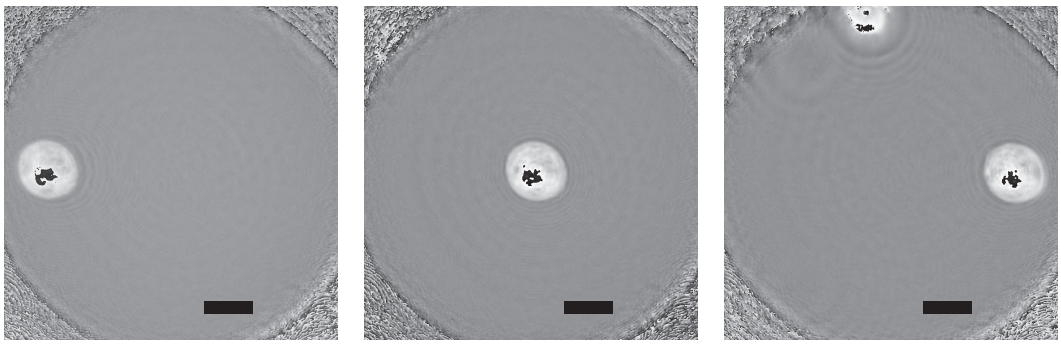

(a) (b) (c)

Figure 4.19: Phase measured on a specimen of pollen grain at different scanning positions. (a) $\Delta x_p = -27.45$ µm, (b) $\Delta x_p = 0$ µm, (c) $\Delta x_p = 25.05$ µm. Scale bar is 10 µm.

4.5.3 Tomographic reconstruction

In order to enable the tomographic inversion, we first must evaluate the angular distribution along the scanning line. For this operation, we employ the reference hologram measured in an empty field of view (cf. Fig. 4.18(b)) which provides the full wavefront curvature. We present in Fig. 4.20(a) the unwrapped phase measured on the line where the sample is scanned during acquisition. The phase profile can straightforwardly provide the angle of propagation of the local k-vector through typically finite differences, as shown in Fig.4.20(b). In the case of a rather limited NA as the one used in this proof of principle, one can see that the spherical wave can still be very well approximated by a parabola, as seen by the linear distribution of angles. By estimating the distribution by linear regression, one can find that the maximum angle is $\alpha_{\max} = \pm 16.7°$, leading to an effective NA = 0.41 when considering the refractive index of the immersion medium.

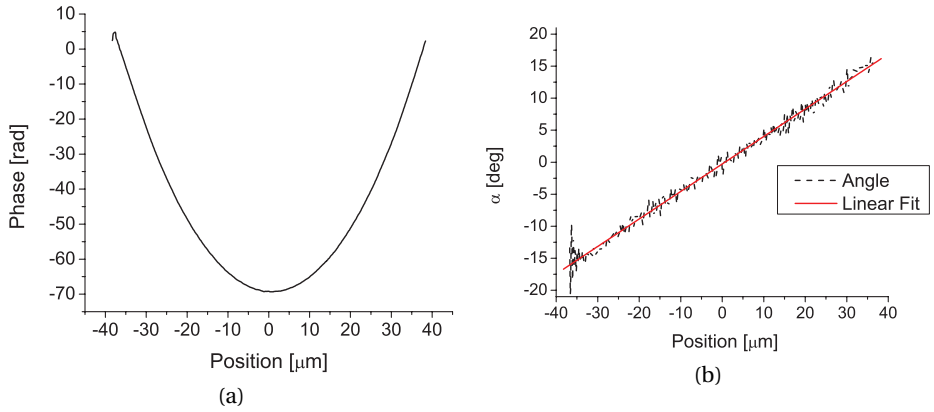

Figure 4.20: Excitation unwrapped phase profile along the scanning line extracted from the reference hologram (cf. Fig. 4.18(b)), leading to (b) an angular distribution along the scanning line.

We then arrange the data set according to the procedure described in subsection 4.4.2, in order to retrieve the data set in a structure similar to a sinogram, as shown in Fig. 4.10(b). We present as an illustration the angular views of the measured pollen grain in Fig. 4.21 for different values of α_x. One should note that due to the data arrangement, the images presented here are different from the ROIs of Fig. 4.19, as each image corresponds at this point to an angular view for a constant α_x on the whole image, thus equivalent to step 10 of the algorithm 4.

Finally, the recovered data set can be inverted through the Fourier mapping analysed in subsection 4.4.3. We thus fill the 2D Cartesian Fourier space, where the mapping is based on the angles retrieved from the reference hologram characterising the excitation pattern, shown in Fig. 4.20(b). The inversion leads to the results shown in Fig. 4.22, for a $x-z$ section situated at the centre of the pollen grain, shown here with isotropic sampling of the matrix, and for units in radians per voxel. One can recognise in the real part of the inversion (cf. 4.22(a))

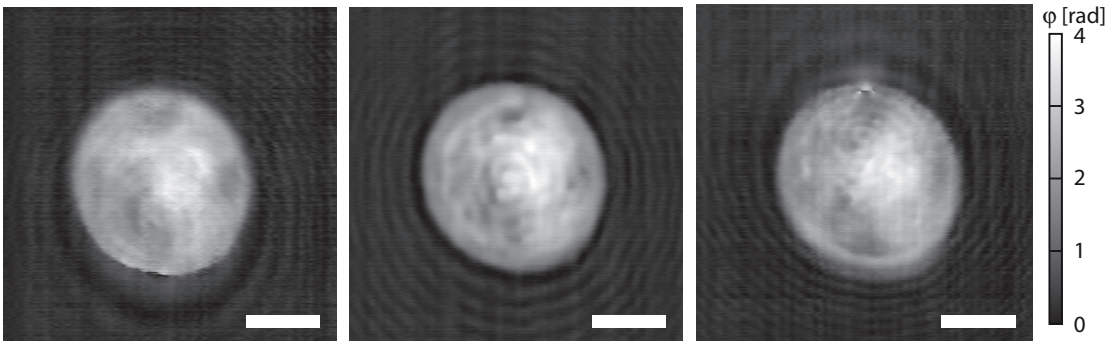

(a) (b) (c)

Figure 4.21: Images of the pollen grain measured at various angles after data arrangement at (a) −15°, (b) −0.3°, (c) 14.4°. Scale bars are 5 μm, and the image scale is in radians.

the structure of the pollen, with sectioning in the z direction. As we employ here an inversion based on the FST, the reconstruction is performed by considering only the phase part of the measurement, so that the retrieved signal should be in principle real-defined. However, due to reconstruction artefacts and numerical errors, the reconstructed signal is commonly complex when employing Fourier mapping methods. We show in Fig. 4.22(b) the imaginary part of the reconstruction, being typically three orders of magnitude lower than the real part, which is an indication of relevant reconstruction.

One can identify in Fig. 4.22(a) the main shape of the specimen, and in particular the nucleus, slightly shifted from the centre of the pollen grain. The resolution is however degraded because of the limited excitation NA, where the triangular artefacts are clearly present, in particular at the interface between the pollen grain and the immersion medium. This can also be identified inside the pollen, where various patterns have an elliptical shape, due to the anisotropic resolution of the reconstruction. One can assume that these patterns are generated by the granular internal structure of this pollen type, as it can be seen in the bright field image shown in Fig. 4.17(a). One can also see the effect of the cell wall at each border of the section, where it induces a large signal variation. This is due to the strong diffraction at the cell wall interface, which is not taken into account in our reconstruction, and the high refractive index gradient at this region, which cannot be resolved at our current resolution.

As each voxel in the tomogram corresponds to a local phase shift induced in the z direction, it is possible to then reconstruct the 3D refractive distribution through the simple formula

$$\Delta n = \frac{\lambda_0}{2\pi\Delta z}\Delta\varphi, \tag{4.10}$$

where Δz is the size of a voxel in the direction of the optical axis, and where the refractive index Δn is expressed relatively to the immersion medium. As discussed before, the sampling on the z axis in the reconstruction is identical to the one in the x direction, as it is performed on cu-

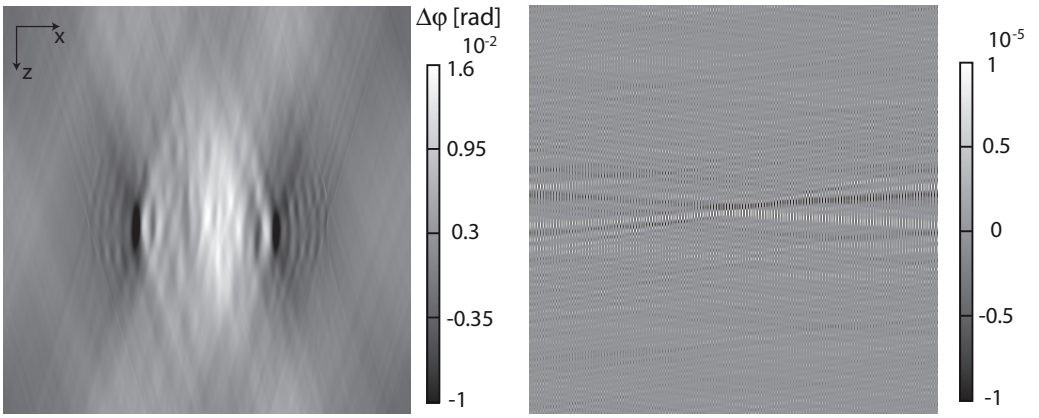

(a) (b)

Figure 4.22: $x-z$ section at the centre of the pollen grain after tomographic inversion. (a) Real part of the Fourier inversion, shown in radians per voxel, and (b) imaginary part of the inversion, saturated to the scale shown in the image, from an original dynamic of $[-2.12\cdot10^{-5}, 2.12\cdot10^{-5}]$.

bic matrices, so that $\Delta z = \Delta x$. The resulting RI distribution is shown in Fig. 4.23 through $x-y$ sections, where Δn is relative to glycerol ($n = 1.473$). The sections are presented at respectively $z = [-3, 0, 4, 8]$ µm in regards to the centre of the pollen grain. These sections are typically chosen to be sufficiently apart compared to the z resolution deduced in subsection 4.4.3, being typically slightly below 1 µm.

The pollen mainly induces refractive index changes in the $[1.45, 1.49]$ range, which is within reasonable values for vegetable cells, and consistent with the observation of similar specimens [Cha06a]. The RI values are however very probably lower than the exact ones, as the reconstruction is smoothed because of the limited resolution, in a similar way as the simulations presented in Fig. 4.15(c).

Sections in the $x-y$ plane are visually far better than the $x-z$ ones, thanks to their isotropic resolution. This visualisation also shows some artefacts of reconstruction which were not visible in Fig. 4.22, resulting from the reconstruction from a one-dimensional scan. Ripples can indeed be identified horizontally, which corresponds to the dimension of the linear scan, while these ones are not present in the vertical direction, as the reconstruction is performed by employing separability. In the different sections of Fig. 4.23, on can identify various features of the pollens, which are consistent with the transmission images of Fig. 4.21. The nucleus can be observed as shifted on the right and on the top of the pollen, as it is still present at $z = 4$ µm but vanishes already at $z = -3$ µm. On the left of the pollen, small features with low RI values can also be observed, which may correspond to the smaller structures observed for example in the bright field images of Fig. 4.17.

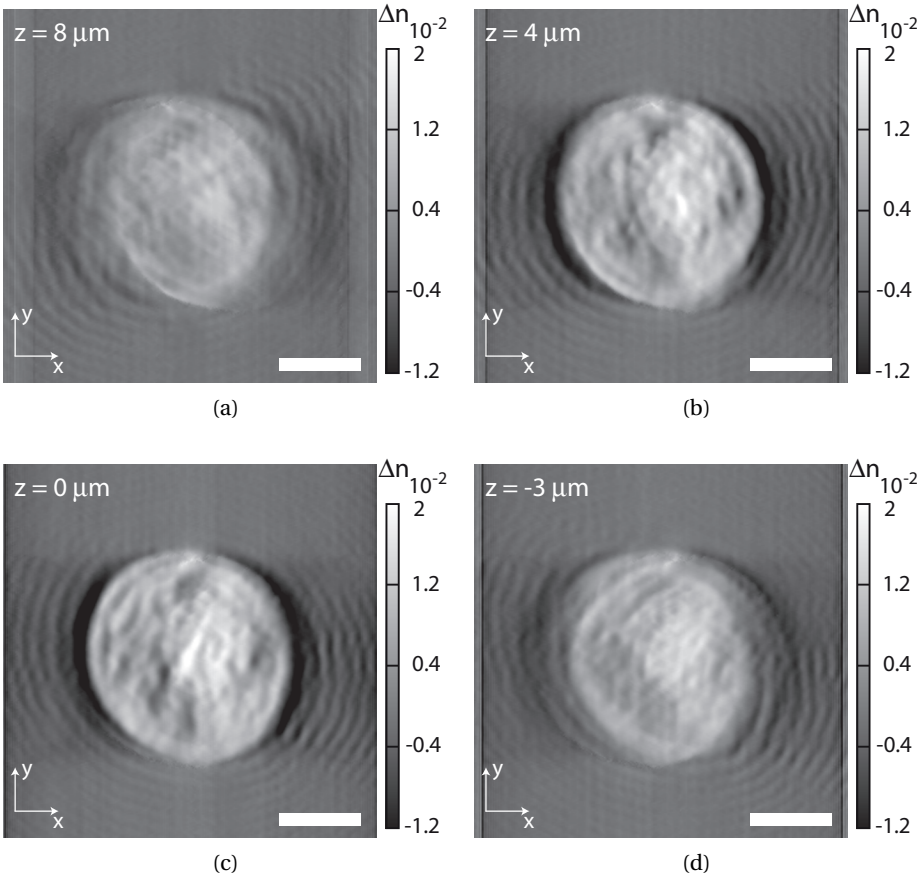

Figure 4.23: $x-y$ sections of the pollen grain at (a) $z = 8$ µm, (b) $z = 4$ µm, (c) $z = 0$ µm, (d) $z = -3$ µm. The scales are given in relative refractive index in regards to the immersion medium (glycerol, $n = 1.473$), and scale bars are 5 µm.

4.6 Discussion and perspectives

While the measurements presented in section 4.5 demonstrate a sectioning capability resulting from the tomographic reconstruction, the resolution is hindered essentially by the limited excitation NA, as predicted in the simulations of subsection 4.4.3. The $x-z$ section presented in Fig. 4.22(a) possesses the same triangular lines artefacts as in Fig. 4.15(b), resulting from the unknown spatial frequencies in the so-called missing cone. The excitation MO has been chosen as a 20× in these preliminary measurements in order to ease the experimental procedure by making it possible to use standard microscopic preparations mounted on glass slides. The resolution of the reconstructions could therefore be greatly enhanced by increasing the excitation NA, although this would make necessary to employ non-standard preparations, to accommodate the short working distances.

Furthermore, the fact of increasing the NA of the excitation would dramatically improve the efficiency of measurement. The present configuration, composed of an excitation of NA =

0.4 and a detector resolution of 1024×1024, corresponds indeed approximately to an angular sampling of $\Delta\alpha = 0.045°$, which is uselessly too fine. It was indeed shown that the resolution is more sensitive to the angular coverage than to the angular sampling, so that this fine angular resolution is not required for such a numerical aperture. Increasing the excitation NA would thus enlarge the angular coverage while reducing the angular sampling, thus maintaining the size of the data set constant while dramatically improving the final resolution in the optical axis direction. Obtaining a better z resolution would also bring the reconstruction to a more isotropic resolution, thus greatly improving the results.

In the measurements above, pollen grains were employed as a specimen because of their ease of manipulation, although they are far from ideal for tomographic reconstruction. Vegetable cells possess strongly diffractive elements such as the cell wall, which are complicated to reconstruct due to their strong refractive index gradient. These specimens typically also break the hypothesis of weak scattering of the FDT, so that even a finer model for inversion may not improve substantially the reconstruction accuracy.

In the present proof of principle, we limited our acquisition and reconstruction procedures to a simple data arrangement method, in order to enable the use of standard algorithms based on the FST, which considers plane waves for excitation. This approach can typically lead to problems in the reconstruction by requiring large interpolation procedures, which depend on the matching conditions between the object pixel size Δx in the acquired image and the scanning step Δx_p. Typically, in cases for which $\Delta x_p = C \cdot \Delta x$, $C \notin \mathbb{N}$, the scanning step does not ensure that the same positions of the specimen are sampled during scanning. While we avoided interpolation in our measurement by matching the scanning step to the sampling of the detector, it requires a highly precise PZT for the scan, which increases the complexity of the measurement setup. Furthermore, a mismatch between Δx and Δx_p can lead to errors in the reconstruction, which may lead to a loss in resolution.

These issues emanating from the data arrangement methodology could be greatly simplified if a more general formalism for inversion could be employed, typically by incorporating directly in the inversion model the spherical wave excitation. In the case of the FST, this would require to reformulate the definition of the projection in Eq. (4.3), in order to take into account the convergent/divergent ray geometry. Furthermore, the proposed scanning strategy also induces a coupling between the angular information and the position, which must be compensated. Similarly, in order to enable the use of diffraction tomography algorithm to this approach, it would be necessary to incorporate the spherical waves in the inversion of the FDT, which would require to change the function employed for $u_0(\boldsymbol{r})$ in the Born approximation expressed in Eq. (C.16). The quadratic terms introduced in this fashion however imply that the Fourier relation between the object and the scattered field cannot be derived directly anymore, so that the FDT does not hold in a straightforward way for spherical waves. Similarly, the Rytov approximation also requires the hypothesis of a plane wave in order to enable the linearisation of the phase term of u_0, as shown in Eq. (C.34).

In our present experimental protocol, we also limited our scanning geometry to a line, in order to enable reconstruction through separability and thus retrieve the 3D volume from the 2D reconstruction of sections, implying that we neglected the angular distribution in one direction of the spherical wave of excitation. More refined scanning trajectories, based in this case on fully three-dimensional inversion methods, may increase the reconstruction quality, by typically suppressing the directional artefacts which were identified in Fig. 4.23. While this type of scanning could be performed through the arrangement protocol employed in here, this approach would again greatly benefit from a more general framework, in which the illumination pattern is taken into account in the inversion procedure.

The scanning approach could also be improved in a technological point of view. At this stage, we performed the linear scanning step by step with a PZT, leading to a rather long acquisition time due to the mechanical stabilisation. Instead of steps, scanning based on a constant speed coupled with camera triggering could dramatically decrease the acquisition duration. With the present configuration and a standard camera frame rate of 20 frames per second, an acquisition could be performed in typically 1 minute, while inducing a motion blur of less than 2 nm, i.e. approximately 2% of the optical resolution. Furthermore, this approach would enable the use of standard moving stages mounted on microscopes, which possess typically excellent performances when driven on speed settings, while dramatically increasing the measurement range.

The proposed method presents mainly the advantage of employing a scanning which is in a geometry identical to standard planar biological preparations, classically mounted on slides. Consequently, as the acquisition of the angular information is already based on a scanning in the $x-y$ plane, it could lead to an easy approach for the tomography of large specimens, such as wide fields of view of cell culture preparations. On the other hand, as it relies on a fixed illumination pattern during scanning, the calibration procedures are made simpler compared to other approaches, thus potentially easing the way to routine measurements. Furthermore, it could enable an easier combination of deconvolution techniques with tomographic acquisition, as the PSF stays in principle constant during the whole scanning, in order to further improve the reconstruction resolution.

References

[Ana05] M. Anastasio, D. Shi, Y. Huang, and G. Gbur, "Image reconstruction in spherical-wave intensity diffraction tomography," *J. Opt. Soc. Am. A* **22** (12), pp. 2651–2661 (2005).

[Bah01] K. Bahlmann, S. Jakobs, and S. Hell, "4Pi-confocal microscopy of live cells," *Ultramicroscopy* **87** (3), pp. 155–164 (2001).

[Bar00] A. Barty, K. A. Nugent, A. Roberts, and D. Paganin, "Quantitative phase tomography," *Opt. Commun.* **175**, pp. 329–336 (2000).

[Bor99] M. Born and E. Wolf, "Scattering from inhomogeneous media," in *Principles of Optics*, 7th ed., Cambridge University Press (1999), pp. 695–734.

[Cha06a] F. Charrière, F. Monfort, A. M. J. Kühn T. Colomb, E. Cuche, P. Marquet, and C. Depeursinge, "Cell refractive index tomography by digital holographic microscopy," *Opt. Lett.* **31** (2), pp. 178–180 (2006).

[Cha06b] F. Charrière, N. Pavillon, T. Colomb, C. Depeursinge, T. Heger, E. Mitchell, P. Marquet, and B. Rappaz, "Living specimen tomography by digital holographic microscopy: Morphometry of testate amoeba," *Opt. Express* **14** (16), pp. 7005–7013 (2006).

[Che98] B. Chen and J. Stamnes, "Validity of diffraction tomography based the first Born and the first Rytov approximations," *Appl. Opt.* **37** (14), pp. 2996–3006 (1998).

[Cho07] W. Choi, C. Fang-Yen, K. Badizadegan, S. Oh, N. Lue, R. Dasari, and M. Feld, "Tomographic phase microscopy," *Nat. Methods* **4** (9), pp. 717–719 (2007).

[Dän70] R. Dändliker and K. Weiss, "Reconstruction of the three-dimensional refractive index from scattered waves," *Opt. Commun.* **1** (7), pp. 323–328 (1970).

[Deb08] M. Debailleul, B. Simon, V. Georges, O. Haeberlé, and V. Lauer, "Holographic microscopy and diffractive microtomography of transparent samples," *Meas. Sci. Tech.* **19** (7), 074009 (8 pages) (2008).

[Deb09] M. Debailleul, V. Georges, B. Simon, R. Morin, and O. Haeberlé, "High-resolution three-dimensional tomographic diffractive microscopy of transparent inorganic and biological samples," *Opt. Lett.* **34** (1), pp. 79–81 (2009).

[Dev82] A. Devaney, "A filtered backpropagation algorithm for diffraction tomography," *Ultrason. Imaging* **4** (4), pp. 336–350 (1982).

[Dra08] N. Dragomir, X. Goh, and A. Roberts, "Three-dimensional refractive index reconstruction with quantitative phase tomography," *Microsc. Res. Tech.* **71** (1), pp. 5–10 (2008).

[Fau05] M. Fauver and E. J. Seibel, "Three-dimensional imaging of single isolated cell nuclei using optical projection tomography," *Opt. Express* **13** (11), pp. 4210–4223 (2005).

[Fio09] R. Fiolka, K. Wicker, R. Heintzmann, and A. Stemmer, "Simplified approach to diffraction tomography in optical microscopy," *Opt. Express* **17** (15), pp. 12 407–12 417 (2009).

[Fuj03] J. Fujimoto, "Optical coherence tomography for ultrahigh resolution in vivo imaging," *Nat. Biotechnol.* **21** (11), pp. 1361–1367 (2003).

[FY11] C. Fang-Yen, W. Choi, Y. Sung, C. Holbrow, R. Dasari, and M. Feld, "Video-rate tomographic phase microscopy," *J. Biomed. Optics* **16** (1), 011005 (5 pages) (2011).

[Gbu01] G. Gbur and E. Wolf, "Relation between computed tomography and diffraction tomography," *J. Opt. Soc. Am. A* **18** (9), pp. 2132–2137 (2001).

[Gbu02] G. Gbur and E. Wolf, "Hybrid diffraction tomography without phase information," *J. Opt. Soc. Am. A* **19** (11), pp. 2194–2202 (2002).

[Gor06] W. Gorski, "Tomographic microinterferometry of optical fibers," *Opt. Eng.* **45** (12), p. 125 002 (2006).

[Gor07] W. Gorski and W. Osten, "Tomographic imaging of photonic crystal fibers," *Opt. Lett.* **32** (14), pp. 1977–1979 (2007).

[Gu92] M. Gu and C. J. R. Sheppard, "Confocal fluorescent microscopy with a finite-sized circular detector," *J. Opt. Soc. Am. A* **9** (1), pp. 151–153 (1992).

[Gus99] M. Gustafsson, D. Agard, and J. Sedat, "I^5M: 3D widefield light microscopy with better than 100 nm axial resolution," *J. Microsc.* **195** (1), pp. 10–16 (1999).

[Hel92] S. Hell and E. H. Stelzer, "Properties of a 4Pi confocal fluorescence microscope," *J. Opt. Soc. Am. A* **9** (12), pp. 2159–2166 (1992).

[Kak79] A. C. Kak, "Computerized tomography with X-ray, emission, and ultrasound sources," *P. IEEE* **67** (9), pp. 1245–1272 (1979).

[Kak87] A. C. Kak and M. Slaney, *Principles of computerized tomographic imaging*. IEEE Press, New York (1987).

[Kaw87] S. Kawata, O. Nakamura, and S. Minami, "Optical microscope tomography. I. Support constraint," *J. Opt. Soc. Am. A* **4** (1), pp. 292–297 (1987).

[Kaw90] S. Kawata, O. Nakamura, T. Noda, K. Ooki, K. Ogino, Y. Kuroiwa, and S. Minami, "Laser computed-tomography microscope," *Appl. Opt.* **29** (26), pp. 3805–3809 (1990).

[Kim00] M. K. Kim, "Tomographic three-dimensional imaging of a biological specimen using wavelength-scanning digital interference holography," *Opt. Express* **7** (9), pp. 305–310 (2000).

[Kou08] S. S. Kou and C. J. R. Sheppard, "Image formation in holographic tomography," *Opt. Lett.* **33** (20), pp. 2362–2364 (2008).

[Kou09] S. S. Kou and C. J. R. Sheppard, "Image formation in holographic tomography: high-aperture imaging conditions," *Appl. Opt.* **48** (34), H168–H175 (2009).

[Küh09] J. Kühn, F. Montfort, T. Colomb, B. Rappaz, C. Moratal, N. Pavillon, P. Marquet, and C. Depeursinge, "Submicrometer tomography of cells by multiple-wavelength digital holographic microscopy in reflection," *Opt. Lett.* **34** (5), pp. 653–655 (2009).

[Lau02] V. Lauer, "New approach to optical diffraction tomography yielding a vector equation of diffraction tomography and a novel tomographic microscope," *J. Microsc.* **205** (2), pp. 165–176 (2002).

[Mai10] G. Maire, J. Girard, F. Drsek, H. Giovannini, A. Talneau, K. Belkebir, P. C. Chaumet, and A. Sentenac, "Experimental inversion of optical diffraction tomography data with a nonlinear algorithm in the multiple scattering regime," *J. Mod. Optic* **57** (9), pp. 746–755 (2010).

[MF06] C. Meneses-Fabian, G. Rodriguez-Zurita, and V. Arrizón, "Optical tomography of transparent objects with phase-shifting interferometry and stepwise-shifted Ronchi ruling," *J. Opt. Soc. Am. A* **23** (2), pp. 298–305 (2006).

[Mon06] F. Montfort, T. Colomb, F. Charrière, J. Kühn, P. Marquet, E. Cuche, S. Herminjard, and C. Depeursinge, "Submicrometer optical tomography by multiple-wavelength digital holographic microscopy," *Appl. Opt.* **45** (32), pp. 8209–8217 (2006).

[Nod90] T. Noda, S. Kawata, and S. Minami, "Three-dimensional phase contrast imaging by an annular illumination microscope," *Appl. Opt* **29** (26), pp. 3810–3815 (1990).

[Nod92] T. Noda, S. Kawata, and S. Minami, "Three-dimensional phase-contrast imaging by a computed-tomography microscope," *Appl. Opt.* **31** (5), pp. 670–674 (1992).

[Pan83] S. Pan and A. Kak, "A computational study of reconstruction algorithms for diffraction tomography: Interpolation versus filtered backpropagation," *IEEE T. Acoust. Speech* **31** (5), pp. 1262–1275 (1983).

[Paw06] J. B. Pawley, Ed., *Handbook of biological confocal microscopy*, 3rd ed. Springer, New York (2006).

[Sch99] J. Schmitt, "Optical Coherence Tomography (OCT): a review," *IEEE Journal on Selected Topics in Quantum Electronics* **5** (4), pp. 1205–1215 (1999).

[Sla84] M. Slaney, A. C. Kak, and L. E. Larsen, "Limitations of Imaging with First-Order Diffraction Tomography," *IEEE T. Microw. Theory* **32** (8), pp. 860–874 (1984).

[Str85] N. Streibl, "Three-dimensional imaging by a microscope," *J. Opt. Soc. Am. A* **2** (2), pp. 121–127 (1985).

[Sun09] Y. Sung, W. Choi, C. Fang-Yen, K. Badizadegan, R. Dasari, and M. Feld, "Optical diffraction tomography for high resolution live cell imaging," *Opt. Express* **17** (1), pp. 266–277 (2009).

[Tam81] K. Tam and V. Perez-Mendez, "Tomographical imaging with limited-angle input," *J. Opt. Soc. Am.* **71** (5), pp. 582–592 (1981).

[Ver09] S. Vertu, J.-J. Delaunay, I. Yamada, and O. Haeberlé, "Diffraction microtomography with sample rotation: Influence of a missing apple core in the recorded frequency space," *Cent. Eur. J. Phys.* **7** (1), pp. 22–31 (2009).

[Wed95a] T. Wedberg, J. Stamnes, and W. Singer, "Comparison of the filtered backpropagation and the filtered backprojection algorithms for quantitative tomography," *Appl. Opt.* **34** (28), pp. 6575–6581 (1995).

[Wed95b] T. C. Wedberg and J. J. Stamnes, "Experimental examination of the quantitative imaging properties of optical diffraction tomography," *J. Opt. Soc. Am. A* **12** (3), pp. 493–500 (1995).

[Wed96] T. Wedberg and J. Stamnes, "Recent results in optical diffraction microtomography," *Meas. Sci. Technol.* **7** (3), pp. 414–418 (1996).

[Wol69] E. Wolf, "Three-dimensional structure determination of semi-transparent objects from holographic data," *Opt. Commun.* **1** (4), pp. 153–156 (1969).

5 Applications of DHM in neurobiology

We present in this chapter some applications of DHM for observation of cellular cultures *in vitro*. As previously mentioned in this manuscript, DHM can be seen as a phase imaging technique, which is well suited in transmission for probing nearly transparent objects such as cellular structures. Furthermore, the quantitative nature of the retrieved signal, which depends on the cell height and its intracellular concentration, can be employed as an indicator of cell regulation capabilities, as it will be detailed in this chapter.

The DHM approach presents various very specific features which makes it suited for cellular observation applications. Typically, the one-shot capability of off-axis holography enables monitoring rapid phenomena, as the acquisition speed is only limited by the frame rate of the digital detector. Furthermore, thanks to the very low light power employed, cells can be observed at high rates for long times without risking any photo-damage problems. Acquisition can typically be performed with shutter times in the hundreds of microseconds range with an optical power as low as 1 mW. These features distinguish DHM technology from for example fluorescence methods, as frame rate, photo-damage and bleaching are common issues in this case. Finally, since DHM relies on intracellular refractive index changes to generate the image, it can be seen as an intrinsic contrast method, where no labelling is required for imaging the sample.

The applications presented in this thesis are based on cellular observation in the context of neuroscience, where co-cultures (neurons and glial cells) are monitored through time. It has been demonstrated that the quantitative phase signal measured on cells can be employed to derive various biologically relevant quantities, such as dry mass, or haemoglobin content in the context of red blood cells. In the case of neurons, cells have some specific features which make the study with DHM rather specific in terms of interpretation. As discussed in the introduction below, they are polarised cells, so that they possess the ability of modulating the ionic currents through their cellular membrane. Quantitative phase measurements can therefore be linked in this context with ionic movements, a key parameter driving neuronal activity.

In this chapter, we thus first provide in section 5.1 an introduction on cellular neurobiology, in order to define the context in which the measurements are performed, and to provide the tools for interpreting the results. We also briefly discuss the motivation leading to the research projects of this chapter in section 5.2 and then describe our methods and experimental protocols in section 5.3. We then present the first research topic in section 5.4, where DHM is employed to detect cell death at early stage, and provide in a second stage some elements linking cell death detection with ionic homeostasis. We then develop in sections 5.5–5.7 the second research topic, where DHM is related to intracellular ionic concentrations through comparison with fluorescent ionic indicators. The analysis is performed firstly by comparing temporally simultaneously recorded signals (cf. section 5.5). The origins of the phase signal are then decomposed through pharmacological tool in section 5.6. Finally, quantitative comparisons between phase and calibrated fluorescent signals are performed in section 5.7. As it can already be seen at this stage, the two approaches are closely related in terms of cellular ionic homeostasis. Finally, the various results obtained in this chapter are discussed along with perspectives in section 5.8.

The material presented in this chapter was partly adapted from various publications. The work on cell death was published in [Pav11b; Pav11a], and the work on intracellular ionic concentration monitoring was published in [Pav10a; Pav10b].

5.1 Fundamentals of neuroscience

We present in this section some fundamental concepts of neuronal cell biology, in order to provide the context enabling the interpretation of the results of this chapter. This introduction should however not been considered as a proper state of the art, since many aspects of neuroscience are overlooked, as we limit our discussion to subjects directly related to the research field described in this chapter, consisting in neuronal processes at cellular level, and focus our discussion to neurons of the central nervous system (CNS). This approach implies that some descriptions may seem simplistic to specialists, as we do not consider for instance directly molecular biology, even though many results, such as the classification of neuronal receptors, follows from results using these methods. For the same reasons, we do not provide specialised references during this general discussion. Most of the material described in this introduction can be found for instance in textbooks such as [Ham01] or [Pur08].

5.1.1 Morphology and cellular processes in neurons

Neuronal cells possess most of the organelles and functions of eukaryotic cells, where some of their most distinguishable properties consist in the fact that they commonly do not divide after their differentiation, and develop a network between cells. Their morphology is typically easily recognised by the presence of growths from their cell body—or soma, as shown in Fig. 5.1. Several types of neurons exist in various part of the body, and in the CNS. Although

these cells have different functions and morphologies, most of the general considerations given here are valid for any neuron type.

During brain development, the growths emerge from differentiated cells, interconnecting and creating the neuronal network. They can be divided in two main categories, which are different at both structural and functional levels. On one side, dendrites have essentially a receptive role, and aim at transmitting the information from the dendritic tree to the soma. On the other hand, axons typically have a function of transmission from the cell body to the neuronal network. A more detailed discussion of the neuronal connections and network is provided in subsection 5.1.3.

One primary function of a cellular body is to maintain a physiological equilibrium (chemical, electrical, volume) — commonly defined as homeostasis — between the intracellular body and the external medium, delimited by the lipid bilayer composing the cell membrane. In particular, an equilibrium is maintained for ions in solution, which can generate strong concentration gradients, as shown in Table 5.1 for the most common ions in physiological solutions. These gradients imply that there is, at physiological equilibrium, an electrical difference of potential through the membrane which is defined as $V_m = V_i - V_e$, where the indices i, e respectively denote for the intracellular and extracellular electrical potentials. The membrane potential (MP) is induced by the ionic concentration gradients. For example, the most common negatively charged elements in cells consist in organic molecules. In the case of neurons, the overall MP in equilibrium conditions, also denoted as the resting potential, can be determined to be approximately $V_m = -60$ mV, although this value can vary between neuron types.

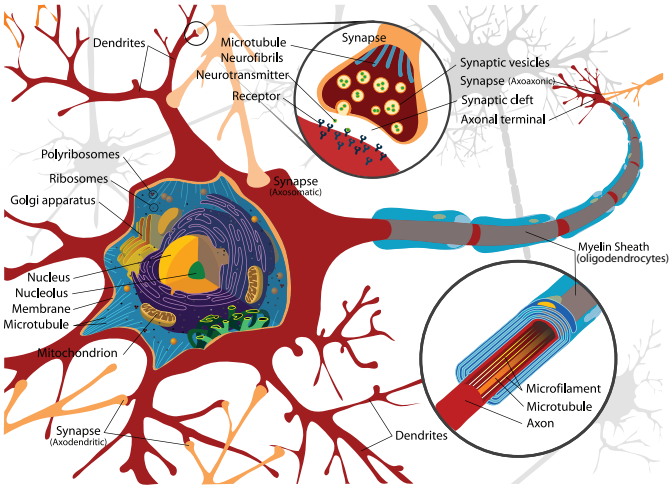

Figure 5.1: Typical morphology of a neuronal cell. (Adapted from [Vil11])

One main characteristic of neurons is that their MP varies greatly depending on their excitation state, so that they are classically denoted as polarised cells. The MP can thus change from typically −90 mV in a hyperpolarised state to +30 mV in a depolarised state. The ability

to adapt their MP implies that neurons possess mechanisms to change the intracellular ionic concentrations, which should depend on physiological parameters to enable ionic homeostasis. The main pathways for ionic fluxes and regulation capabilities are presented in subsection 5.1.2.

Ion	Concentration [mM]	
	Intracellular	Extracellular
K^+	140	3
Na^+	7	140
Cl^-	7	140
Ca^{2+}	10^{-4}	1.5

Table 5.1: Typical intracellular and extracellular ionic concentrations for neuron cells.

In the context of ionic regulation, it is worth to detail the case of calcium, which is rather particular. As it can be seen in Table 5.1, intracellular Ca^{2+} concentration ($[Ca^{2+}]$) is extremely low compared to other ions. This is essentially due to the fact that part of the intracellular calcium is not contained as solute in the cytosol (commonly called "free calcium"), but is stored in various organelles, such as endoplasmic reticulum or mitochondria. These organelles provide a second regulation way for free $[Ca^{2+}]$, through Ca^{2+} uptake in those so-called calcium compartments.

Finally, the external environment encompassing neurons is composed of various cellular types, commonly referred to as glial cells. The functions of these cells and their interaction with neurons has been a subject of increasing interest in recent research. Fundamentally, glial cells have as a primary function to regulate the environment in which neurons are contained, which consists for example in controlling the energetic exchange with blood vessels through astrocytes cells, or isolating axons from the external medium in the CNS through oligodendrocytes cells. Of particular interest in the context of this chapter are astrocytes; their functions are multiple and still under study, but one of their tasks is to regulate the external concentration of neurotransmitters, as detailed in subsection 5.1.3.

5.1.2 Neuronal dynamics

In order to enable the ability of modulating their MP, neuron cells require to have ways to change their intracellular ionic concentration. As the lipid bilayer is essentially impermeable to solutes, due to the hydrophobic part inside the cell membrane, ionic transmembranar movements must be made possible through specific sites on the membrane. These movements can occur through passive pathways, called channels, and active ones, such as pumps and co-transporters, as detailed below.

Ionic fluxes

Ionic channels consist in an ensemble of protein subunits situated through the whole cellular membrane, providing pathways for ionic transfer, as depicted schematically in Fig. 5.2(a–b), where its two states (closed and opened) are respectively represented. Channels have indeed the property of expressing a variable ionic permeability depending on external factors. Without entering into details of their chemical composition, they are essentially composed of hydrophobic and hydrophilic regions, enabling them to be chemically stable within the membrane. Furthermore, their complex three-dimensional conformation make them classically permeable to specific ions through complex electric charges distribution. An example is schematically provided in Fig. 5.2(c), for the case of the NMDA receptor, consisting in a ligand-gated channel. The change of state happens in a passive way by a variation in the environment, which can be of different nature depending of the channel type, such as an electrical, chemical, or mechanical variation.

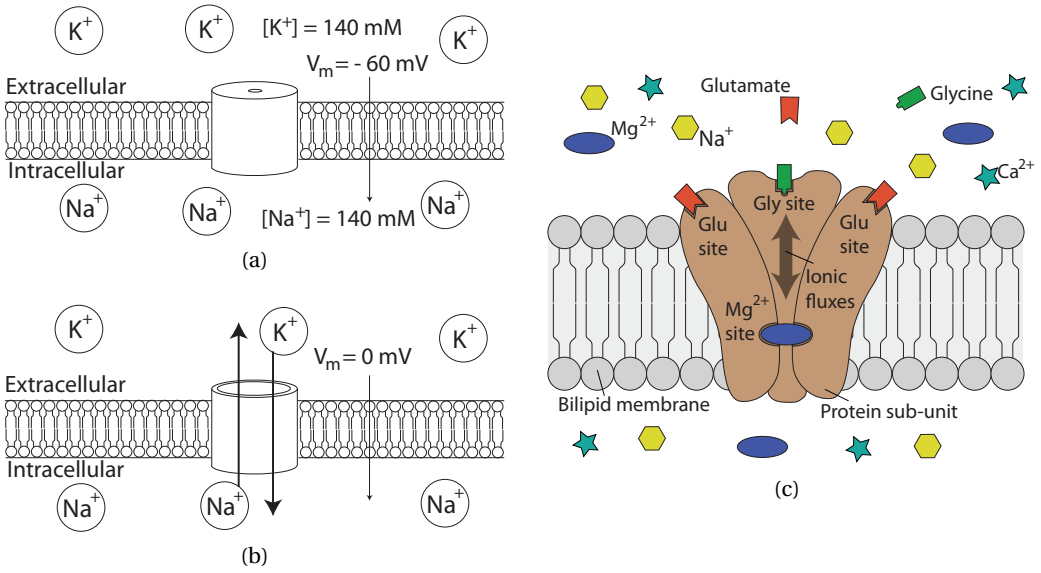

Figure 5.2: Schematic representation of a transmembranar voltage-gated channel in its (a) closed and (b) opened state and (c) 3D representation of a ligand-gated channel, for the particular case of the NMDA receptor. The conformation of sub-units can make the channel specifically permeable to some cations.

Channels dependent on electrical changes—usually called voltage-gated channels—are typically controlled through MP variations. Therefore, since the state of the channel depends on the MP, and as channels are usually permeable to specific ions, it implies that the conductance for a given ion will depend on the global ionic concentrations across the cellular membrane.

On the other hand, chemically stimulated channels—or ligand-gated channels—are activated through the bonding of a molecule. They are typically receptive to neurotransmitters, which are molecules of various nature, secreted by neurons for chemical transmission of

information and excitatory/inhibitory purposes. Typical neurotransmitters are for example acetylcholine, γ-aminobutyric acid (GABA) or glutamate, which is discussed in more details in subsection 5.1.4. Ligand-gated channels are commonly defined by the name of a molecule which specifically activates them, and defined as an agonist. Most neurotransmitters are typically non-specific agonists, as they can usually activate various types of receptors. On the other hand, one defines an antagonist as a molecule bonding with a receptor without activating it, and thus blocking the effect of agonist molecules.

One should note that channels can be considered as passive elements, as most of them are opened through external physical factors such as chemical bonding or voltage changes. Ionic fluxes are then driven through passive diffusion, and thus tend only to establish a physical equilibrium state between the two sides of the cellular membrane. Consequently, according to Table 5.1, channels only allow for entrance of K^+, and exit of Na^+, Cl^- and Ca^{2+}.

Apart from the purely physical causes for opening channels, cells possess also regulation capabilities. In particular, some molecules can typically inactivate or desensitise channels, so that their state would remain closed although the threshold MP has been reached for voltage-gated one, or although the bonding with an agonist occurred for a ligand-gated one.

In order to counter the diffusion mechanisms, cells require also ways to transfer ions across their membrane against ionic concentrations. These ways are denoted as active, as they require energy, and their ionic conductivity is typically lower than the one of channels. Typical active pathways imply for example ATP hydrolyse to provide the energy necessary for moving ions across the membrane against the diffusion direction (ATPases). Another pathway consists in employing the concentration gradient of an ion to provide the energy for transporting a second ion against its diffusion direction. For example, employing the energy released through entrance of sodium is employed by the so-called Na^+/Ca^{2+} co-transporter to evacuate intracellular calcium. ATPases and transporters require an activation, which is typically triggered by secondary messengers such as intracellular Ca^{2+} or proteins. The complex molecular mechanisms involved in this type of indirect activation is however out of the scope of this introduction.

Action potentials

An action potential is a rapid and transient change in the membrane potential of a neuron, and corresponds to an excited state of the cell, for which the various stages are shown in Fig. 5.3. The action potential usually results from an external stimulation, which induces an initial membrane depolarisation. This then turns into a strong depolarisation of the cell through cascade events, which is followed by a repolarisation, aiming at returning gradually to the resting state.

The strong membrane depolarisation results from the opening of voltage-gated channels, under a small initial MP variation. These channels can typically be permeable either to Na^+

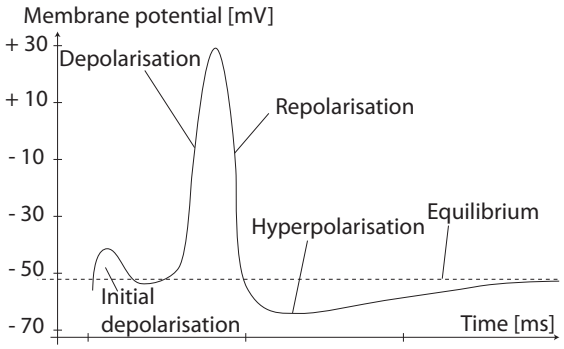

Figure 5.3: Typical membrane potential dynamics during an action potential.

or Ca^{2+} ions. Their entry in the intracellular content increase the depolarisation, which in turn favours the opening of channels, thus inducing a chain reaction which generates the action potential. This phenomenon is then gradually stopped by regulation capabilities of the cell, through inactivation of the voltage-gated channels, and opening of K^+ channels, which ensure the exit of cations to repolarise the membrane, and gradually retrieve an equilibrium. The respective ionic concentrations can then be regulated through ATPases and co-transporters, as discussed previously. This regulation process usually involves an oscillatory behaviour leading to hyperpolarisation around the resting potential, as the equilibrium is gradually reached.

The chain reaction of channel opening through initial depolarisation enables also the propagation of the action potential along dendrites and axons, through gradual depolarisation along the membrane on long distances. Depending on the action potential type, a typical attenuation is present during propagation, along with a temporal spread of the depolarisation peak.

An action potential is thus stimulated by an initial depolarisation, which can be induced in various ways. The most usual case is based on action potentials transmitted from other neurons, which is then propagated to other cells through neuronal connections, as detailed in subsection 5.1.3. More particular cases worth mentioning are oscillating neurons which generate action potentials at periodic intervals without external stimulation, or sensory neurons, which emit action potentials under external stimulation, such as the detection of specific chemicals (olfactory system), or mechanical strain (sensation or auditory system). Experimentally, an action potential can typically be induced through patch clamp, thus directly enabling MP electrical driving, or the perfusion of specific substances such as neurotransmitters, as detailed in subsection 5.1.4.

5.1.3 Neuronal network

One of the main ability of neurons is to create networks through their dendrites and axons. The network is constructed by connections between cells, which are based on so-called

synaptic connections. A synapse is basically a narrow space between two cell membranes, where a very high concentration of receptors enables the transmission of information through chemical means, as shown schematically in Fig. 5.4. The space between the two membranes, of classically tens of nanometres, is usually called the synaptic cleft, in which a very high concentration of neurotransmitter can be found. The synapse can be divided in a pre-synaptic zone (the emitter) and a post-synaptic zone (the receptor) between which the chemical interaction between neurotransmitters molecules and receptors can occur. Synaptic connections are typically made by axons, the transmitting part of the neuron, to dendrites, the receptive part. One should note however that other types of connections exist, such as axon-soma or axon-axon synapses, depending on the function of the connection.

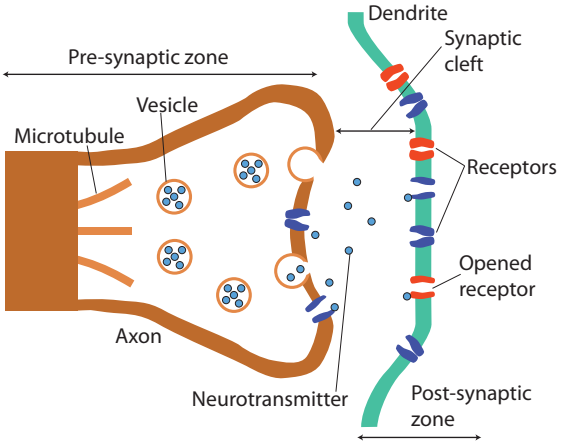

Figure 5.4: Schematic of a synaptic connection, showing the neurotransmitter release in the synaptic cleft through vesicle exocytosis, then activating receptors on the post-synaptic zone.

Synaptic transmission

The main function of synaptic connections is thus to transmit and regulate action potentials, which are transferred from the pre-synaptic region by local secretion of neurotransmitters to the post-synaptic region through detection of the neurotransmitter by receptors. The synaptic transmission, based on a chemical means, is therefore classically slower than the propagation of the action potential through dendrites or axons, where the propagation is based on ionic movements and consequent MP changes, and implies a delay in the transmission.

The basic transmission dynamics of the action potential at synaptic level (cf. Fig. 5.4) implies (i) the propagation of the action potential to the axon termination, (ii) the secretion of neurotransmitter molecules in the synaptic cleft from the pre-synaptic zone, typically through exocytosis of vesicles, (iii) the bonding of the neurotransmitter to receptors situated at post-synaptic level, locally changing the MP of the post-synaptic membrane and potentially triggering a post-synaptic potential, either excitatory (EPSP), or inhibitory (IPSP), which propagates to the soma, (iv) the repolarisation of the membrane and disposal of the released neurotransmitter.

The receptors at post-synaptic level are essentially of two classes, ionotropic and metabotropic. The ionotropic receptors consist in ligand-gated channels, which are activated by the bonding of the neurotransmitter, leading to membrane depolarisation at post-synaptic level through ionic fluxes. This mechanism is the primary effect which initiates the post-synaptic potential, again through opening of voltage-gated channels passed a certain MP threshold, where it will then again propagate along the post-synaptic dendrites.

Metabotropic receptors have a more complex functioning principle, which involves secondary messengers after ligand bonding. Globally, the main difference compared to ionotropic receptors is their temporal behaviour, which is much slower. While ionotropic receptors are opening in a matter of milliseconds, and are then very rapidly inactivated, metabotropic receptors can stay opened for seconds to minutes, and thus have far longer effects. One should note finally that the pre-synaptic region also contains a high concentration of receptors, which can serve mainly for regulation. The activation of these pre-synaptic receptors can typically lead to the inhibition of the secretion of neurotransmitters some time after an action potential occurred.

Quite rapidly after the generation of the post-synaptic potential, the neurotransmitter requires to be removed from the synaptic cleft, in order to avoid toxic effects induced by a too strong stimulation. In the case of glutamate, this is typically performed by astrocytes, a certain type of glial cells, which rapidly absorb the neurotransmitter and synthesise it to glutamine, which is then commonly transferred back to neurons, where it is processed again to glutamate for further use.

The initiation of an action potential to a neuron soma is thus based on the accumulation of transmitted post-synaptic potentials at dendritic level, which can potentially reach the triggering membrane potential at soma level to initiate the action potential on the neuron. One should note however that this cumulative effect depends on various parameters. Typically, synaptic transmissions can be composed of EPSP and IPSP, which are then summed on all the dendritic tree. Furthermore, the cell itself can also be inhibited by internal means, such as temporary inactivation of voltage-gated channels. All those phenomena will determine globally the cellular state for a neuron type at a given time, and influence the possible triggering of an action potential.

5.1.4 Effect of neurotransmitters: case of glutamate

Glutamate is one of the major neurotransmitters in the CNS. We focus more specifically in this subsection on the effect of this substance, as it is the main stimulation mean employed for exciting neurons during experimental observation presented in this chapter. As described briefly in the paragraphs above, the effect of a neurotransmitter is expressed by the receptors with which it bonds. In the case of glutamate, results of molecular biology made possible to classify receptors in subtypes, depending on the expression of subunits composed of various proteins which influence their functional behaviour.

Glutamatergic ionotropic receptors can be divided in two main types, depending on their sensitivity to the NMDA agonist. Then, in non-NMDA receptors, a separation is classically done between AMPA and Kainate receptors, which possess different behaviours. The main characteristics of those receptors are summarised in Table 5.2, along with classical antagonists and inhibitors. The list of substances presented is far from exhaustive, but tends to present all the drugs employed during the experiments presented in this chapter.

Type	NMDA	AMPA	Kainate
Agonists	Glutamate		
	NMDA, [Glycine]	AMPA	Kainate
Antagonist	MK-801	DNQX	
Ionic permeability	Non-specific Na^+, K^+, Ca^{2+},...	Cations Na^+, K^+, ...	Cations and partly divalent cations Na^+, K^+, Ca^{2+},...

Table 5.2: Main classification of glutamate receptors and substances employed in the experiments as blockers.

NMDA receptors

NMDA receptors (NMDAr) enclose a wide class of subunits composition, which nevertheless possess mostly identical characteristics. Those receptors are essentially ligand-gated ionotropic channels, sensitive in a non-selective way to glutamate, but are very particular in various aspects. The first one would be the presence of two ligand sites, with only one of them sensitive to glutamate (Glu site), while the other is typically triggered by the bonding of glycine (Gly site), another neurotransmitter (cf. Fig. 5.2(c)). Glycine typically potentiates the NMDAr, greatly improving their conductance upon bonding of glutamate, and is thus considered as a co-agonist. The second particularity is that the ionic permeability of NDMAr is greatly influenced by the presence of magnesium, which blocks the channel in physiological conditions (resting membrane potential, standard ionic concentrations), so that they stay in a closed state even when bonded to glutamate.

This implies that NMDAr, although being fundamentally ligand-gated, are in practise voltage-gated, as a depolarisation of the membrane can suppress the inhibition induced by the so-called Mg^{2+} block, and enable ionic fluxes through the channel. When activated, the NMDA channels are essentially permeable to any cations without discrimination, univalent or divalent.

On a functional aspect, NMDAr are usually activated with a certain delay, due to their voltage dependence. It is thus classically required that other receptors activated in order to initiate the membrane depolarisation and thus remove the Mg^{2+} block before NMDAr can have an influence on the ionic fluxes. After activation, these receptors are mainly responsible for the Ca^{2+} entry through the membrane, which is responsible for more complex phenomena such as cascade signalling, leading to an increase of conductance of other receptors, and post-

synaptic effects such as the density increase of AMPAr. NMDAr can typically be inhibited by the channel blocker dizocilpine, also denoted as MK-801.

AMPA-Kainate receptors

AMPA and Kainate receptors are generally denoted as non-NMDA receptors (non-NMDAr), and are classical ligand-gated channels, activated non-selectively by glutamate. AMPAr are permeable to univalent ions, and thus essentially contribute to Na^+ entrance under glutamate application. On the other hand, Kainate receptors conductance depends on the subunit considered. While some of them are essentially permeable to univalent ions such as Na^+, some others are also conductive for divalent ions and especially Ca^{2+}. These classes of receptors are often generically denoted as non-NMDA, as their effect is often difficult to separate in pharmacological studies, and possess various common characteristics.

Non-NMDAr thus contribute to the initial membrane depolarisation, which can potentially activate indirectly NMDAr by bypassing the Mg^{2+} block through MP changes. Their activity is also enhanced through cascade signalling, as Ca^{2+} entering through NMDAr can then enhance their conductance to Na^+, thus creating a chain reaction. Non-NMDAr can typically be inhibited non-selectively by the antagonist DNQX.

Global effect of glutamate

As it can be seen from the discussion above, glutamate affects neurons through the activation of various receptors so that its effect is thus primarily located on synapses, where the density of receptors is far greater. It contributes in generating EPSP, potentially yielding neuronal action potentials. It is also known that glutamate can have strong excitotoxic effects, essentially by inducing high $\left[Ca^{2+}\right]$, potentially leading to neuronal death (cf. subsection 5.4.1).

5.1.5 Phase signal in the context of neuronal cultures observation

In the context of cell observation, the quantitative phase signal corresponds to the relative phase shift induced by the cell body compared to one induced by the external medium, and thus relates to the integrated refractive index (RI) along the optical axis and the cell height, according to Eq. (2.16). This equation can be further simplified, by considering the mean refractive index along the optical axis. The phase value can thus be defined as an optical path difference (OPD) between the phase shift induced by the cell and the phase shift defined on a zone without specimen, giving

$$\begin{aligned}\varphi_i(x,y) - \varphi_m(x,y) = \Delta\varphi(x,y) &= \frac{2\pi}{\lambda}\mathrm{OPD}(x,y) \\ &= \frac{2\pi}{\lambda}\left(n_i(x,y) - n_m\right)h(x,y),\end{aligned} \tag{5.1}$$

where n is the mean RI along z, the indices i, m correspond respectively to the intracellular body and to the perfusion medium, and h is the height of the cell at position (x, y) in the field of view. This implies that the phase signal can be considered as an indirect indicator of volume, as changes in intracellular dilution also imply volume variations through osmotic pressure.

In the context of neuronal cells, ionic fluxes through the cellular membrane are of great importance for neuron functions such as information transmission and regulation, as ionic currents regulate the generation and propagation of post-synaptic and action potentials. The opening of ionic channels can therefore be indirectly monitored through phase measurements, as they induce strong ionic currents, which will imply both intracellular concentration changes and consequent volume variations. The exact relation between phase and volume is however usually complicated to derive, due to the multiplicity of mechanisms involved in the generation of the phase shifts at specimen level.

It is worth mentioning at this point that various methods were proposed to resolve the ambiguity in the expression of the phase, which can make the interpretation of the signal sometimes difficult, by decoupling the two variables, namely the RI n_i and the cell height $h(x, y)$. One approach consists in using different perfusion solutions, for which the difference in refractive index is well known. This leads to two measurements for the same cell body, thus making possible to fully determine the system [Rap05]. Typically, it could be shown through this method that volume changes are not isotropic in the case of cell cultures, i.e. volume changes are less important along the optical axis direction than in the $x-y$ plane [Pav10a]. This approach has however the drawback of providing two measurements at different times, so that phase variations can occur between the change of perfusion medium. Another technique consists in employing different wavelengths for measurement in a solution with a dye enhancing the dispersion, so that the refractive index of the solution changes significantly for the two wavelengths [Rap08a]. This approach is very promising for rapid phase monitoring, as it can potentially be performed during one acquisition, through spatial multiplexing of the interference signals, in a similar way as demonstrated in the case of reflection configuration DHM [Küh07].

5.2 Context and motivation

The work presented in this chapter has been motivated by preliminary works showing an excellent temporal correlation between intracellular Ca^{2+} dynamics measured through fluorescence and quantitative phase [Mar03; Rap08b], where the two signal types had been measured on identical cell cultures in similar conditions, but with different experimental setups at various times. Some temporal discrepancies could not be explained, leading to think that experimental bias could be present, and showing the need for an arrangement where simultaneous measurements could be performed.

On the other hand, some works demonstrated the possibility of measuring phase and fluorescence signals in a common-path configuration with the same detector [Par06], although this was preventing simultaneous acquisition, because of the different exposure times required for the two signals. Furthermore, preliminary measurements performed with the setup of Fig. 2.16 demonstrated the possibility of measuring both signals with two dedicated cameras, where the temporal delay between the two measurements was only due to the flipping time of the mirror determining on which camera the image was performed.

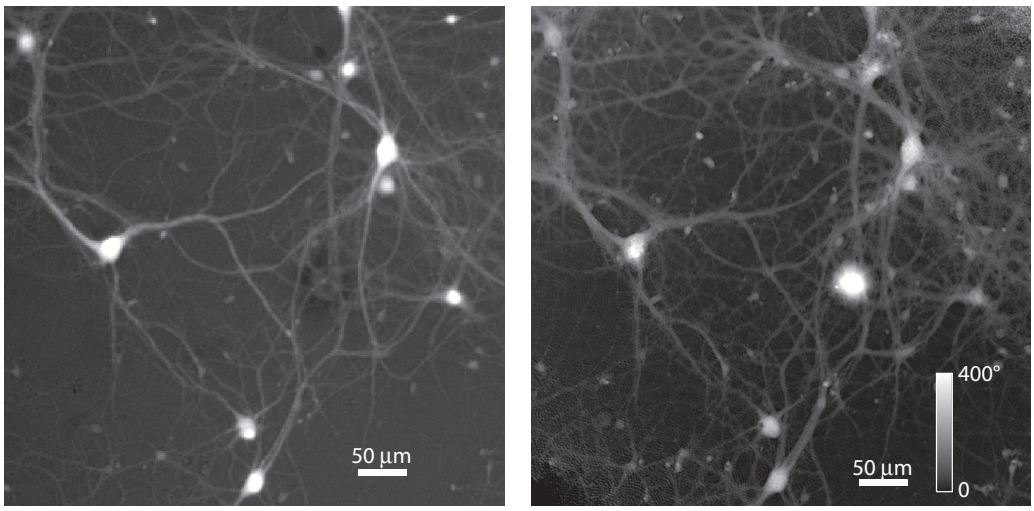

(a) (b)

Figure 5.5: Simultaneous measurement of (a) fluorescent signal of the Ca^{2+} indicator Fluo-4 during a glutamate-induced action potential and (b) the corresponding phase image.

The recent availability of a fluorescence module developed by Lyncée Tec for the transmission DHM T1000 opened the possibility of systematic biological measurements thanks to the simultaneity of measurements through spectral selections of the various signals (cf. subsection 2.4.3), on a well-characterised setup which does not present the drawbacks of a lab-made setup which reproducibility of measurements is sometimes difficult to ensure. Some results obtained with this implementation are shown in Fig. 5.5, with the fluorescent image measured on neuron cells with the Fluo-4 $\left[Ca^{2+}\right]$ indicator during a stimulation through perfusion of glutamate (cf. Fig. 5.5(a)), and the corresponding phase image (cf. Fig. 5.5(b)), where the quantitative scale is provided. The measurements were acquired with a 10× (NA = 0.3) MO [Pav10a].

The preliminary results obtained in this fashion demonstrated a striking simultaneity between calcium bursts measured with fluorescence and quantitative phase measured on glutamate-stimulated neurons, as it can be identified in Fig. 5.6, where the calcium increase induced by the action potential is correlated with a decrease in phase.

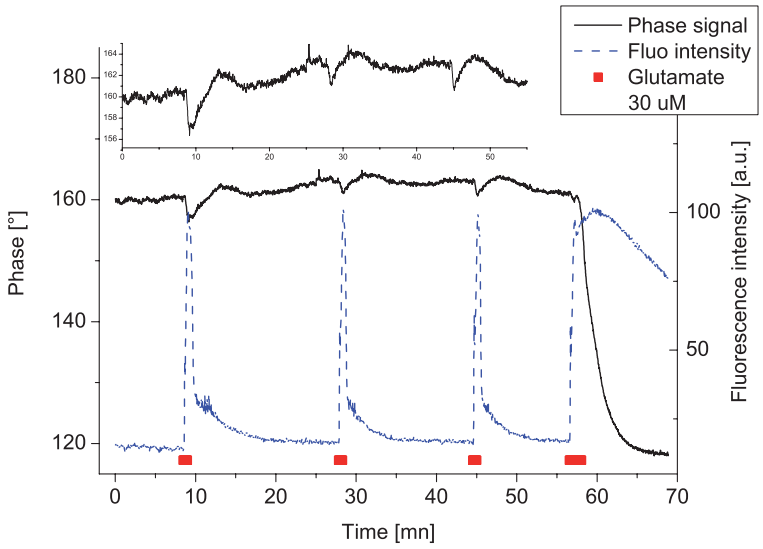

Figure 5.6: Quantitative phase and Fluo-4 fluorescence monitored on a neuronal soma during stimulation with glutamate, where the temporal correlation between the two signals can be identified.

Although the temporal similarities are important in the results shown in Fig. 5.6, a conclusive interpretation of the biological relations of the phase signal and $[Ca^{2+}]$ concentration is difficult, as no direct correspondence between the slower phase signal shape and the rapid calcium burst could be deduced. The need for other indicators was thus identified; however, one of the main issue with most of fluorescent indicators is their absorption band in the UV range, making usually difficult to provide a satisfactory excitation with standard optics. Furthermore, passing from ionic imaging to quantitative data is experimentally not trivial, as it requires calibrations and evenness of excitation. A new fluorescent excitation module was thus designed and characterised specifically to satisfy those requirements, leading to the results presented in sections 5.5–5.7.

On the other hand, previous studies of neuronal dynamics with DHM methods showed that the signals measured on cell body could be divided in several kinds, depending on the cellular state after stimulation [Jou11]. In particular, certain types of phase responses seemed to be typical for cells undergoing death mechanisms triggering [Mar03]. An interest thus rose to demonstrate the possibility of detecting cell death with DHM by comparing it with known methods for cell viability assessment. These considerations led to the work presented in section 5.4.

5.3 Materials and methods

5.3.1 Experimental procedure

Culture preparation

The studies are performed on primary cultures of mouse cortical neurons, obtained according to the method described by Brewer *et al.* [Bre93], briefly described here. Cortices are removed under a dissecting microscope from brains and collected in a small Petri dish in PBS-glucose. Single-cell suspension is obtained by gentle pummelling with a fire-polished Pasteur pipette in Neurobasal medium supplemented with B27 and GlutaMAX (Invitrogen). Cells are then plated at an average density of 15000 cells/cm^2 in supplemented Neurobasal medium on poly-ornithine coated glass coverslips. After 3-4 hours, coverslips are transferred to dishes containing glial cell monolayers in supplemented Neurobasal medium. Neurons are maintained at 37 °C in a humidified atmosphere of 95% air / 5% CO_2 and are used after 21-35 days *in vitro*.

Perfusion chambers and washing methods

For observation under the microscope, slides with cell cultures are placed in a perfusion chamber, and immersed in a HEPES-buffered physiological perfusion medium containing (in mM): NaCl 140, KCl 3, $CaCl_2$ 3, $MgCl_2$ 2, Glucose 5, HEPES 10, adjusted to a pH of 7.3 with NaOH, according to concentrations proposed by Tao *et al.* [Tao00]. All experiments are performed at room temperature.

Depending on the type of experiment, the employed perfusion chamber is “opened”, as shown in Fig. 5.7(a), where the cover slip is maintained between two metal pieces with vacuum grease to ensure waterproofness, while the immersion liquid is maintained on top of it. When using this chamber, the change of perfusion medium is performed by employing a micropipette. In order to guarantee a stable phase signal free of perturbation induced by liquid movements, a tube is immersed in the liquid, thus providing a stable air-liquid interface defined by the glass window.

On the other hand, a “closed” chamber is also employed when frequent changes of the perfusion medium are required, as shown in Fig. 5.7(b). In this case, a plastic piece ensures a constant spacing between the slide and a window glass, thus containing the cell culture in a closed environment. The perfusion is sent in the chamber through tubes, so that the medium change can be performed with an automatic valve (Kloehn), with the shape of the chamber ensuring a rapid washout of the medium.

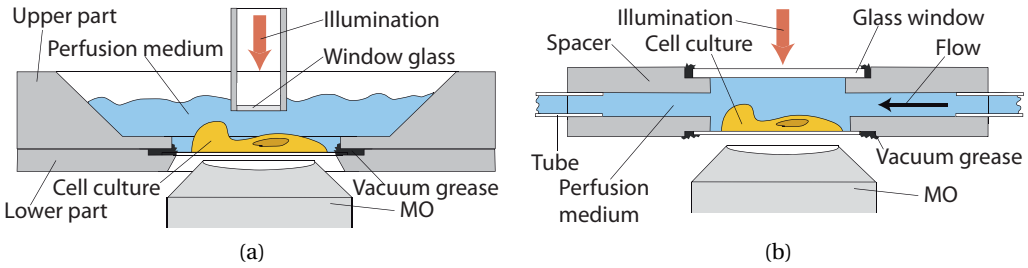

Figure 5.7: Perfusion chambers (a) opened chamber, where the perfusion medium is static, with a window glass ensuring a stable medium-air interface, and (b) closed chamber, where a flow is used to change the perfusion solution.

5.3.2 Colour and fluorescent dyes procedures

Trypan blue assay

Trypan blue is a dye employed for cell viability assessment. It relies on the membrane permeability change upon cell death, and bonds essentially to the nucleus. This implies that, after immersion of the culture in a dye solution and subsequent wash, nuclei of non-viable cells can be identified in blue.

The trypan blue dye (0.4% reagent, diluted (10×) in water with 0.85% NaCl (Lonza)) is typically used during the experiments presented in section 5.4. The reagent is directly diluted in the perfusion medium at a proportion 1:10. No specific procedures are performed to compensate for the osmolarity change due to the dilution.

Cells are typically immersed during 3 minutes in the trypan blue dilution before washing out the reagent with standard perfusion medium. This low concentration and short exposure time is chosen in order to avoid staining healthy cells, as a too long exposure to trypan blue can lead to cytotoxic effects and false positives through viable cells staining [Hud80; Jon85]. Measurements are performed with the setup described in subsection 2.16, where holograms and colour images acquisitions are performed with separated cameras.

Fluorescent dye observation

Fluorescence is detected with the setup presented in subsection 2.4.3, which consists for the fluorescence of a standard wide field epifluorescence system. The fluorescent excitation is sent to the specimen with a dichroic mirror (cutting wavelength at 506 nm) with a large spectral bandwidth, enabling its use also with UV light. The collected signal is then filtered with a long-pass emission filter ($500-750$ nm), and detected with an EMCCD camera. The spectral properties of the system make the measurement at various colours possible without any mechanical movements, and is thus used for all fluorescent measurements presented in this chapter.

Propidium iodide assay

Propidium iodide (PI) is a fluorescent indicator (λ_{exc} = 530 nm, λ_{em} = 630 nm) which bonds with DNA. It is thus employed for cell viability assessment, as a fluorescence signal implies a loss of membrane integrity through dye insertion. The detection can be made by detecting light emitted from nuclei on a dark background and thus do not require a wash of the reagent.

PI solution in water (1 mg/ml, BioChemika (Fluka)) is employed for cell viability assessment, performed *in situ* during experiments. The dye is thus diluted in the perfusion medium at a concentration of 5 µg/ml, and let in the medium during the whole experiment, enabling detection of gradual loss of membrane integrity.

The dye is excited at λ_{exc} = 490 nm, by using the same dichroic mirror as other experiments, with its emission detected in the 500 – 750 nm range, with an exposure time of 300 ms.

Calcium imaging with Fura-2

Fura-2 is a ratiometric Ca^{2+} indicator dye (λ_{exc} = 340 – 380 nm, λ_{em} = 510 nm) which absorption band varies upon bonding with calcium (cf. subsection 2.3.3).

Fura-2-AM salt (Invitrogen) is diluted at 2 mM in DMSO to prepare stock. For cell loading, stock is diluted at 4 µM in 1 ml of perfusion medium with 1% BSA to improve solubility of the dye. Cells are immersed in the loading solution and incubated at 37 °C for 30 min. The loading solution is then washed 2–3 times with perfusion medium, and cells are then incubated again for 15 min to ensure complete deesterification of the dye before measurement.

The dye is excited at $\lambda_{exc,1}$ = 340 nm and $\lambda_{exc,2}$ = 380 nm, with the fluorescence detected in the 500 – 750 nm range, with an exposure time of 500 ms. The fluorescence ratio is then calculated as described in subsection 5.3.3.

Calcium imaging with Fluo-4

Fluo-4 is a single-wavelength Ca^{2+} indicator dye (λ_{exc} = 494 nm, λ_{em} = 515 nm) which absorption efficiency varies upon bonding with calcium (cf. subsection 2.3.3).

Fluo-4-AM salt (Invitrogen) is diluted at 2 mM in DMSO to prepare stock. For cell loading, stock is diluted at 6 µM in 1 ml of perfusion medium with 0.1% Pluronic to improve solubility of the dye. Cells are immersed in the loading solution and incubated at 37 °C for 20 min. The loading solution is then washed 2–3 times with perfusion medium, and cells are then incubated again for 15 min to ensure complete deesterification of the dye before measurement.

The dye is excited at λ_{exc} = 490 nm, with the fluorescence detected in the 500 – 750 nm range, with an exposure time of 300 ms. The fluorescence signal is then obtained according to the procedure described in subsection 5.3.3.

Sodium imaging with SBFI

Benzofuran isophthalate (SBFI) is a ratiometric Na^+ indicator dye ($\lambda_{exc} = 340 - 380$ nm, $\lambda_{em} = 540$ nm) which absorption band varies upon bonding with sodium (cf. subsection 2.3.3).

SBFI-AM salt (Invitrogen) is diluted at 5 mM in DMSO to prepare stock. For cell loading, stock is diluted at 15 µM in 1 ml of perfusion medium with 0.1% Pluronic to improve solubility of the dye. Cells are immersed in the loading solution and incubated at 37 °C for 70 min. The loading solution is then washed 2–3 times with perfusion medium, and cells are then incubated again for 15 min to ensure complete deesterification of the dye before measurement.

The dye is excited at $\lambda_{exc,1} = 340$ nm and $\lambda_{exc,2} = 380$ nm, with the fluorescence detected in the $500 - 750$ nm range, with an exposure time of 500 ms. The fluorescence ratio is then calculated as described in subsection 5.3.3.

In the case of combined Fluo-4–SBFI measurements, cells are immersed for 60 min in the SBFI loading medium, time at which the Fluo-4 loading solution is added, for an incubation of 30 min in the mixed solutions. The mixing implies that loading concentrations are smaller than in standard protocols, which is partly compensated by the longer loading times.

Quantitative fluorescence calibration

In order to retrieve quantitative values from fluorescence measurements, an *in situ* calibration is performed at the end of the experiment, as described in subsection 2.3.3, to obtain the values (F_{min}, F_{max}), or (R_{min}, R_{max}), respectively for single-wavelength or ratiometric indicators. Calibration procedures are here performed for Ca^{2+} imaging exclusively. To reach the minimum calcium levels, a perfusion solution free of calcium (no $CaCl_2$ is inserted) is perfused with 8 mM of EGTA, a Ca^{2+} chelator [ED94], suppressing the extracellular calcium and inducing a Ca^{2+} release from cells. After reaching stable fluorescence levels, a solution free of Ca^{2+}, with 8 mM of EGTA and 5 µM of ionomycin, a Ca^{2+} ionophore [Erd00], is used to ease the suppression of intracellular calcium. This perfusion is maintained until reaching stable fluorescence signals; one should note that this procedure can be time consuming, because of Ca^{2+} compartments inside the cell making difficult to reach a proper minimum signal. Then, to reach the maximum calcium levels, a perfusion solution containing 10 mM of Ca^{2+} is then used to saturate cells. In order to accelerate the intracellular Ca^{2+} uptake, 5 µM of ionomycin is added. Furthermore, it has been noted that depolarising cells in order to open voltage-gated channels was dramatically accelerating the saturation by adding 80 mM of KCl in the perfusion medium.

5.3.3 Data extraction procedures

Phase extraction procedure

In the experiments of this chapter, holograms are acquired either with the setup shown in Fig. 2.16, with the extraction of the quantitative phase performed with a dedicated Matlab®

software, or with the setup shown in Fig. 2.17, with the phase recovery performed in this case with Koala^{TM} software, provided with Lyncée DHM® microscopes. State of the art reconstruction methods are described in subsection 2.2.5. When necessary, digital focusing is employed to compensate for potential specimen movements, thus ensuring a focused image throughout the whole experiment. Depending on the type of experiment, holograms are typically acquired from 0.1 Hz to 4 Hz. The phase is then unwrapped to suppress the phase ambiguity with a 2D unwrapping method (cf. for example [Tak88; Su04]).

The OPD induced by a cell body is then averaged on a constant region enclosed in the soma, and extracted from the whole temporal data set, thus providing a phase signal curve for each cell studied. When necessary, the cell body is tracked in the $x-y$ plane, to compensate for specimen movements during the experiment. The temporal phase signal is then filtered with a median filter to suppress aberrant values, so that phase values differing of more than 10° than the median value on five samples are replaced by the average value on the five samples. A baseline, measured on a portion of the field of view without cells is then subtracted to the phase signal. Finally, when appropriate, a temporal averaging is performed on curves, by averaging typically on three samples to reduce noise.

Fluorescence extraction procedure

Fluorescence images are acquired with the setup shown in Fig. 2.17, and the MetaFluor® software, with typical rates of 0.1 Hz for resting cells, or 0.5 Hz during stimulation. When necessary, mechanical refocusing is performed between glutamate pulses to ensure consistency of the fluorescence intensity throughout the experiment. The fluorescence values are then extracted with the same program, by measuring the averaged intensity on a constant region enclosed in the cell body. When necessary, the cell body is tracked in the $x-y$ plane to compensate for specimen movements or mechanical relaxation during the experiment.

From the fluorescence curves, a baseline measured on a region of the field of view where no cell is present is subtracted, to suppress the influence of parasitic reflection, stray light, etc. The presented data is then processed to the fluorescence ratio R in case of a ratiometric fluorophore (Fura-2 or SBFI), or a pseudo-ratio R' in the case of a single-wavelength indicator (Fluo-4), defined as (cf. subsection 2.3.3)

$$R = \frac{F_{\lambda_1}}{F_{\lambda_2}}, \qquad R' = \frac{F}{F_0}, \tag{5.2}$$

where F_0 is the fluorescence signal emitted by the cell at resting state.

In the case of simultaneous measurements between typically Fluo-4 and SBFI as presented in the next sections, some cross-talk occurs between the two fluorescence signals, so that a compensation procedure must be applied before processing the data, which is detailed in the control experiments of subsection 5.5.

Fusion of phase and fluorescence signals
In order to merge the signals of phase and fluorescence, a temporal synchronisation is necessary to ensure the adequacy of measurements, as the systems are driven by different computers, thus leading to an asynchronous acquisition. During the experiment, simultaneous events are generated, so that temporal synchronisation can be performed during data processing.

5.4 Early cell death detection

The detection of cell death and techniques for determining cell viability are of great importance in various fields, including studies of severity or progression of diseases, the efficacy of therapies, or drug safety evaluation. The effect of drugs can be indeed assessed *in vitro* by testing them on standard cellular types with various concentrations, the amount of non-viable cells being in this context one of the relevant indicators for drug toxicity. In the context of neuroscience, studies on cell death are of primary importance, as cell regeneration in the CNS does usually not occur. Neuronal cell death is thus a field of key studies for the understanding of neurodegenerative diseases such as Parkinson's or Alzheimer's for instance.

As discussed briefly in subsection 5.2, the use of DHM for cellular monitoring showed that various temporal signals could be retrieved from experiments where cells were stimulated, and that the type of phase signature seemed to be dependent on the cellular state at the end of the experiment [Jou11]. In particular, strong and irreversible phase drops seemed to be linked with a cellular death. The purpose of this section is thus to study systematically the link between the phase signal characteristics and cell viability, to potentially to derive criteria for detecting non-viable cells through the phase response. DHM measurement indeed provides valuable features in this context, as a detection performed through phase analysis may lead to label-free detection. Furthermore, thanks to the low optical power required, its non-invasive capability is particularly suited for toxicity assessment.

5.4.1 Cell death dynamics and classification

Cellular death types
Cell death can proceed by several pathways which are characterised by a distinct set of temporal, morphological, biochemical and genetic characteristics [Kry08; Dup09]. On a general point of view, one typically differentiates cell death pathways consisting of a controlled breakdown of cellular functions, such as apoptosis or autophagy, and pathological ones such as necrosis. The latter type indeed leads to a loss of membrane permeability, and consequent release of the intracellular content into the extracellular matrix, which yields toxic exposure for adjacent cells and inflammation of surrounding tissues [Wol04]. On the other hand, controlled cell death avoids any release of intracellular content through recycling mechanisms and are part of healthy processes [Kry08]; one of the most striking examples is the differenti-

ation of fingers in the embryo, based on the controlled death of tissues between fingers from the undeveloped hand [Jac97; Ric99].

Apoptosis is the most common cell death pathway occurring in the body, and have thus been the subject of many studies in the past decades. It is characterised morphologically by a cell shrinkage, membrane blebbing and a condensation of the nucleus. At a later stage, the nucleus and the organelles are fragmented and the cell fragments in small compartments commonly called apoptotic bodies, which can be processed by immune cells through phagocytosis [Dup09]. Other processes also lead to cell death, such as autophagy, which primarily aims at controlling the quality and adequacy of intracellular content such as proteins, by degrading organelles and compounds in so-called autophagosomes. However, in stress conditions, autophagy can become a competing process to apoptosis, and leads to cell death through the over-degradation of the intracellular content [Col10]. Finally, necrosis is characterised by a cellular swelling leading to a spherical shape, denoting the breakdown of cellular control and homeostasis. It is followed by a loss of membrane integrity, yielding the release of the intracellular content in the external medium through lysis [Dup09].

The various cell death pathways are commonly concurrent processes, so that it is often difficult to tag a certain event to be purely of one type. In many cases, it results from a combination of factors that leads ultimately to cell death. Furthermore, *in vitro*, cultures lack immune functions enabling the proper disposal of cellular material, so that all cell death pathways proceed to an end-stage called secondary necrosis, which shares many features with primary necrosis, in particular the loss of cell membrane integrity and the subsequent release of the cellular content into the surrounding extracellular medium [Kry08; Wol04].

Consequently, *in vitro*, assays usually differentiate between viable and non-viable cells by assessing membrane integrity thanks to inclusion and/or exclusion dyes. Most used inclusion dyes are for example trypan blue, a colour dye staining the nucleus [Alt93; Str01], or propidium iodide (PI), a fluorescent indicator activated upon bonding with DNA [Lec02; Zam96]. These dyes require the membrane to be permeable to enter the cell body and must bond to the nucleus in order to be visible, so that they enable detection of non-viable cells through staining. For this reason, they are mainly employed for control before experiment or in flow cytometry [Lec02]. Another approach consists in detecting specific compounds in the extracellular medium such as lactate deshydrogenase (LDH) [Kor83]. This method typically enables detection of cell death processes in a culture, but without identifying cells individually. These assays thus rely on late stages of cell death, i.e. loss of membrane integrity, which implies that a rather long delay can occur between a drug exposure and the consequent cell death. Furthermore, the use of extrinsic contrast agents usually requires several steps (washing, harvesting, solubilisation etc..) which take several hours for completion [Ban87], and the potential toxicity of the detection dye must be taken into account [Hud80].

Meaning of cell volume regulation

On the other hand, as mentioned before, specific morphological features accompany cell death processes and are often used to define the different pathways [Kry08]. For example, the loss of cell volume or cell shrinkage that occurs during apoptosis is a key morphological characteristic separating this physiological cell death process from an accidental one as necrosis, characterised by an initial cell swelling. These morphological characteristics can indeed be employed to detect cell death through automated detection of nucleus shape, for example.

However, minor variations in cell volume occur in accordance with the normal activity, and cells have inherited volume regulatory mechanisms to compensate for these physiological variations in order to maintain an appropriate balance of ions across their cell membrane [Bor04]. Within this framework, it has been recently showed that it is less the cell volume variations (shrinkage, swelling) which play a critical role in the activation/inactivation of the cell death processes than the cell capability to successfully regulate its volume through the activation of various ionic pathways in order to return to a near normal cell size and to maintain ionic homeostasis [Hof09; Che08]. Practically, if cell volume regulation (CVR) mechanisms are inactivated or overridden, resulting in an uncontrollable change in cell volume with an alteration of ionic homeostasis, cell death processes are activated.

The purpose of this section is therefore to employ the quantitative phase measurement as an indicator for detecting cell death through criteria based on CVR, as the phase can be linked indirectly with volume regulation through osmotic pressure and transmembranar water movements. We thus develop criteria based on the phase signal to discriminate between viable and non-viable cells and compare the detection results with standard assessment procedures such as trypan blue or PI.

Study on glutamate-induced neuronal cell death

We study in particular the effect of glutamate-mediated excitotoxicity on neuronal co-cultures, which consists in an important form of neuronal death involved in many neurodegenerative and ischemic diseases of the CNS, that triggers apoptosis or necrosis pathways [Ank95; Yua03]. Glutamate-mediated excitotoxicity is characterised in particular by a neuronal swelling resulting from transmembranar water movements accompanying a strong increase of the Ca^{2+} and Na^{+} intracellular concentrations [Cho94]. It was shown that the glutamate excitotoxicity is mainly induced by the strong Ca^{2+} influx, and that preferred cell death pathways depend on the calcium uptake of mitochondria [Sto98], as the subsequent ATP depletion may determine the favoured pathway [Zam97; Egu97]. Typically, it was shown that exposure to strong concentrations of glutamate was leading to a first wave of neuronal death through necrosis, followed later by a second wave several hours after application through apoptosis [Ank95].

5.4.2 Control experiments

We present in this subsection control experiments which were performed to ensure for example the absence of toxicity of trypan blue to cells, or the detectability through the use of cell viability assays. The experimental procedures are identical to the ones described in subsection 5.4.3.

Potential effects of trypan blue

We first performed experiments to assess any effect of the trypan blue on the phase signal, and that the diluted dye is harmless to cells despite repeated applications, as it was shown that long exposures to the reagent can lead to cytotoxic effects [Hud80; Jon85]. Practically, cells were periodically immersed in the reagent medium during periods of 3 minutes, similarly to the protocol employed in following experiments, and the DHM phase signal measured and processed according to the description in subsection 5.3.3.

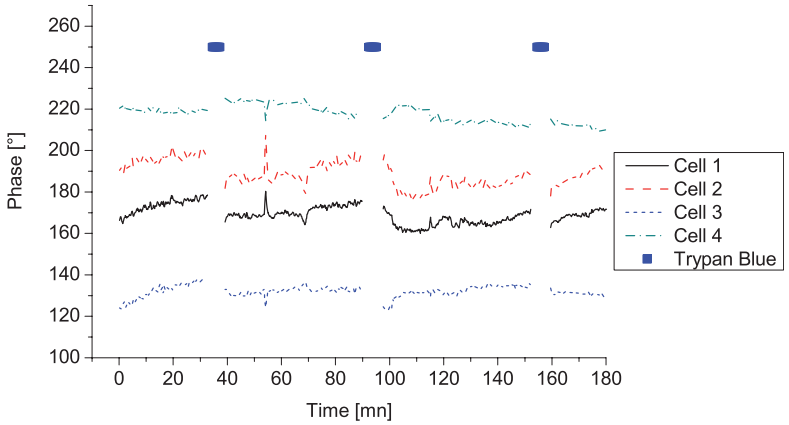

Figure 5.8: Control experiment to test for possible effects on the phase signal by periodic reagent immersion, measured on several cell bodies.

The typical phase signal measured on four cell bodies is shown in Fig. 5.8 (curves representative of approximately $n = 20$ cells), while reagent has been periodically applied for 3 minutes periods separated by one hour interval. One can identify a small phase signal change after the application of the reagent (typically at approximately $t = 35$ and $t = 155$ min), which corresponds to the consequence of a small osmotic shock, as the osmolarity of the perfusion medium is slightly changed by the 1:10 dilution of trypan blue. These variations are however within the range of physiological phase fluctuations exhibited by "healthy" living neurons in culture, and are gradually regulated as it can be identified by the slow recovery of the phase signal after each application.

This experiment shows that repeated exposures to the inclusion dye do not stain healthy cells even several hours after the first application, as shown in Fig. 5.9(a), where cells having been exposed to three trypan blue applications over a 155 minutes interval are presented.

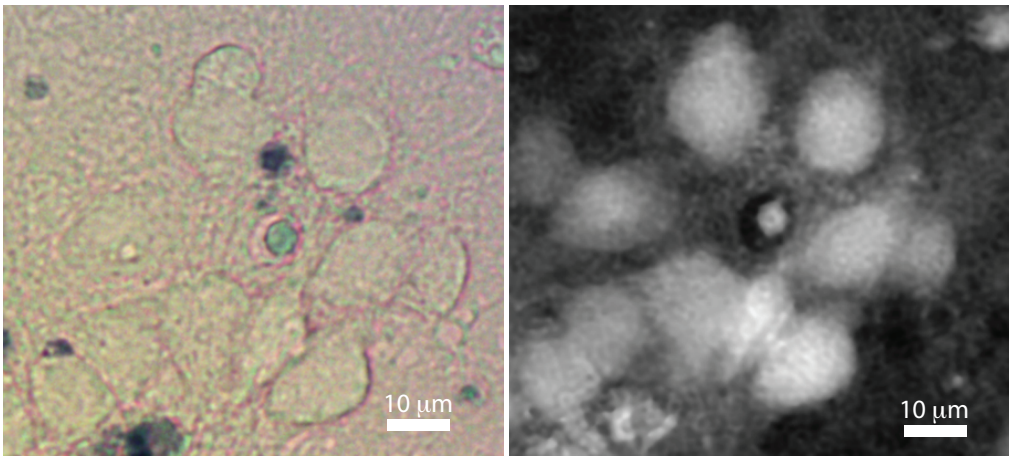

(a) (b)

Figure 5.9: Images of the cells monitored in Fig. 5.8 at t = 155 min, shown (a) in colour, where cells are viable and not stained after repeated exposure to the exclusion dye, and (b) in phase.

The stained biological material corresponds to small fragments originating from dead cells in the culture. This stresses that within the typical time range of the experiments presented in this article, repeated applications of 3 minutes do not lead to a significant cellular staining. Furthermore, it shows that the phase signal is stable during typical experiments duration, despite repeated immersion in trypan blue.

Rapidity of detection with trypan blue

The purpose of this paragraph is to determine the rapidity of detection of cell death when employing trypan blue, in order to determine the typical experiment duration required to avoid missing staining because of early interruption of the experiment (false negative). It was indeed shown in various studies that the glutamate concentration influences the amount of dead cells after exposure, but not the temporal behaviour of cellular mechanisms. Prolonged glutamate application (30 min) with various glutamate concentrations (1 µM–3 mM) were typically not inducing new staining of trypan blue 3 hours after application [Ank95]. The fact that most glutamate-induced cell deaths can be detected within the first 3 hours was also corroborated at lower concentrations (10 µM) and for lower application durations, as stimulations from 1 min to 20 min generate a constant death rate [Sch01].

We thus check that our experimental conditions are following this temporal course, by performing an experiment with a strong glutamate application (100 µM, 10 min), generally ensuring cell death, while being in concentration and duration ranges making the results comparable with our standard experimental protocol. Typical phase images corresponding to this experiment are shown in Fig. 5.10. The effect of glutamate characterised initially by a cell swelling can be seen by comparing cells before glutamate application (which occurred at t = 195 min) in Fig. 5.9(b) at t = 155 min, and in Fig. 5.10(a) at t = 202 min, seven minutes after

glutamate application. The morphological changes ongoing after the stimulation can be seen in Figs. 5.10(b–c), respectively at $t = 217$ min and $t = 383$ min.

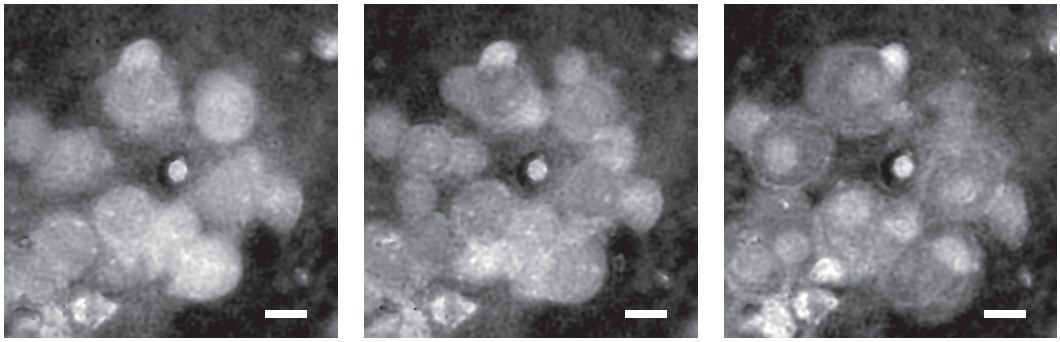

(a) (b) (c)

Figure 5.10: Quantitative phase image of the cells corresponding to the control experiment (100 µM, 10 min), checking for no missed staining during a typical measurement duration. Images are shown at (a) $\Delta t = 7$ min, (b) $\Delta t = 22$ min, and (c) $\Delta t = 188$ min after glutamate application. Scale bar is 10 µm.

As in standard experiments, repeated dye immersion was performed approximately every hour, showing that more than half of cells were stained after Δt = 2h15, and more than 90% were stained in blue after Δt = 3h30, out of 30 cells. Typical staining is shown for a part of the field of view in Fig. 5.11. Furthermore, all cells presented a pathological morphology characterised typically by a cellular swelling and nucleus condensation. This temporal behaviour is in well accordance with interruption approximately 4h30 after glutamate application, as performed in the next experiments.

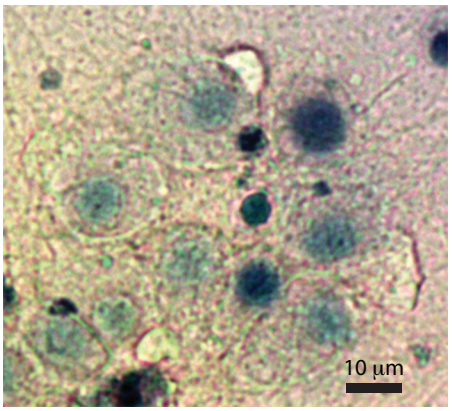

Figure 5.11: Colour image of cells corresponding to the ones of Fig. 5.10 (100 µM, 10 min), where all nuclei are stained by the trypan blue reagent 3h30 after glutamate application.

5.4.3 Experimental results

We then present the experiments of cell death detection through DHM, and results showing the relation between cell death and ionic deregulation, coupled with phase signal monitoring. All measurements involving comparison between trypan blue assay and phase signal were performed on the multimodal setup shown in Fig. 2.16, where the phase images and the colour images are measured on different cameras, by employing flipping mirrors. Consequently, no phase signal is measured during dye application. DHM illumination is generated with a laser diode ($\lambda = 680$ nm), with the interference measured on a CCD camera (8-bit, $\Delta x = 6.45$ µm). Colour images are acquired with a CMOS detector (8-bit, $\Delta x = 3.6$ µm). The measurements are performed with a 20× (NA = 0.45) MO in air, at a frequency of typically 0.1 Hz. Cell cultures are mounted in the opened chamber, and perfusion changes are performed by washing the medium with a micropipette. In all the experiments of this section, glycine (10 µM) is added to glutamate solutions to ensure activation of NMDA receptors.

All the measurements implying fluorescence measurement such as propidium iodide or ionic indicators are performed on the setup presented in Fig. 2.17. Ca^{2+} and Na^{+} are monitored respectively with Fluo-4 and SBFI indicators, according to the protocols described in subsections 5.3.2–5.3.3. The images are collected with a 10× MO (NA = 0.2) in air.

Excitotoxicity experiments

We measured the effect of application of glutamate to cell cultures in several conditions, by changing the application duration (60–120 seconds) and concentration ($25-100$ µM). We

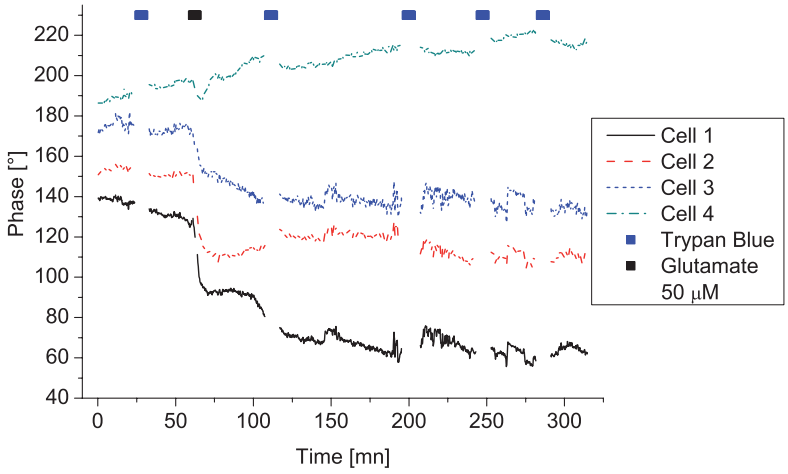

Figure 5.12: Time monitoring of the phase signal on several cells under a (50 µM, 90 s) glutamate pulse.

present in Fig. 5.12 a typical experiment where a glutamate pulse (50 µM, 90 s) was applied to the culture, with periodic application of trypan blue. The phase signals presented correspond to the cells shown in Fig. 5.13(a). One can identify that among the four curves shown, three

(cells 1–3) present a strong phase signal drop comprised between 40° and 80°, while the phase signal of cell 4 recovers after a period of time of approximately 10 minutes. The final cell morphology is shown at $t = 300$ min in Fig. 5.13(b).

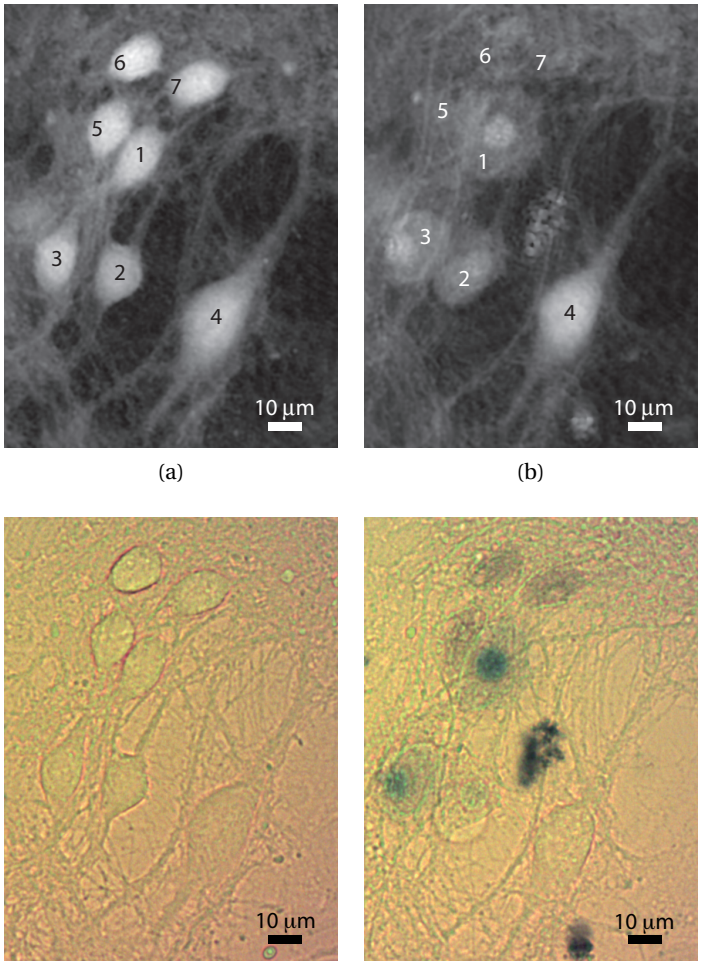

Figure 5.13: Image of cells corresponding to the experiment depicted on Fig. 5.12 when the glutamate pulse occurred at $t = 60$ min. Phase images at (a) $t = 50$ min (before stimulation), and (b) at $t = 300$ min (after stimulation), where cells 1-3, in contrast to viable cell 4, present morphological changes such as round cell shape or nucleus condensation. Corresponding colour images are shown at (c) $t = 30$ min and (d) $t = 290$ min, where cells 1–3 are clearly stained by the reagent at $t = 290$ min, contrarily to cell 4.

Bright field colour images of the culture are presented in Figs. 5.13(c–d), respectively at $t =$ 30 min before the glutamate application and $t = 290$ min, when non viable cells are identified by the blue staining. The comparison between Fig. 5.13(c) and Fig. 5.13(d) shows that cells 1–3 are stained and present strong morphological changes after glutamate application, while cell 4 remains unstained with a stable unchanged morphology.

In addition, cells 5–7 exhibit a faint staining (cf. Fig. 5.13(d)) while not producing any significant phase signal in Fig. 5.13(b) at $t = 290$ min, which is very likely due to a large dilution of the intracellular RI, which is consistent with the loss of cellular morphology in colour measurement. These three cells were typically stained very rapidly after glutamate exposure, and lost all cellular morphological characteristics at the time of end of the experiment, while experiencing an abrupt irreversible phase drop ($> 100°$) after glutamate application.

The results presented in Fig. 5.12 could be reproduced on several cultures with concentrations ranging from 25 µM to 100 µM ($n = 9$ for a total of 71 cells), as shown for typical responses in Fig. 5.14, where slightly different parameters of stimulation were employed. In Fig. 5.14(a), a glutamate pulse of 90 seconds (25 µM) produced reversible phase responses, similar to the one of cell 4 in the previous experiment. The viability of cells could be confirmed with trypan blue up to 4 hours and 30 minutes after stimulation, time at which the experiment was interrupted, with all cells being unstained and having a morphology similar to the one before the onset of the glutamate perfusion ($n = 6$). In Fig. 5.14(b), a pulse of 120 seconds (50 µM) produced irreversible phase drops of typically 40° to 60°. In a similar way, cell death could be confirmed by a positive staining approximately 3–4 hours after the stimulation ($\Delta t = 195$ min for cells 1 and 2, and $\Delta t = 255$ min for cell 3, $n = 10$).

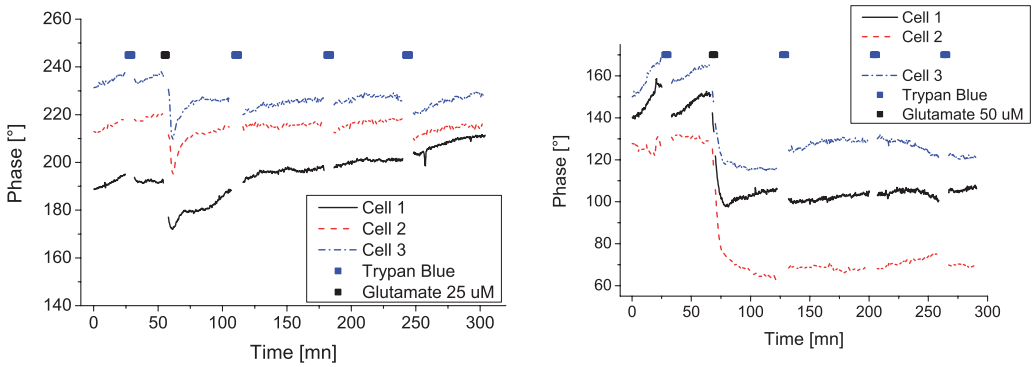

Figure 5.14: Various phase responses resulting from different glutamate applications including (a) reversible responses under a (25 µM, 90 s) glutamate pulse, and (b) irreversible responses under a (50 µM, 120 s) glutamate pulse.

One can identify from the different experiments presented above two main types of signals, consisting either in a large irreversible phase drop or a reversible response characterised by a phase recovery. These two types of signals are in very good agreement with viability assessment performed with dye staining. Indeed, cells expressing an irreversible phase drop are stained several hours later, while those exhibiting a phase recovery remain unstained up to the end of the experiment. In both cases, the transient response to glutamate application stabilises to a steady-state phase after 10–20 minutes, either to a value similar to the one before application (reversible) or smaller by tens of degrees (irreversible), enabling discrimination

between the two responses in these time frames. This temporal behaviour can also be reproduced with various concentrations and application durations (cf. Fig. 5.14).

Comparison between phase signal and ionic homeostasis

As discussed in the previous sections, the excitotoxicity effect of glutamate resides essentially in the intracellular Ca^{2+} uptake consequent of the activation of receptors. Consequently, by considering the quantitative signal as an indicator of CVR capability, we compare the intracellular $[Ca^{2+}]$ under glutamate stimulation and correlate the ionic regulation with the phase signal.

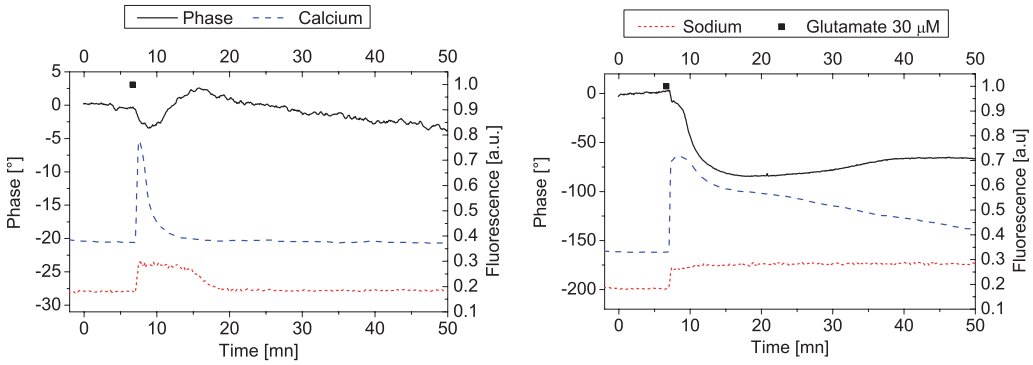

Figure 5.15: Typical neuron responses to a glutamate pulse (30 µM, 30 s), measured in phase, $[Ca^{2+}]$ and $[Na^{+}]$, for (a) a reversible phase response, and (b) an irreversible one. One can see that the phase irreversible response is well correlated with an absence of ionic regulation.

We present in Fig. 5.15 typical signals under a glutamate pulse (30 µM, 30 s) comparable to signals measured previously, corresponding to a reversible phase response (cf. Fig. 5.15(a)) and an irreversible one (cf. Fig. 5.15(b)). The reversible phase signal, in the order of 5°, is linked with a rapid regulation of intracellular $[Ca^{2+}]$, and a slower recovery of $[Na^{+}]$ to resting levels. On the other hand, an irreversible phase response of approximately 70° is correlated with an absence of rapid $[Ca^{2+}]$ regulation, where the slower decrease may be attributed to bleaching (cf. subsection 5.5.2). On the other side, $[Na^{+}]$ stays constantly at saturated levels. These measurements show the relation between the phase signal type (irreversible or reversible) and the presence or not of an efficient ionic homeostasis, as the strong phase drop is correlated with saturating levels of both $[Ca^{2+}]$ and $[Na^{+}]$ for more than 30 minutes. The measurements presented here are representative of approximately $n = 10$ cells each. Measurements exploring the correlation between phase and ionic concentrations signals are further developed in sections 5.5–5.7.

Correlation between cell death and ionic deregulation

In the previous experiments, the link between ionic homeostasis of $[Ca^{2+}]$ and $[Na^{+}]$ and the type of phase signal has been shown. The aim of the present experiment is to illustrate the relation between ionic deregulation and consequent cell death. We thus performed measurements during which the ionic intracellular concentration could be combined with cell death viability assessment. We employ propidium iodide (PI), a fluorescent indicator which can be measured simultaneously with ionic concentration probes through successive fluorescent excitation. In this case, $[Ca^{2+}]$ is monitored with the Fura-2 indicator, in order to enable measurements during long periods without implying any bias due to bleaching.

We present in Fig. 5.16 typical results measured in this fashion for two different cells, where a glutamate pulse (50 µM, 2 min) is applied, with the excitotoxic effects monitored both in phase and intracellular $[Ca^{2+}]$ imaging. The glutamate application leads to an irreversible phase response, linked with a saturation of calcium levels, in agreement with previous measurements. One can note that the $[Ca^{2+}]$ saturated signal does not decrease in time in this case, as no photo-bleaching effects are present through ratiometric measurements. Some time after glutamate application onset (Δt = 70 min), PI is added to the perfusion medium, with its emission monitored on the same cell bodies. In both cases presented in Fig. 5.16, the PI signal gradually increases compared to a baseline measured on an empty part of the field of view (PI signals are arbitrarily normalised to fit the intensity of Fura-2 ratios). This increase corresponds to a gradual staining of the nucleus, upon loss of membrane integrity, as PI emits light when bonded with DNA. At t = 113 min, a wash of the perfusion medium has been performed, in order to ensure that the PI signal increase was not impeded by a gradual decrease of dye concentration. After the medium change, apart from an offset on both signal and baseline, the rate of increase did not change. These responses, characterised by a combined irreversible phase drop and subsequent increase of PI signals could be reproduced on approximately n = 10 cells.

We present in Fig. 5.17 a typical field of view stained by PI in Fig. 5.17(a), compared with the corresponding field of view in phase (cf. Fig. 5.17(b)), measured at the end of the experiment presented in Fig. 5.16. The PI clearly stained several nuclei, confirming cell death which can be linked with typical morphological indicators of glutamate excitotoxicity such as swelling in the phase image. The stain is typically very strong in the nucleus, with a faint cytoplasmic staining, occurring when the dye has been present for a long time in the solution.

5.4.4 Discussion

Phase signal interpretation

As expressed in Eq. (5.1), the meaning of the phase signal is dependent on both the height and RI of the cells, related to the intracellular content. Both parameters are indeed indicators of the regulation capability of cells, as volume changes are essentially driven by water movements induced by ionic homeostasis mechanisms, which also influence the RI through

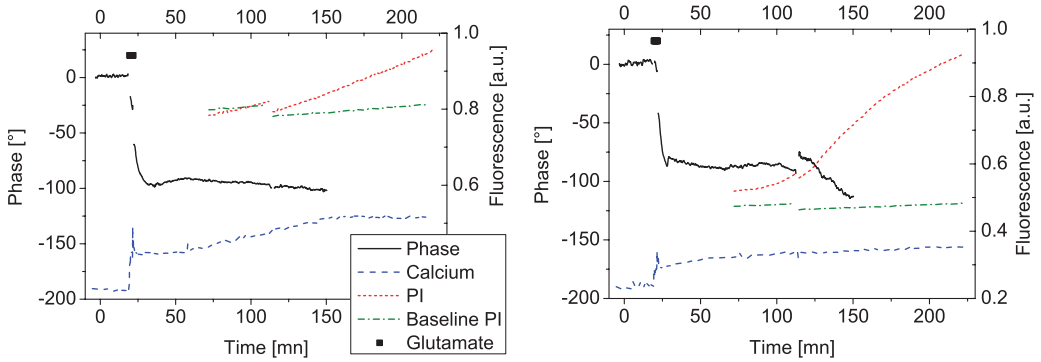

Figure 5.16: Experiment showing the quantitative phase signal monitored in time, in conjugation with $[Ca^{2+}]$ signal, showing calcium saturation under glutamate excitoxicity, and PI fluorescence, where the increase compared to the baseline demonstrates cell death because of membrane integrity loss.

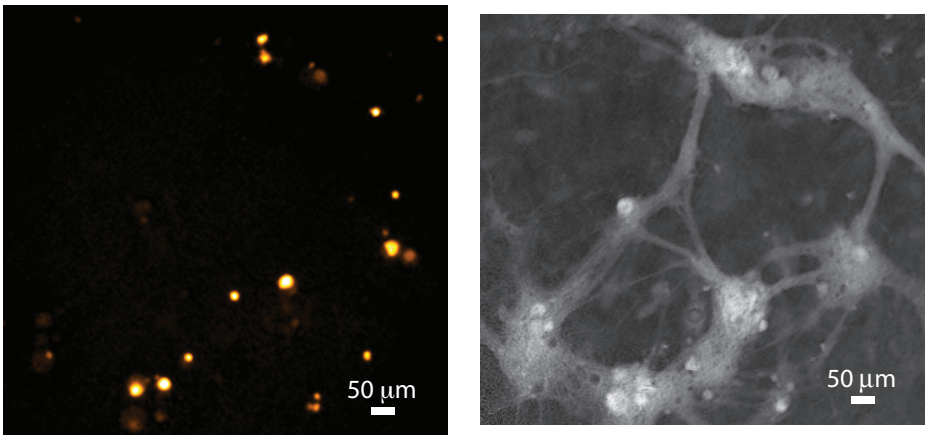

Figure 5.17: Image of neuron cells corresponding to the experiment shown in Fig. 5.16, taken at the end of the experiment (t = 230 min). (a) Fluorescence image of PI staining, mainly concentrated on cell nuclei, indicating the loss of membrane integrity. (b) Corresponding phase image, where the effects of excitotoxicity can be identified through cell swelling.

dilution of the intracellular content, and particularly proteins. Decoupling procedures confirmed that the large phase decrease monitored during the well-known glutamate-mediated neuronal volume swelling, induced by a water influx accompanying Na^+ and Ca^{2+} entrance [Cho94], results from an intracellular RI decrease [Rap05; Pav10a].

Consequently, within this framework, the phase signal is firstly sensitive to any mechanisms modifying the intracellular concentrations, including transmembranar water movements, which accompany various ionic pathways involved in the maintenance of ionic homeosta-

sis. The phase signal can thus be interpreted as a dynamics indicator of both cell morphology as well as ionic homeostasis mechanisms coupled to CVR.

On the other hand, volume changes are known to be a key consequence of cell death mechanisms. Typically, necrosis results in a cell swelling linked with a morphological change to a spherical shape, and apoptosis is characterised by a cell shrinkage coupled with blebbing, during the formation of the so-called apoptotic bodies [Dup09]. Furthermore, it was shown that inefficient CVR is very likely to lead to a subsequent cell death triggering [Che08]. Consequently, DHM allows to measure CVR within the range of milliseconds, and is used here to derive a criterion for early cell death detection.

Phase signal criterion for cell death detection

In the experiments presented in subsection 5.4.3, one can identify two different kinds of phase signals, a large and irreversible phase drop as well as a reversible response corresponding to a phase recovery. The latter, also characterised by a rapid neuronal morphology restoration, is compatible with an efficient ionic homeostasis. In contrast, the irreversible one can be interpreted as a persistent deregulation of the intracellular ionic concentration underlying the observed irreversible cell volume swelling. Furthermore, some cells encounter after the irreversible phase decrease a dramatic drop of phase signal (cf. cells 5–7 in Fig. 5.13), which is very likely due to a large dilution of the intracellular RI, consistent with the loss of cellular morphology observed in Fig. 5.13(d). This rapid dilution can be interpreted as a lysis following a rapidly triggered excitotoxicity [Cho94]. Consistent with suggestions made in other studies [Hof09; Che08], we consider the irreversible phase drop as an early indicator of subsequent cell death mechanisms triggered by a persistent ionic deregulation.

The discrimination between the two signal types can be determined through various indicators. First, the magnitude of the phase changes are dramatically different, being approximately $10°$ for a reversible response, and several tens of degrees (typically $40-80°$) in the case of an irreversible one, for which the cell is very likely not to recover and for which death mechanisms are irreversibly engaged. These considerations yield different criteria which can be employed for early cell death detection, either by employing the difference in quantitative phase value before and after glutamate application, for which a threshold value can be defined, or by using a criterion based on the temporal phase signal, being either a bell-shaped curve in the case of a reversible response, or a strong phase drop in the other. Typically, a threshold value can be chosen at $20°$, clearly separating the reversible responses of approximately $10°$ range, and irreversible responses of $40-80°$, leading to an automated detection which could yield applications for high throughput screening, for instance.

In practise, the various experiments present a very good agreement between viability assessment through inclusion dye and DHM phase signal monitoring for cell death detection. In the first experiments, cells identified by the phase signal as not being able to rapidly regulate their volume are detected as non-viable cells several hours later through trypan blue

staining, as shown for example in Fig. 5.14. These results are also corroborated when employing propidium iodide (PI) as a detection dye, such as the ones presented in Fig. 5.16. One can note that the PI signal is characterised by a certain increase rate, which changes in time, as shown in particular in Fig. 5.16(b). This change of curve slope denotes for the gradual loss of membrane integrity, as its higher permeability increases the fluorophore influx across the membrane. The loading rate then decreases at the end of the experiment, due probably to bonding saturation in the nucleus. This observation shows the time evolution of the inclusion dye signal, which becomes more reliable as time passes, through a better separation between nucleus staining and the baseline.

The various experiments show that the transient response stabilises to a steady-state value for the phase signal in a duration ranging in the tens of minutes, defining the capability of detection rapidity. This temporal behaviour can be compared with ionic fluxes between the extracellular medium and the cell, as shown in Fig. 5.15 for $\left[Ca^{2+}\right]$ and $\left[Na^{+}\right]$. The reversible response is indeed linked with a rapid ionic regulation, with the phase dynamics following closely the one of ionic concentrations. On the other hand, the irreversible response can be correlated with a saturation of both Ca^{2+} and Na^{+}. These results confirm the interpretation of the phase signal to monitor CVR, as ionic fluxes are closely linked with intracellular concentration and consequent water movements [Cho94]. This rapidity of detection is to be compared with dye assessment techniques, which require typically several hours before enabling a subsequent staining.

Comparison of detection time

This strong difference in detection time can indeed be explained by the very different principles on which both methods rely. The phase signal is highly sensitive to CVR processes related in particular to the water transmembranar movements involved in the ionic homeostasis, which are required to avoid the activation of cell death process [Hof09; Che08]. On the other hand, trypan blue and PI rely on the loss of membrane integrity which occurs from a necrosis, occurring either as the primary cause of cell death mechanism, or as a secondary necrosis *in vitro* [Kry08], yielding nucleus staining for non-viability assessment. The membrane integrity loss is however a late stage of cell death, which can occur hours after the mechanisms started, as it can be identified in the case of glutamate-mediated neuronal death in our experiments in subsection 5.4.3, or in other studies [Ank95; Sch01]. One should note also that inclusion dyes such as trypan blue or PI require a long time in order to stain the nucleus, as the dye must pass through the cell membrane, but also through the nucleus membrane before being detectable. This implies that both are altered, classically creating a residual stain in the cell body before clearly staining the nucleus [Zam96], for both trypan blue (cf. Fig. 5.13(d)) and PI (cf. Fig. 5.17(a)), potentially leading to the risk of false positive detection.

Cell death triggering mechanisms

In other studies [Ank95], glutamate-mediated cell death was identified to occur both through necrosis and apoptosis with different temporal behaviours, depending on the glutamate concentration. The preferred death pathway triggered by glutamate exposure was shown to depend on the calcium uptake of mitochondria [Sto98], directly linked to the subsequent ATP depletion [Zam97; Egu97]. Furthermore, recent research in the field tends to describe the various cell death mechanisms as concurrent phenomena, making difficult in most cases to reach a definitive conclusion about the cell death type [Yua03; Dup09].

In the experiments presented above, several indicators seem to show that apoptotic mechanisms are at least partly involved in most of the cell death processes. Apoptosis is indeed characterised mainly by cell shrinkage, nucleus condensation, and cell fragmentation. The nucleus condensation can be readily identified in most of the observed cells, either by considering the nucleus staining of trypan blue or the phase shift induced by the condensed nucleus in phase images (cf. cells 1–3 respectively in Fig. 5.13(d) and Fig. 5.13(b)). Another indicator of apoptotic behaviour consists in the formation of blebs after glutamate application which are gradually compensated, as it can be identified in Figs. 5.10(a–c). These characteristics, which were identified in a vast majority of the observed cells in the various experiments presented, are to be compared with the absence of visible nucleus and the diffuse blue staining of cells 5–7 at the top of the field of view presented in Fig. 5.13. These cells may have been the site of a purely necrotic death followed by a lysis, as no nucleus condensation can be identified, even though staining occurred, and their intracellular content suddenly disappeared in phase imaging.

On the other hand, other typical indicators of apoptotic cell death could not be identified in our experiments, such as cell shrinkage or fragmentation. One may consider that shrinkage is prevented in our case of glutamate-induced excitotoxicity, as it is characterised by a swelling induced by receptors activation and subsequent water movements. Furthermore, the ATP depletion could impede the continuation of apoptotic mechanisms, preventing cell fragmentation, and thus finally leading to necrosis. One should note finally that cells considered as viable by the absence of trypan blue staining and efficient CVR processes do not present any morphological indicators of cell death triggering, either necrotic or apoptotic. Typically, no nucleus condensation is occurring, and the cellular body does not present the typical spherical shape of necrotic death.

Even though the present experiments are not conclusive to discriminate among the different cell death pathways, a finer analysis of the early phase signal could potentially be employed for the detection of various cell death types. As purely necrotic death is characterised by the loss of homeostasis capability and subsequent swelling followed by lysis, while purely apoptotic death can be distinguished by a dramatic cell shrinkage, a method based on the detection of CVR may enable to differentiate, at an early stage, the two different cell death forms through the quantitative measurements of specific morphological features.

Specificity of measurements

One should note however that the type of signals measured in this article are specific to excitotoxicity, implying that dynamics and amplitudes of the phase signal changes would be different in the case another substance is used. Glutamate typically induces cell swelling through the activation of various receptors, implying that the detection in this case is nearly instantaneous, as volume and intracellular ionic regulation is a direct consequence of the exposition to the neurotransmitter. When using other substances, volume regulation changes would not necessarily occur in such time frames and could thus may be detected only some time after the drug effect. However, even if the employed substance does not directly imply volume changes as in the case of glutamate, CVR is a central process required for cell viability, and deregulation in volume or intracellular RI would occur later in the cell death process, typically during cell shrinkage in the case of apoptosis or during organelles swelling in the case of necrosis. Those phenomena would still enable fast detection compared to exclusion dyes, as they occur in early stages of cell death, while membrane permeability is a late symptom of cell non-viability, in particular in the case of apoptosis.

5.5 Neuronal dynamics measured with DHM and fluorescent ionic indicators

The work presented in this section has been motivated by the early results presented in subsection 5.2, where the temporal correlation between the phase signal and the intracellular calcium concentration ($[Ca^{2+}]$) in neurons could be identified. However, the calcium dynamics does not correlate in terms of amplitude, and thus does not fully explain the phase signal shape (cf. Fig. 5.6). The work in this section tends to study the phase signal in correlation with other indicators, with the aim of deducing some causes of the phase dynamics, mainly dependent on transmembranar fluxes and in particular water movements. As discussed briefly in subsection 5.1, $[Ca^{2+}]$ is contained at very low concentrations, compared to other ions such as Na^+ or K^+. One could thus hypothesise that the influence on phase dynamics of such components would be greater. In this section, we start in subsection 5.5 by studying in more details the temporal behaviour of the phase signal in comparison with $[Ca^{2+}]$ and $[Na^+]$, during glutamate-induced neuronal activity. We then study in subsection 5.6 the influence of the various receptors to glutamate on the phase signal, correlated with the ionic signals. Finally, in subsection 5.7, we present preliminary results comparing the phase signal with calibrated fluorescence measurements, where the intrinsically quantitative and global phase can be compared with the extrinsically quantitative and specific fluorescent signals.

5.5.1 Context

The main purpose of this section consists in measuring simultaneously intracellular calcium and sodium in conjunction with phase. This is performed by employing two fluorophores with different spectral properties, thus making possible to extract the two signals through two

excitation spectra simultaneously during one experiment. The measurements are thus essentially dependent on the available fluorophores for a given ions, and must have separate excitation spectra. While calcium imaging can be performed with many various fluorophores, developed for different wavelengths and sensitivities, the possible choices for sodium are rather restricted. We chose here SBFI, the most common $[Na^+]$ indicator to our knowledge. This fluorophore being employed in the same spectral range as Fura-2, this requires to employ it simultaneously with Fluo-4, which absorbs in blue. While other sodium indicators are available, their use in the context of our measurements would probably not have been adequate, as they possess poor properties in terms of leakage [Mei06], so that they are essentially used with patch clamp, in order to perfuse the fluorophore continuously.

Another possibility which could potentially provide as much insight as the one presented here would have been to monitor K^+ instead of Na^+, as their concentration gradient is opposed but similar (cf. Table 5.1), so that one could hypothesise that their influence on intracellular dilution could be comparable. Furthermore, while Na^+ increase is known to participate to membrane depolarisation during an action potential, K^+ is known to contribute to membrane repolarisation afterwards. However, $[K^+]$ indicators are usually less efficient than sodium ones, so that the measurement SNR would be lower, and thus less suitable for preliminary measurements such as the ones presented in this section.

5.5.2 Control experiments

We first present in this subsection control experiments performed to characterise the acquisition system. The controls consist essentially in assessments of the measurement procedures with fluorescent indicators, as various experimental biases can occur, such as bleaching of Fluo-4. The reproducibility of cellular responses under multiple glutamate exposures is also assessed.

Characterisation of working range of fluorophores

As mentioned in subsection 2.3.3, the response of an ionic indicator is not linear with the concentration (cf. Fig. 2.13). It is thus necessary to ensure that the fluorophore is working in the proper range during the experiments. In the context of $[Ca^{2+}]$ imaging, the dynamic range could be straightforwardly controlled during quantitative experiments (cf. subsection 5.7), where on can see that the minimum and maximum fluorescence signals reached for calibrated $[Ca^{2+}]$ are clearly situated beyond the fluorescence intensity at physiological concentrations (cf. for example Fig. 5.30). Those results are in agreement with literature, where it is known that highly sensitive dyes such as Fura-2 or Fluo-4 are well adapted for intracellular $[Ca^{2+}]$ measurements on neurons in the context of bright field fluorescence [Kie95].

In the case of $[Na^+]$ imaging, although we did not perform calibration experiments in the context of this thesis, the knowledge about standard $[Na^+]$ reasonably leads to the belief that the range is accurate. As SBFI possesses a dissociation constant of approximately K_d =

11 mM, its dynamic range should be comprised from fractions of millimolars to hundreds of millimolars, as demonstrated from calibration curves [Mei06]. This encloses the standard intracellular concentrations in neurons, ranging typically from 5 mM (resting) to 70 mM (excited) [Dia01]. Saturation levels are therefore fairly avoided in the context of bright field measurements such as ours in regards to literature.

Characterisation of cross-talk between fluorophores

When performing multiple colour measurements, such as in the case of Ca^{2+}-Na^{+} monitoring, a compensation for cross-talk between the signals provided by the two fluorophores must be performed. Typically, Fluo-4 absorption in the UV is not negligible (cf. Fig. 2.11(b)), so that excitation of SBFI in the $340-380$ nm range results in both fluorophores emitting light. A compensation procedure can be defined in order to suppress this cross-talk as

$$\begin{aligned} F'_{\text{SBFI},1} &= F_{\text{SBFI},1} - \alpha_1 \cdot \frac{t_{\text{Fluo-4}}}{t_{\text{SBFI}}} \cdot F_{\text{Fluo-4}}, \\ F'_{\text{SBFI},2} &= F_{\text{SBFI},2} - \alpha_2 \cdot \frac{t_{\text{Fluo-4}}}{t_{\text{SBFI}}} \cdot F_{\text{Fluo-4}}, \end{aligned} \tag{5.3}$$

where F corresponds to the measured fluorescence signals for each fluorophore, and α_1, α_2 are the respective correction coefficients for λ_1 and λ_2, denoting the proportionality relation between the Fluo-4 emission through excitation in its main band of absorption (490 nm) and in the UV range. The coefficients are generically defined for an identical exposure time for both fluorophores, and are thus multiplied by the ratio of respective exposure times $t_{\text{Fluo-4}}$ and t_{SBFI}.

In order to determine the compensation coefficients, a control experiment was performed *in situ*, by measuring fluorescence with excitations at $340, 380, 490$ nm on cells loaded only with Fluo-4. The coefficients α_1, α_2 can then be determined in order to minimise the signal emitted for 340, 380 nm, as it consists only in parasitic contributions from the Fluo-4 dye. Linear regression performed for measurement on approximately 10 cells provided coefficients as $\alpha_1^{-1} = 97.1190$ and $\alpha_2^{-1} = 7.6488$ for our particular experimental configuration. Similar experiments showed that SBFI does not influence the signal in the blue band of Fluo-4, so that no compensation is required in this case.

One should note that this calibration is valid only for one optical configuration, as the measured signals are dependent on specific conditions such as excitation power, light collection efficiency, etc. However, for a given configuration, the determination of the coefficients is general, in the sense that the uncertainty involved by the cultures preparation protocol, such as the intracellular dye concentration, are taken into account in the compensation model given in Eq. (5.3), as the fluorescence intensity is employed to deduce the subtraction. An example of compensation performed in this fashion is shown in Fig. 5.18, where the unprocessed data is shown with the compensated one in Fig. 5.18(a). One can see that the sodium increase is reduced in accordance with the Fluo-4 intensity, and the peak generated by the cross-talk

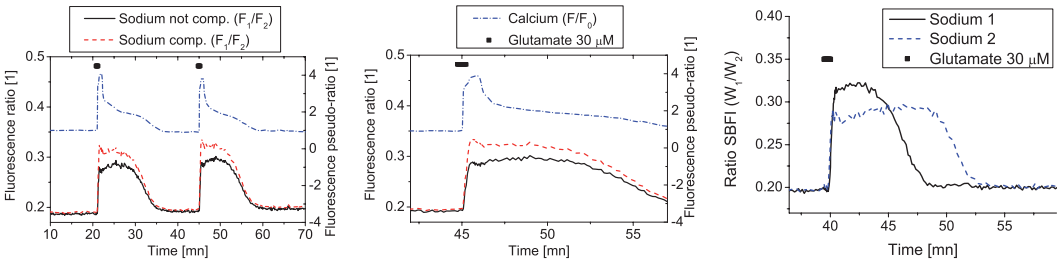

Figure 5.18: Illustration of the compensation procedure for the $[Na^+]$ monitoring when measured simultaneously with $[Ca^{2+}]$. (a) $[Na^+]$ curves display an artefactual peak coming from contribution of the Fluo-4 dye, as shown on multiple pulses. In the compensated curve, the artefact is minimised by subtraction. (b) Inset on one glutamate pulse, where the artefact is shown to artificially accelerate the sodium rise. (c) Experiment with cells loaded only with SBFI, showing the sodium response without any bias from Fluo-4.

between fluorescence signals at the Ca^{2+} burst time can clearly be identified in the raw curve, which is minimised in the compensated one. This effect is emphasised in Fig. 5.18(b), where only one glutamate pulse is presented.

These results can be compared with curves obtained on cells loaded only with SBFI, and thus free of cross-talk artefacts, as shown in Fig. 5.18(c). In this case, the sodium rise takes typically several tens of seconds to reach the maximum value, and the curve is free of parasitic peaks (cf. cell 1). However, in the case of a minority of cell responses (approx. 16% out of $n = 42$ cell responses considered), a small peak is still present, thus denoting a physiological responses such as in cell 2. These peaks are however classically smaller and shorter than the ones identified in unprocessed curves when measured simultaneously with Fluo-4. This implies that it is not possible to determine if the remaining peaks seen after cross-talk compensation are parasitic signals or part of the $[Na^+]$ response.

Characterisation of bleaching for single-wavelength fluorophores

In our experiments, we employ in particular the Fluo-4 dye, which is based on single wavelength measurements, and is thus dependent on photo-bleaching. In this context, the Ca^{2+} signal can become gradually biased during the experiment due to loss of emission efficiency of the dye. In order to estimate the importance of this parameter during measurements, we loaded cells with both Fura-2 and Fluo-4 dyes, in order to compare the single-wavelength measurement with a ratiometric counterpart, which is independent of bleaching.

It is known that the insertion of a high-affinity dye in cells can impede proper ionic dynamics, as a non-negligible part of cytosol ions become bonded to fluorophores [Par08]. This measurement implying two dyes is thus not necessarily physiologically relevant as two high-affinity dyes are loaded in cells, but it enables nevertheless the *in situ* characterisation of the

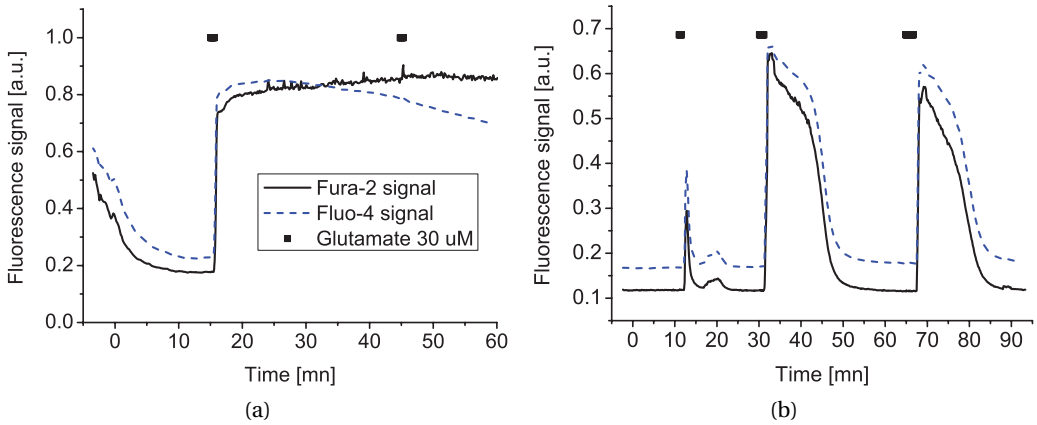

Figure 5.19: Experiment to characterise bleaching of the single wavelength indicator Fluo-4, compared with the ratiometric Fura-2, both loaded in cells and measured simultaneously. (a) case of calcium saturation, where the influence of photo-bleaching can be identified, and (b) case without saturation, where the influence of bleaching can be neglected.

bleaching properties of Fluo-4, by comparing the two measurements. We present in Fig. 5.19 typical curves of the fluorescence intensity provided by the two fluorophores, where the Fluo-4 signal has been arbitrarily scaled to fit approximately the values of the Fura-2 ratio, with an offset to enhance visibility. One can appreciate the adequacy of both signals, although some discrepancies can be seen at maximal values. These differences can be attributed to the non-linearities of the responses, as both fluorophores have slightly different dynamics ranges. The bleaching of Fluo-4 can have dramatic effects, as shown in Fig. 5.19(a) for the case of a cell where Ca^{2+} saturates after the glutamate perfusion. In this case, a clear linear decrease of the fluorescence intensity can be seen, resulting in strongly biased values at the end of the experiment. However, it could be identified that bleaching can be fairly neglected for most of cells where no Ca^{2+} saturation occurs, as the time with high emission rate for the single-wavelength fluorophore is short, making the influence of bleaching negligible. For this type of responses, Fluo-4 follows the same trend as Fura-2 throughout the whole experiment as shown for example in Fig. 5.19(b). This negligible bleaching could be confirmed on 95% of cells (out of $n = 21$ cells) having transient responses, while most of Ca^{2+}-saturating cells were experiencing strong bleaching on their signal.

Reproducibility of glutamate pulses

In many results presented below, the glutamate excitation is performed several times on cell cultures during a single experiment, in various conditions. We thus first ensure here that the response to the neurotransmitter can be reproduced several times with similar results when performed in same conditions. The preliminary results presented in Fig. 5.6 already seem to indicate that phase responses as well as $[Ca^{2+}]$ signals are reproducible for standard glutamate pulses, as three excitations generated similar phase decreases and calcium bursts.

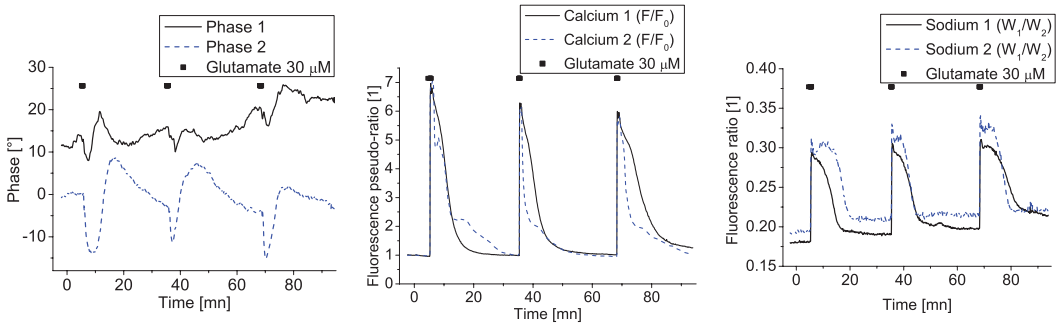

(a) (b) (c)

Figure 5.20: Assessment of reproducibility of signal on 2 typical cell responses with successive glutamate pulses for (a) quantitative phase measurement, (b) intracellular $\left[Ca^{2+}\right]$ signal and (c) intracellular $\left[Na^{+}\right]$ signal.

These results could also be confirmed when measuring simultaneously phase, $\left[Ca^{2+}\right]$ and $\left[Na^{+}\right]$, as shown in Fig. 5.20 for two typical cells (results representative of $n = 20$ cells). The successive application of (30 µM, 30 s) glutamate pulses provides reproducible signals in terms of response amplitude and temporal behaviour for the three measured signals. The reproducibility shown here defines our standard experimental protocol, where we typically wait 30 min between each glutamate pulse, in order to ensure proper cell regulation before applying the next stimulation.

5.5.3 Analysis of the phase signal

As discussed already in section 5.4, the phase signal can take several forms, depending on the capability of the cell to regulate its cellular volume, yielding two main types of phase responses, being either irreversible or reversible. We noted in the experiments of this subsection that within the signal previously defined as reversible, one can distinguish two signal sub-classes, as presented in Fig. 5.21 for several cell responses. One one side, one can define a purely reversible signal, characterised by a decrease in the order of $10-20°$, which is then regulated in the order of tens of minutes, as shown in Fig. 5.21(a). On the other hand, a more complex type of signal can often be identified, which can be described as "biphasic". This response is characterised by an initial phase decrease typically smaller than 10°, rapidly followed by a phase increase above the initial level, before reaching back the initial phase value (cf. Fig. 5.21(b)).

Although these two types of signals are different in their general shape, they share many characteristics which makes possible to define a general classification for the various stages of the phase response. We present in Fig. 5.22 a typical phase response for the reversible and biphasic cases (cf. resp. Figs. 5.22(a) and 5.22(b)), where the different stages are shown, which can be described as:

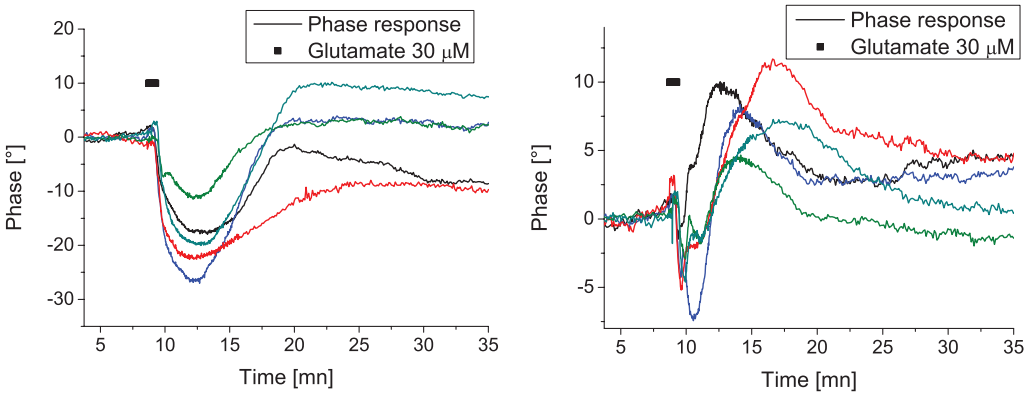

Figure 5.21: Multiple phase responses corresponding to (a) reversible responses and (b) biphasic responses.

Initial decrease A rapid and abrupt initial phase decrease lasting during approximately 20 to 40 seconds. We express this duration as Δt_p.

Slope change An abrupt phase recovery, followed by a global phase slope change.

Second decrease A second decrease at the new slope, gradually reaching a plateau. This decrease is sometimes absent in biphasic responses, with the phase increasing directly.

Phase recovery A gradual recovery of the phase signal, reaching back the initial phase value, or even reaching a higher value in the case of a biphasic response.

Final regulation A stage where the phase reaches back its original value, either through a slow increase in the case of a reversible response, or a decrease in the case of a biphasic response.

In both type of responses, one can identify that their duration is situated in a time range of approximately 15 minutes for (30 µM, 30 s) glutamate pulses. Interestingly, irreversible response such as described in section 5.4 can also be decomposed in the stages described here, as the successive initial decrease, slope change and second decrease are present. The main difference consists in the absence of phase recovery, with the second decrease being fast and irreversible.

These observations are made based on the observation of tens of cell responses, which can in a vast majority of cases be classified either as irreversible, reversible or biphasic. Furthermore, cells not providing a phase response within this classification are usually also unresponsive in $[Ca^{2+}]$ and $[Na^{+}]$ imaging, indicating that no physiological response is present at all.

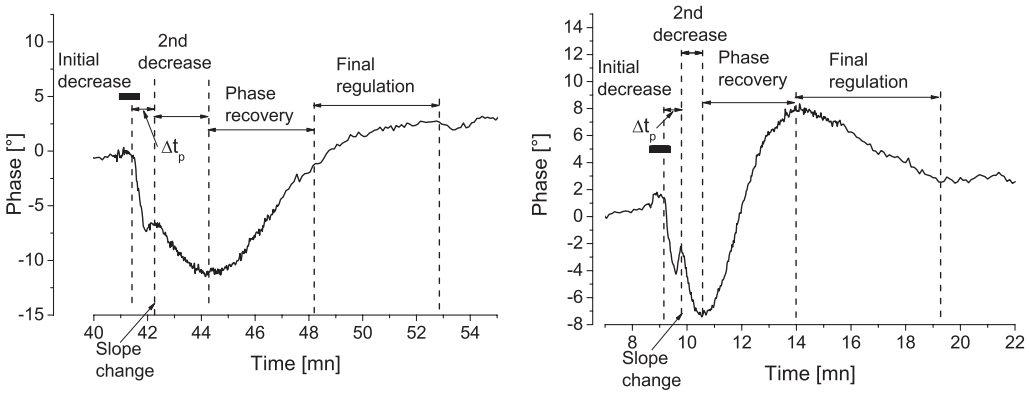

Figure 5.22: Decomposition of typical phase signals in different stages, for both (a) reversible response and (b) biphasic response. See text for details.

5.5.4 Comparison of signals dynamics

After having analysed the dynamics of the phase signal, we now compare its temporal behaviour with the $[Ca^{2+}]$ and $[Na^{+}]$ signals. We present in Fig. 5.23 typical responses which will be analysed in details. The quantitative phase signals are composed of either reversible or biphasic signals, as shown in Fig. 5.23(a).

As it can be seen in Fig. 5.23(b), calcium signal under glutamate excitation is characterised by a rapid Ca^{2+} influx, saturating in a matter of seconds. The intracellular $[Ca^{2+}]$ then drops rapidly during an initial decrease during the first minutes following the glutamate exposure, followed afterwards by a slower decrease, reaching back resting levels in a matter of tens of minutes. Typically, the time during which Ca^{2+} is at saturated level can last some minutes (cf. cells 1 and 3 in Fig. 5.23(b)), or drops back to lower levels nearly instantaneously (cf. cells 2 and 4). This rapid $[Ca^{2+}]$ regulation can be compared with the pathological Ca^{2+} saturation encountered during cell death studies, as shown for example in Fig. 5.16.

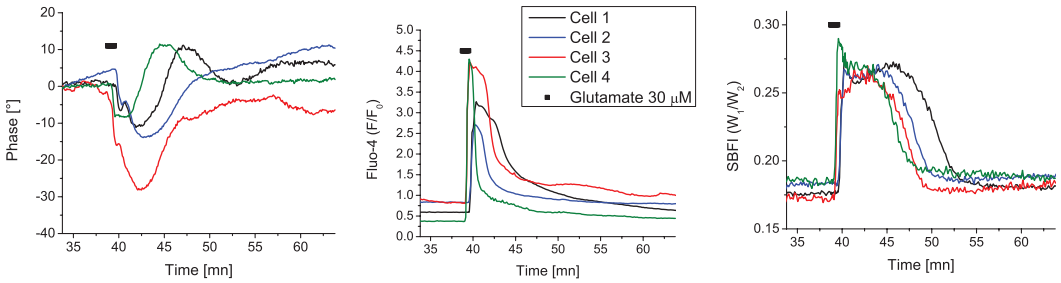

Figure 5.23: Multiple cell responses monitored simultaneously in (a) quantitative phase signal, (b) calcium imaging with Fluo-4 and (c) sodium imaging with SBFI.

On the other hand, $[Na^+]$ temporal behaviour (cf. Fig. 5.23(c)) is characterised by a slower rise, reaching saturation levels in approximately ten seconds. The rapid rise which can be identified in some cases such as cells 2 or 4 can be considered as an artefact of measurement which could not be compensated, as described in subsection 5.5.2. The sodium typically stays at saturated levels for several minutes, before decreasing in a bell-shaped curve after 10 to 15 minutes.

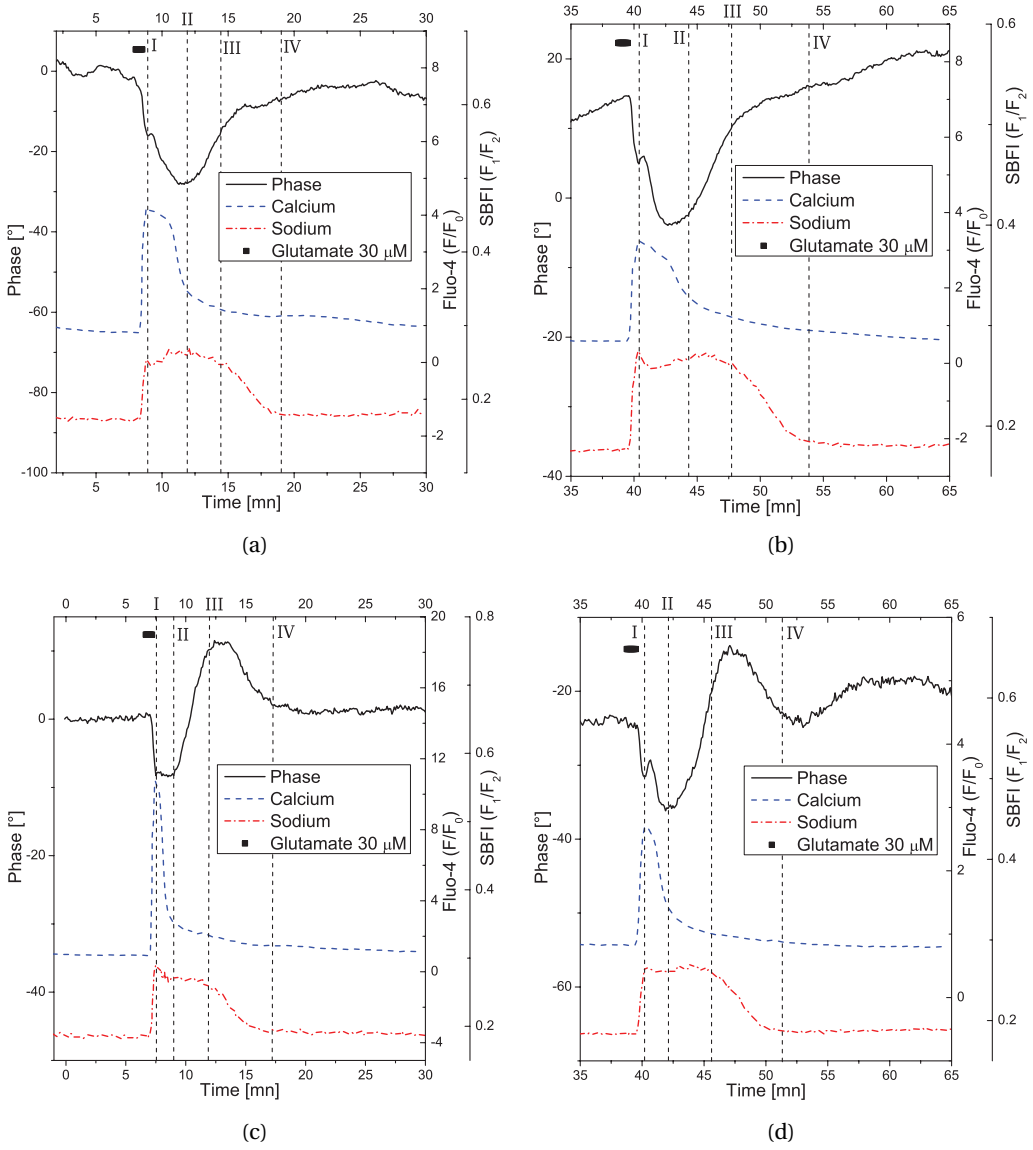

Figure 5.24: Temporal comparison of Ca^{2+}, Na^+ and quantitative phase signals for typical cell responses.

We then present the curves shown in Fig. 5.23 for each cell, enabling detailed comparison between the various signals for each cell response in Fig. 5.24. This comparison makes it possible to identify many various features. Firstly, one can see that the biphasic phase responses are generally linked with shorter Ca^{2+} bursts, where the saturation levels are nearly instantaneously reduced, while reversible responses are generally linked with Ca^{2+} saturation times of some minutes, where reversible responses are typically characterised by stronger phase decreases ($10-20°$) compared to biphasic ones (10° or less). These observations are to be compared with the pathological responses characterising cell death, where strong phase drops of $40-80°$ were identified, linked with irreversible Ca^{2+} saturation.

The next observations relate to the temporal behaviour of each signals, where the correspondences of particular interest are highlighted in Fig. 5.24 with numbered vertical lines. Firstly, the global phase response seems to be correlated with the $[Na^+]$ dynamics, where the phase regulation time matches well the one of $[Na^+]$ (cf. line IV). Furthermore, the end of the phase recovery stage seems to be temporally linked with the beginning of the decrease of $[Na^+]$ (cf. line III), characterised either by the end of strong increase in phase in the case of a reversible response (cf. Fig. 5.24(a–b)), or by the inflexion point preceding the phase decrease in the case of a biphasic response (cf. Fig. 5.24(c–d)). Furthermore, the second phase decrease stage seems to correspond to the rapid $[Ca^{2+}]$ decrease, as it ends approximately when $[Ca^{2+}]$ reaches back non-saturated levels (cf. line II). The final observation relates to the slope change stage, which matches temporally the Ca^{2+} saturation (cf. line I). This can be seen either through the abrupt phase modulation before the second decrease in Figs. 5.24(a, b, d), or the rapid slope change without modulation in Fig. 5.24(c). This temporal agreement concerns only $[Ca^{2+}]$, as it was shown in subsection 5.5.2 that the rapid rise of $[Na^+]$ is essentially an artefact of measurement. All the considerations given here and below are based on observations made on approximately $n = 60$ cells.

5.5.5 Discussion

Ionic fluxes dynamics

The signals as measured above with fluorescent indicators are in agreement with results reported in literature for ionic fluxes in neuron cells [Kie94]. In particular, the $[Ca^{2+}]$ transients, rapidly regulated to resting levels, possess similar dynamics than reported in other studies [Whi95; Ver99]. The duration of high Ca^{2+} levels is however rather long (up to several minutes), and may have various causes. Firstly, as our measurements are performed at room temperature, the cell dynamics is greatly slowed down compared to measurements made at 37 °C. Furthermore, as it could be seen for example in our results about neuronal cell death detection, the direct perfusion of glutamate in the external medium provides strong transient excitation, so that cell regulation may take more time compared to other excitation ways, such as local perfusion of glutamate, or electrical depolarisation through electrophysiology.

On the other hand, the measured $[Na^+]$ dynamics are significantly slower than $[Ca^{2+}]$ ones, where the regulation of sodium levels takes 10–20 minutes in our experimental conditions, with the rise speed during excitation taking approximately 10 seconds. These results are also consistent with literature [Kie94], as it is known that $[Na^+]$ dynamics are slower than $[Ca^{2+}]$.

The rapid rise of the $[Ca^{2+}]$ can be explained by the activation of various glutamate receptors, and in particular NMDAr which are highly permeable to Ca^{2+}. The consequent membrane depolarisation also activates voltage-gated Ca^{2+}-channels, which are known to possess very short activation times (typically milliseconds [Ham01]). The $[Ca^{2+}]$ is then characterised by a rapid first decrease, which can be interpreted as an intracellular uptake, as the dynamics of this first decrease is indeed very fast compared to other concentration changes observed in our experiments. Finally, the $[Ca^{2+}]$ decreases gradually to resting levels, where this slower decrease can be interpreted as the effect of regulation mechanisms, such as the Ca^{2+} ATPase or the Na^+/Ca^{2+} exchanger.

Similarly to $[Ca^{2+}]$, the initial rise of $[Na^+]$ can be understood through the effect of glutamate receptors, as non-NMDAr are particularly permeable to univalent ions, as well as NMDAr which are partially conductive for Na^+. The membrane depolarisation also activates voltage-gated Na^+-channels, thus enhancing the overall ionic flux. The initial rapid rise is then followed usually by a bell-shaped curve, starting with a slower rise of $[Na^+]$. The abrupt change in the Na^+ flux can be understood by the inactivation of voltage-gated channels, followed by the desensitisation of non-NMDAr [Sil96]. The slower increase in intracellular $[Na^+]$ may be interpreted as the effect of regulation mechanisms, such as Na^+/Ca^{2+} exchangers, which require the entrance of Na^+ to evacuate the intracellular Ca^{2+}; the strong concomitant decrease of $[Ca^{2+}]$ at the time of $[Na^+]$ bell-shaped curve is in agreement with this observation. This would however imply that the effect of this exchange is initially stronger than other ones, such as the Na^+/K^+ATPase, which is responsible for Na^+ exit. This interpretation for which $[Ca^{2+}]$ regulation would occur in priority during regulation is also consistent with the fact that intracellular $[Na^+]$ is decreasing only after a time when the $[Ca^{2+}]$ signal reached a significantly lower level, near resting one. This observation is also in agreement with studies showing that the $[Na^+]$ saturation occurring after glutamate challenges increases excitotoxic effects by impeding a rapid regulation of $[Ca^{2+}]$, compared to K^+-mediated depolarisation, for example [Kie94]. Then, the final part of the signal consists in a $[Na^+]$ regulation to resting levels which may happen through active pathways such as Na^+/K^+ ATPases or Na^+-K^+-Cl^- (NKCC) co-transporters.

One should however keep in mind that the amplitude of the signals shown in our experiments can be misleading. Firstly, the curves are not calibrated for quantitative results, so that the scales are arbitrary and some non-linearity can be present, as shown in Fig. 2.13. Secondly, the two ionic indicators possess different dynamic ranges, as Fluo-4 (Ca^{2+}) has a dissociation constant of K_d = 345 nM, while SBFI (Na^+) has a K_d = 11.3 mM (cf. Table 2.1). This implies that the changes in both curves do not represent fluxes of same orders of magnitude.

Phase signal dynamics

The phase signal measured in the experiments of this section are in accordance with previous measurements performed in section 5.4. Typically, most of signals are of reversible nature, which is consistent with the lower concentrations and shorter application times of glutamate, thus reducing the excitotoxic effects during experiments. As shown for example in Fig. 5.16, the irreversible phase response could be linked with an absence of $\left[Ca^{2+}\right]$ regulation, while the reversible one is following a concomitant $\left[Ca^{2+}\right]$ regulation, consistent with ionic homeostasis.

The experiments of this section also enable a finer analysis for the reversible responses, as shown in Fig. 5.21. One can typically distinguish between bell-shaped curves (cf. Fig. 5.21(a)), thus denoted as "reversible", and oscillating curves, where the phase value reaches a maximum higher than the resting value (cf. Fig. 5.21(b)), referred to as "biphasic", in accordance with previous classifications [Jou11]. The distinction between these two signals is however more difficult than between reversible and irreversible, so that clear criteria to separate the two are difficult to define.

These two types of reversible signals however present many common characteristics, that we identified through different stages proposed and detailed in subsection 5.5.3, where these two signals can be interpreted as different responses induced by similar causes. While the phase decrease is rather similar in both cases, the phase increase during the phase recovery stage consists is more important in the biphasic case. Similarly, the final regulation case consists either in a slower increase (reversible) or in a final decrease (biphasic), which is a consequence of the present phase value to reach back initial levels. Both signals are thus different only in the phase increase amplitude, and in some temporal characteristics, as the phase decrease is classically shorter in the biphasic case.

The phase decreases (both initial and second) can be interpreted as the direct effect of glutamate, through a dilution of the intracellular content resulting from the water entry concomitant with glutamate receptors activation [Cho94]. This decrease is then followed by an efficient CVR, identified by the phase regulation, occurring through the so-called phase recovery and final regulation stages. In this point of view, the phase increase occurring in biphasic responses can be seen as a strong cellular regulatory response to glutamate, where the regulation mechanisms yield an increase of the intracellular density, in response to the initial neuronal swelling induced by glutamate.

Comparison of temporal behaviours

The comparison between ionic fluxes monitoring and the phase signal confirms the very good temporal concordance that had been briefly discussed in the motivation of subsection 5.2. From the observation of the three simultaneous signals, $\left[Na^{+}\right]$, $\left[Ca^{2+}\right]$ and phase, it can be seen firstly that the global duration of the phase signal is well correlated with the $\left[Na^{+}\right]$ dy-

namics. Furthermore, as briefly expressed during the presentation of experimental results, various temporal relations can be identified at this stage:

- The end of the initial decrease stage, characterised by an abrupt phase slope change, seems to be temporally linked with the time when saturation of $[Ca^{2+}]$ occurs (cf. line I).
- The end of the second decrease stage, characterised by the beginning of the phase increase, seems to be linked to the end of the strong $[Ca^{2+}]$ decrease (cf. line II).
- The beginning of the final regulation stage, characterised by a slower phase increase for reversible responses or a phase decrease for biphasic responses, seems to be linked to the beginning of the $[Na^{+}]$ decrease (cf. line III).
- Finally, the end of the final regulation stage seems to be linked with the time at which $[Na^{+}]$ reaches back resting levels (cf. line IV).

The temporal correlation between the phase slope change and the Ca^{2+} saturation (line I) seems to indicate an abrupt change in the CVR when the Ca^{2+} flux changes. This correlation is difficult to interpret with the present results, as it is known that free $[Ca^{2+}]$ is influenced both by intracellular uptake, and active transmembranar outfluxes. However, the slope change in phase correlated with $[Ca^{2+}]$ saturation seems to indicate that the first strong phase drop is at least partly due to the huge Ca^{2+} entrance under glutamate excitation.

On the other hand, the fact that the end of the phase signal is correlated with $[Na^{+}]$ reaching resting levels (line IV) is in accordance with the previous observation that sodium was starting its decrease only after $[Ca^{2+}]$ had reached unsaturated levels. Furthermore, one may hypothesise that the end of $[Na^{+}]$ regulation corresponds to the time at which the cell reaches back its resting state. The sodium concentration should indeed variate until the final stages of regulation, as the membrane repolarisation is achieved through typically entrance of K^{+} [Ham01], which is then regulated after the hyperpolarised stage through typically Na^{+}/K^{+} ATPases. This implies that the end of phase regulation is in agreement with the ionic homeostatic process, so that CVR and ionic homeostasis are closely linked, and that their regulation both denotes the time at which the cell reaches back a global resting state after the glutamate excitation.

Finally, the intermediate part of the phase signal is the most difficult to interpret, since various phenomena can occur at this stage, as it can be identified in ionic monitoring. It is however interesting to identify that the end of the phase decrease, for both reversible and biphasic responses, is simultaneous to $[Ca^{2+}]$ rapidly reaching back lower levels (line II). This may indicate that CVR begins after $[Ca^{2+}]$ saturation finished, so that the strong intracellular dilution following glutamate excitation can be regulated after $[Ca^{2+}]$ levels could be brought to unsaturated values. This interpretation is in accordance with the observation that biphasic responses, characterised by smaller phase decreases, seem to occur for cases where $[Ca^{2+}]$

is rapidly regulated, so that saturation duration is shorter. In this fashion, the reversible response can be seen as an intermediate response between the physiological biphasic phase response without strong Ca^{2+} saturation, and the irreversible one, where $[Ca^{2+}]$ cannot be regulated, leading to cell death triggering, as discussed in subsection 5.4.4.

One should remember however that the phase signal is a global indicator, interpreted here as CVR, which can thus be influenced by various biological factors, such as water movements, volume changes, and intracellular concentration. This difficulty can be identified in the discussion above, where various temporal correlations can be identified, although these links cannot be interpreted in terms of precise biological mechanisms.

5.6 Pharmacological analysis

The results presented in section 5.5 show interesting temporal links between the various signals, enabling the interpretation of the effects of ionic fluxes on the quantitative phase. The study presented in this section aims at improving the understanding of the phase responses measured on neurons under glutamate excitation, by decomposing them through pharmacological tools. Typically, specific receptors to glutamate such as NMDAr and non-NMDAr (AMPA and Kainate) are studied, which have specific functions for the triggering of action potentials as described in section 5.1.4.

5.6.1 Experimental results

We present here results obtained under the same procedure as in section 5.5, with simultaneous $[Na^+]$, $[Ca^{2+}]$ and quantitative phase measurements, where blockers are employed in the course of the experiment. The protocol for the various pharmacological experiments consists in performing first a standard glutamate pulse (30 µM, 30 s), in order to check for cell viability and responsiveness. Then, after reaching back resting levels, the inhibiting drug is perfused during 20–30 minutes, in order to ensure its effectiveness. The experiment with blocked channels is then performed through glutamate perfusion. For each experiment type, two curves typical of the global response of cultures are presented. Whenever possible, the curves are chosen to present both biphasic and reversible phase responses types, as described in subsection 5.5.3.

Responses with NMDA receptors blocked

The first experiments are performed by blocking the NMDAr, through the use of MK-801, an inhibitor of this receptor (cf. Table 5.2). One should note that MK-801 does not block the NMDAr as a classical antagonist, since it consists in an inhibition of the active channels [Hue88]. During experiment, MK-801 is perfused at a concentration of 40 µM.

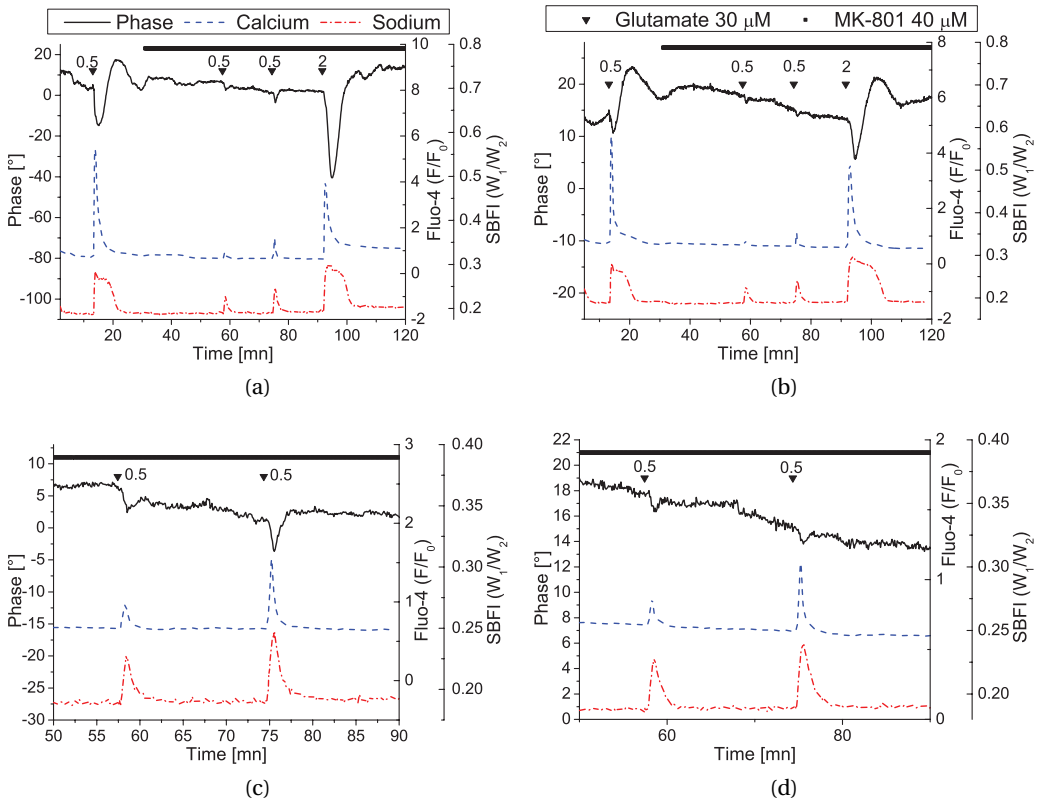

Figure 5.25: Cell response under glutamate excitation (30 µM, duration shown on graphs), with blockage of NMDAr. (a–b) typical full experiments, with (a) reversible and (b) biphasic responses during inhibitor perfusion. (c–d) Respective temporal insets of the experiments, showing in more details the small responses of (30 µM, 30 s) pulses under NMDAr blockage.

Typical cell responses under blockage of NMDA receptors are presented in Fig. 5.25, after a first glutamate pulse (30 µM, 30 s) showing clear biphasic phase responses. Contrarily, stimulation under MK-801 inhibition provides far lower responses for the three measured signals, as shown in the insets shown in Figs. 5.25(c–d). One should note also that the two (30 µM, 30 s) pulses are similar, showing that the blockage of NMDAr is effective, as activated receptors during the first pulse would have been blocked by MK-801 at the second stimulation, thus diminishing the cell response.

A longer pulse (30 µM, 2 min) performed at the end of the experiment generates phase responses which are comparable with standard ones, for both reversible and biphasic types, shown respectively in Fig. 5.25(a) and Fig. 5.25(b). While the $[Na^+]$ increase is similar in time and strength or even slightly longer than the standard responses, $[Ca^{2+}]$ response is typically lower than the one triggered in standard conditions. These results are representative of measurements performed on $n = 19$ cells.

The phase response is globally consistent with ionic concentration signals, as a decrease in responsiveness for both $[Ca^{2+}]$ and $[Na^{+}]$ corresponds to a decrease of the amplitude of the phase signal. Interestingly, it is also possible to see that the temporal behaviour deduced in section 5.5 is also valid in this case, as the global phase dynamics is well correlated with the $[Na^{+}]$ signal, as well as the various temporal correlation identified in Fig. 5.24.

Response with AMPA/Kainate receptors blocked

We present in this paragraph measurements where non-NMDAr are blocked through the use of DNQX, an antagonist specific to these receptors. As we specifically stimulate NMDAr in these experiments, we also employ for some cases glycine, a co-agonist for this class of receptors (cf. subsection 5.1.4). Its effect is thus to increase the glutamate sensitivity of the receptor, and as a consequence to increase the ionic fluxes under glutamate stimulation. During experiment, DNQX is perfused at a concentration of 40 µM, and glycine is added to glutamate solutions at a concentration of 10 µM.

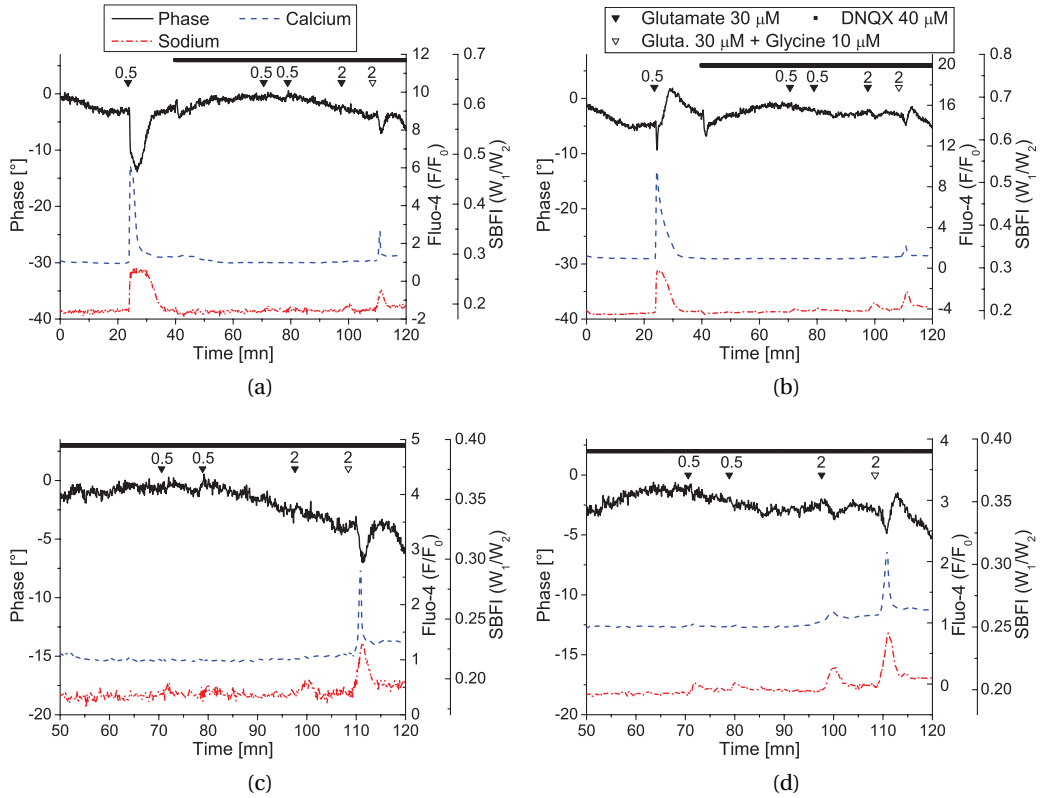

Figure 5.26: Cell response under glutamate excitation (30 µM, duration shown on graphs), with blockage of AMPA/Kainate receptors. (a–b) typical full experiments, with slightly different responses. (c–d) Respective temporal insets of the experiments, showing in more details the small responses of (30 µM, 30 s or 2 min) pulses under AMPA/Kainate receptors blockage.

Typical cellular responses under blockage of AMPA/Kainate receptors are shown in Fig. 5.26, after a first standard glutamate pulse assessing cell responsiveness. One can identify that under non-NMDAr blockage, no response can be identified through (30 µM, 30 s) pulses, showing a full blockage of glutamate activation. In the same fashion, longer excitations (2 min) produce no response (cf. Fig. 5.26(c)) or a very small one (cf. Fig. 5.26(d)). When perfusing glycine, the response is enhanced, and $[Ca^{2+}]$, $[Na^{+}]$ influxes can be detected under a (30 µM, 2 min) pulse. These results are representative of measurements performed on $n = 17$ cells.

As previously, the phase signal is in well accordance with ionic fluxes, as an absence of $[Ca^{2+}]$ and $[Na^{+}]$ rise is linked with no phase responses, for both 30 s and 2 min glutamate pulses. The addition of glycine then generates a small signals on all channels, where $[Ca^{2+}]$ is proportionally higher than in the case of MK-801 inhibition.

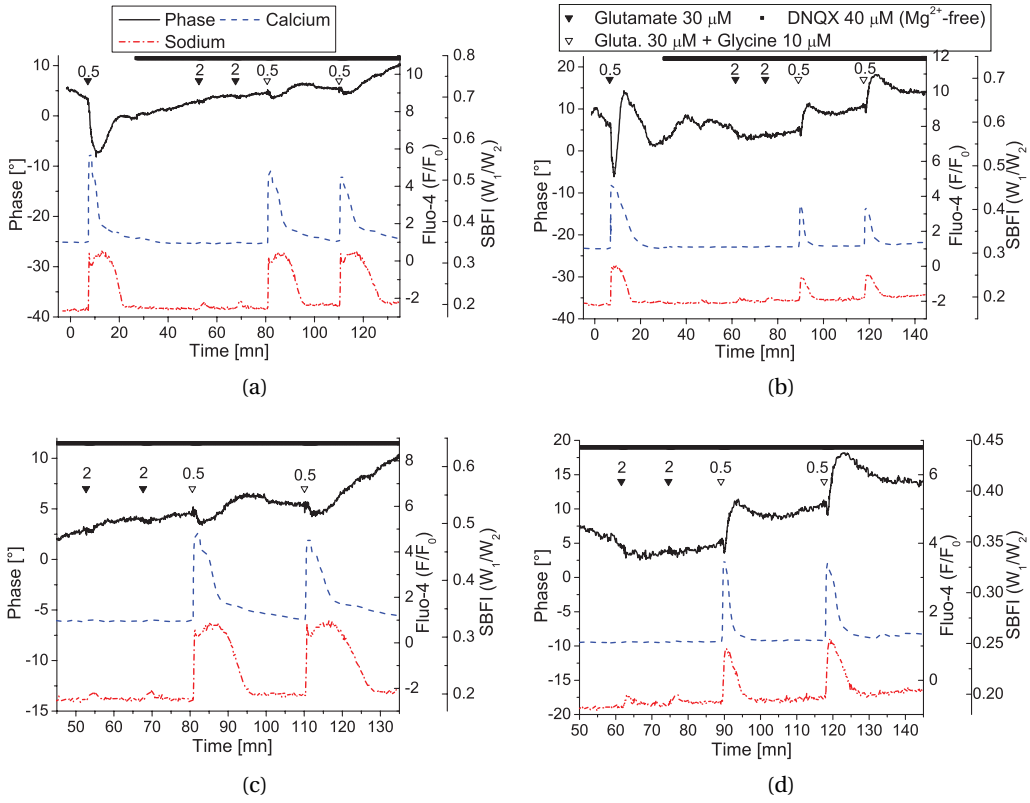

Figure 5.27: Cell response under glutamate excitation (30 µM, duration shown on graphs), with blockage of AMPA/ Kainate receptors, without the inhibition of the Mg^{2+} block on NMDAr. (a–b) typical full experiments, with (a) reversible and (b) biphasic responses during DNQX perfusion. (c–d) Respective temporal insets of the experiments, showing in more details the small responses of (30 µM, 30 s or 2 min) pulses with and without glycine.

In the case when non-NMDAr are blocked, the response is produced mainly by the NMDAr. However, as described in subsection 5.1.4, this receptor class is inhibited by the so-called

magnesium block, which prevents activation under physiological conditions. The Mg^{2+} block is then typically bypassed in the case of an initial depolarisation, which potentially does not occur when non-NMDAr are pharmacologically blocked. In order to study the influence of the magnesium block, experiments in Mg^{2+}-free conditions have been performed. Practically, it was ensured that no Mg^{2+} was present in the solution containing DNQX. One should note that it is mandatory to ensure that no Mg^{2+} residue is present in solutions, as even submicromolar concentrations can significantly block NMDA receptors [Sch01]. The fact of perfusing Mg^{2+}-free solution only with the antagonist ensures that cells are at resting state without external stimulation, as it was indeed identified that perfusing Mg^{2+}-free solution from the beginning of the experiment leads to cell constantly in excited state, even potentially leading to cell death. These measurements also showed that perfusing Mg^{2+}-free solutions only simultaneously with DNQX provides similar cell responses while avoiding parasitic excitations. As phase measurements is very sensitive to osmolarity of solution, we ensured a constant osmolarity by replacing the Mg^{2+} concentration with Ca^{2+}, so that the original ($CaCl_2$ 3 mM, $MgCl_2$ 2 mM) concentrations were replaced by ($CaCl_2$ 5 mM, $MgCl_2$ 0 mM).

Typical cellular responses under blockage of non-NMDAr with Mg^{2+}-free solutions are shown in Fig. 5.27, after a first standard glutamate pulse assessing cell responsiveness. As in the case with DNQX and Mg^{2+}, long glutamate pulses (2 min) provide only barely detectable responses. However, in the case when glycine is added to the glutamate perfusion, strong responses can be obtained even with shorter pulses (30 s), for reversible (cf. Fig. 5.27(c)) and biphasic (cf. Fig. 5.27(d)) responses. Those results are representative of measurements performed on $n = 41$ cells.

These results show far greater responses than in the previous case, thanks to the removal of the Mg^{2+} block. They are even comparable in amplitude to standard ones, when glycine is employed. It can be identified that in the absence of glycine, long exposures to glutamate (2 min) generate a small response in $[Na^+]$, but without identifiable signal in $[Ca^{2+}]$ nor in phase. Interestingly, it was also noticed that a non-negligible part of cells presenting biphasic responses in phase under DNQX-Mg^{2+}-free perfusion were not fully recovering in phase, as a residual offset is present after phase recovery, as shown in Fig. 5.27(d).

Response with AMPA/Kainate and NMDA receptors blocked

In a final experiment, we present cellular responses for which both NMDAr and non-NDMAr are blocked, through the combined use of MK-801 (40 µM) and DNQX (40 µM). As these two classes cover the known receptors activated by glutamate, this experiment can be considered as a control, in the sense that the expectation is to identify no effect of glutamate perfusion under these conditions. As previously, drugs are perfused for 20 – 30 min before performing measurements under glutamate excitation.

Typical results under these conditions are presented in Fig. 5.28, where an initial glutamate pulse (30 µM, 30 s) has been applied to ensure cell responsiveness. Although standard glu-

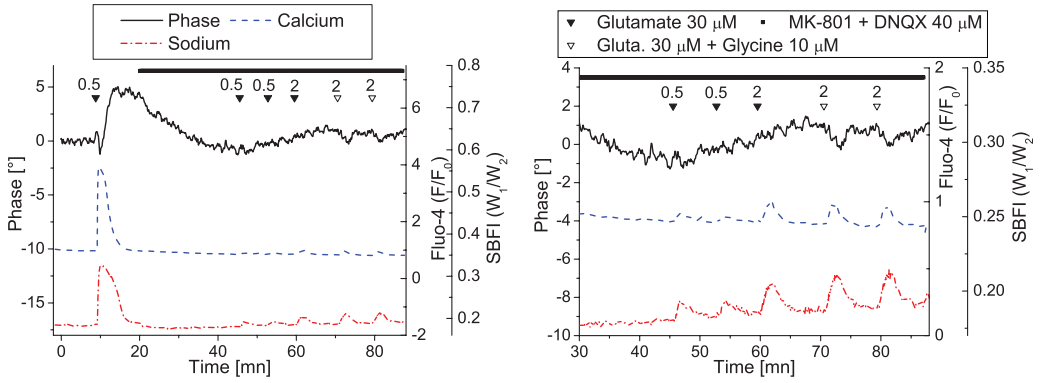

Figure 5.28: Cell response under glutamate excitation (30 µM, duration shown on graphs), with blockage of both NMDAr and non-NMDAr. (a) Typical full experiments, with barely no response during perfusion of MK-801 and DNQX. (b) Temporal inset of the experiment, showing in more details the small responses of (30 µM, 30 s or 2 min) pulses with and without glycine.

tamate pulses do not produce any response, one can identify that a small ionic influx in the case of (30 µM, 2 min) perfusion, although no signal seems to be detected in phase. In comparison, pulses (30 µM, 2 min) with glycine enhance slightly the ionic response, and provide a small response in phase. Those results are representative of $n = 8$ cells.

The fact that glutamate generates an ionic response in both $[Ca^{2+}]$ and $[Na^{+}]$ is not explained by the simple model developed in section 5.1, as blockage of both NMDAr and non-NMDAr should inhibit completely responses to glutamate. This implies either that more complex phenomena are occurring and are not explained by the interaction with the considered receptors, or that the inhibition by both MK-801 and DNQX is not fully effective, thus letting some active receptors. In both cases, the results of this experiment can be considered as a reference baseline, in the sense that the response corresponds to a case where all influence of glutamate should be blocked to our understanding.

This experiment also consists in the first case where the phase signal is not fully consistent with ionic responses under our interpretation, as no phase signal is detected for a (30 µM, 2 min) pulse, while small ionic responses can be identified. However, one can note that ionic influxes are not similar to the ones measured for other conditions in the previous experiments of this section. In particular, their temporal dynamics is rather different, as the $[Ca^{2+}]$ signal rise is rather slow, while all other experiments were consistent with a rapid intracellular $[Ca^{2+}]$ increase. The signal shown in Fig. 5.28(b) is far slower, as the rise ranges in the minutes ranges, compared with at most tens of seconds in the other cases. Furthermore, $[Na^{+}]$ also presents slower dynamics with its rise and decrease occurring at similar rates.

Results analysis

As it can be seen from the various results presented above, the responses in phase to glutamate under various excitations are rather different. One of the first difference consists in the response amplitude, that differs greatly depending on the receptor inhibited during glutamatergic stimulation. Those results are usually correlated with a change in the ionic fluxes measured through fluorescence, where smaller responses in phase are commonly linked with reduced responses in both $[Na^+]$ and $[Ca^{2+}]$.

In addition to differences in the response amplitude, some variations in the phase response shape could also be identified. In particular, the phase slope change, as described in subsection 5.5.3, seems to disappear in some cases. We thus checked for its occurrence in the various experimental conditions presented above. We present in Fig. 5.29(a) the percentage of cells where the slope change can be identified for the different experiment types. Errors bars indicate here the standard deviation of the percentages computed individually for each cell culture, which are then averaged to provide the measured value; the n value shown in graphs then represents the total amount of cells considered for these measurements. It appears that the phase slope change occurs in significantly less cases when DNQX is perfused, as it is replaced by a more gradual curve, as shown in Figs. 5.26(c–d). On the other hand, this initial decrease is again present when employing a Mg^{2+}-free medium, where the occurrence is situated in ranges where the discrepancy falls below uncertainties of measurement.

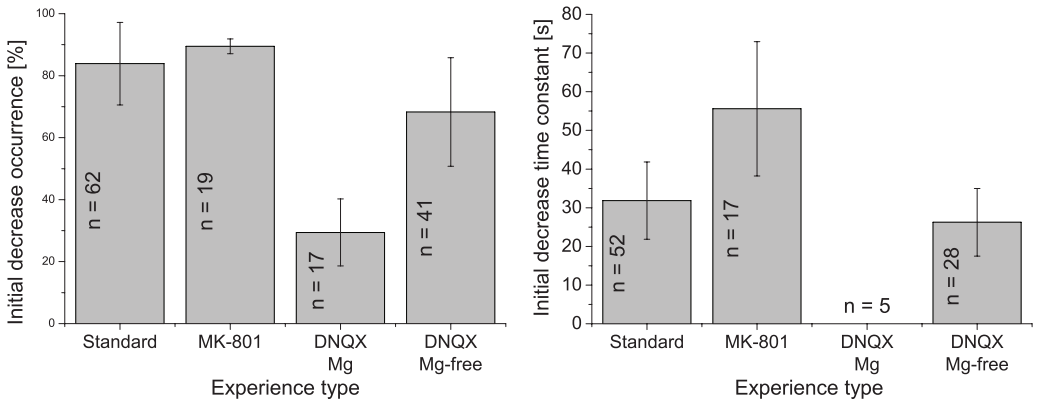

Figure 5.29: (a) Occurrence percentage of the slope change after the initial decrease of the phase signal (cf. Fig. 5.22) for the various experimental conditions. (b) Mean time constant Δt_p of the initial decrease in phase for the various experimental conditions. The amount of cells considered is given for each bar in graphs.

Furthermore, this initial decrease appears to change in behaviour depending on the inhibitor employed. We measured the time constant Δt_p of this response, defined as the time between the beginning of the phase response and change of slope in phase (cf. Fig. 5.22). We present in Fig. 5.29(b) measurements of this time constant for the different experiment types.

Error bars here indicate the standard deviation computed on the time constants considered for measurements; the amount of cells n employed are indicated in the graphs, being smaller than previously, as only cells presenting this initial decrease were considered. It appears that the duration of the time constant is more important for cells on which MK-801 has been applied, while Δt_p for other cases are in fairly comparable ranges. The measurements for DNQX with Mg^{2+} are not presented here, as the amount of cells presenting an initial decrease is not high enough to be statistically relevant.

One should note that those results need be taken with some care, as the amount of cells considered is not very high in some cases, thus making the measurements subject to potential strong uncertainties due the small n values. Furthermore, no automatic procedure was developed to generate those statistics, which were computed through manual interpretation of curves.

5.6.2 Discussion

Cell responses with pharmacological blockage
Globally, the results obtained with pharmacological tools are in accordance with known results from literature, as detailed below. Furthermore, the phase signal generally behaves in accordance with expectations, as a reduction of ionic fluxes through blockage of glutamate receptors results in a corresponding reduction in the phase signal.

Blockage of NMDAr through perfusion MK-801 greatly reduces the cell response, so that an increase of the glutamate perfusion duration to 2 min is necessary to retrieve a comparable response (cf. Fig. 5.25). Interestingly, one can identify that the Ca^{2+} influx is relatively reduced with NMDAr blocked, compared to a stimulation performed in standard conditions. This result is in accordance with the high permeability of NMDA receptors to Ca^{2+} [Ham01]. As in the case of standard conditions, the phase signal can be either reversible or biphasic, where the type of response seems to depend on the Ca^{2+} saturation, as a rapid regulation of $[Ca^{2+}]$ to resting levels yields a biphasic response (cf. Fig. 5.25(d)).

In comparison, blockage of non-NMDAr further reduces the cell response, as shown in Fig. 5.26. This can be explained by the nature of NMDA receptors, which are also voltage-dependent in physiological conditions because of the so-called Mg^{2+}-block [Bro93]. The voltage dependence of NMDAr can be further identified in this case through the dynamics of the response, which is far slower than for standard conditions. The cell response may indeed increase gradually, as some NMDAr are activated through depolarisation because of the initial activation of a small amount of receptors. This behaviour can also explain the low effect of glycine, supposed to potentiate NMDAr. The phase signal presents a behaviour in accordance with the ionic fluxes, as the phase decreases are rather low, and also occurring within slower time frames.

As expected from this interpretation, experiments performed with blockage of non-NMDA receptors without the presence of Mg^{2+} in the external medium greatly increases the response compared to previous conditions, as shown in Fig. 5.27, and the dramatic influence of glycine, as pulses of 30 s provide comparable responses to standard conditions. One can also identify the faster dynamics of cell response for all signals, showing in this case the rapid responsiveness of NMDAr. Like in the responses with NMDAr blocked, it is possible to identify both reversible and biphasic responses in phase. Interestingly, in the case of non-NMDAr blocked, the relative strength of $[Ca^{2+}]$ and $[Na^{+}]$ signals is comparable to standard conditions, which can be understood by the fact that NMDAr are non-selective in their conductance for various ions.

The only result which does not follow expectations on the correlation between the phase signal and ionic fluxes consists in the experiment where both NMDAr and non-NMDAr are blocked, as shown in Fig. 5.28, where small ionic fluxes for both Na^{+} and Ca^{2+} are detected, although no phase response can be identified. The absence of phase signal may be due to an insufficient SNR, so that the small phase responses are hidden in noise. However, the amplitude of ionic signals seems to be comparable to other experiments, such as the blockage of non-NMDAr (cf. Fig. 5.26). Another factor may be the dynamics of the ionic fluxes, which are extremely slow in the case of blockage with both MK-801 and DNQX. The response in this case may be indeed due to unblocked receptors, which amount should be low. Regulation mechanisms may thus be able in this case to maintain CVR during ionic influx thanks to their low dynamics, thus minimising the phase response.

Influence of pharmacological blockage on phase signal

As discussed briefly above, the main characteristics of the various experiments of this subsection is the consistency of the phase signal compared to ionic fluxes, for both the temporal dynamics and strength of the response. The various experiments indeed show that the phase signal decreases accordingly to $[Ca^{2+}]$ and $[Na^{+}]$ response strengths.

Another interesting point is that the phase response type—reversible or biphasic—is clearly independent on the type of receptor involved in the cell response, as both response type can be identified with NMDAr blocked, or non-NMDAr blocked when the influence of the Mg^{2+} block is removed, for glutamate excitations strong enough to provide phase responses which can be differentiated. Furthermore, the classification between biphasic and reversible is in agreement with previous observations, as reversible responses seem to occur for cases which present a stronger Ca^{2+} saturation. This may indicate that the phase response type is more dependent on regulation mechanisms than on the pathways responsible for the activation of ionic influxes. One should also remember that various mechanisms were not studied at this point, such as voltage-gated channels, which are responsible for an important part of ionic fluxes, implying that the study performed above by blocking the main glutamate-dependent receptors changes the cell responsiveness under glutamate stimulation, but does not modify the behaviour of many ionic pathways, activated after membrane depolarisation. This may

explain the consistency of the phase signal through various mechanisms which are invariant during the different experiments presented above.

Some minor differences can however be identified in some cases. It was for example identified that biphasic phase responses in the case of non-NMDAr blocked was often not reaching back resting levels, as shown for example in Fig. 5.27(b, d). Those effects were however not investigated more deeply at this stage, and are difficult to interpret.

Influence of receptor type on initial phase signal dynamics

While the global phase dynamics is independent of the type of receptor blocked during glutamate stimulation, some discrepancies can be identified between the various responses. Typically, as shown in Fig. 5.29(a), the occurrence of the so-called phase slope change, varies significantly depending on the type of receptor active during stimulation. In particular, its occurrence greatly drops in the case of blockage of NMDAr in presence of Mg^{2+} (20% compared to 80% for standard conditions), but reappears with similar occurrence percentage when Mg^{2+}-free medium is used. This can be compared with the signal dynamics, which were identified as far slower. In this context, the decrease in phase slope occurrence is consistent with the absence of calcium saturation, which does not occur due to the partial and gradual activation of NMDAr. On the contrary, this saturation occurs in the case of NMDAr activation without Mg^{2+}, and to a lower extent with non-NMDAr activation.

Furthermore, significant differences in the time constant Δt_p could be identified, defined as the time between the start of the phase response and the occurrence of the phase slope change, and shown in Fig. 5.22. As shown in Fig. 5.29(b), the time constant for standard conditions is approximately 30 seconds. However, in the case of NMDAr blockage, the time constant rises to 55 seconds, while non-NMDAr blockage without Mg^{2+} produces similar time constants as standard conditions. According to previous discussions, where we linked the phase slope change with the time at which Ca^{2+} saturation is occurring, this change in Δt_p could be due to the longer time for $\left[Ca^{2+}\right]$ to reach saturation under inactivation of NMDAr, as the conductivity for Ca^{2+} of non-NMDAr is known to be lower [Bro94]. The Ca^{2+} saturation may thus appear at a later stage of the cell response, thus delaying the phase slope change. This interpretation is also in accordance with the temporal curves shown typically in Fig. 5.25(a), where the Ca^{2+} saturation is still simultaneous to the phase slope change.

5.7 Quantitative comparison

In this final section, we present preliminary results where the ionic signals have been quantified through calibration procedures, in conjunction with quantitative phase measurements. The main interest of quantifying ionic fluxes in the context of our experiments is to enable better comparison between signals obtained with ionic indicators and the phase measurements, by linearising the fluorescence response. Furthermore, it may potentially enable quantitative

comparison between the phase signal and calibrated ionic fluxes imaging. In this section, we limit ourselves to $[Ca^{2+}]$ imaging curves quantification, as a separate procedure needs to be developed for each type of ionic flux.

As described in subsection 2.3.3, quantifying the fluorescence signal recorded from an ionic indicator requires recording the fluorescence at minimum and maximum ionic concentrations. This is performed by employing chelators in the absence of the calibrated ion to prevent the indicator to bond with it, and perfuse then a saturating ionic concentration to ensure that most of the fluorophores loaded in the cell are bonded, as described in details in subsection 5.3.2. The mathematical procedures then employed from measurements in order to calculate the ionic concentration were presented in subsection 2.3.3, and will not be repeated here.

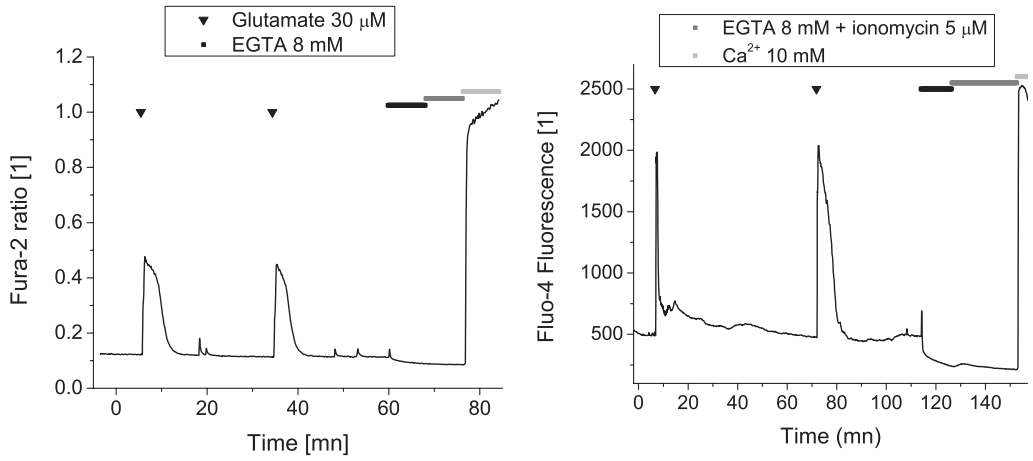

Figure 5.30: Typical curves of a calibrated experiment for $[Ca^{2+}]$ imaging, where EGTA and ionomycin are used to retrieve the F_{min} signal, when fluorophores are not bonded to Ca^{2+}, and a saturating concentration of $[Ca^{2+}]$ to retrieve the F_{max} signal, respectively in the case of (a) Fura-2 and (b) Fluo-4.

We present in Fig. 5.30 typical complete experiments including calibration, for the two $[Ca^{2+}]$ indicators employed in our measurements. In Fig. 5.30(a), an experiment performed with Fura-2 is presented. Although it was not employed systematically when comparing signals with phase measurements, this indicator presents the advantages of being extensively described in literature for quantitative $[Ca^{2+}]$ imaging, and thus enables to assess our measurements in regards to state of the art results. Furthermore, its ratiometric approach ensures that no bias induced by photo-bleaching is present. In Fig. 5.30(b), we present a complete calibration experiment performed with Fluo-4, with an identical procedure. While this indicator has been employed extensively in sections 5.5–5.6 thanks to its separate spectral bandwidth in regards to SBFI, it is far less described in literature for quantitative imaging.

These experiments show that one practical experimental difficulty consists in emptying cells from their intracellular Ca^{2+}, as a perfusion of chelator is necessary during typically 30 minutes. This long procedure is essentially due to calcium compartments inside the cell, which may release only gradually their stored Ca^{2+} as it disappears from cytosol [Par08]. This implies that cells are immersed for a long time in calibration media, increasing the risk that measures are performed in non-physiological conditions. Another issue consists in getting the $F_{\max}$ value for single-wavelength indicators. As discussed in subsection 5.5.2, the photobleaching influence can usually be neglected for cells providing transient responses, as the fluorophore does not emit too much light for long times. The effect of bleaching can however be important when saturating the indicator, as the fluorescence intensity is maximal, thus increasing the probability of quenching. As it can be seen for example in Fig. 5.30(b), the maximum value rapidly decreases at the end of the experiment, probably because of bleaching, implying that the $F_{\max}$ value must be measured rapidly.

5.7.1 Control experiments

As mentioned previously, the Fluo-4 indicator is far less documented in literature than Fura-2. We thus present here some control experiments aiming at briefly characterising its properties. One should note that the measurements presented below are only roughly estimating some main characteristics of the fluorophore, without providing a fully rigorous analysis, which would require various experimental techniques which were not employed in the framework of this thesis.

Assessing *in situ* dissociation constants

As described in subsection 2.3.3, the value of the dissociation constant K_d of ionic indicators, employed to relate the calibrated fluorescence signal to ionic concentrations, can greatly vary between *in vitro* conditions and cytoplasmic ones [Par08]. Experiments can typically show a two-fold to three-fold increase in the affinity of the indicator when loaded in the cell. For example, the *in vitro* dissociation constant of Fura-2 was shown to be $K_d = 145$ nM [Gry85], while its *in situ* affinity has been estimated at typically $K_d = 230$ nM [Par08], although this value can vary depending on references. The issue of knowing precisely the *in situ* dissociation constant value is particularly true for $\left[Ca^{2+}\right]$ imaging. In most cases, the calibration can indeed be done by perfusing known ionic concentration with the cell membrane made permeable to the considered ion, as for instance for $\left[Na^{+}\right]$ measurements [Dia01]. However, in the case of Ca^{2+}, the huge capacity for intracellular uptake, such as in mitochondria or the endoplasmic reticulum, where so-called Ca^{2+}-compartments are stored [Par08], prevents such simple approaches for calibration, so that *in vitro* calibration are usually preferred [Pet97].

As we could not find in literature an estimation of the *in situ* value of the dissociation constant of Fluo-4, we performed an experiment with cells loaded with both Fura-2 and Fluo-4, enabling comparison of the signals. By assuming that the *in situ* dissociation constant

of Fura-2 is $K_d = 230$ nM, we calculated $\left[Ca^{2+}\right]$ according to Eq. (2.47). On the other hand, we linearised the Fluo-4 signal according to Eq. (2.45), and fitted both signals through linear regression in order to estimate the effective K_d value of Fluo-4 to fit the results provided by Fura-2. The results of the fitting procedure for various cells are presented in Fig. 5.31(a), which are to be compared with its *in vitro* value of $K_d = 345$ nM [Gee00]. From those results, the average apparent dissociation constant is measured to be $K_d \approx 166$ nM. Typical quantitative measurements for both fluorophores obtained with *in situ* K_d are shown in Fig. 5.31(b), where quantitative values after fitting are fairly comparable.

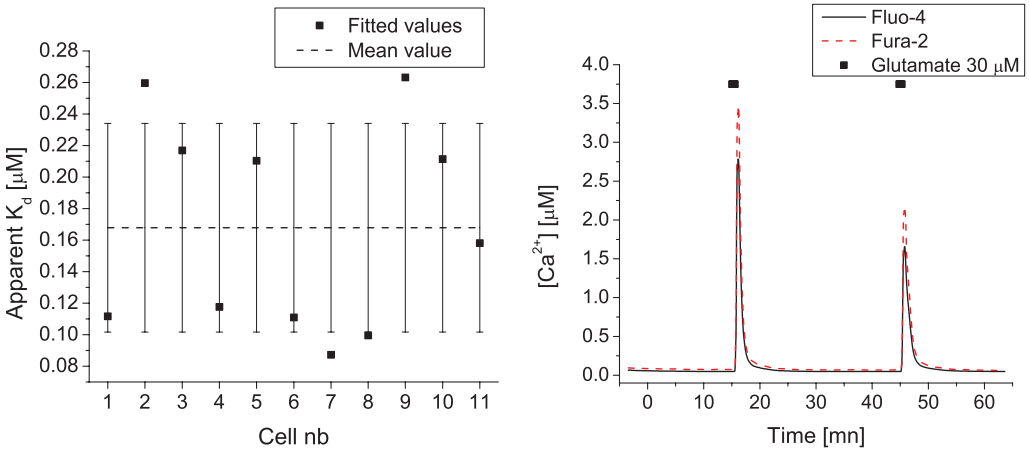

(a) (b)

Figure 5.31: (a) Dissociation constants K_d values for Fluo-4 fitted to match Fura-2 signals calculated with an assumed *in situ* $K_d = 230$ nM for various cell responses. The mean value and the standard deviation of the data set are respectively represented with a dashed line and error bars. (b) Typical fitted cell response of Fluo-4, shown with its corresponding Fura-2 curve.

The fairly low apparent K_d of Fluo-4 measured through our experiment is in disagreement with the literature describing the general behaviour of ionic indicators, which dissociation constant tends to increase in the cytosol, due to the interaction with intracellular compounds. This leads to consider that important experimental biases could be present. An influencing factor can consist in the presence of two high-affinity Ca^{2+} indicators in the cytoplasm, so that the two fluorophores may compete for bonding with Ca^{2+} in the medium, leading to an apparent K_d lower than in reality. Another factor, which was identified in some curves is due to photo-bleaching. As the emission intensity of Fluo-4 decreases with time, it implies that the measured $F_{\max}$ value may be fairly lower than the real one. This leads to higher values in the computation of the linearised curve, which are then compensated during fitting with a lower dissociation constant value.

Nevertheless, this experiment also shows that the linearisation of curves is rather similar for both fluorophores, as a compensation through a multiplicative factor provides a good agree-

ment between the two signals. This implies that although the absolute quantitative values we may obtain with Fluo-4 are questionable, the relative shapes and values may be compared in terms of amplitude of $[Ca^{2+}]$ spikes. Furthermore, as the determination of a reliable *in situ* K_d value for Fluo-4 is inconclusive through our simple experiment, we will assume a value of $K_d = 345$ nM for the measurements presented below, according to *in vitro* calibrations.

Assessing calibration methods without minimum values

As it can be seen for example in Fig. 5.30, it is rather difficult and lengthy in the case of $[Ca^{2+}]$ imaging to obtain the minimum value F_{min}. The difficulty in obtaining this F_{min} value is considered to be one of the main source of bias in quantitative $[Ca^{2+}]$ measurements, leading generally to over-estimated Ca^{2+} concentrations [Mar00].

As presented in subsection 2.3.3, alternative calibration methods were proposed for single-wavelength indicators, where the minimum value is not required, as given in Eq. (2.46) [Mar00]. quantitative measurements obtained through the standard method (cf. Eq. (2.45)), and through the method described by Eq. (2.46), for experiments in which both F_{min} and F_{max} were obtained through calibration. We assumed in this case a dynamic range for Fluo-4 of $R_f = 85$, according to [Mar00].

The quantitative results obtained with both methods are presented in Fig. 5.32, for a typical cell response. It is possible to identify that curves are very similar for higher concentrations (cf. Fig. 5.32(a)), while the method based only on the maximum value seems to slightly over-estimate Ca^{2+} levels for lower concentrations, as shown on the log-scale of Fig. 5.32(b). Values at resting levels are typically at $30-40$ nM, with $[Ca^{2+}]$ spikes corresponding approximately to a 500-fold $[Ca^{2+}]$ increase. Those values are in the range of known resting $[Ca^{2+}]$ and calcium spikes for neurons [Ham01; Hoc89], although spikes may be slightly overestimated due to the difficulty of obtaining a fully reliable F_{max} value.

Those results imply that both methods provide similar values, thus enabling to avoid the long experimental procedure required to obtain F_{min}. This approach makes it possible to obtain quantitative results much faster, and suppresses one *in situ* parameter for computation of $[Ca^{2+}]$, thus suppressing a part of the potential measurement errors, as the R_f value is an intrinsic property of the fluorophore [Mar00]. Furthermore, reducing the experiment duration also improves the accuracy of the measurement of F_{max}, as bleaching is reduced thanks to shorter experiments.

5.7.2 Experimental results

We present in this section similar results as in section 5.5, where $[Ca^{2+}]$ curves have been quantified with the maximum value method described in Eq. (2.46). Results for typical cell responses are shown in Fig. 5.33, where both reversible and biphasic responses can be identified. Insets for one glutamate pulse are shown in Figs. 5.33(c–d), where the temporal corre-

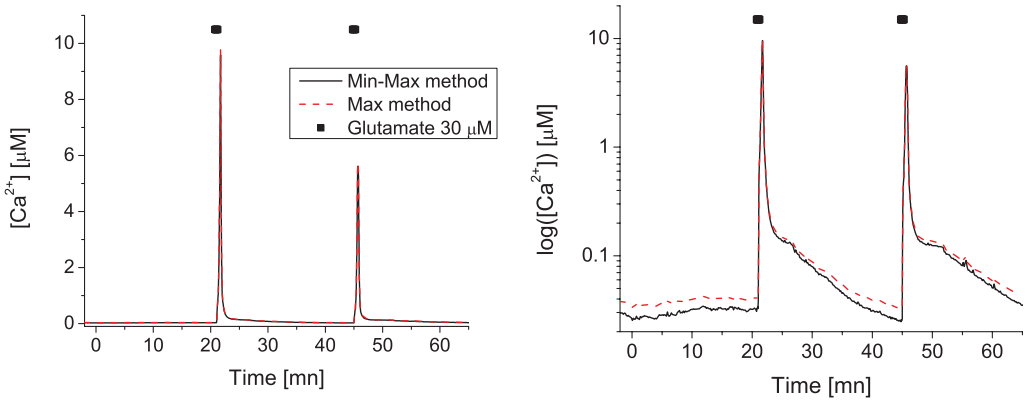

(a) (b)

Figure 5.32: Comparison of the calibration methods for single-wavelength fluorophores, expressed respectively by Eq. (2.45) (Min-Max) and Eq. (2.46) (Max), shown on (a) linear and (b) log scales.

spondence between signals can be better identified. Those results are representative of measurements performed on $n = 16$ cells.

The results presented in Fig. 5.33 are very similar to the ones shown in Fig. 5.24, apart from the fact that $[Ca^{2+}]$ response has been quantified through calibration procedures. One can identify the very good temporal correspondence between the initial phase decrease and the $[Ca^{2+}]$ spike, which is enhanced compared to previous results thanks to the curve linearisation. In particular, it is possible to see that the slope change, characterised by an abrupt change in phase signal, occurs simultaneously with the initial $[Ca^{2+}]$ decrease, as shown in particular in Fig. 5.33(c). Interestingly, for cases where $[Ca^{2+}]$ stays at saturated levels for longer times, such as in the case shown in Fig. 5.33(d), the slope change stage seems to be correlated with an initial $[Ca^{2+}]$ decrease, which precedes the main decrease occurring later.

Effect of calcium on initial phase decrease

Finally, we present in Fig. 5.34 typical cell responses, where the influence of the intracellular $[Ca^{2+}]$ on the initial phase decrease can be further appreciated. For the sake of visibility, we do not present here the corresponding $[Na^{+}]$ signals. These results emphasise the temporal relation between the first rapid $[Ca^{2+}]$ regulation and the initial phase decrease, in particular in Figs. 5.34(a–c), where a clear rapid $[Ca^{2+}]$ spike followed by a slower regulation can be seen. Similarly, a long saturation after the first $[Ca^{2+}]$ burst is linked with an absence of abrupt phase change with only a small slope variation, as shown in Fig. 5.34(d). Nevertheless, the link between the first $[Ca^{2+}]$ regulation and the initial phase break can also be seen in this particular case, where the phase slope change is smaller, as the initial calcium regulation.

Although these preliminary results show a striking correspondence between this initial phase decrease and $[Ca^{2+}]$ monitoring, they were not yet reproduced for a sufficient cell

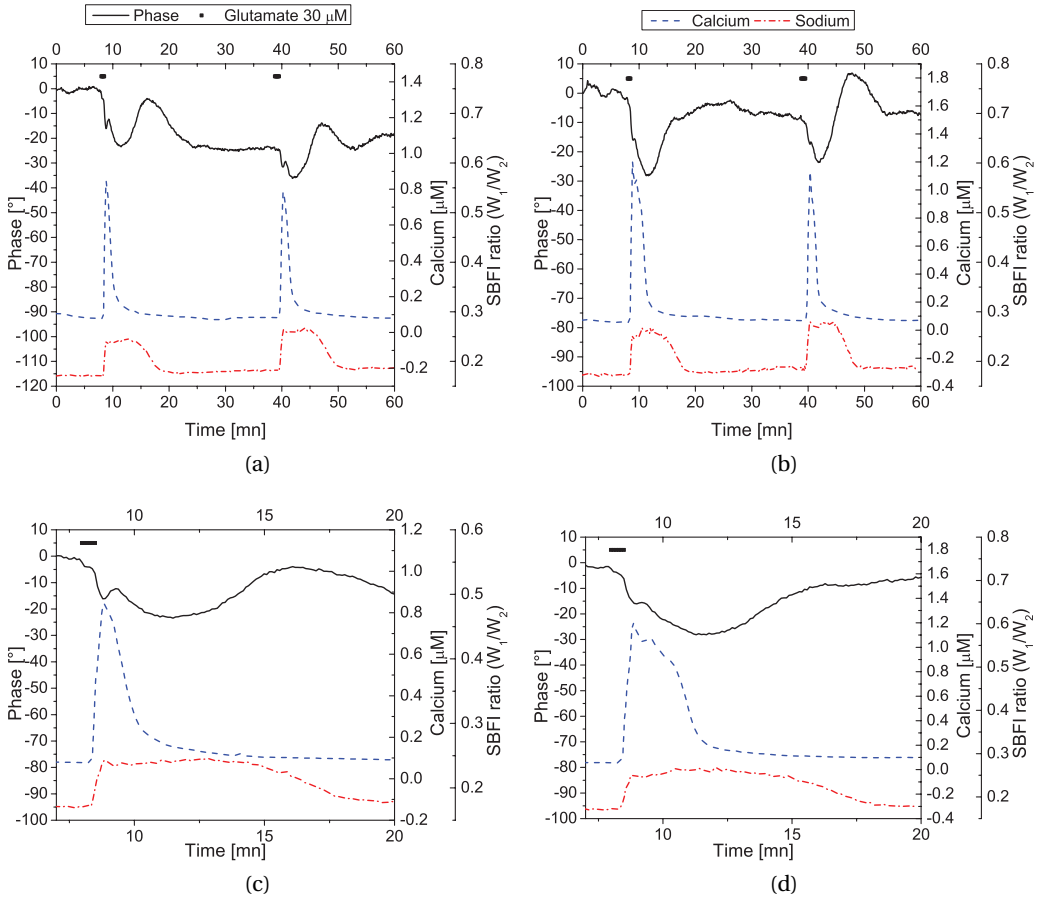

Figure 5.33: Temporal comparison of $[Ca^{2+}]$, $[Na^{+}]$ and quantitative phase signals for typical cell responses, where $[Ca^{2+}]$ has been calibrated to quantitative values.

amount to be fully reliable on a statistical point of view. Furthermore, the great variety of signal types, for both phase and $[Ca^{2+}]$, make the possibilities of statistical treatment not trivial. Nevertheless, these results show the great importance of linearisation of fluorescence curve, as detailed dynamics studies can clearly be misled with raw curves.

5.7.3 Discussion

The preliminary measurements with quantitative $[Ca^{2+}]$ measured through calibration procedures present values being typically around 20 nM at resting levels, with 100 to 1000-fold increases during glutamate response. While the accuracy of the obtained values is questionable, as shown in our control experiments, they lie in the proper order of magnitude according to literature [Kie94]. Furthermore, the experimental calibrations required to retrieve quantitative values are rather complicated and can impede the reproducibility of results. While we assessed an alternative method which prevents the acquisition of $F_{\min}$ values for single-wavelength indicators, which simplifies greatly the experimental protocol and prevents mea-

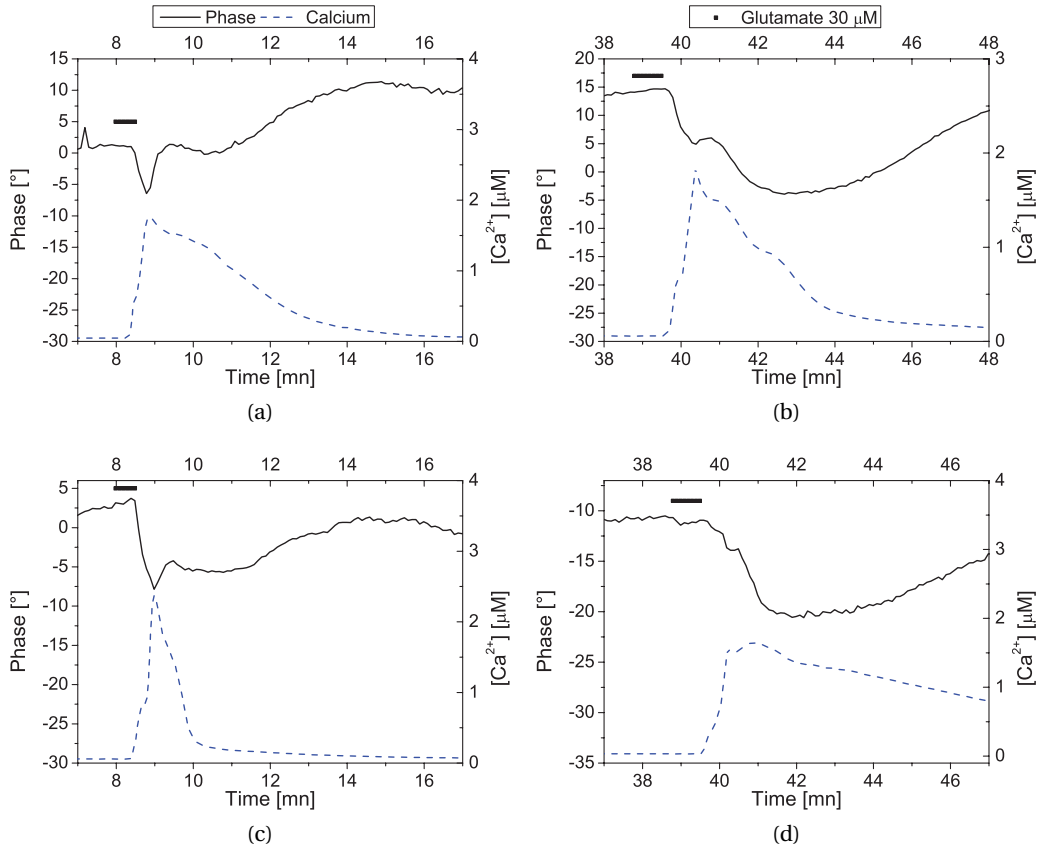

Figure 5.34: Comparison of cell responses in phase and calibrated $[Ca^{2+}]$, showing the correlation between the intracellular calcium concentration and the initial phase break.

surement errors at low Ca^{2+} levels, the reliability of the F_{max} value is of primary importance for high $[Ca^{2+}]$, in particular for high-sensitivity fluorophores as the ones employed in our experiments. This implies typically that the values obtained at saturation are less reliable than the ones at resting levels. Nevertheless, calibration procedures present the advantage of linearising the curves, enabling an easier interpretation for comparison of signals, which is one of the primary objective of the work presented here.

In this context, the calibrated $[Ca^{2+}]$ curves seem to corroborate the proposed interpretation of the phase slope change discussed previously, in the sense that the saturation duration of the $[Ca^{2+}]$ signal is very well correlated with the phase slope change, as shown for example in Fig. 5.33(c–d). Moreover, the phase curves present an excellent simultaneity with the $[Ca^{2+}]$ signal, where both the phase decrease and the small phase increase during slope change are correlated respectively with the $[Ca^{2+}]$ rise and the rapid Ca^{2+} regulation. This result in is accordance with our previous observations during both temporal comparison and pharmacological analysis.

In case of quantitative curves, this correlation can be further extended, as various results seem to indicate that the strength of the abrupt phase change is directly linked with the intensity and shape of the $[Ca^{2+}]$ signal, as shown for various examples in Fig. 5.34, where various $[Ca^{2+}]$ responses correspond very well to their respective phase signals. While those observations are based on preliminary results which were not analysed on a sufficient amount of cells to be statistically fully relevant, they seem to corroborate the previous interpretation, even by indicating a potential quantitative relation both in dynamics and amplitude between the initial phase signal and the corresponding $[Ca^{2+}]$ burst of neuronal responses to glutamate.

5.8 Discussion and perspectives

The results presented in this chapter showed various applications of DHM measurements in the context of neuronal dynamics. In particular, the quantitative phase signal was shown to present specific features depending on the cellular state, where it can be interpreted as a measure of both the intracellular dilution and volume, which are intimately correlated with transmembranar water movements, and can thus be considered as an measure of the cell volume regulation (CVR).

Typical cell responses could be classified in mainly three types, i.e. irreversible, reversible and biphasic, in accordance with previous studies [Jou11]. These response types are closely related to ionic fluxes, such as calcium and sodium, which were simultaneously measured along with the phase signal. Furthermore, the differentiation between typically irreversible and both reversible or biphasic signals can be performed easily through various criteria, such as the value of the phase decrease, or the shape of the phase temporal response.

Within this interpretation, the phase signal can be employed for applications such as early cell death detection, where the irreversible phase response can be understood as a symptom of cell volume and intracellular ionic deregulation, an early indicator of death mechanisms triggering. The CVR capability measurement can typically be performed in the case of glutamate-mediated excitotoxicity in a time range of tens of minutes, which is to be compared with typical detection times of usual cell death assessment methods based on the loss of membrane integrity, which occurs several hours after drug application in a late state of necrosis. The early detection of cell death through this method which presents the advantage of being label-free, non-invasive and full-field could lead to valuable applications in high-throughput applications, which require the acquisition of data on a large amount of cells within time ranges as short as possible.

On more fundamental aspects, the links between ionic fluxes and the phase signal could be further studied by comparing the phase signal measurement with functional imaging through fluorescent ionic indicators. The influence of ionic fluxes such as Ca^{2+} and Na^{+} could be analysed, showing that the phase signal possesses various features generated by specific mechanisms underlined by ionic movements. In particular, the global response of the phase sig-

nal appears to follow essentially the slower trend of $[Na^+]$, while a specific $[Ca^{2+}]$ signature could be identified in the phase signal during the well known Ca^{2+} burst occurring under glutamate stimulation. Correlated to $[Ca^{2+}]$ and $[Na^+]$ imaging, the quantitative phase signal also presents specific features under pharmacological analysis, where the blockage of certain types of glutamate receptors changes the response type, in accordance with ionic fluxes measurements, where the changes can be interpreted in terms of biological mechanisms implied by the specifically activated receptors. Furthermore, the calibration of ionic signals in order to retrieve quantitative values makes possible to compare directly phase signal, a global intrinsically quantitative indicator, with fluorescent ionic imaging, a specific extrinsically quantitative indicator.

These close links between ionic intracellular concentrations and the phase signal, essentially dependent on the intracellular dilution occurring through water movements, show the close link between various biological mechanisms in cellular environments, such as ionotropic receptors activation, voltage-gated channels and co-transporters. In this context, phase signal measurement can bring further insights in cellular dynamics studies, by bringing information which is classically not covered by standard investigation tools such as fluorescence imaging or electrophysiology.

References

[Alt93] S. A. Altman, L. Randers, and G. Rao, "Comparison of trypan blue dye exclusion and fluorometric assays for mammalian cell viability determinations," *Biotechnol. Progr.* **9** (6), pp. 671–674 (1993).

[Ank95] M. Ankarcrona, J. Dypbukt, E. Bonfoco, B. Zhivotovsky, S. Orrenius, S. Lipton, and P. Nicotera, "Glutamate-induced neuronal death: A succession of necrosis or apoptosis depending on mitochondrial function," *Neuron* **15** (4), pp. 961–973 (1995).

[Ban87] H. Bank, "Assessment of islet cell viability using fluorescent dyes," *Diabetologia* **30** (10), pp. 812–816 (1987).

[Bor04] C. Bortner and J. Cidlowski, "The role of apoptotic volume decrease and ionic homeostasis in the activation and repression of apoptosis," *Pflug. Arch. Eur. J. Physiol.* **448** (3), pp. 313–318 (2004).

[Bre93] G. Brewer, J. Torricelli, E. Evege, and P. Price, "Optimized survival of hippocampal neurons in B27-supplemented Neurobasal^{TM}, a new serum-free medium combination," *J. Neurosci. Res.* **35** (5), pp. 567–576 (1993).

[Bro93] J. Brocard, S. Rajdev, and I. Reynolds, "Glutamate-induced increases in intracellular free Mg2+ in cultured cortical neurons," *Neuron* **11** (4), pp. 751–757 (1993).

[Bro94] J. Brorson, P. Manzolillo, and R. Miller, "Ca2+ entry via AMPA/KA receptors and excitotoxicity in cultured cerebellar Purkinje cells," *J. Neurosci.* **14** (1), pp. 187–197 (1994).

[Che08] M. Chen, S. Sepramaniam, A. Armugam, M. Choy, J. Manikandan, A. Melendez, K. Jeyaseelan, and N. Cheung, "Water and ion channels: Crucial in the initiation and progression of apoptosis in central nervous system?," *Curr. Neuropharmacol.* **6** (2), pp. 102–116 (2008).

[Cho94] D. W. Choi, "Glutamate receptors and the induction of excitotoxic neuronal death," in *Neuroscience: From the Molecular to the Cognitive*, F. E. Bloom, Ed., vol. 100, ser. Prog. Brain Res. Elsevier (1994), pp. 47–51.

[Col10] M. I. Colombo and H.-U. Simon, "Autophagy," in *Cell Death*, G. Melino and D. Vaux, Eds., John Wiley & Sons, Inc., New York (2010), pp. 175–188.

[Dia01] A. Diarra, C. Sheldon, and J. Church, "In situ calibration and $[H^+]$ sensitivity of the fluorescent Na^+ indicator SBFI," *Am. J. Physiol.-Cell Ph.* **280** (6), pp. C1623–C1633 (2001).

[Dup09] L. Duprez, E. Wirawan, T. Berghe, and P. Vandenabeele, "Major cell death pathways at a glance," *Microbes Infect.* **11** (13), pp. 1050–1062 (2009).

[ED94] G. C. R. Ellis-Davies and J. H. Kaplan, "Nitrophenyl-EGTA, a photolabile chelator that selectively binds Ca^{2+} with high affinity and releases it rapidly upon photolysis," *P. Natl. Acad. Sci. USA* **91** (1), pp. 187–191 (1994).

[Egu97] Y. Eguchi, S. Shimizu, and Y. Tsujimoto, "Intracellular ATP Levels Determine Cell Death Fate by Apoptosis or Necrosis," *Cancer Res.* **57** (10), pp. 1835–1840 (1997).

[Erd00] W. L. Erdahl, C. J. Chapman, R. W. Taylor, and D. R. Pfeiffer, "Ionomycin, a Carboxylic Acid Ionophore, Transports Pb^{2+} with High Selectivity," *J. Biol. Chem.* **275** (10), pp. 7071–7079 (2000).

[Gee00] K. Gee, K. Brown, W.-N. Chen, J. Bishop-Stewart, D. Gray, and I. Johnson, "Chemical and physiological characterization of fluo-4 Ca^{2+}-indicator dyes," *Cell Calcium* **27** (2), pp. 97–106 (2000).

[Gry85] G. Grynkiewicz, M. Poenie, and R. Tsien, "A new generation of Ca^{2+} indicators with greatly improved fluorescence properties," *J. Biol. Chem.* **260** (6), pp. 3440–3450 (1985).

[Ham01] C. Hammond, *Cellular and Molecular Neurobiology*, 2nd ed. Academic Press (2001).

[Hoc89] P. Hockberger, H. Tseng, and J. Connor, "Fura-2 measurements of cultured rat Purkinje neurons show dendritic localization of Ca2+ influx," *J. Neurosci.* **9** (7), pp. 2272–2284 (1989).

[Hof09] E. Hoffmann, I. Lambert, and S. Pedersen, "Physiology of cell volume regulation in vertebrates," *Physiol. Rev.* **89** (1), pp. 193–277 (2009).

[Hud80] L. Hudson and F. Hay, *Practical Immunology*. Blackwell Scientific Publications (1980), pp. 29–31.

[Hue88] J. E. Huettner and B. P. Bean, "Block of N-methyl-D-aspartate-activated current by the anticonvulsant MK-801: selective binding to open channels," *P. Natl. Acad. Sci. USA* **85** (4), pp. 1307–1311 (1988).

[Jac97] M. D. Jacobson, M. Weil, and M. C. Raff, "Programmed Cell Death in Animal Development," *Cell* **88** (3), pp. 347–354 (1997).

[Jon85] K. H. Jones and J. A. Senft, "An improved method to determine cell viability by simultaneous staining with fluorescein diacetate-propidium iodide," *J. Histochem. Cytochem.* **33** (1), pp. 77–79 (1985).

[Jou11] P. Jourdain, N. Pavillon, C. Moratal, D. Boss, B. Rappaz, C. Depeursinge, P. Marquet, and P. J. Magistretti, "Transmembrane water fluxes in neurons revealed by Digital Holographic Microscopy: application to the study of glutamate ionotropic receptors and of the co-transporters KCC2 and NKCC1," *J. Neurosci.*, (2011), (accepted).

[Kie94] L. Kiedrowski, G. Brooker, E. Costa, and J. T. Wroblewski, "Glutamate impairs neuronal calcium extrusion while reducing sodium gradient," *Neuron* **12** (2), pp. 295–300 (1994).

[Kie95] L. Kiedrowski and E. Costa, "Glutamate-induced destabilization of intracellular calcium concentration homeostasis in cultured cerebellar granule cells: role of mitochondria in calcium buffering.," *Mol. Pharmacol.* **47** (1), pp. 140–147 (1995).

[Kor83] C. Korzeniewski and D. M. Callewaert, "An enzyme-release assay for natural cytotoxicity," *J. Immunol. Methods* **64** (3), pp. 313–320 (1983).

[Kry08] D. Krysko, T. Vanden Berghe, K. D'Herde, and P. Vandenabeele, "Apoptosis and necrosis: Detection, discrimination and phagocytosis," *Methods* **44** (3), pp. 205–221 (2008).

[Küh07] J. Kühn, T. Colomb, F. Montfort, F. Charrière, Y. Emery, E. Cuche, P. Marquet, and C. Depeursinge, "Real-time dual-wavelength with digital holographic microscopy with a single hologram acquisition," *Opt. Express* **15** (12), pp. 7231–7242 (2007).

[Lec02] H. Lecoeur, "Nuclear apoptosis detection by flow cytometry: Influence of endogenous endonucleases," *Exp. Cell Res.* **277** (1), pp. 1–14 (2002).

[Mar00] M. Maravall, Z. Mainen, B. Sabatini, and K. Svoboda, "Estimating intracellular calcium concentrations and buffering without wavelength ratioing," *Biophys. J.* **78** (5), pp. 2655–2667 (2000).

[Mar03] P. Marquet, "Développement d'une nouvelle technique de microscopie optique tridimensionnelle, la microscopie holographique digitale. Perspectives pour l'étude de la plasticité neuronale," PhD Thesis, Université de Lausanne, (2003).

[Mei06] S. Meier, Y. Kovalchuk, and C. Rose, "Properties of the new fluorescent Na^+ indicator CoroNa Green: Comparison with SBFI and confocal Na^+ imaging," *J. Neurosci. Methods* **155** (2), pp. 251–259 (2006).

[Par06] Y. Park, G. Popescu, K. Badizadegan, R. Dasari, and M. Feld, "Diffraction phase and fluorescence microscopy," *Opt. Express* **14** (18), pp. 8263–8268 (2006).

[Par08] R. Paredes, J. Etzler, L. Watts, W. Zheng, and J. Lechleiter, "Chemical calcium indicators," *Methods* **46** (3), pp. 143–151 (2008).

[Pav10a] N. Pavillon, A. Benke, D. Boss, C. Moratal, J. Kühn, P. Jourdain, C. Depeursinge, P. J. Magistretti, and P. Marquet, "Cell Morphology and Intracellular Ionic Homeostasis explored with a Multimodal Approach combining Epifluorescence and Digital Holographic Microscopy," *J. Biophotonics* **3** (7), pp. 432–436 (2010).

[Pav10b] N. Pavillon, A. Benke, D. Boss, C. Moratal, P. Jourdain, Y. Emery, C. Depeursinge, P. J. Magistretti, and P. Marquet, "Study of Intracellular Ion Dynamics with a Multimodality Approach Combining Epifluorescence and Digital Holographic Microscopy," in *Digital Holography and Three-Dimensional Imaging (DH)*, JMA26, OSA, Miami, FL (2010).

[Pav11a] N. Pavillon, J. Kühn, P. Jourdain, C. Depeursinge, P. J. Magistretti, and P. Marquet, "Cell Death and Ionic Regulation Detection with Digital Holographic Microscopy," in *Digital Holography and Three-Dimensional Imaging (DH)*, OSA, Tokyo, Japan (May 2011).

[Pav11b] N. Pavillon, J. Kühn, C. Moratal, P. Jourdain, C. Depeursinge, P. J. Magistretti, and P. Marquet, "Early Cell Death Detection with Digital Holographic Microscopy," *J. Cell Biol.*, (2011), (to be submitted).

[Pet97] M. Petr and R. Wurster, "Determination of in situ dissociation constant for Fura 2 and quantitation of background fluorescence in astrocyte cell line U373-MG," *Cell Calcium* **21** (3), pp. 233–240 (1997).

[Pur08] D. Purves, Ed., *Neuroscience*, 4th. Sinauer Associates, Inc. (2008).

[Rap05] B. Rappaz, P. Marquet, E. Cuche, Y. Emery, C. Depeursinge, and P. Magistretti, "Measurement of the integral refractive index and dynamic cell morphometry of living cells with digital holographic microscopy," *Opt. Express* **13** (23), pp. 9361–9373 (2005).

[Rap08a] B. Rappaz, F. Charrière, C. Depeursinge, P. Magistretti, and P. Marquet, "Simultaneous cell morphometry and refractive index measurement with dual-wavelength digital holographic microscopy and dye-enhanced dispersion of perfusion medium," *Opt. Lett.* **33** (7), pp. 744–746 (2008).

[Rap08b] B. Rappaz, "Cellular Dynamics Explored with Digital Holographic Microscopy," PhD Thesis, Ecole Polytechnique Fédérale de Lausanne, (2008).

[Ric99] T. Rich, C. Watson, and A. Wyllie, "Apoptosis: The germs of death," *Nat. Cell Biol.* **1** (3), E69–E71 (1999).

[Sch01] D. Schubert and D. Piasecki, "Oxidative glutamate toxicity can be a component of the excitotoxicity cascade," *J. Neurosci.* **21** (19), pp. 7455–7462 (2001).

[Sil96] R. Silver, D. Colquhoun, S. Cull-Candy, and B. Edmonds, "Deactivation and desensitization of non-NMDA receptors in patches and the time course of EPSCs in rat cerebellar granule cells," *J. Physiol.* **493** (1), pp. 167–173 (1996).

[Sto98] A. Stout, H. Raphael, B. Kanterewicz, E. Klann, and I. Reynolds, "Glutamate-induced neuron death requires mitochondrial calcium uptake," *Nat. Neurosci.* **1** (5), pp. 366–373 (1998).

[Str01] W. Strober, "Trypan Blue Exclusion Test of Cell Viability," in *Current Protocols in Immunology*, John Wiley & Sons, Inc. (2001), A.3B.1—A.3B.2.

[Su04] X. Su and W. Chen, "Reliability-guided phase unwrapping algorithm: A review," *Opt. Laser Eng.* **42** (3), pp. 245–261 (2004).

[Tak88] H. Takajo and T. Takahashi, "Noniterative method for obtaining the exact solution for the normal equation in least-squares phase estimation from the phase difference," *J. Opt. Soc. Am. A* **5** (11), pp. 1818–1827 (1988).

[Tao00] H.-Z. Tao, L. Zhang, G.-Q. Bi, and M.-M. Poo, "Selective presynaptic propagation of long-term potentiation in defined neural networks," *J. Neurosci.* **20** (9), pp. 3233–3243 (2000).

[Ver99] O. Vergun, J. Keelan, B. Khodorov, and M. Duchen, "Glutamate-induced mitochondrial depolarisation and perturbation of calcium homeostasis in cultured rat hippocampal neurones," *J. Physiol.* **519** (2), pp. 451–466 (1999).

[Vil11] M. R. Villarreal. (Feb. 2011). Neuron - Wikipedia, the free encyclopedia, [Online]. Available: http://en.wikipedia.org/wiki/Neuron.

[Whi95] R. White and I. Reynolds, "Mitochondria and Na+/Ca2+ exchange buffer glutamate-induced calcium loads in cultured cortical neurons," *J. Neurosci.* **15** (2), pp. 1318–1328 (1995).

[Wol04] F. Wolbers, H. Andersson, A. Van Den Berg, and I. Vermes, "Apoptosis induced kinetic changes in autofluorescence of cultured HL60 cells-possible application for single cell analysis on chip," *Apoptosis* **9** (6), pp. 749–755 (2004).

[Yua03] J. Yuan, M. Lipinski, and A. Degterev, "Diversity in the mechanisms of neuronal cell death," *Neuron* **40** (2), pp. 401–413 (2003).

[Zam96] L. Zamai, E. Falcieri, G. Marhefka, and M. Vitale, "Supravital exposure to propidium iodide identifies apoptotic cells in the absence of nucleosomal DNA fragmentation," *Cytometry* **23** (4), pp. 303–311 (1996).

[Zam97] N. Zamzami, T. Hirsch, B. Dallaporta, P. Petit, and G. Kroemer, "Mitochondrial implication in accidental and programmed cell death: Apoptosis and necrosis," *J. Bioenerg. Biomembr.* **29** (2), pp. 185–193 (1997).

6 Conclusion

We presented various applications of digital holographic microscopy (DHM), where we employed different specific features of this technique such as its coherent imaging properties or its capacity to retrieve quantitative phase information, for applications in the enhancement of the DHM reconstruction quality, three-dimensional quantitative phase imaging, and neuronal cell biology. Since various subjects were tackled in this manuscript, we provide as a conclusion a brief summary of the main results obtained, along with some perspectives.

We studied mathematical ways to suppress the so-called zero-order, which consists in incoherent terms recorded with interferometric methods. In the context of off-axis holography, the zero-order reduces the bandwidth available for the cross-correlation terms in which the complex wavefront is recorded through spatial encoding. We could show that through efficient zero-order suppression, diffraction-limited imaging can be obtained in off-axis DHM, independently of the magnification employed. We proposed two different methods in order to suppress the zero-order, either through iterative treatment based on relations between the coherent and incoherent imaging, or through nonlinear operators, by transferring the signal to an additive space in which the zero-order can be intrinsically suppressed. Both methods were developed with the aim of maintaining the one-shot feature of off-axis holography, so that they are based on processing a single hologram at a time. They were characterised theoretically, and assessed experimentally with different types of holograms, such as speckle interferograms in the context of rough surfaces investigated at low magnification, or phase images in the context of topographic measurements or imaging of biological specimens. We could demonstrate experimentally the potential increase in spatial resolution by employing these methods, without having to cope with additional noise generated by the incoherent terms. The iterative method proved to be less restrictive in the measurement conditions required for its applicability, but at the cost of non-exact reconstruction. On the other hand, the performances are generally better when using the nonlinear technique, as long as the more constraining experimental conditions are satisfied.

We applied the quantitative phase measurement provided by digital holographic microscopy to three-dimensional imaging. The fundamental imaging conditions of digital holography being essentially based on full field illumination, it implies that no resolution in the direction of the optical axis is provided through this approach. It was thus proposed to take advantage of the coherent imaging properties of interferometry to coherently superpose frames with different angular information, in order to computationally reconstruct a 3D-resolved image. Most of the measurement procedures up to now base their acquisition on rotations, either of the measured specimen or of the illuminating beam, leading potentially to measurement errors due to for instance mechanical imprecision. We thus investigated a new measurement procedure based on a linear scanning, as provided by a standard moving stage, while acquiring the angular information through the use of convergent beams as an excitation pattern, instead of the classical plane wave illumination. We developed a reconstruction algorithm based on an arrangement of the data to retrieve data sets to be fed to standard tomographic inversion algorithm, in a similar way to the so-called fan beam measurement method in computerised tomography. We could demonstrate experimentally the validity of our measurement approach by reconstructing 3D images of pollen grains. The tomographic reconstruction approach also presents the advantage of suppressing the ambiguity between object height and intracellular refractive index that occurs in phase measurement. We thus quantified our measurements in order to retrieve the refractive index distribution of our measured specimens. The preliminary results obtained at this stage however suffer from a degraded resolution in the direction of the optical axis, mainly due to the reduced numerical aperture of the employed excitation pattern. Nevertheless, the fact of employing a fixed illumination during tomographic measurements can greatly reduce the long calibration procedures that are necessary when typically scanning the beam, as the illumination pattern and phase shifts change during the acquisition. Furthermore, it could lead to the combination with other techniques such as image deconvolution, in order to further improve the resolution of the 3D images.

We also employed DHM in the context of neuronal biology, where the quantitative phase signal can be interpreted as an indicator of cell regulation processes, such as volume regulation or ionic homeostasis, while being fully non-invasive and label-free. We first employed this measurement as an early indicator of cell death, which we could detect through so-called irreversible phase responses, which can be understood as a dramatic dilution of the intracellular content and subsequent absence of volume regulation. Based on other publications showing the importance of cell volume regulation in the death mechanisms triggering, we used the phase signal in order to measure the regulation capability of cells, and thus detect the subsequent cell death. We compared our method with standard cell viability assessment methods based on dyes such as trypan blue or propidium iodide, which rely on the loss of membrane integrity following the necrosis death stage occurring *in vitro*, showing an excellent agreement in detection capability, while enabling detection typically hours before methods based on dyes, thanks to its principle relying on early cell death triggering mechanisms. On a second stage, we compared the phase signal with intracellular ionic concentration, mea-

sured through quantitative fluorescence. We could show that the phase signal is concomitant with ionic fluxes during neuronal dynamics occurring under stimulation with a neurotransmitter such as glutamate, which is well-known to generate strong ionic currents during the action potential triggered on neurons. In particular, we could demonstrate that the phase signal is generally following the dynamics of sodium, an ion present at high intracellular concentration, while being part of the ionic regulation following action potentials. On the other hand, we could show that a specific phase signature during glutamate stimulation is linked to the well-known calcium burst occurring during membrane depolarisation. This relation could be identified first through quantification of the fluorescence signal, which enabled to demonstrate a striking resemblance in the dynamics of signals during the initiation of the action potential. Furthermore, pharmacological analysis showed strong changes in the behaviour of this phase signature when various membrane receptors were activated, which calcium permeability is known to be drastically different. These results show the capability of phase to measure various cellular processes, through the measurement of the intracellular dilution, which occurs by volume changes and consequent water movements through the cell membrane. While these signals are not easy to interpret due to their global nature compared to specific and functional measurements as in the case of fluorescence, the potential of phase imaging for the measurement of biological processes is very promising as a non-invasive and label-free detection method providing quantitative information.

As a final note, we would like to stress that while the different subjects covered in this thesis are rather diverse, they nevertheless share similar ultimate goals. The phase signal measured on cell dynamics can be quite small, and even be at the limit of the SNR level of standard DHM measurements. The zero-order suppression is typically one of the approaches to reduce the noise of quantitative phase measurements, in order to increase the SNR for finer detection. Furthermore, the phase signal can also provide relevant information about cellular dynamics, but can be difficult to interpret, particularly because of the ambiguity between the specimen height and its internal refractive index distribution. Tomographic reconstruction is typically an approach which solves this ambiguity of the phase signal, by recovering three-dimensional information enabling the resolution of the 3D morphology of the specimen, and consequently the recovery of the 3D refractive distribution and volume. These various multidisciplinary approaches are in our opinion necessary in order to overcome the limitations that phase imaging and more particularly DHM are experiencing after having reached a mature stage for their fundamental features.

A Effective magnification calibration

When performing measurements with microscope objectives, it is common that some slight variations occur compared to nominal conditions, such as condenser lens position, field lens position, variations of microscope objective working distance, etc. Therefore, there are often some discrepancies between the nominal magnification as announced by the manufacturer and effective magnification of the optical system. For this reason, it is common to calibrate the pixel size of the optical system before performing measurements. This is even more important in digital holography, as digital processing, and in particular phase masks employed to compensate for aberrations can change the curvature of the digital representation of the field, and thus change slightly the imaging conditions.

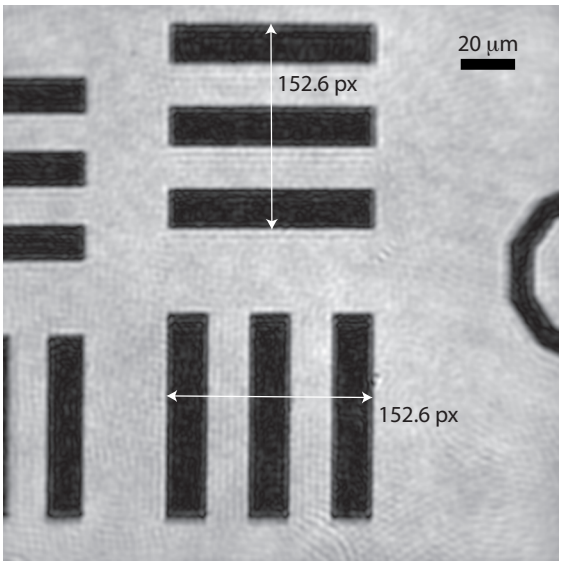

Figure A.1: USAF 1951 target (element 5-1), imaged in transmission with DHM reconstruction, with its amplitude shown.

For calibration, a USAF 1951 test target is classically employed for measuring the pixel size in the object plane. It consists in lines made by chromium deposit, as shown in Fig. A.1, where

an element of the target is imaged in transmission, with its amplitude image shown. The measurement was performed with a transmission DHM, and the image was reconstructed with standard procedures (cf. chapter 2). Imaging the target directly with DHM enables to measure the pixel size as imaged by the experimental setup and the numerical reconstruction procedure.

As the target is classically employed for tests of resolution performance, each elements are characterised by a unit analog to spatial frequency, namely line pairs per millimetres (lp/mm), where a line pair corresponds to a black a with line. The standard procedure for determining the pixel size is thus to select an element filling the field of view, and to measure the length in pixels of each orthogonal elements. Choosing an element big enough ensures to minimise uncertainties of measurements, and measuring on both elements enables to detect an eventual astigmatism, as shown in Fig. A.1. The pixel size in the object space can then be calculated as

$$\Delta x_o = \frac{2.5 \cdot 10^{-3}}{a \cdot p} \text{ [µm]}, \tag{A.1}$$

where a is the length of the the element in pixels, and p is the amount of line per millimetres for the particular elements. The factor of 2.5 accounts for the measurement made on 2 and a half lines, in order again to minimise uncertainty. The units of the pixel size are kept in micrometers for convenience, as the effective magnification can then be calculated by calculating the ratio between Δx_o and the pixel size of the detector Δx, which is classically given in micrometers in sensors datasheets, giving

$$M_{\text{eff}} = \frac{\Delta x}{\Delta x_o} = \frac{\Delta x \cdot 2.5 \cdot 10^{-3}}{a \cdot p}. \tag{A.2}$$

In the particular case presented in Fig. A.1, the measured element is the no. 5-1, having a frequency of $p = 32$ lp/mm, and having a length of $a = 152.6$ px, giving a pixel size in the object space of $\Delta x_o = 511.96$ nm/px, and an effective magnification of $M_{\text{eff}} = 12.59$, while it was measured with a 10× MO. Through the thesis, all images provided with a scale bar were calibrated in this fashion.

B Quantitative fluorescence

We derive in this appendix the equations employed in quantitative ionic concentration monitoring through fluorescence, as described in subsection 2.3. Various models are used depending on the type of fluorophore measured and on the experimental parameters available for calibrating curves obtained through ionic concentration monitoring.

On a general point of view, calibration equations are essentially based on one hand on the law mass equation

$$A_xB_y \rightleftharpoons xA + yB, \quad K_d = \frac{[A]^x \cdot [B]^y}{[A_xB_y]}, \tag{B.1}$$

where K_d is the dissociation constant, and A, B are two chemical compounds. In the context of ionic monitoring, Eq. (B.1) can be simplified to

$$K_d = \frac{[C^{n+}]\, c_f}{c_b}, \tag{B.2}$$

where C^{n+} is a generic ion, and c_f, c_b are respectively the free and bonded concentrations of fluorophore. A complexation of 1:1 is here assumed for the chemical equilibrium, as fluorophores are usually bonding to one ion. On the other hand, one relies on a model of the fluorescence signal measured on the detector as

$$F = S_f \cdot c_f + S_b \cdot c_b, \tag{B.3}$$

where S_f, S_b are coefficients of fluorescence efficiency for respectively the free and bonded fluorescent molecules. One should note that the effects of the detection system can be included in those coefficients, so that they can be considered as macroscopic indicators.

Intensity-based fluorophores

The derivation in this paragraph is based on fluorophores which emission efficiency changes with ionic concentration, such as Fluo-4 (cf. Fig. 2.11), and for which the measurement at only one wavelength is employed.

One can first consider that the total intracellular concentration of fluorophore is the sum of free and bonded concentrations, giving

$$c_t = c_f + c_b. \tag{B.4}$$

By substituting Eq. (B.4) into Eq. (B.1), one obtains

$$\frac{c_b}{c_t} = \frac{\left[\mathrm{C}^{n+}\right]}{K_d + [\mathrm{C}^{n+}]}. \tag{B.5}$$

In the same manner, substituting Eq. (B.4) into Eq. (B.3) yields a fluorescence signal given by

$$F = S_f(c_t - c_b) + S_b \cdot c_b = S_f \cdot c_t + (S_b - S_f)c_b. \tag{B.6}$$

One can then consider that the maximum and minimum fluorescence $F_{\max}$ and $F_{\min}$ are defined by

$$F_{\max} = S_b c_t, \qquad F_{\min} = S_f c_t, \tag{B.7}$$

corresponding to the respective bonded or free ion coefficient, as all fluorophores are either bonded or in free form. Substituting Eq. (B.7) into Eq. (B.6) yields

$$\begin{aligned} F &= F_{\min} + (F_{\max} - F_{\min}) \frac{c_b}{c_t}, \\ &= F_{\min} + (F_{\max} - F_{\min}) \frac{\left[\mathrm{C}^{n+}\right]}{K_d + [\mathrm{C}^{n+}]}, \end{aligned} \tag{B.8}$$

so that the intracellular free ionic concentration is finally given by

$$\left[\mathrm{C}^{n+}\right]_{\text{free}} = K_d \frac{F - F_{\min}}{F_{\max} - F}. \tag{B.9}$$

Intensity-based fluorescence without minimum calibration

As described in subsection 2.3, the calibration to obtain the values $F_{\min}$ and $F_{\max}$ can be cumbersome, as they involve the use of various substances to bond the measured ion (chelators), and membrane permeabilisation to ease ionic transfer through the membrane. Particularly in the case of Ca^{2+}, where calcium compartments are present in the cell (cf. subsection 5.1), the value $F_{\min}$ is difficult to measure and is often overestimated. Furthermore, the high membrane permeability induced pharmacologically during calibration implies that cells are under stressful conditions, so that long calibration may lead to values which are not accurate anymore for physiological conditions.

For these reasons, suppressing parameters to be measured *in situ* can greatly simplify the experimental procedure, and increase the accuracy of measurement. By rearranging Eq. (B.9), on can get

$$\left[\mathrm{C}^{n+}\right]_{\text{free}} = K_d \frac{\frac{F}{F_{\max}} - \frac{F_{\min}}{F_{\max}}}{1 - \frac{F}{F_{\max}}} = K_d \frac{\frac{F}{F_{\max}} - \frac{1}{R_f}}{1 - \frac{F}{F_{\max}}}, \tag{B.10}$$

where $R_f = {}^{F_{\max}}/_{F_{\min}}$ is the dynamic range of the fluorophore. This equation is typically interesting for fluorophores with high dynamic ranges, as the term R_f^{-1} becomes negligible compared to the fluorescence signal. This parameter can be characterised *in vitro*, as it depends only on the fluorescent molecule characteristics.

Ratiometric fluorescence

The ratiometric fluorescence measurement is based on fluorophores which absorption spectrum changes with the concentration of monitored ion, so that two measurements are acquired at different wavelengths, as in the case of Fura-2 and SBFI fluorophores (cf. Figs. 2.12 and 2.14). The calibration method provided here is attributed to Grynkiewicz *et al.*, and was proposed with the first developments of Fura-2, one of the first ratiometric fluorophore developed. In this case, the equation modelling the fluorescence signal is identical to Eq. (B.3), but considers the two wavelengths of excitation, giving

$$\begin{aligned} F_{\lambda_1} &= S_{f1} \cdot c_f + S_{b1} \cdot c_b, \\ F_{\lambda_2} &= S_{f2} \cdot c_f + S_{b2} \cdot c_b, \end{aligned} \tag{B.11}$$

where four S coefficients are present in this case. The ratio is then defined by

$$\frac{F_{\lambda_1}}{F_{\lambda_2}} = R = \frac{S_{f1} \cdot c_f + S_{b1} \cdot c_b}{S_{f2} \cdot c_f + S_{b2} \cdot c_b}, \tag{B.12}$$

where it is possible to substitute Eqs. (B.4) and (B.5) in Eq. (B.12), giving

$$R = \frac{S_{f1} \cdot \left(c_t \left(K_d + \left[\mathrm{C}^{n+}\right]\right) - \left[\mathrm{C}^{n+}\right] c_t\right) + S_{b1} \left[\mathrm{C}^{n+}\right] c_t}{S_{f2} \cdot \left(c_t \left(K_d + \left[\mathrm{C}^{n+}\right]\right) - \left[\mathrm{C}^{n+}\right] c_t\right) + S_{b2} \left[\mathrm{C}^{n+}\right] c_t}. \tag{B.13}$$

Solving for $\left[\mathrm{C}^{n+}\right]$ then gives

$$\left[\mathrm{C}^{n+}\right] = K_d \frac{S_{f2} R - S_{f1}}{S_{b1} - S_{b2} R} = K_d \frac{R - {}^{S_{f1}}/_{S_{f2}}}{{}^{S_{b1}}/_{S_{b2}} - R} \cdot \frac{S_{f2}}{S_{b2}}. \tag{B.14}$$

It is then possible to note that S_{f2} corresponds to the maximum of the fluorescence at λ_2, and S_{b2} to its minimum, according to the equations

$$\begin{aligned} F_{\lambda_2,\min} &= F_{\lambda_2}(c_f = 0) = S_{b2} \cdot c_t, \\ F_{\lambda_2,\max} &= F_{\lambda_2}(c_b = 0) = S_{f2} \cdot c_t, \end{aligned} \tag{B.15}$$

so that the ratio of fluorescence signals become

$$\frac{F_{\lambda_2,\max}}{F_{\lambda_2,\min}} = \frac{S_{f2}}{S_{b2}}. \tag{B.16}$$

By similar considerations, it is possible to identify the minimum and maximum ratio as

$$\begin{aligned} R_{\min} &= R(c_b = 0) = \frac{S_{f1}}{S_{f2}}, \\ R_{\max} &= R(c_f = 0) = \frac{S_{b1}}{S_{b2}}. \end{aligned} \tag{B.17}$$

By substituting Eqs. (B.15) and (B.17) into Eq. (B.14), the free intracellular ionic concentration for a ratiometric fluorophore becomes

$$\left[C^{n+}\right]_{\text{free}} = K_d \frac{R - R_{\min}}{R_{\max} - R} \cdot \frac{F_{\lambda_2,\max}}{F_{\lambda_2,\min}}. \tag{B.18}$$

C Fourier Diffraction Theorem

We provide in this section a derivation of the Fourier diffraction theorem (FDT) for the three-dimensional case. One common demonstration is the one derived by Born & Wolf, which is sometimes considered as hard to follow. We thus base the demonstration below on the one of Kak & Slaney, which is originally for two dimensions, that we generalised.

The theorem we want to prove is as follows:

When an object is illuminated with a plane wave $u_0(\mathbf{r})$, the Fourier transform of the forward scattered field measured on a plane perpendicular to the propagation vector $\mathbf{k_0}$ of $u_0(\mathbf{r})$ at a distance l_0 from the centre of rotation of the object gives the values of the 3D Fourier transform of the scattering potential $\hat{o}(\mathbf{k})$ along a half-sphere of radius k_0.

$$\hat{u}(k_x, k_y, l_0) = \frac{\mathrm{i}}{2k_z} e^{\mathrm{i}k_z l_0} \hat{o}(k_x, k_y, k_z - k_0) \tag{C.1}$$

Born approximation

The first part of the derivation requires to retrieve the so-called Born integral, which is the starting point for the demonstration of the theorem. This equation relates a field outside the object and its refractive index distribution under a perturbation method at a certain order (the 1$^{\text{st}}$ one in our case). This equation can be derived from the inhomogeneous Helmholtz equation, representing the field behaviour under a forced excitation, as

$$\left(\nabla^2 + k_0^2\right) u(\mathbf{r}) = -u(\mathbf{r}) o(\mathbf{r}), \tag{C.2}$$

which describes the behaviour of the field $u(\mathbf{r})$ under the presence of a diffractive object $o(\mathbf{r})$, represented by its scattering potential, defined as

$$o(\mathbf{r}) = k_0^2 \left[n^2(\mathbf{r}) - 1\right], \tag{C.3}$$

where $n(\mathbf{r})$ is the complex refractive index distribution of the object, and $k_0 = {}^{2\pi}/_{\lambda_0}$ is the wave number in vacuum.

In order to solve Eq. (C.2), one usually divides the field u into $u(\mathbf{r}) = u_0(\mathbf{r}) + u_s(\mathbf{r})$, where u_0 is the solution of the homogeneous equation

$$\left(\nabla^2 + k_0^2\right) u_0(\mathbf{r}) = 0, \tag{C.4}$$

and u_s accounts for the portion of the field scattered by the object. Substituting the separation of the field u into Eq. (C.2) and employing Eq. (C.4) yields

$$\left(\nabla^2 + k_0^2\right) u_s(\mathbf{r}) = -u(\mathbf{r}) o(\mathbf{r}), \tag{C.5}$$

which relates the diffracted field u_s with the incoming wave u and the object function o.

In order to find a solution to this differential equation, we employ the Green's function, which is employed for differential equations of the type $L \cdot u(\mathbf{r}) = f(\mathbf{r})$, so that the equation becomes:

$$L \cdot g(\mathbf{r}|\mathbf{r}') = \delta(\mathbf{r} - \mathbf{r}'), \tag{C.6}$$

where L is a general linear differential operator, and $\delta(\mathbf{r})$ is the multidimensional Dirac function. The advantage of the Green's function resides in the fact that

$$\begin{aligned} L \cdot u(\mathbf{r}) = f(\mathbf{r}) &= \int_\Omega f(\mathbf{r}')\delta(\mathbf{r} - \mathbf{r}')\mathrm{d}\mathbf{r} = \int_\Omega f(\mathbf{r}') L \cdot g(\mathbf{r}|\mathbf{r}')\mathrm{d}\mathbf{r} \\ \Rightarrow u(\mathbf{r}) &= \int_\Omega g(\mathbf{r}|\mathbf{r}') f(\mathbf{r}')\mathrm{d}\mathbf{r}. \end{aligned} \tag{C.7}$$

In the case of the inhomogeneous Helmholtz equation, it is thus defined as

$$\left(\nabla^2 + k_0^2\right) g(\mathbf{r}|\mathbf{r}') = \delta(\mathbf{r} - \mathbf{r}), \tag{C.8}$$

which can be considered as the solution of the inhomogeneous Helmholtz equation for an impulse response .

In this fashion, we can express the scattered field as a convolution of the impulse response and the forcing function of the inhomogeneous differential equation, with $L = -\left(\nabla^2 + k_0^2\right)$ given as

$$\begin{aligned} L \cdot u_s(\mathbf{r}) = u(\mathbf{r}) o(\mathbf{r}) &= \int_V u(\mathbf{r}') o(\mathbf{r}') \delta(\mathbf{r} - \mathbf{r}')\mathrm{d}^3\mathbf{r}, \\ &= \int_V u(\mathbf{r}') o(\mathbf{r}') \cdot L \cdot g(\mathbf{r}|\mathbf{r}')\mathrm{d}^3\mathbf{r}', \\ \Rightarrow u_s(\mathbf{r}) &= \int_V u(\mathbf{r}') o(\mathbf{r}') g(\mathbf{r}|\mathbf{r}')\mathrm{d}^3\mathbf{r}', \end{aligned} \tag{C.9}$$

where differentio-integrals operators permutations have been employed, and V is the integration domain, taken as the volume of the object function. This equation cannot be resolved

directly, as the integrated field is itself function of the scattered field through $u = u_0 + u_s$, where u_0 is the incoming (excitation) field.

The Born approximation relies on a perturbation method, where the scattered field is considered as small compared to the excitation, so that we divide the scattered field in $u(\mathbf{r}) = u_0(\mathbf{r}) + u_s(\mathbf{r})$, $u_s \ll u_0$, so that Eq. (C.9) becomes

$$\begin{aligned} u_s(\mathbf{r}) &= \int_V o(\mathbf{r}')u_0(\mathbf{r}')g(\mathbf{r}|\mathbf{r}')\mathrm{d}^3\mathbf{r}' + \int_V o(\mathbf{r}')u_s(\mathbf{r}')g(\mathbf{r}|\mathbf{r}')\mathrm{d}^3\mathbf{r}', \\ u_s(\mathbf{r}) &\simeq u_B(\mathbf{r}) = \int_V o(\mathbf{r}')u_0(\mathbf{r}')g(\mathbf{r}|\mathbf{r}')\mathrm{d}^3\mathbf{r}', \end{aligned} \tag{C.10}$$

as we neglect the contribution of the perturbation on the final field. This equation can be solved, as now the scattered field u_s depends only on the incoming field u_0.

One should note that the Born approximation can be employed for higher orders of diffraction than the 1$^{\text{st}}$ order described in Eq. (C.10). A more general representation, based on a recurrent approach, yields

$$u_B^{(m+1)}(\mathbf{r}) = \int_V o(\mathbf{r}') \left[u_0(\mathbf{r}') + u_B^{(m)}(\mathbf{r}') \right] g(\mathbf{r}|\mathbf{r}')\mathrm{d}^3\mathbf{r}', \quad m \in \mathbb{N}^*, \quad u_B^{(0)} \equiv 0, \tag{C.11}$$

where m represents the order of diffraction.

Green's function

From the Born integral derived in the previous paragraph, it is now possible to try to solve the problem of inverting the diffraction equation. The first key point is to provide an expression for the Green's function, which can be expressed in 3D as

$$g(\mathbf{r}|\mathbf{r}') = \frac{e^{\mathrm{i}k_0|\mathbf{r}-\mathbf{r}'|}}{4\pi|\mathbf{r}-\mathbf{r}'|}, \qquad \mathbf{r} \in \mathbb{R}^3. \tag{C.12}$$

This equation corresponds to a spherical wave emanating from a scattering point, and can be intuitively understood as an impulse response, so that the Born integral corresponds to a sum of convoluted spherical waves, and the object is modelled as an infinite sum of scattering points.

In order to derive the theorem, the Green function must be expanded in a plane wave expression, also commonly referred to as the angular spectrum. By considering that the measurement plane is placed perpendicularly to the optical axis z, the plane wave expansion of the Green's function can be expressed as

$$g(\mathbf{r}|\mathbf{r}') = \frac{\mathrm{i}}{8\pi^2} \iint_{-\infty}^{\infty} \frac{1}{k_z} e^{\mathrm{i}[\alpha(x-x')+\beta(y-y')+k_z|z-z'|]} \mathrm{d}\alpha\mathrm{d}\beta, \tag{C.13}$$

where the discontinuity on the z dimension accounts for the forward- ($z - z' > 0$) and back-propagating ($z - z' < 0$) fields, and where the projections of the wave number are expressed as

$$\begin{cases} k_x = \alpha = \boldsymbol{k} \cdot \boldsymbol{e}_x \\ k_y = \beta = \boldsymbol{k} \cdot \boldsymbol{e}_y. \end{cases} \tag{C.14}$$

Explicit expression of Born integral

By inserting Eq. (C.13) into Eq. (C.10), we get the Born integral with the explicit Green's function, expressed as

$$u_B(\mathbf{r}) = \int_V o(\mathbf{r}') u_0(\mathbf{r}') \left[\frac{\mathrm{i}}{8\pi^2} \iint_{-\infty}^{\infty} \frac{1}{k_z} e^{\mathrm{i}[\alpha(x-x')+\beta(y-y')+k_z|z-z'|]} \mathrm{d}\alpha \mathrm{d}\beta \right] \mathrm{d}^3\mathbf{r}'. \tag{C.15}$$

As in the theorem, we consider an excitation wave $u_0(\boldsymbol{r})$ as a plane wave, i.e. $u_0 = e^{i\mathbf{k_0}\cdot\mathbf{r}}$. For simplicity, it is considered to propagate along the z axis, in order to be in accordance with the plane wave expansion of the Green's function, so that $\mathbf{k_0} = (0, 0, k_0)$. By inserting this expression into (C.15) and arranging the terms, the integral becomes

$$u_B(\mathbf{r}) = \frac{\mathrm{i}}{8\pi^2 k_z} \int_V o(\mathbf{r}') e^{\mathrm{i}k_0 z'} \left[\iint_{-\infty}^{\infty} e^{\mathrm{i}[\alpha(x-x')+\beta(y-y')+k_z|z-z'|]} \mathrm{d}\alpha \mathrm{d}\beta \right] \mathrm{d}^3\mathbf{r}'. \tag{C.16}$$

We now consider the fact that the measurement plane will be perpendicular to the propagation vector $\mathbf{k_0}$, and will be situated above the origin and outside the object, at a distance $z = l_0$. This implies that $l_0 - z' > 0, \forall z'$. This makes it possible to suppress the discontinuity in the integral, thus giving

$$u_B(x, y, l_0) = \frac{\mathrm{i}}{8\pi^2 k_z} \int_V o(\mathbf{r}') e^{\mathrm{i}k_0 z'} \left[\iint_{-\infty}^{\infty} e^{\mathrm{i}[\alpha(x-x')+\beta(y-y')+k_z(l_0-z')]} \mathrm{d}\alpha \mathrm{d}\beta \right] \mathrm{d}^3\mathbf{r}'. \tag{C.17}$$

Under the hypothesis of continuity, we now permute the integration order and arrange the terms, yielding

$$u_B(x, y, l_0) = \frac{\mathrm{i}}{8\pi^2 k_z} \iint_{-\infty}^{\infty} e^{\mathrm{i}[\alpha x+\beta y]} \left[\int_V o(\mathbf{r}') e^{-\mathrm{i}[\alpha x'+\beta y'+(k_z-k_0)z']} \mathrm{d}^3\mathbf{r}' \right] e^{\mathrm{i}k_z l_0} \mathrm{d}\alpha \mathrm{d}\beta. \tag{C.18}$$

We can note that the term in brackets in Eq. (C.18) is the Fourier transform of the function $o(\mathbf{r}')$, so that the integral can be expressed as

$$u_B(x, y, l_0) = \frac{\mathrm{i}}{8\pi^2 k_z} \iint_{-\infty}^{\infty} \hat{o}(\alpha, \beta, k_z - k_0) e^{\mathrm{i}k_z l_0} e^{\mathrm{i}[\alpha x+\beta y]} \mathrm{d}\alpha \mathrm{d}\beta. \tag{C.19}$$

Fourier transform of the measured field

The derivation of the theorem from this point is made easier by first demonstrating a certain Fourier property, which can be derived from standard conversions. As this part of the theorem

deals with a 2D measurement, we employ (k'_x, k'_y) coordinates to avoid confusion with the 3D space. In particular, the 2-dimensional Fourier transform of the unitary function is

$$1 \quad \xrightarrow{\mathscr{F}} \quad 2\pi\delta(k'_x)2\pi\delta(k'_y). \tag{C.20}$$

By using the definition of the Fourier transform, separability and the relation (C.20), we get

$$\begin{aligned} \iint e^{-\mathrm{i}(k'_x x + k'_y y)}\mathrm{d}x\mathrm{d}y &= 4\pi^2\delta(k'_x, k'_y), \\ \Rightarrow \iint e^{-\mathrm{i}[(k'_x-\alpha)x+(k'_y-\beta)y]}\mathrm{d}x\mathrm{d}y &= 4\pi^2\delta(k'_x-\alpha, k'_y-\beta), \\ \Rightarrow \iint e^{\mathrm{i}[(\alpha-k'_x)x+(\beta-k'_y)y]}\mathrm{d}x\mathrm{d}y &= 4\pi^2\delta(k'_x-\alpha, k'_y-\beta). \end{aligned} \tag{C.21}$$

The two-dimensional Fourier transform of the measured field $u_B(\boldsymbol{x})$ on the measurement plane l_0 can be expressed by definition as

$$\hat{u}_B(k'_x, k'_y, l_0) = \iint_{-\infty}^{\infty} u_B(x, y, l_0) e^{-\mathrm{i}[k'_x x + k'_y y]}\mathrm{d}x\mathrm{d}y. \tag{C.22}$$

Inserting Eq. (C.19) into Eq. (C.22) leads to

$$\hat{u}_B(k'_x, k'_y, l_0) = \iint_{-\infty}^{\infty} \left[\frac{\mathrm{i}}{8\pi^2 k_z} \iint_{-\infty}^{\infty} \hat{o}(\alpha, \beta, k_z - k_0) e^{\mathrm{i}k_z l_0} e^{\mathrm{i}[\alpha x + \beta y]}\mathrm{d}\alpha\mathrm{d}\beta \right] e^{-\mathrm{i}[k'_x x + k'_y y]}\mathrm{d}x\mathrm{d}y. \tag{C.23}$$

Again, under the hypothesis of continuity, permuting integration order in Eq. (C.23) leads to

$$\begin{aligned} &\hat{u}_B(k'_x, k'_y, l_0) \\ &= \frac{\mathrm{i}}{8\pi^2 k_z} \iint_{-\infty}^{\infty} \hat{o}(\alpha, \beta, k_z - k_0) e^{\mathrm{i}k_z l_0} \left[\iint_{-\infty}^{\infty} e^{\mathrm{i}[\alpha x + \beta y]} e^{-\mathrm{i}[k'_x x + k'_y y]}\mathrm{d}x\mathrm{d}y \right] \mathrm{d}\alpha\mathrm{d}\beta \\ &= \frac{\mathrm{i}}{8\pi^2 k_z} \iint_{-\infty}^{\infty} \hat{o}(\alpha, \beta, k_z - k_0) e^{\mathrm{i}k_z l_0} \left[\iint_{-\infty}^{\infty} e^{\mathrm{i}[(\alpha-k'_x)x+(\beta-k'_y)y]}\mathrm{d}x\mathrm{d}y \right] \mathrm{d}\alpha\mathrm{d}\beta \end{aligned} \tag{C.24}$$

On can note that the term in brackets in Eq. (C.24) corresponds exactly to the expression of Eq. (C.21), so that substitution leads to

$$\begin{aligned} \hat{u}_B(k'_x, k'_y, l_0) &= \frac{\mathrm{i}}{8\pi^2 k_z} \iint_{-\infty}^{\infty} \hat{o}(\alpha, \beta, k_z - k_0) e^{\mathrm{i}k_z l_0} 4\pi^2\delta(k'_x-\alpha, k'_y-\beta)\mathrm{d}\alpha\mathrm{d}\beta \\ &= \frac{\mathrm{i}}{2k_z} e^{\mathrm{i}k_z l_0} \iint_{-\infty}^{\infty} \hat{o}(\alpha, \beta, k_z - k_0)\delta(k'_x-\alpha, k'_y-\beta)\mathrm{d}\alpha\mathrm{d}\beta. \end{aligned} \tag{C.25}$$

The expression in Eq. (C.25) then corresponds to a 2-dimensional convolution of the object spectrum with a Dirac function, so that Eq. (C.25) can be simply expressed as

$$\hat{u}_B(k'_x, k'_y, l_0) = \frac{\mathrm{i}}{2k_z} e^{\mathrm{i}k_z l_o} \hat{o}(\alpha, \beta, k_z - k_0), \tag{C.26}$$

which completes the derivation.

Comments on the theorem

The expression in Eq. (C.26) can be slightly changed in order to make the appearance of object frequencies on a sphere more obvious. One can use the relation $k_z = \sqrt{k_0^2 - \alpha^2 - \beta^2}$ for propagating waves, and consider that couples (k'_x, k'_y) and (α, β) represent the same physical quantities, so that Eq. (C.26) becomes

$$\begin{aligned} \hat{u}_B(\alpha, \beta, l_0) &= \frac{\mathrm{i}}{2k_z} e^{\mathrm{i}k_z l_o} \hat{o}\left(\alpha, \beta, \sqrt{k_0^2 - \alpha^2 - \beta^2} - k_0\right), \\ &= \frac{\mathrm{i}}{2k_z} e^{\mathrm{i}k_z l_o} \hat{o}\left(\alpha, \beta, k_0\left(\sqrt{1 - \frac{\alpha^2}{k_0^2} - \frac{\beta^2}{k_0^2}} - 1\right)\right). \end{aligned} \tag{C.27}$$

showing that the spectral components of the measured field correspond to spectral components of the object situated on a cap of sphere of radius k_0, as it can be readily identified from the expression of k positions.

Rytov approximation

Identically to Born approximation, the Rytov approach is based on a perturbation formalism, but considers another Ansatz to solve Eq. (C.2), taken as

$$u(\mathbf{r}) = e^{\varphi(\mathbf{r})}. \tag{C.28}$$

The substitution of Eq. (C.28) into Eq. (C.2) yields (spatial coordinates are omitted for the sake of readability)

$$\begin{aligned} \left(\nabla^2 + k_o^2\right) e^{\varphi} &= -o(\mathbf{r}) e^{\varphi}, \\ \nabla\left(\nabla\varphi \cdot e^{\varphi}\right) + k_o^2 e^{\varphi} &= -o(\mathbf{r}) e^{\varphi}, \\ \nabla^2\varphi \cdot e^{\varphi} + \left(\nabla\varphi\right)^2 e^{\varphi} + k_o^2 e^{\varphi} &= -o(\mathbf{r}) e^{\varphi}, \\ \nabla^2\varphi + \left(\nabla\varphi\right)^2 + k_0^2 &= -o(\mathbf{r}). \end{aligned} \tag{C.29}$$

The perturbation method is then applied to the phase function, as

$$\varphi(\mathbf{r}) = \varphi_0(\mathbf{r}) + \varphi_s(\mathbf{r}), \qquad u_0(\mathbf{r}) = e^{\varphi_0(\mathbf{r})}. \tag{C.30}$$

By substituting Eq. (C.30) into Eq. (C.29), it yields

$$\begin{aligned}
\nabla^2\left(\varphi_0+\varphi_s\right)+\left[\nabla\left(\varphi_0+\varphi_s\right)\right]^2+k_0^2&=-o(\mathbf{r}),\\
\nabla^2\varphi_0+\nabla^2\varphi_s+\left(\nabla\varphi_0\right)^2+2\nabla\varphi_0\cdot\nabla\varphi_s+\left(\nabla\varphi_s\right)^2+k_0^2&=-o(\mathbf{r}),\\
\nabla^2\varphi_s+2\nabla\varphi_0\cdot\nabla\varphi_s+\left(\nabla\varphi_s\right)^2&=-o(\mathbf{r}),\\
2\nabla\varphi_0\cdot\nabla\varphi_s+\nabla^2\varphi_s&=-\left(\nabla\varphi_s\right)^2-o(\mathbf{r}),
\end{aligned} \tag{C.31}$$

where the solution of the homogeneous equation $\nabla^2\varphi_0+\left(\nabla\varphi_0\right)^2+k_0^2=0$ has been employed. At this point, Eq. (C.31) is still inhomogeneous. Its linearisation can then be performed by considering the relation

$$\begin{aligned}
\nabla^2\left(u_0\varphi_s\right)&=\nabla\left(\nabla u_0\cdot\varphi_s+u_0\cdot\nabla\varphi_s\right),\\
&=\nabla^2u_0\cdot\varphi_s+2\nabla u_0\cdot\nabla\varphi_s+u_0\cdot\nabla^2\varphi_s.
\end{aligned} \tag{C.32}$$

Assuming a plane wave, i.e. $u_0(\mathbf{r})=e^{\varphi_0}=e^{\mathrm{i}\mathbf{k_0}\cdot\mathbf{r}}$ leads to

$$\begin{aligned}
\nabla u_0&=\mathrm{i}k_0e^{\mathrm{i}\mathbf{k_0}\cdot\mathbf{r}}=\nabla\varphi_0u_0,\\
\nabla^2u_0&=(\mathrm{i}k_0)^2e^{\mathrm{i}\mathbf{k_0}\cdot\mathbf{r}}=-k_0^2u_0.
\end{aligned} \tag{C.33}$$

Substituting Eqs. (C.33) into Eq. (C.32) yields

$$\begin{aligned}
\nabla^2\left(u_0\varphi_s\right)&=-k_0^2u_0\cdot\varphi_s+2u_0\nabla\varphi_0\cdot\nabla\varphi_s+u_0\cdot\nabla^2\varphi_s,\\
\nabla^2\left(u_0\varphi_s\right)+k_0^2u_0\cdot\varphi_s&=2u_0\cdot\nabla\varphi_0\cdot\nabla\varphi_s+u_0\cdot\nabla^2\varphi_s.
\end{aligned} \tag{C.34}$$

Finally, substituting Eq. (C.34) into Eq. (C.31) yields

$$\begin{aligned}
\nabla^2\left(u_0\varphi_s\right)+k_0^2u_0\cdot\varphi_s&=-u_0\left(\nabla\varphi_s\right)^2-u_0\cdot o(\mathbf{r}),\\
\left(\nabla^2+k_0^2\right)u_0\varphi_s&=-u_0\left[\left(\nabla\varphi_s\right)^2+o(\mathbf{r})\right].
\end{aligned} \tag{C.35}$$

The structure of Eq. (C.35) is identical to Eq. (C.4), and can therefore be solved by employing a Green's function, and by using the Rytov approximation, i.e. $\left(\nabla\varphi_s\right)^2+o(\mathbf{r})\simeq o(\mathbf{r})$

$$\begin{aligned}
u_0\varphi_s&=\int_V u_0(\mathbf{r}')\left[\left(\nabla\varphi_s\right)^2+o(\mathbf{r}')\right]g(\mathbf{r}|\mathbf{r}')\mathrm{d}^3\mathbf{r}',\\
&\simeq\int u_0(\mathbf{r}')o(\mathbf{r}')g(\mathbf{r}|\mathbf{r}')\mathrm{d}^3\mathbf{r}'.
\end{aligned} \tag{C.36}$$

This implies that the Rytov approximation can be expressed in terms of the Born approximation

$$\varphi_s(\mathbf{r})=\frac{u_B(\mathbf{r})}{u_0(\mathbf{r})}. \tag{C.37}$$

Under the same demonstration as presented above, the Fourier diffraction theorem under Rytov's approximation can be expressed as

$$\mathscr{F}\left\{u_0\varphi_s\right\}(k'_x,k'_y,l_0)=\frac{\mathrm{i}}{2k_z}e^{\mathrm{i}k_z l_o}\hat{o}(\alpha,\beta,k_z-k_0). \tag{C.38}$$

Index

Nicolas Pavillon

Ch. de la Colline 5bis
1007 Lausanne
Switzerland
Tel: +41 (0)21 311 59 42

Born on Sep 25, 1982
Swiss Citizen
Married
E-mail: nicolas.pavillon@a3.epfl.ch

Education

2007–2011	**PhD in Photonics** Topic: Cellular Dynamics and Three-dimensional Refractive Index Distribution with Quantitative Phase Imaging	Swiss Institute of Technology in Lausanne (EPFL)
2004–2006	**Master** in Microengineering (spec. Applied Photonics) Master Topic: Cell tomography by digital holography	Swiss Institute of Technology in Lausanne (EPFL)
2001–2004	**Bachelor** in Microengineering	Swiss Institute of Technology in Lausanne (EPFL)
1998–2001	**Highschool**, specialisation in Mathematics & Physics Optional lectures: Chemistry and Latin	Lausanne, CH

Work Experience

2007–to date	**Scientific assistant** Research in the context of digital holography and microscopy, involving the responsibility of several experimental setups, and teaching activities in applied photonics.	EPFL (Advanced Photonics Laboratory), CH
2006–2007	**Intern** This internship was made in the software development group under the theme "Usage and evaluation of hybrid vision measuring system, and development of application software".	株式会社ミツトヨ / Mitutoyo Corp. (KDC), JP
March 2006	**Scientific assistant** Experimental work involving measurements on living organisms, with a digital holographic method applied to tomographic microscopy.	EPFL (Microvision & Microdiagnostic Group), CH
2002–2003	**Teaching assistant** Teaching during exercises and project development in C programming language.	EPFL (Virtual Reality Lab), CH

Membership & Affiliations

Optical Society of America (OSA) Student Member
Swiss-Japan Chamber of Commerce (SJCC) Alumni Member

Languages

French	Mother Tongue
English	Independent use of language. Able to adapt his vocabulary depending on the situation. Training course in Exeter, UK in 1999 (1 month) First Certificate of Cambridge obtained in 2002 (Telc B2)
Japanese	Middle use of language. Can lead a conversation in a daily life context. Language course in Kanazawa, JP (金沢、日本) in 2007 (3 month) Japanese-Language Proficiency Test (Level 3) obtained in 2008 (equivalent to Telc B2)
German	Average use of language. Understand and is understood in almost every situation. Zertifikat Deutsch obtained in 2005 (Telc B1)

Computer Skills

Good knowledge of	Windows XP, MacOS, Unix (BSD) Microsoft Office Suite, Adobe Suite, LaTeX, ProEngineer C, C++, Matlab, Labview, Visual Basic Access, HTML, PHP, SQL
Knowledge of	Java, R language, Cuda programming Zemax, GUI on MacOS (Carbon, Cocoa)

External Activities

2003–2004 **President of the Cineclub EPFL**

This activity required to lead a team of seven people to provide films at low price for students. It also implied to negotiate with firms about the prices of diffusion rights.

Hobbies

Role-Playing Games	Permits to develop creativity and organization faculties
Classical Guitar	Trains rigor and concentration in a creative way
Reading	Permits to discover different ways of thinking and new fields of knowledge

Publications

Peer-reviewed publications

First author

- N. Pavillon, C. Arfire, I. Bergoënd, and C. Depeursinge, "Iterative method for zero-order suppression in off-axis digital holography," *Opt. Express* **18** (15), pp. 15 318–15 331 (2010).
- N. Pavillon, A. Benke, D. Boss, C. Moratal, J. Kühn, P. Jourdain, C. Depeursinge, P. J. Magistretti, and P. Marquet, "Cell Morphology and Intracellular Ionic Homeostasis explored with a Multimodal Approach combining Epifluorescence and Digital Holographic Microscopy," *J. Biophotonics* **3** (7), pp. 432–436 (2010).
- N. Pavillon, C. S. Seelamantula, J. Kühn, M. Unser, and C. Depeursinge, "Suppression of the zero-order in off-axis digital holography through nonlinear filtering," *Appl. Opt.* **48** (34), H186–H195 (2009).

Co-author

- P. Jourdain, N. Pavillon, C. Moratal, D. Boss, B. Rappaz, C. Depeursinge, P. Marquet, and P. J. Magistretti, "Determination of transmembrane water fluxes in neurons elicited by glutamate ionotropic receptors and by the co-transporters KCC2 and NKCC1: a Digital Holographic Microscopy study," *J. Neurosci.*, (2011), (accepted).
- C. S. Seelamantula, N. Pavillon, C. Depeursinge, and M. Unser, "Exact Complex-Wave Reconstruction in Digital Holography," *J. Opt. Soc. Am. A* **28** (6), pp. 983–992 (2011).
- Y. Delacrétaz, E. Shaffer, N. Pavillon, J. Kühn, F. Lang, and C. Depeursinge, "Endoscopic low coherence topography measurement for upper airways and hollow samples," *J. Biomed. Opt.* **15** (6), p. 066 014 (2010).
- Y. Cotte, M. F. Toy, N. Pavillon, and C. Depeursinge, "Microscopy image resolution improvement by deconvolution of complex fields," *Opt. Express* **18** (19), pp. 19 462–19 478 (2010).
- Y. Cotte, M. F. Toy, E. Shaffer, N. Pavillon, and C. Depeursinge, "Sub-Rayleigh resolution by phase imaging," *Opt. Lett.* **35** (13), pp. 2176–2178 (2010) .
- T. Colomb, N. Pavillon, C. Depeursinge, and Y. Emery, "Extended depth-of-focus by digital holographic microscopy," *Opt. Lett.* **35** (11), pp. 1840–1842 (2010).
- T. Colomb, S. Krivec, H. Hutter, A. A. Akatay, N. Pavillon, F. Montfort, E. Cuche, J. Kühn, C. Depeursinge, and Y. Emery, "Digital holographic reflectometry," *Opt. Express* **18** (4), pp. 3719–3731 (2010).
- Y. Delacrétaz, N. Pavillon, C. Depeursinge, and F. Lang, "Off-axis low coherence interferometry contouring," *Opt. Commun.* **282** (23), pp. 4595–4601 (2009).
- E. Shaffer, N. Pavillon, J. Kühn, and C. Depeursinge, "Digital holographic microscopy investigation of second harmonic generated at a glass/air interface," *Opt. Lett.* **34** (16), pp. 2450–2452 (2009).
- J. Kühn, F. Montfort, T. Colomb, B. Rappaz, C. Moratal, N. Pavillon, P. Marquet, and C. Depeursinge, "Submicrometer tomography of cells by multiple-wavelength digital holographic microscopy in reflection," *Opt. Lett.* **34** (5), pp. 653–655 (2009).
- F. Charrière, N. Pavillon, T. Colomb, C. Depeursinge, T. J. Heger, E. A. D. Mitchell, P. Marquet, and B. Rappaz, "Living specimen tomography by digital holographic microscopy: morphometry of testate amoeba," *Opt. Express* **14** (16), pp. 7005–7013 (2006).

Patents

- Y. Cotte, N. Pavillon, and C. Depeursinge, "Complex index refraction tomography with sub $\lambda/6$-resolution," pat. PCT/IB2011/051306, (pending) (2011).
- N. Pavillon, J. Kühn, P. Jourdain, E. Cuche, C. Depeursinge, P. J. Magistretti, and P. Marquet, "Apparatus and method for early diagnosis of cell death," pat. PCT/IB2010/053768, (pending) (2010).
- N. Pavillon, C. S. Seelamantula, M. Unser, and C. Depeursinge, "A method and apparatus for enhanced spatial bandwidth wavefronts reconstructed from digital interferograms or holograms," pat. WO 2010/122530 (2010).

Books

- C. Depeursinge, P. Marquet, and N. Pavillon, "Application of Digital Holographic Microscopy in Biomedicine," in *Handbook of Biomedical Optics*, D. A. Boas, C. Pitris, and N. Ramanujam, Eds., CRC Press (Jun. 2011).

Proceedings

First author

- N. Pavillon, J. Kühn, P. Jourdain, C. Depeursinge, P. J. Magistretti, and P. Marquet, "Cell Death Detection and Ionic Homeostasis monitoring with Digital Holographic Microscopy," in *Novel Optical Instrumentation for Biomedical Applications V*, vol. 8090, p. 809 004, SPIE, Munich, Germany (Jun. 2011).
- N. Pavillon, J. Kühn, P. Jourdain, C. Depeursinge, P. J. Magistretti, and P. Marquet, "Cell Death and Ionic Regulation Detection with Digital Holographic Microscopy," in *Digital Holography and Three-Dimensional Imaging (DH)*, OSA, DTuC25, Tokyo, Japan (May 2011).
- N. Pavillon, J. Kühn, P. Jourdain, C. Depeursinge, P. J. Magistretti, and P. Marquet, "Early Glutamate-mediated Cell Death Detection with Digital Holographic Microscopy," in *Novel Techniques in Microscopy*, JTuA13, OSA, Monterey, CA (Apr. 2011).
- N. Pavillon, C. S. Seelamantula, M. Unser, and C. Depeursinge, "Artifact-free reconstruction from off-axis digital holograms through nonlinear filtering," in *Optics, Photonics, and Digital Technologies for Multimedia Applications*, vol. 7723, 77231U–9, SPIE, Brussels, Belgium (Apr. 2010).
- N. Pavillon, A. Benke, D. Boss, C. Moratal, P. Jourdain, Y. Emery, C. Depeursinge, P. J. Magistretti, and P. Marquet, "Study of Intracellular Ion Dynamics with a Multimodality Approach Combining Epifluorescence and Digital Holographic Microscopy," in *Digital Holography and Three-Dimensional Imaging (DH)*, JMA26, OSA, Miami, FL (Apr. 2010).
- N. Pavillon, C. S. Seelamantula, M. Unser, and C. Depeursinge, "A Nonlinear Technique for Automatic Twin-Image and Zero-Order Term Suppression in Digital Holographic Microscopy," in *Fringe 2009, The 6th International Workshop on Advanced Optical Metrology*, pp. 160–163, Springer, Nürtingen, Germany (Sep. 2009).
- N. Pavillon, J. Kühn, F. Charrière, and C. Depeursinge, "Optical tomography by digital holographic microscopy," in *Novel Optical Instrumentation for Biomedical Applications IV*, vol. 7371, pp. 737 104–6, SPIE, Munich, Germany (Jul. 2009).

Co-author

- S. S. Kou, C. J. R. Sheppard, N. Pavillon, P. Marquet, and C. Depeursinge, "Quantitative phase from defocus," in *Novel Techniques in Microscopy*, NTuC6, OSA, Monterey, CA (Apr. 2011).
- T. Colomb, Y. Emery, I. Bergoënd, A. A. Akatay, N. Pavillon, J. Kühn, and C. Depeursinge, "Réflectométrie holographique numérique appliquée à la métrologie des fluides.," in *1^{re} rencontre francophone d'holographie numérique appliquée à la métrologie des fluides*, Rouen, France (Oct. 2010).
- P. Marquet, J. Kühn, D. Boss, P. Jourdain, P. Magistretti, N. Pavillon, and C. Depeursinge, "Progress and perspectives in digital holographic microscopy applied to life sciences," in *9th Euro-American Workshop on Information Optics, WIO*, pp. 1–4, IEEE, Helsinki, Finland (Jul. 2010).
- I. Bergoënd, C. Arfire, N. Pavillon, and C. Depeursinge, "Diffraction tomography for biological cells imaging using digital holographic microscopy," in *Laser Applications in Life Sciences*, vol. 7376, p. 737 613, SPIE, Oulu, Finland (Jun. 2010).
- Y. Cotte, M. F. Toy, N. Pavillon, and C. Depeursinge, "Studies on synthetic deconvolution of complex fields with digital holographic microscopy," in *Proceedings of Focus on Microscopy*, ser. Phase microscopy, MO–MOPAR–C–, Shanghai, China (Mar. 2010).
- C. Depeursinge, I. Bergoënd, N. Pavillon, J. Kühn, T. Colomb, F. Montfort, E. Cuche, and Y. Emery, "Measuring Shape and Surfaces down to the Nanometer and Nanosecond scales by Digital Holographic Microscopy," in *Fringe 2009, The 6th International Workshop on Advanced Optical Metrology*, pp. 411–415, Springer, Nürtingen, Germany (Sep. 2009).
- I. Bergoënd, N. Pavillon, F. Charrière, and C. Depeursinge, "Optical tomography with digital holographic microscopy," in *3rd EOS Topical Meeting on Optical Microsystems*, EOS, Capri, Italy (Sep. 2009).
- I. Bergoënd, T. Colomb, N. Pavillon, Y. Emery, and C. Depeursinge, "Depth-of-field extension and 3D reconstruction in digital holographic microscopy," in *Modeling Aspects in Optical Metrology II*, vol. 7390, pp. 73901C–10, SPIE, Munich, Germany (Jun. 2009).
- C. Depeursinge, J. Kühn, P. Jourdain, D. Boss, N. Pavillon, Y. Emery, P. Marquet, and P. Magistretti, "La microscopie holographique digitale appliquée à l'imagerie cellulaire," in *Imagerie pour les sciences du vivant et la médecine (IMVIE)*, Mulhouse, France (Jun. 2009).
- C. S. Seelamantula, N. Pavillon, C. Depeursinge, and M. Unser, "Zero-order-free image reconstruction in digital holographic microscopy," in *IEEE International Symposium on Biomedical Imaging: From Nano to Macro, ISBI.*, pp. 201–204, IEEE, Boston, MA (Jun. 2009).
- J. Kühn, F. Montfort, T. Colomb, B. Rappaz, C. Moratal, N. Pavillon, P. Marquet, and C. Depeursinge, "Tomography of Red Blood Cells by Multiple-Wavelength Digital Holographic Microscopy," in *Digital Holography and Three-Dimensional Imaging (DH)*, DTuA3, OSA, Vancouver, Canada (Apr. 2009).
- I. Bergoënd, T. Colomb, N. Pavillon, Y. Emery, and C. Depeursinge, "Extended Depth-of-Field and 3D Information Extraction in Digital Holographic Microscopy," in *Digital Holography and Three-Dimensional Imaging (DH)*, DWB5, OSA, Vancouver, Canada (Apr. 2009).
- E. Shaffer, N. Pavillon, J. Kühn, and C. Depeursinge, "Second Harmonic and Fundamental Wavelength Digital Holographic Microscopy," in *Novel Techniques in Microscopy (NTM)*, JTuA3, OSA, Vancouver, Canada (Apr. 2009).
- J. Kühn, F. Montfort, T. Colomb, B. Rappaz, C. Moratal, N. Pavillon, P. Marquet, and C. Depeursinge, "Red blood cell tomography in reflection by multiple-wavelength digital holographic microscopy," in *Focus On Microscopy*, ser. Holography and data storage, WE–MO1PAR–D–, Krakow, Poland (Apr. 2009).
- C. Depeursinge, N. Pavillon, J. Kühn, T. Colomb, and P. Marquet, "Refractive Index Tomography by Digital Holographic Microscopy," in *Digital Holography and Three-Dimensional Imaging (DH)*, DTuC3, OSA, St. Petersburg, FL (Mar. 2008).
- F. Charrière, N. Pavillon, T. Colomb, E. Cuche, Y. Emery, P. Marquet, B. Rappaz, and C. Depeursinge, "Quantitative refractive index micro-tomography with Digital Holographic Microscopy: an efficient tool for metrology in nanotechnology and life sciences," in *The 10th Annual European Conference On Micro&Nanoscale Technologies for the Biosciences*, vol. 10, Montreux, Switzerland (Nov. 2006).

- F. Charrière, N. Pavillon, T. Colomb, T. Heger, E. Mitchell, P. Marquet, B. Rappaz, and C. Depeursinge, "Digital Holographic Microscopy for quantitative micro-tomography of living specimen: volume estimation of Hyalosphenia papilio," in *Annual Meeting of the European Optical Society: Biophotonics and Biomedical Optics (QEOD/EPS and EOS)*, EOS, Paris, France (Oct. 2006).

Conference presentations

- N. Pavillon, J. Kühn, P. Jourdain, C. Depeursinge, P. J. Magistretti, and P. Marquet, "Cell Death Detection and Ionic Homeostasis monitoring with Digital Holographic Microscopy," in *Novel Optical Instrumentation for Biomedical Applications V*, Munich, Germany (Jun. 2011).
- M. F. Toy, J. Kühn, J. Parent, C. Pache, M. Egli, and C. Depeursinge, "Real Time 3-D Cytomorphological Imaging Using Digital Holographic Microscopy and Fluorescence Microscopy for Space Biology," in *Digital Holography and Three-Dimensional Imaging (DH)*, Miami, FL (Apr. 2010).
- C. Depeursinge, I. Bergoënd, N. Pavillon, J. Kühn, T. Colomb, F. Montfort, E. Cuche, and Y. Emery, "Measuring Shape and Surfaces down to the Nanometer and Nanosecond scales by Digital Holographic Microscopy," in *Fringe 2009, The 6th International Workshop on Advanced Optical Metrology*, Nürtingen, Germany (2009).
- N. Pavillon, J. Kühn, F. Charrière, and C. Depeursinge, "Optical tomography by digital holographic microscopy," in *Novel Optical Instrumentation for Biomedical Applications IV*, Munich, Germany (Jul. 2009).
- T. Colomb, F. Charrière, J. Kühn, P. Marquet, and C. Depeursinge, "Advantages of digital holographic microscopy for real-time full field absolute phase imaging," in *Three-Dimensional and Multidimensional Microscopy: Image Acquisition and Processing XV*, San Jose, CA (Jan. 2008).
- J. Kühn, T. Colomb, C. Pache, F. Charrière, F. Montfort, E. Cuche, Y. Emery, P. Marquet, and C. Depeursinge, "Real-time dual-wavelength digital holographic microscopy for extended measurement range with enhanced axial resolution," in *Three-Dimensional and Multidimensional Microscopy: Image Acquisition and Processing XV*, San Jose, CA (Jan. 2008).
- P. Marquet, B. Rappaz, F. Charrière, T. Colomb, J. Kühn, N. Pavillon, C. Depeursinge, and P. J. Magistretti, "Cell dynamics revealed by digital holographic microscopy," in *Three-Dimensional and Multidimensional Microscopy: Image Acquisition and Processing XV*, San Jose, CA (Feb. 2008).
- B. Rappaz, A. Barbul, F. Charrière, J. Kühn, P. Marquet, R. Korenstein, C. Depeursinge, and P. Magistretti, "Erythrocytes analysis with a Digital Holographic Microscope," in *Novel Optical Instrumentation for Biomedical Applications III*, Munich, Germany (Jun. 2007).